AFRL-AFOSR-UK-TR-2017-0004

Magneto-Hydro-Dynamics Liquid Wheel Actuator for Spacecraft Attitude

Fabio Curti
UNIVERSITA' DEGLI STUDI DI ROMA LA SAPIENZA

01/26/2017
Final Report

Air Force Research Laboratory
AF Office Of Scientific Research (AFOSR)/ IOE
Arlington, Virginia 22203
Air Force Materiel Command

REPORT DOCUMENTATION PAGE

Form Approved
OMB No. 0704-0188

1. REPORT DATE *(DD-MM-YYYY)*	2. REPORT TYPE	3. DATES COVERED *(From - To)*
02-02-2017	Final	30 Sep 2014 to 29 Sep 2016

4. TITLE AND SUBTITLE
Magneto-Hydro-Dynamics Liquid Wheel Actuator for Spacecraft Attitude Control

5a. CONTRACT NUMBER

5b. GRANT NUMBER
FA9550-14-1-0387

5c. PROGRAM ELEMENT NUMBER
61102F

6. AUTHOR(S)
Fabio Curti

5d. PROJECT NUMBER

5e. TASK NUMBER

5f. WORK UNIT NUMBER

7. PERFORMING ORGANIZATION NAME(S) AND ADDRESS(ES)
UNIVERSITA' DEGLI STUDI DI ROMA LA SAPIENZA
VIA EUDOSSIANA 18
ROMA, 00184 IT

8. PERFORMING ORGANIZATION REPORT NUMBER

9. SPONSORING/MONITORING AGENCY NAME(S) AND ADDRESS(ES)
EOARD
Unit 4515
APO AE 09421-4515

10. SPONSOR/MONITOR'S ACRONYM(S)
AFRL/AFOSR IOE

11. SPONSOR/MONITOR'S REPORT NUMBER(S)
AFRL-AFOSR-UK-TR-2017-0004

12. DISTRIBUTION/AVAILABILITY STATEMENT
A DISTRIBUTION UNLIMITED: PB Public Release

13. SUPPLEMENTARY NOTES

14. ABSTRACT
A novel actuator for spacecraft attitude control with liquid flywheel is presented. The main characteristic of this new concept of reaction wheel is that a conductive liquid rather than a solid mass is accelerated to change the angular momentum of the equipment and, as a consequence, to provide torque to the spacecraft. The conductive liquid is accelerated using a conductive Magneto-Hydro-Dynamic (MHD) pump. Two different configurations of the device have been studied on the basis of the optimization of the dimensionless moment of inertia and the minimization of the viscous shear. A 2-dimensional Finite Difference Hybrid Model (FDHM) has been developed on the basis of the MHD set of equations under the hypothesis of low Magnetic Reynolds. The model solves numerically the time dependent axially symmetric problem of an electrically conductive liquid rotating in a torus with rectangular cross section due to the interaction of a radial magnetic field and an axial electric field. The electric side of the problem has been solved by means of the node method applied to a network of electric resistances and voltage generators representing the back electromotive voltage induced by the spinning liquid through the magnetic field. The fluid-dynamics side of the problem has been solved using a Crank-Nicolson method over a non uniform and collocated grid. The grid generator has been written to be sensitive to the Hartmann number of the problem. Several simulations has been made, over 600, in order to test the FDHM and in order to outline the performances of the device. The model has been tested numerically checking the accuracy of the computed dynamic and electric quantities.

15. SUBJECT TERMS
EOARD, ADCS, spacecraft attitude control, liquid wheel actuator, magneto-hydro-dynamics, momentum management, angular momentum

16. SECURITY CLASSIFICATION OF:			17. LIMITATION OF ABSTRACT	18. NUMBER OF PAGES	19a. NAME OF RESPONSIBLE PERSON
a. REPORT	b. ABSTRACT	c. THIS PAGE			MILLER, KENT
Unclassified	Unclassified	Unclassified	SAR	10	19b. TELEPHONE NUMBER *(Include area code)* 011-44-1895-616022

Standard Form 298 (Rev. 8/98)
Prescribed by ANSI Std. Z39.18

Awards Number:
FA9550-14-1-0387

Period of Performance:
30th September 2015 - 29th December 2016

Research Title:

Magneto-Hydro-Dynamics Liquid Wheel Actuator for Spacecraft Attitude Control

Final Report

Principal Investigator:
Prof. Fabio Curti
Institution:
Sapienza - University of Rome.

Contents

List of Figures

List of Tables

List of Symbols

Symbol	Units	Description
r		Radial direction
θ		Azimuthal direction
z		Axial direction
s		Dimensionless radius
t	$[s]$	Time
ρ	$[Kg/m^3]$	Density
μ	$[Pa\ s]$	Viscosity
σ	$[S\ m]$	Electric Conductivity
μ_m	$[N/A^2]$	Magnetic Permeability
r_i	$[m]$	Inner Radius
r_e	$[m]$	Outer Radius
L	$[m]$	$r_e - r_i$
h	$[m]$	Height
$\mathbf{J}$	$[A/m^2]$	Electric Current Density
$\mathbf{j}$		Dimensionless Electric Current Density
$\tilde{\mathbf{j}}$	$[A/m^2]$	Infinitesimal perturbation of the Electric Current Density
$\mathbf{E}$	$[V/m]$	Electric Field
$\mathbf{e}$		Dimensionless Electric Field
$\tilde{\mathbf{e}}$	$[V/m]$	Infinitesimal perturbation of the Electric Field
$\mathbf{B}$	$[T]$	Magnetic Field
$\mathbf{b}$		Dimensionless Magnetic Field
$\tilde{\mathbf{b}}$	$[T]$	Infinitesimal perturbation of the Magnetic Field
$\mathbf{U}$	$[m/s]$	Velocity
u		Dimensionless Velocity
ϕ	$[V]$	Electric Potential
I_z	$[Kg\ m^2]$	Moment of inertia
$\tilde{I}_z$		Dimensionless moment of inertia
m	$[Kg]$	Mass
Re_m		Magnetic Reynolds Number
Re		Reynolds Number
Ha		Hartmann Number
K_{vis}	$[Nm/s]$	Coefficient of viscous shear moment
K_I	$[Nm/A]$	Coefficient of Lorentz force moment
c_ω		Coefficient of the moment of inertia

I'_z	$[Kg\ m^2]$	Modified moment of inertia - c_ω/I_z
K_V	$[V/s]$	Coefficient of the induced voltage
R_eq	$[\Omega]$	Electrical Resistance
τ_c	$[s]$	Characteristic time
Γ	$[Nms]$	Angular Momentum
$\dot{\Gamma}$	$[Nm]$	Torque
I	$[A]$	Supplied electric current
I_z^c	$[A]$	Electric current in the axial branches
a	$[A/s]$	Current slope
b	$[V/s]$	Voltage slope

List of Acronyms

Acronyms	Meaning
MHD	Magneto Hydro Dynamics
FDM	Finite Difference Model
$FDHM$	Finite Difference Hybrid Model
LPM	Lumped Parameter Model
EOS	End Of Simulation

Summary

A novel actuator for spacecraft attitude control with liquid flywheel is presented. The main characteristic of this new concept of reaction wheel is that a conductive liquid rather than a solid mass is accelerated to change the angular momentum of the equipment and, as a consequence, to provide torque to the spacecraft. The conductive liquid is accelerated using a conductive Magneto-Hydro-Dynamic (MHD) pump. Two different configurations of the device have been studied on the basis of the optimization of the dimensionless moment of inertia and the minimization of the viscous shear.

A 2-dimensional Finite Difference Hybrid Model (FDHM) has been developed on the basis of the MHD set of equations under the hypothesis of low Magnetic Reynolds. The model solves numerically the time dependent axially symmetric problem of an electrically conductive liquid rotating in a torus with rectangular cross section due to the interaction of a radial magnetic field and an axial electric field. The electric side of the problem has been solved by means of the node method applied to a network of electric resistances and voltage generators representing the back electromotive voltage induced by the spinning liquid through the magnetic field. The fluid-dynamics side of the problem has been solved using a Crank-Nicolson method over a non uniform and collocated grid. The grid generator has been written to be sensitive to the Hartmann number of the problem.

Several simulations has been made, over 600, in order to test the FDHM and in order to outline the performances of the device. The model has been tested numerically checking the accuracy of the computed dynamic and electric quantities.

A Lumped Parameter Model (LPM) has been developed using two stationary analytical solutions of the MHD set of equations. The LPM has been compared with the results obtained with the FDHM, showing good agreement in the estimation of the coefficients of the model in both the cases of high and low electrically conductive liquid. Finally a parametric performance analysis has been conducted by means of the best set of formulas to compute the LPM coefficients in order to outline the performances of the device for several geometric dimension of the torus containing the conductive liquid and for several values of electric conductivity of the liquid.

Chapter

1 Introduction

The ability to control spacecraft attitude and the reliability of the attitude control system are key components of space missions. Also, future Earth observation missions, as well as astronomical observation missions, require satellites which are more agile and with high pointing stability over the higher lifetime possible.
A number of techniques have been developed and refined to underpin attitude control and re-pointing, but basically since the beginning of the space exploration era all techniques used for high performance attitude control exploit the use of reaction and, in some cases, momentum wheels.
The technology improvement during this time allowed reaction wheels to improve their performance in terms of control resolution and reliability and efficiency of the electronic part but there are some drawbacks related to standard reaction wheel design that were not improved over time. In particular we can mention some of the more important drawbacks like:

- Standard reaction wheels use moving mechanical parts which reduce the overall reliability of the equipment and increase its overall complexity.
- Jitter and other unbalances associated with moving masses lead to unwanted high frequency disturbances on the satellite itself which could be critical for demanding high resolution observation missions.
- The presence of electric motors in standard reaction wheels induces a ripple disturbance on the torque provided.
- The torque provided by standard reaction wheels is typically non linear in the neighbourhood of the zero angular velocity.

In the last years some articles have been published regarding the possibilities to use active fluid loops as actuator for spacecraft attitude control, [1] [2]. This kind of actuators uses hydraulic pumps to accelerate a low viscosity liquid inside a torus with circular cross section. These devices have the advantage to reduce the mechanical unbalances typical of classical reaction wheels with solid flywheel but they do not increase the reliability of the actuator because of the presence of a spinning electric engine in the hydraulic pump.
A novel actuator for spacecraft attitude control is proposed. The main characteristic of this new concept of a reaction wheel is that a conductive liquid

rather than a solid mass is accelerated to change the angular momentum of the equipment and, as a consequence, to provide the torque to the spacecraft. The conductive liquid inside an annulus with rectangular cross section is accelerated using the Lorentz force originated from the interaction between an electric current flowing through the fluid and a magnetic field. In this way the electric engine can be removed with the advantage to remove any ripple disturbance and to improve the overall reliability of the equipment.
In the past and in particular in the last years the interest in this kind actuators increased, [3] [4] [5] [6] [7] [8] [9].
The lack of accurate mathematical models describing the behaviour of the device brought this study to start from the basis of the magneto-hydro-dynamics problem to obtain a numeric model able to model the real physics of the problem. The model is then used to better characterize the actuator and to have information about its performances and limitations.

Chapter

2 Configurations: Distributed Magnetic Field

In this chapter, a preliminary analysis of the optimal configuration for a reaction wheel with distributed conduction Magneto-Hydro-Dynamics pumps is presented.

2.1 Working principle

The main feature of this new concept of reaction wheel is that an electrically conductive fluid rather than a solid mass is accelerated to change the angular momentum and to provide a controlling torque to the spacecraft. The Lorentz force is used to accelerate the conductive liquid [10]. This driving force originates from the interaction between a magnetic field and an electric current flowing through the fluid, Figure 2.1.
The externally applied magnetic field is provided by permanent magnets because the use of magnetic coils would increase the total power consumption of the actuator and this is not convenient for a device whose use is addressed to space application, where power resources are usually limited. The magnetic field in this section is considered distributed to all the volume where the liquid is placed.

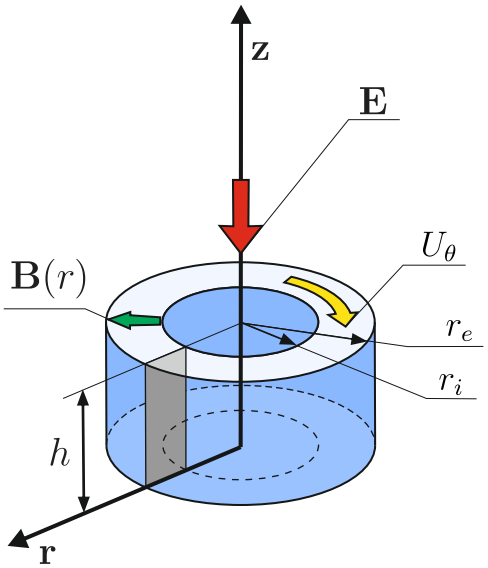

Figure 2.1: *Section of an annulus with applied electric field* $\mathbf{E}$ *and radial magnetic field* $\mathbf{B}(r)$.

The spin of the liquid can be controlled in intensity and direction by means of the electric current sent to device. The inversion of the direction of the electric current switches the direction of the Lorentz force acting as body force on the fluid.

The liquid is placed in an annulus with a rectangular cross section and it rotates along the azimuthal direction. The Lorentz force acts in the direction in which the electrically conductive fluid is free to flow.

2.2 Configurations of the device

The maximum Lorentz force obtainable from the interaction between an electric current and a magnetic field appears when the two fields are mutually perpendicular [11]. This, together with the advantage to have the conductive liquid placed in an axially-symmetric container leads to two possible arrangements of magnetic field and electric current and two different configurations for the MHD actuator, Figure (2.2):

- *Axial magnetic field configuration*: this configuration takes into account an electric current along the radial direction r and a magnetic field along the axial direction z [5] [12] [4].
- *Radial magnetic field configuration*: this configuration switches the first configuration considering an electric current along the axial direction z and a magnetic field along the radial direction r [11] [3].

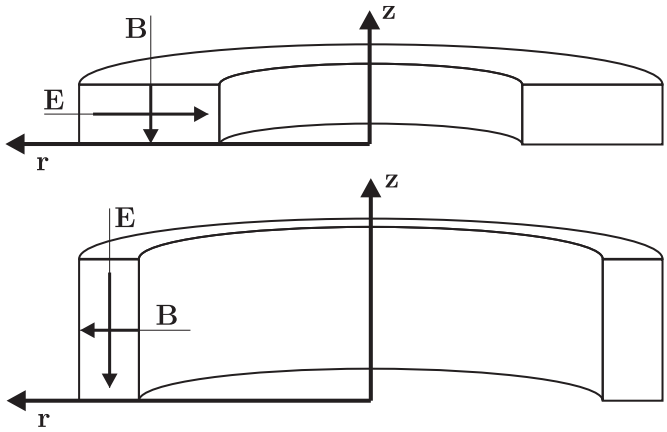

Figure 2.2: *First (top) and second configuration (bottom) for electric field E and magnetic field B*

Both the configurations provide a force in the requested direction. The advantage to use one of two configurations has been evaluated on the basis of the maximization of the dimensionless moment of inertia.

2.3 Dimensionless Moment of Inertia

The dimensionless moment of inertia $\tilde{I}_z$ gives a numerical indication of how efficiently a mass is used to generate angular momentum. To obtain the value of $\tilde{I}_z$ for a hollow cylinder we need to divide the dimensional moment of inertia by the mass and the squared external radius of the cylinder. We obtain:

$$I_z = \frac{m\,(r_e^2 + r_i^2)}{2} \qquad \tilde{I}_z = \frac{I_z}{m r_e^2} = \frac{1+\beta^2}{2} \tag{2.3.1}$$

where r_e is the outer radius of the hollow cylinder, r_i is the inner radius of the hollow cylinder, β is the ratio r_i/r_e and m is the mass of the liquid.

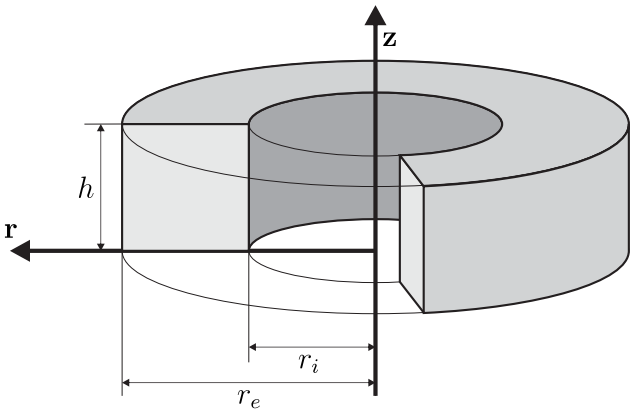

Figure 2.3: *Hollow Cylinder and symbols meaning*

We can see that $\tilde{I}_z$ is independent from the height of the cylinder. It assumes its maximum value when the inner radius approaches the outer radius, i.e. for thin cylinders.

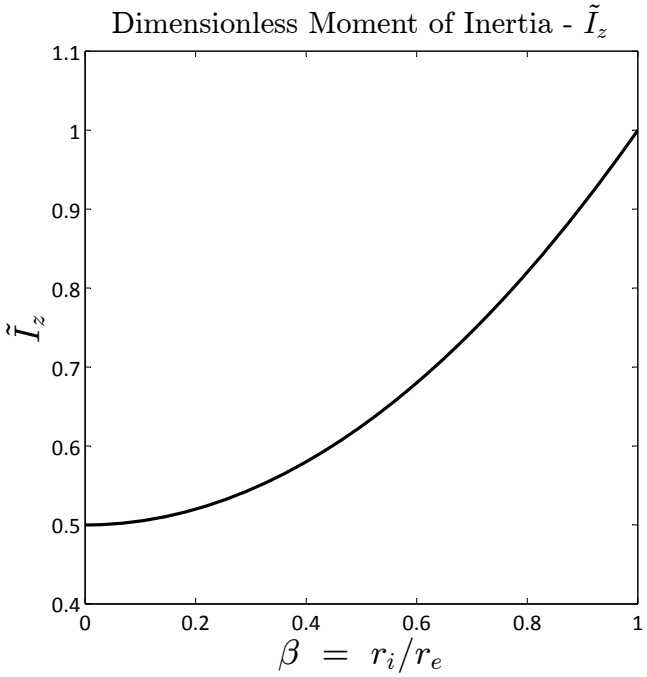

Figure 2.4: *Dimensionless Moment of Inertia*

2.4 Comparison between configurations

We start pointing out that in both the configurations the dimension parallel to the magnetic field is constrained in order to have a homogeneous magnetic field in the air gap of the magnetic circuit. It means that the height h of the device in the first configuration and the radial length of the cross section, $L = r_e - r_i$, in the second one cannot be greater than a certain value.
In Figure (2.5) it is evident that where the dimensionless moment of inertia has its maximum we have the minimum of the dimensional moment of inertia. For the axial magnetic field configuration, if the device has an almost optimal dimensionless moment of inertia it is not possible to have a great dimensional moment of inertia due to the limitation of the height h of the device.

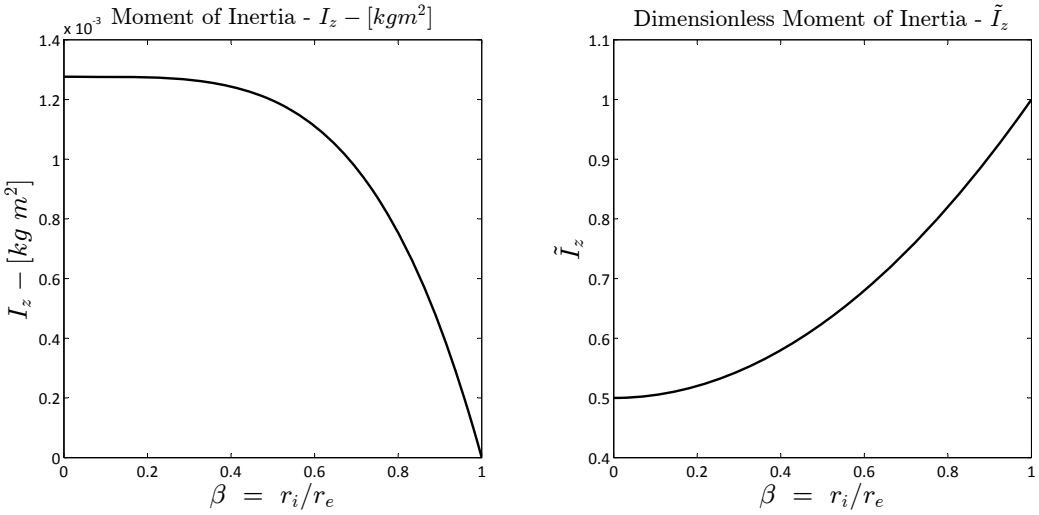

Figure 2.5: *Dimensional and Dimensionless Moment of Inertia - 1^{st} Configuration*

For the radial magnetic field configuration the device can be characterized by an almost optimal dimensionless moment of inertia and it it is possible to obtain the desired dimensional moment of inertia modifying the height of the device, not constrained in this configuration.

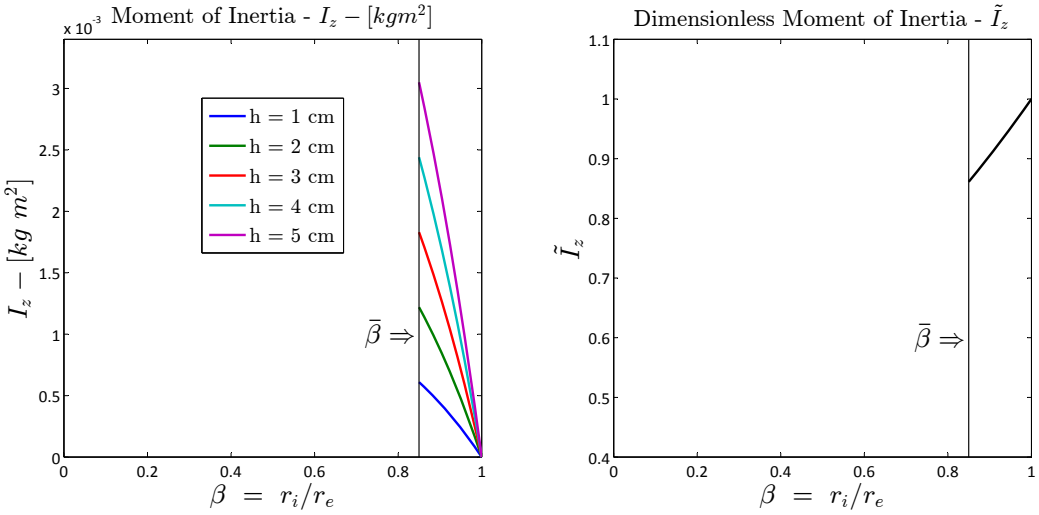

Figure 2.6: *Dimensional and Dimensionless Moment of Inertia - 2^{st} Configuration*

We could think to stack several annuli according to the axial magnetic field

configuration in order to obtain the desired moment of inertia while optimizing the dimensionless moment of inertia, Figure (2.7), as already studied in [5]. This approach, anyway, would increase the contact surface between the liquid and cavity, and then the viscous shear, more than how it would increase choosing the second configuration.

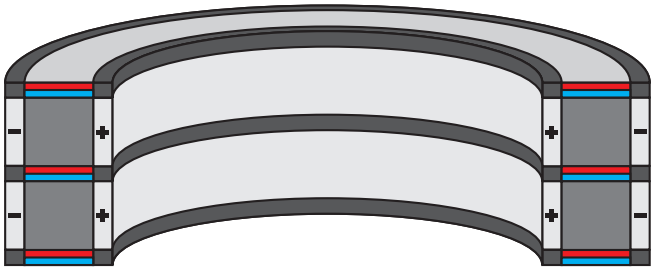

Figure 2.7: *MHD Fluid Loop - 1^{st} Configuration*

We can conclude that the second configuration, characterized by a radial magnetic field and an axial electric field, maximizes the dimensionless moment of inertia while optimizing the contact surface of the conductive liquid. It represents a more easily scalable configuration in which the required moment of inertia of the liquid flywheel can be met just varying the height of device.
The device, according to the selected configuration, has electric plates on the top and on the bottom sides and two concentric cylindrical magnets generating a radial magnetic field. The conductive fluid is placed in the air gap of the hollow cylinder, Figure (2.8). The spin direction of the liquid can be switched by changing the direction of the electric field between the two plates.

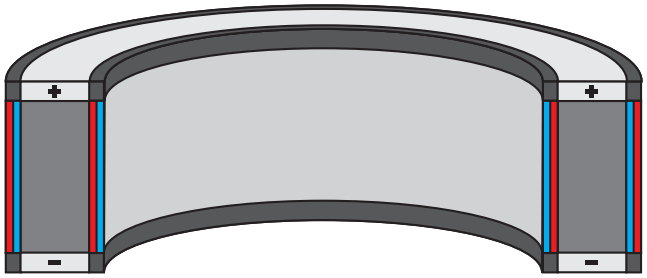

Figure 2.8: *MHD Fluid Loop - 2^{nd} Configuration*

Chapter

3 Assumptions: Axially-symmetric MHD problem and Low Re_m approximation.

In this chapter, the MHD set of equations describing the problem are presented in details. The equations are set to solve the 2-dimensional axially-symmetric problem of an electrically conductive liquid rotating in a torus with rectangular cross section under the interaction of a radial magnetic field and an axial electric field.

3.1 Complete MHD set of equations

The physics of the Magneto-Hydro-Dynamics (MHD) phenomena is generally described by a set of equations taking into account the mutual interactions among the velocity field, the electric field and the magnetic field, [13] [14].
The complete MHD set of equations includes Maxwell's equations, (3.1.1) (3.1.2) (3.1.3) and (3.1.4), Ohm's law applied to a moving conductive medium (3.1.5), together with the fluid-dynamics equation for a viscous fluid on which acts an electromagnetic body force (3.1.6) and the continuity equation (3.1.7).

$$\nabla \times \mathbf{E} = -\frac{\partial \mathbf{B}}{\partial t} \tag{3.1.1}$$

$$\nabla \cdot \mathbf{B} = 0 \tag{3.1.2}$$

$$\nabla \times \mathbf{B} = 4\pi\mu_m \mathbf{J} \tag{3.1.3}$$

$$\nabla \cdot \mathbf{J} = 0 \tag{3.1.4}$$

$$\mathbf{J} = \sigma(\mathbf{E} + \mathbf{U} \times \mathbf{B}) \tag{3.1.5}$$

$$\rho\frac{\partial \mathbf{U}}{\partial t} + \rho(\mathbf{U} \cdot \nabla)\mathbf{U} = -\nabla P_n + \nu\rho\Delta\mathbf{U} + \mathbf{J} \times \mathbf{B} \tag{3.1.6}$$

$$\nabla \cdot \mathbf{U} = 0 \tag{3.1.7}$$

where $\mathbf{E}$ is the electric field, $\mathbf{B}$ is the magnetic field, $\mathbf{J}$ is the electric current density, $\mathbf{U}$ is the velocity of the fluid and μ, ρ, μ_m and σ are respectively the dynamic viscosity, density, magnetic permeability and electric conductivity of the working liquid. In order to simplify the set three assumptions are considered:

- The flow is considered laminar
- The problem is considered axially-symmetric and it is solved over the $r - z$ domain.

- The hypothesis of Low Magnetic Reynolds, Low-Re_m, is applied.

The hypothesis of axially-symmetric problem is a direct consequence of the distribution of magnetic field, considered to be radial all over the annulus, and consequence of the presence of the electric armatures extending all over the upper and lower surface of the actuator. The hypothesis of laminar flow is consistent considering a limited maximum velocity of the flow and the typical stabilizing effect that Lorentz force induces in MHD flows. The hypothesis of Low-Re_m will be discussed in detail in the next section.

3.1.1 The Low Magnetic Reynolds Approximation

The Magnetic Reynolds number, Re_m, gives information about how the magnetic field is influenced by the velocity field and the electric current. We look at the effect of a prescribed magnetic field on the flow. To ensure that $\mathbf{B}$ remains unaffected by $\mathbf{U}$ we must restrict ourselves to low magnetic Reynolds numbers:

$$R_m = \frac{|\mathbf{U_0}|L}{\nu} = \mu_m \sigma |\mathbf{U_0}| L \ll 1 \tag{3.1.8}$$

where $\mathbf{U_0}$ is the mean velocity of the fluid. However, this is not overly restrictive, at least not in the case of liquid-metal MHD. For example for case we are going to analize $\nu \sim 1m^2/s$, $L \sim 0.005$ and internal friction keeps $|\mathbf{U_0}|$ to a level of around $0.01m/s \sim 1m/s$. This gives $R_m \sim 10^{-3} \div 10^{-4}$.
The essence of the low Magnetic Reynolds R_m approximation is that the magnetic field associated with induced currents, $|\mathbf{J}| \sim \sigma |\mathbf{U_0}| \times |\mathbf{B}|$, is negligible by comparison with the imposed magnetic field.
There are three distinct cases which commonly arise.

1 The imposed magnetic field is static, the flow is induced by some external agent, and friction keeps u to a modest level in the sense that $|\mathbf{U_0}| \ll \eta/l$

2 The imposed magnetic field travels or rotates uniformly. This induces a flow which, due to friction in the fluid, is somewhat slower than the speed of the field.

3 The imposed magnetic field oscillates extremely rapidly, in the sense that the skin-depth $\delta = (2/\mu_m \sigma f)^{1/2}$ is much less than the characteristic

length of the problem, f being the field frequency. The magnetic field is then excluded from the interior of the conductor and inertia or friction in the fluid ensures that $|\mathbf{U_0}| \ll fL$

Categories $(1) - (3)$ cover the majority of flows in engineering applications. Typical examples are the magnetic damping of jets, vortices or turbulence (1), magnetic stirring using a rotating magnetic field (2) and magnetic levitation (3). In the cases we are going to study the applied magnetic field will be steady and as said, the Magnetic Reynolds is $R_m \ll 1$. We can then assert that all the case we are going to simulate belong to the first case.
We now discuss the simplifications which result in the governing equations when R_m is low and the imposed magnetic field is steady. Let $\mathbf{E}_0$, $\mathbf{J}_0$ and $\mathbf{B}_0$ represent the fields which would exist in a given situation if $\mathbf{U} = 0$, and let $\tilde{\mathbf{e}}$, $\tilde{\mathbf{j}}$ and $\tilde{\mathbf{b}}$ be the infinitesimal perturbations in $\mathbf{E}$, $\mathbf{J}$ and $\mathbf{B}$ which occur due to the presence of a vanishingly small velocity field. These quantities are governed by:

$$\nabla \times \mathbf{E}_0 = 0 \tag{3.1.9}$$

$$\mathbf{J_0} = \sigma \mathbf{E}_0 \tag{3.1.10}$$

$$\nabla \times \tilde{\mathbf{e}} = -\frac{\partial \tilde{\mathbf{b}}}{\partial t} \tag{3.1.11}$$

$$\tilde{\mathbf{j}} = \sigma \left(\tilde{\mathbf{e}} + \mathbf{U} \times \mathbf{B}_0 \right) \tag{3.1.12}$$

where we have neglected the second-order term $\mathbf{U} \times \tilde{\mathbf{b}}$ in (3.1.12). Now Faraday's equation gives $\tilde{\mathbf{e}} \sim \mathbf{U}\tilde{\mathbf{b}}$ and so the perturbation in the electric field may also be neglected in (3.1.11). Ohm's law now becomes:

$$\mathbf{J} = \sigma \left(\mathbf{E}_0 + \mathbf{U} \times \mathbf{B}_0 \right) \tag{3.1.13}$$

However, $\mathbf{E}_0$ is irrotational and so may be written as $-\nabla\phi$, where ϕ is an

electrostatic potential. Our final version of Ohm's law is therefore:

$$\mathbf{J} = \sigma \left(-\nabla\phi + \mathbf{U} \times \mathbf{B}_0 \right) \tag{3.1.14}$$

while the leading-order term in the Lorentz force per unit volume is:

$$\mathbf{F} = \mathbf{J} \times \mathbf{B}_0 \tag{3.1.15}$$

Eqs. (3.1.14) and (3.1.15) are all that we need to evaluate the Lorentz force in low-R_m MHD.
There is no need to calculate $\tilde{\mathbf{b}}$ since it does not appear in the Lorentz force. Moreover, $\mathbf{J}$ is uniquely determined by (3.1.14) since:

$$\nabla \cdot \mathbf{J} = 0 \tag{3.1.16}$$

$$\nabla \times \mathbf{J} = \sigma \nabla \times (\mathbf{U} \times \mathbf{B}_0) \tag{3.1.17}$$

and a vector field is unambiguously determined if its divergence and curl are known.
From now on we shall drop the subscript on $\mathbf{B}_0$ and $\mathbf{E}_0$, on the understanding that $\mathbf{B}$ represents the imposed, steady magnetic field and $\mathbf{E}$ is the externally applied electric field [15].

3.2 Axially symmetric MHD equations

The set of equations on which the numerical model has been built is:

$$\nabla \cdot \mathbf{B} = 0 \tag{3.2.1}$$

$$\nabla \times \mathbf{E} = 0 \tag{3.2.2}$$

$$\nabla \cdot \mathbf{J} = 0 \tag{3.2.3}$$

$$J = \sigma(\mathbf{E} + \mathbf{U} \times \mathbf{B}) \tag{3.2.4}$$

$$\rho\frac{\partial \mathbf{U}}{\partial t} + \rho(\mathbf{U} \cdot \nabla)\mathbf{U} = -\nabla P_n + \nu\rho\Delta\mathbf{U} + \mathbf{J} \times \mathbf{B} \tag{3.2.5}$$

$$\nabla \cdot \mathbf{U} = 0 \tag{3.2.6}$$

where Eq.(3.2.1) states the conservation of the magnetic field flux density, Eqs.(3.2.2)-(3.2.4) model the electric side of the problem while Eqs.(3.2.5)-(3.2.6) the fluid-dynamics side, [16].
The shape of the previous set of equations in the cylindrical coordinates r and z is given in detailed way in the following paragraphs.

3.2.1 Magnetic Field

The Eq.(3.2.1) represents the conservation of the magnetic flux density:

$$\nabla \cdot \mathbf{B} = \frac{1}{r}\frac{\partial\,(rB_r)}{\partial r} + \frac{\partial B_z}{\partial z} = 0 \tag{3.2.7}$$

The low-Re_m approximation implies that the induced magnetic field generated by the electric current flowing through the liquid is neglectable compared to the applied magnetic field. In this way the magnetic field $\mathbf{B}$ can be considered steady over the time and it can be solved independently from Eqs.(3.2.2)-(3.2.6).
As we assume the device to be characterized by a pure radial magnetic field with an assigned value B_0 at the inner radius r_i, the Eq.(3.2.6) can be reduced to:

$$\nabla \cdot \mathbf{B} = \frac{1}{r}\frac{\partial(rB_r)}{\partial r} = 0 \tag{3.2.8}$$

and then:

$$rB_r = const = r_i B_0 \quad \Rightarrow \quad B = \frac{r_i B_0}{r} \tag{3.2.9}$$

From now we will not specify anymore the direction of magnetic field.

3.2.2 Navier-Stokes equations and continuity equation for the velocity

In this paragraph Eqs.(3.2.5) and (3.2.6) will be simplified using the hypothesis of laminar flow and axial symmetry.
The Eq.(3.2.6) is the continuity equation for the velocity and it can be rewritten as:

$$\nabla \cdot \mathbf{U} = \frac{1}{r}\frac{\partial \left(rU_r\right)}{\partial r} + \frac{\partial U_z}{\partial z} = 0 \tag{3.2.10}$$

in which the azimuthal component has been neglected due to the hypothesis of axial symmetry.
Limiting the analysis to the the laminar case, we can consider the vorticity equation along the direction θ:

$$\nabla \times \mathbf{U} = \frac{\partial U_r}{\partial z} - \frac{\partial U_z}{\partial r} = 0 \tag{3.2.11}$$

and introducing the potential of the velocity Φ we can say that Eq.(3.2.11) is satisfied everywhere in the plane $r - z$ if:

$$\begin{cases} U_r = -\dfrac{\partial \Phi}{\partial r} \\ \\ U_z = -\dfrac{\partial \Phi}{\partial z} \end{cases} \tag{3.2.12}$$

Substituing Eq.(3.2.12) into Eq.(3.2.10) we obtain:

$$\nabla \cdot \mathbf{U} = \frac{1}{r}\frac{\partial}{\partial r}\left(r\frac{\partial \phi}{\partial r}\right) + \frac{\partial^2 \Phi}{\partial z^2} = \nabla^2 \Phi \tag{3.2.13}$$

Eq.(3.2.13) is the Laplace equation in the space $r-z$ and it is well-known that if there is no source term and all the boundary conditions are Neumann homogeneous boundaries conditions the solution is constant all over the domain. We can then say that the radial and axial components of the velocity are zero under the hypothesis of laminar flow.
Thanks to this conclusion, Eq.(3.2.5) can be reduced to the only azimuthal component:

$$\rho\frac{\partial U_\theta}{\partial t} = \mu\left[\frac{1}{r}\frac{\partial}{\partial r}\left(r\frac{\partial U_\theta}{\partial r}\right) + \frac{\partial^2 U_\theta}{\partial z^2} - \frac{U_\theta}{r^2}\right] + J_z B_r \tag{3.2.14}$$

in which the hypothesis of laminar flow has been applied and pressure gradient along the azimuthal coordinate has been neglected [17] [18].

3.2.3 Electric current density and Back electromotive force

The electric side of the problem is classically solved reducing the Eqs.(3.2.2)-(3.2.4) to a single equation in the electrostatic potential. The solution of this equation gives information about the electric current necessary to integrate the Navier-Stokes equation. This model will be solved with a classical Finite difference algorithm and for this reason will be called FDM, Finite Difference Model.
The Eq.(3.2.2), also called Faraday Law, states that a variable magnetic field generates a not null curl of the electric field. In the case in study the magnetic field is constant over the time and the electric field will be considered irrotational. Moreover the low-Re_m approximation implies that the induced magnetic field generated by the electric current flowing through the liquid is neglectable compared to the applied magnetic field. We then have

$$\nabla \times \mathbf{E} = \hat{\theta}\left(\frac{\partial E_r}{\partial z} - \frac{\partial E_z}{\partial r}\right) = 0 \tag{3.2.15}$$

In order to satisfy the (3.2.15) we introduce the potential of the electric field ϕ defined as:

$$\begin{cases} E_r = -\dfrac{\partial \phi}{\partial r} \\ \\ E_z = -\dfrac{\partial \phi}{\partial z} \end{cases} \tag{3.2.16}$$

In this way Eq.(3.2.15) is solved in all the $r - z$ domain.
The Eq.(3.2.3) describes the conservation of electric current; as for the Eq.(3.2.2) it can be expressed in cylindrical coordinates as:

$$\nabla \cdot \mathbf{J} = \frac{J_r}{r} + \frac{\partial J_r}{\partial r} + \frac{\partial J_z}{\partial z} = 0 \tag{3.2.17}$$

Finally Eq.(3.2.4) also called Ohm's law for moving conductors links the velocity field with the magnetic field, electric current and electric field. We rewrite its components along r and z and using Eq.(3.2.16) we have:

$$\begin{aligned} J_r &= \sigma \left(E_r + (\mathbf{U} \times \mathbf{B}) \cdot \hat{r} \right) = \\ &= \sigma E_r = -\sigma \frac{\partial \phi}{\partial r} \end{aligned} \tag{3.2.18}$$

$$\begin{aligned} J_z &= \sigma \left(E_z + (\mathbf{U} \times \mathbf{B}) \cdot \hat{z} \right) = \\ &= \sigma \left(E_z - U_\theta \mathbf{B} \right) = -\sigma \left(\frac{\partial \phi}{\partial z} + U_\theta \mathbf{B} \right) \end{aligned} \tag{3.2.19}$$

It is convenient to assemble Eqs.(3.2.16), (3.2.17), (3.2.18) and (3.2.19) in order to have all the electric quantities function of the only electrostatic potential. We compute the derivatives with respect of r and z of the homologous components of the electric current density:

$$\frac{\partial J_r}{\partial r} = -\sigma \frac{\partial^2 \phi}{\partial r^2} \tag{3.2.20}$$

$$\frac{\partial J_z}{\partial z} = -\sigma \left(\frac{\partial^2 \phi}{\partial z^2} + \frac{\partial U_\theta}{\partial z} \mathbf{B} \right) \tag{3.2.21}$$

Substituting these results in Eq.(3.2.17) we obtain the equation in the electrostatic potential:

$$\frac{1}{r}\frac{\partial \phi}{\partial r} + \frac{\partial^2 \phi}{\partial r^2} + \frac{\partial^2 \phi}{\partial z^2} = -\frac{\partial U_\theta}{\partial z}\mathbf{B} \tag{3.2.22}$$

An alternative method to investigate the electric current distribution is to apply the node-voltage analysis to an electric network consistent with the mesh-grid used for solving the Navier-Stokes equation. Thanks to low-Re_m, we can say that the electric network will be only made by electric resistances and voltage generators representing the back electromotive voltage induced by the spinning liquid through the magnetic field. This approach will be described in the discussion of the numerical method used to solve the problem with the name $FDHM$, Finite Differences Hybrid Model because the Finite differences approach will be used only for the fluid-dynamics part of the problem while the algebraic node-voltage analysis will be used for the electric part of the problem.

3.2.4 Boundary and Initial Conditions

The complete set of equations for the low-R_m MHD has been reduced to a system of two PDE equations, Eq.(3.2.14) and Eq.(3.2.22), in the unknowns U_θ, velocity of the fluid, and ϕ, electrostatic potential. A further relation is needed to link the two PDE equations; the relation chosen, Eq.(3.2.19), provides the conversion of the electrostatic potential to the z-component of the electric current density needed to compute the azimuthal velocity field.
In order to obtain a solution for the problem we have to set the right boundary conditions for all the unknown taken into account.
The liquid is enclosed in a torus with rectangular cross section. Neglecting the effect of the capillarity in the zones next to the corners and the effect that a not wetting liquid could have on the velocity field, we set the no-slip condition on all the boundaries of the cross section. It means that the azimuthal velocity of the fluid at the boundaries is set to the same velocity of the torus, and considering the torus at rest and bounded to a fixed reference system the velocity of the fluid at the boundaries is set to zero.

$$U_\theta(r_i, z, t) = U_\theta(r_e, z, t) = U_\theta(r, 0, t) = U_\theta(r, h, t) = 0 \tag{3.2.23}$$

The initial condition for the velocity is:

$$U_\theta(r, z, 0) = 0 \tag{3.2.24}$$

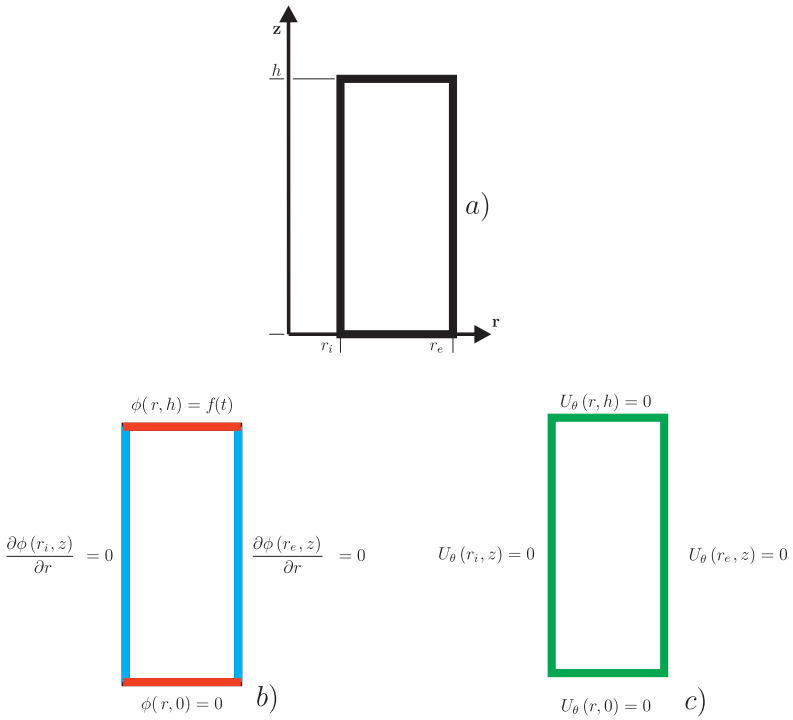

Figure 3.1: *Boundary Condition applied to the Finite Difference model.*
a) Reference system and dimension of the cross section
b) Electric boundary conditions
c) Fluid-dynamics boundary conditions

On the electric side we shall impose boundary conditions allowing the electric current to flow through the liquid. We choose an external electric field along z and then we consider a net flux of electric current only through the boundaries parallel to the r axis while insulating the boundaries parallel to the z axis. The external electric field is generated by time varying electrostatic potential at the upper boundary, $z = h$ and we consider a null, constant over the time,

reference electrostatic potential at the lower boundary, $z = 0$.

$$\phi(r, 0) = 0 \tag{3.2.25}$$

$$\phi(r, h) = f(t) \tag{3.2.26}$$

The condition of isolated wall for the boundaries parallel to the z axis can be assigned with the use of Eq.(3.2.18), putting the radial component of the velocity equal to zero:

$$J_r = -\sigma \frac{\partial \phi}{\partial r} = 0 \tag{3.2.27}$$

and obtaining:

$$\frac{\partial \phi(r_i, z)}{\partial r} = 0 \tag{3.2.28}$$

$$\frac{\partial \phi(r_e, z)}{\partial r} = 0 \tag{3.2.29}$$

Chapter

4 Methods and Procedures: Axially-symmetric Numeric Models

In this chapter a classical 2-dimensional Finite Differences model (FDM) will be described and applied. A second, alternative method, called Finite Difference Hybrid Model (FDHM), is developed on the base of the MHD set equation. The FDHM is then tested in order to highlight its conservative capabilities.

4.1 FDM: Finite Differences Model

The *FDM* has been solved numerically using a consistent and conservative scheme over a collocated not uniform mesh [19] [20] applied to the following set of equations:

$$\rho\frac{\partial U_\theta}{\partial t} = \mu\left[\frac{1}{r}\frac{\partial}{\partial r}\left(r\frac{\partial U_\theta}{\partial r}\right) + \frac{\partial^2 U_\theta}{\partial z^2} - \frac{U_\theta}{r^2}\right] + J_z\mathbf{B} \tag{4.1.1}$$

$$\frac{1}{r}\frac{\partial \phi}{\partial r} + \frac{\partial^2 \phi}{\partial r^2} + \frac{\partial^2 \phi}{\partial z^2} = -\frac{\partial U_\theta}{\partial z}\mathbf{B} \tag{4.1.2}$$

$$J_r = -\sigma\frac{\partial \phi}{\partial r} \tag{4.1.3}$$

$$J_z = -\sigma\left(\frac{\partial \phi}{\partial z} + U_\theta\mathbf{B}\right) \tag{4.1.4}$$

$$\mathbf{B}\,(r) = \frac{r_i B_0}{r} \tag{4.1.5}$$

In this collocated grid the velocity, U_θ, and electrostatic potential, ϕ, are calculated at the center cell while the radial and axial electric current densities J_r and J_z are evaluated on the cell faces respectively parallel to the z and r axes, Figure 4.1 .

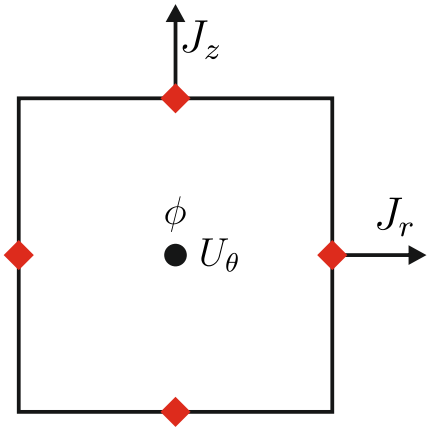

Figure 4.1: *Arrangment of the physical quantities in a collocated grid.*

The algorithm starts from the calculation of the electrostatic potential at the

center cell considering a null initial condition for the velocity field U_θ; once the electrostatic potential is known in all the domain, it is possible to calculate the current densities by means of Eqs.(4.1.3)-(4.1.4). The calculated electric current densities refer to the cell faces and in order to proceed to the calculation of velocity field they need to be interpolated to the center cell in order to have the Lorentz force at the center cell. The mono-dimensional and time-dependant Navier-Stokes equation is then solved used the Crank-Nicolson method over a not uniform grid over the space $r - z$ and a uniform time sequence.
In the following the discrete formulas for Eqs.(4.1.1)-(4.1.4) will be given in details.

4.1.1 Conservative and Consistent Laplace and divergence operator in cylindrical coordinates

In the collocated grid, the conservation of the electric current in differential form refers to the cell faces:

$$\nabla \cdot \mathbf{J} = \frac{J_r}{r} + \frac{\partial J_r}{\partial r} + \frac{\partial J_z}{\partial z} = 0 \tag{4.1.6}$$

The terms of Eq.(4.1.6) can be expressed in the discrete form as follows:

$$\frac{J_r}{r} = \frac{1}{r_k} \frac{(J_r)_{k+1/2,l} + (J_r)_{k-1/2,l}}{2} \tag{4.1.7}$$

$$\frac{\partial J_r}{\partial r} = \frac{(J_r)_{k+1/2,l} - (J_r)_{k-1/2,l}}{r_{k+1/2} - r_{k-1/2}} \tag{4.1.8}$$

$$\frac{\partial J_z}{\partial z} = \frac{(J_z)_{k,l+1/2} - (J_z)_{k,l-1/2}}{z_{l+1/2} - z_{l-1/2}} \tag{4.1.9}$$

The contribution of the electrostatic potential to the electric current $\mathbf{J^s}$ can be separated from the one generated by the electric induction $\mathbf{J^u}$.

$$\mathbf{J} = -\nabla\phi + \mathbf{U} \times \mathbf{B} = \mathbf{J^s} + \mathbf{J^u} \tag{4.1.10}$$

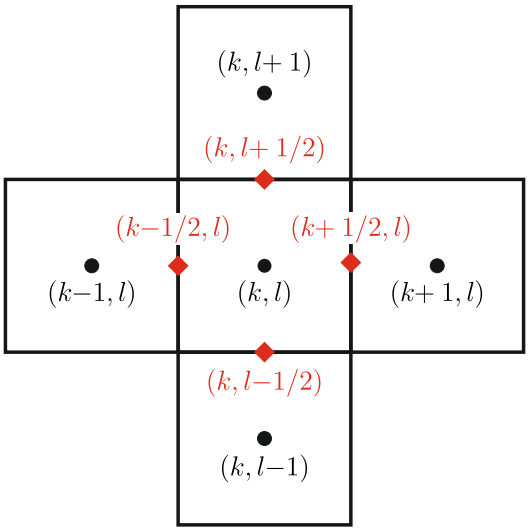

Figure 4.2: *Finite Differences Model stencil.*

The components of the conductive part of electric current density at the cell faces can be related with the values of the electrostatic potential at center cell.

$$\begin{cases} (J_r^s)_{k+1/2,l} = -\dfrac{\phi_{k+1,l} - \phi_{k,l}}{r_{k+1} - r_k} \\ \\ (J_r^s)_{k-1/2,l} = -\dfrac{\phi_{k,l} - \phi_{k-1,l}}{r_k - r_{k-1}} \end{cases} \tag{4.1.11}$$

$$\begin{cases} (J_z^s)_{k+1/2,l} = -\dfrac{\phi_{k,l+1} - \phi_{k,l}}{z_{l+1} - z_l} \\ \\ (J_z^s)_{k-1/2,l} = -\dfrac{\phi_{k,l} - \phi_{k,l-1}}{z_l - z_{l-1}} \end{cases} \tag{4.1.12}$$

Replacing Eqs.(4.1.11)-(4.1.12) into Eqs.(4.1.7)-(4.1.9), for the Eq.(4.1.7) we have:

$$\frac{J_r^s}{r} = a_{11}\ \phi_{k+1,l} + a_{12}\ \phi_{k,l} + a_{13}\ \phi_{k-1,l} \tag{4.1.13}$$

$$\begin{aligned} a_{11} &= \frac{1}{2r_k}\left(-\frac{1}{r_{k+1}-r_k}\right) \\ a_{12} &= \frac{1}{2r_k}\left(\frac{1}{r_{k+1}-r_k}-\frac{1}{r_k-r_{k-1}}\right) \\ a_{13} &= \frac{1}{2r_k}\left(\frac{1}{r_k-r_{k-1}}\right) \end{aligned} \tag{4.1.14}$$

for the Eq.(4.1.8):

$$\frac{\partial J_r^s}{\partial r} = a_{21}\ \phi_{k+1,l} + a_{22}\ \phi_{k,l} + a_{23}\ \phi_{k-1,l} \tag{4.1.15}$$

$$\begin{aligned} a_{21} &= -\left(\frac{1}{r_{k+1/2}-r_{k-1/2}}\right)\left(\frac{1}{r_{k+1}-r_k}\right) \\ a_{22} &= -\left(\frac{1}{r_{k+1/2}-r_{k-1/2}}\right)\left(-\frac{1}{r_{k+1}-r_k}-\frac{1}{r_j-r_{j-1}}\right) \\ a_{23} &= -\left(\frac{1}{r_{k+1/2}-r_{k-1/2}}\right)\left(\frac{1}{r_k-r_{k-1}}\right) \end{aligned} \tag{4.1.16}$$

for the Eq.(4.1.9):

$$\frac{\partial J_z^s}{\partial z} = a_{31}\ \phi_{k,l+1} + a_{32}\ \phi_{k,l} + a_{33}\ \phi_{k,l-1} \tag{4.1.17}$$

$$\begin{aligned} a_{31} &= -\left(\frac{1}{z_{l+1/2}-z_{l-1/2}}\right)\left(\frac{1}{z_{l+1}-z_l}\right) \\ a_{32} &= -\left(\frac{1}{z_{l+1/2}-z_{l-1/2}}\right)\left(-\frac{1}{z_{l+1}-z_l}-\frac{1}{z_l-z_{l-1}}\right) \\ a_{33} &= -\left(\frac{1}{z_{l+1/2}-z_{l-1/2}}\right)\left(\frac{1}{z_l-z_{l-1}}\right) \end{aligned} \tag{4.1.18}$$

Considering that the velocity **U** is purely azimuthal while the magnetic field **B** is purely radial, the inductive part of the Eq.(4.1.10) can be written as:

$$\mathbf{J^u} = \mathbf{U} \times \mathbf{B} = \begin{vmatrix} \hat{r} & \hat{\theta} & \hat{z} \\ U_r & U_\theta & U_z \\ B_r & B_\theta & B_z \end{vmatrix} = \begin{vmatrix} \hat{r} & \hat{\theta} & \hat{z} \\ 0 & U_\theta & 0 \\ B_r & 0 & 0 \end{vmatrix} = -\left(B_r U_\theta\right) \hat{z} \tag{4.1.19}$$

The divergence of $\mathbf{J^u}$ has only the component parallel to the z axis and using the values of B_r and U_θ at the cell faces we have:

$$\begin{aligned} \nabla \cdot \mathbf{J^u} = \frac{\partial J_z^u}{\partial z} =& \frac{\left(J_z^u\right)_{k,l+1/2} - \left(J_z^u\right)_{k,l-1/2}}{z_{l+1/2} - z_{l-1/2}} \\ =& \frac{-\left(B_r\right)_k \left(U_\theta\right)_{k,l+1/2} + \left(B_r\right)_k \left(U_\theta\right)_{k,l+1/2}}{z_{l+1/2} - z_{l-1/2}} = -C \end{aligned} \tag{4.1.20}$$

Finally the equation in the electrostatic potential at the cell center can be expressed as:

$$\begin{gathered} \left(a_{11} + a_{21}\right) \phi_{k+1,l} + \left(a_{12} + a_{22} + a_{32}\right) \phi_{k,l} + \left(a_{13} + a_{23}\right) \phi_{k-1,l} + \\ a_{31}\ \phi_{k,l+1} + a_{33}\ \phi_{k,l-1} = C \end{gathered} \tag{4.1.21}$$

4.1.2 Interpolation Operator for not equispaced grid

The Navier-Stokes equation gives values of U_θ at the center cell but in order to compute the inductive part of the Eq.(4.1.20) values of U_θ at the cell faces are needed. On a collocated grid system, an interpolation operator $\Lambda_{c \to f}$ can be defined, which represents the interpolation from the cell center to cell faces:

$$\mathbf{U}_f = \Lambda_{c \to f}\ \mathbf{U}_c \tag{4.1.22}$$

where $\mathbf{U}$ denotes the velocity vector (U_r, U_θ, U_z). The detailed formula of the interpolation operator on collocated grid is:

$$\mathbf{U}_{k+1/2,l} = \Lambda_{c\to fr+}\ \mathbf{U}_c = \alpha_+ \mathbf{U}_{k,l} + (1-\alpha_+)\,\mathbf{U}_{k+1,l} \tag{4.1.23}$$

$$\mathbf{U}_{k,l+1/2} = \Lambda_{c\to fz+}\ \mathbf{U}_c = \beta_+ \mathbf{U}_{k,l} + (1-\beta_+)\,\mathbf{U}_{k,l+1} \tag{4.1.24}$$

The subscript $c \to fr+$ and $c \to fz+$ denotes the interpolation from the cell center normal to the r and z axes; the symbol + denotes that the cell faces are located to the right and top of the cell center.
The coefficients of the interpolation operator $\Lambda_{c\to f}$ are defined on the base of the grid arrangement:

$$\alpha_+ = \frac{r_{k+1} - r_{k+1/2}}{r_{k+1} - r_k} \qquad \beta_+ = \frac{z_{l+1} - z_{l+1/2}}{z_{l+1} - z_l} \tag{4.1.25}$$

An equivalent operator can be defined for the interpolation from the cell faces to center cell and it can be used to obtain the electric current density at center cell once known it's value at the cell faces. Due to the position of the center cell, considered to be in the middle between the two faces of the cell, we have:

$$\mathbf{J}_c = \Lambda_{f\to c}\,\mathbf{J}_f \tag{4.1.26}$$

where $\Lambda_{f\to c}$ has the meaning of:

$$(J_r)_{k,l} = \left[\Lambda_{fr\to c}\,(J_r)_{fr}\right]_{k,l} = \frac{(J_r)_{k+1/2,l} + (J_r)_{k-1/2,l}}{2} \tag{4.1.27}$$

$$(J_z)_{k,l} = \left[\Lambda_{fz\to c}\,(J_z)_{fz}\right]_{k,l} = \frac{(J_z)_{k,l+1/2} + (J_z)_{k,l-1/2}}{2} \tag{4.1.28}$$

4.1.3 Grid Generator

The mathematical model is solved on a not equispaced grid in order to study with accuracy the boundary effects due to the coupling between the electric and fluid-dynamic problems. It is possible to define two different characteristic lengths for the boundary layers, [21] [22] [23]:

- for the boundaries normal to the magnetic field, parallel to the z axis, the boundary layers are called Hartmann layers and their lengths are:

$$\delta_{Hrtm} = \frac{1}{B}\sqrt{\frac{\mu}{\sigma}} \tag{4.1.29}$$

- for the boundaries parallel to the magnetic field, i.e. parallel to the r axis, the boundary layers are called Shercliff layers and their lengths are:

$$\delta_{Sh} = \sqrt{\frac{L}{B}\sqrt{\frac{\mu}{\sigma}}} \tag{4.1.30}$$

  where L is the difference between the inner and outer radius of the cavity containing the liquid.

With the purpose to make several simulations for different values of magnetic field $\mathbf{B}$, electric conductivity of the fluid σ, length of the magnetic gap L and height of liquid torus h it has been necessary to understand how to modify the computational grid in function of the dimension of δ_{Hrtm} and δ_{Sh}.
The grid generator create four different kinds of grid. For the r axis:

- when $\delta_{Hrtm} \leq (r_e - r_i)/6$ the grid on the r axis is characterized by an equispaced mesh in the zone:

$$r_i \leq r \leq r_i + 2\delta_{Hrtm} \qquad r_e - 2\delta_{Hrtm} \leq r \leq r_e \tag{4.1.31}$$

  while in the zone $r_i + 2\delta_{Hrtm} < r < r_i + 2\delta_{Hrtm}$ the grid is logarithmic

- if $\delta_{Hrtm} > (r_e - r_i)/6$ the grid is logarithmic from r_i to r_e.

For the z axis:

- when $\delta_{Sh} \leq h/6$ the grid on the z axis is characterized by an equispaced mesh in the zone:

$$0 \leq z \leq 2\delta_{Sh} \qquad h - 2\delta_{Sh} \leq z \leq h \tag{4.1.32}$$

  while in the zone $2\delta_{Sh} < r < h + 2\delta_{Sh}$ the grid is logarithmic

- if $\delta_{Sh} > h/6$ the grid is logarithmic from 0 to h.

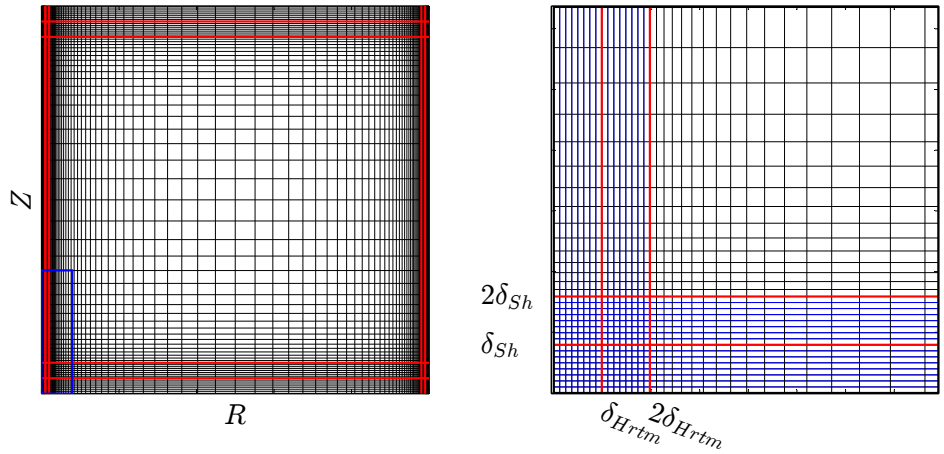

Figure 4.3: *Grid for* $\delta_{Sh} \leq h/6$ *and* $\delta_{Hrtm} \leq (r_e - r_i)/6$.

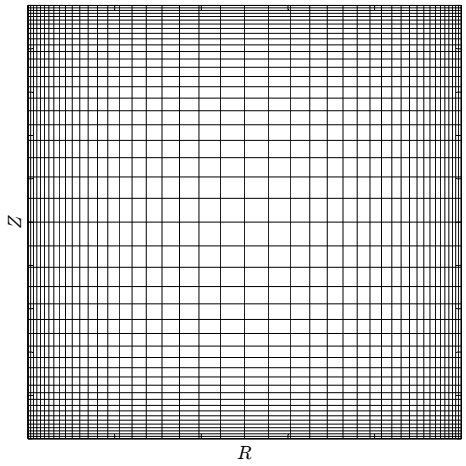

Figure 4.4: *Grid for* $\delta_{Sh} > h/6$ *and* $\delta_{Hrtm} > (r_e - r_i)/6$.

4.1.4 Navier-Stokes Equation

The Navier-Stokes equation Eq.(4.1.1):

$$\rho \frac{\partial U_\theta}{\partial t} = \mu \left[\frac{1}{r} \frac{\partial U_\theta}{\partial r} + \frac{\partial^2 U_\theta}{\partial r^2} + \frac{\partial^2 U_\theta}{\partial z^2} - \frac{U_\theta}{r^2} \right] + J_z \mathbf{B} \qquad (4.1.33)$$

is solved using a Crank-Nicolson scheme on a five points stencil, (Appendix A). The finite difference scheme has been calculated for a not equispaced mesh. The time derivative has been evaluated with a second order finite difference scheme with constant time step. The shape of the discretized version of the derivatives present in Eq.(4.1.33) is:

$$\frac{1}{r}\frac{\partial U_\theta}{\partial r} \rightarrow b_{1,1}\ U_{k+1,l} + b_{1,2}\ U_{k,l} + b_{1,3}\ U_{k-1,l} \tag{4.1.34}$$

$$\begin{aligned} b_{11} &= \frac{1}{r_{k,l}}\left(\frac{1}{r_{k+1,l} - r_{k,l}}\right) \\ b_{12} &= \frac{1}{r_{k,l}}\left(-\frac{1}{r_{k+1,l} - r_{k,l}} + \frac{1}{r_{k,l} - r_{k-1,l}}\right) \\ b_{13} &= \frac{1}{r_{k,l}}\left(\frac{1}{r_{k,l} - r_{k-1,l}}\right) \end{aligned} \tag{4.1.35}$$

$$\frac{\partial^2 U_\theta}{\partial r^2} \rightarrow b_{2,1}\ U_{k+1,l} + b_{2,2}\ U_{k,l} + b_{2,3}\ U_{k-1,l} \tag{4.1.36}$$

$$\begin{aligned} b_{21} &= \frac{1}{r_{k+1,l} - r_{k,l}} \\ b_{22} &= -\frac{1}{r_{k+1,l} - r_{k,l}} - \frac{1}{r_{k,l} - r_{k-1,l}} \\ b_{23} &= \frac{1}{r_{k,l} - r_{k-1,l}} \end{aligned} \tag{4.1.37}$$

$$\frac{\partial^2 U_\theta}{\partial z^2} \rightarrow b_{3,1}\ U_{k,l+1} + b_{3,2}\ U_{k,l} + b_{3,3}\ U_{k,l-1} \tag{4.1.38}$$

$$\begin{aligned} b_{31} &= \frac{1}{z_{k,l+1} - z_{k,l}} \\ b_{32} &= -\frac{1}{z_{k,l+1} - z_{k,l}} - \frac{1}{z_{k,l} - z_{k,l-1}} \\ b_{33} &= \frac{1}{z_{k,l} - z_{k,l-1}} \end{aligned} \tag{4.1.39}$$

$$\frac{U_\theta}{r^2} \rightarrow \frac{u_{k,l}}{r_{k,l}^2} = -b_{4,2}\, U_{k,l} \tag{4.1.40}$$

$$\frac{\partial U_\theta}{\partial t} \rightarrow \frac{U_{k,l}^{n+1} - U_{k,l}^{n}}{\Delta t} \tag{4.1.41}$$

The right side of the discrete version of Eq.(4.1.33) has then the following shape:

$$\begin{aligned} F\left(u, J_z, B, r, z\right) = \mu \left[\left(b_{1,1} + b_{2,1}\right) U_{k+1,l}\right. \\ + \left(b_{1,2} + b_{2,2} + b_{3,2} + b_{4,2}\right) U_{k,l} \\ + \left(b_{1,3} + b_{2,3}\right) U_{k-1,l} \\ \left. + b_{3,1}\, U_{k,l+1} + b_{3,3}\, U_{k,-1}\right] + \left(J_z\right)_{k,l} B_{k,l} \end{aligned} \tag{4.1.42}$$

Applying the Crank-Nicolson algorithm we obtain:

$$\frac{u_{k,l}^{n+1} - u_{k,l}^{n}}{\Delta t} = \frac{1}{2\rho}\left[F^{n+1}\left(u, J_z, B, r, z\right) + F^{n}\left(u, J_z, B, r, z\right)\right] \tag{4.1.43}$$

The (4.1.43) leads to a tridiagonal system that can be easily solved with tridiagonal matrix algorithms.
The computation of the velocity U_θ extends to the all the center cell nodes. The no-slip condition is implemented adding node on the boundaries, where U_θ is known and equal to zero, in $(k - 1/2, l)$ and $(k + 1/2, l)$ for the boundaries parallel to the z axis and nodes in $(k, l - 1/2)$ and $(k, l + 1/2)$ for the boundaries parallel to the r.

4.1.5 Discrete boundary conditions

In order to solve the electrodynamic problem (3.2.22) the boundary conditions (3.2.25)(3.2.26) and (3.2.28)-(3.2.29) shall be applied.
The Dirichlet conditions on the top and bottom side of the cross section are simple to express. They are known values of the electrostatic potential and they appear inside the vector of known terms of the algebraic system.
The Neumann conditions on the right and left side of the cross section needs to be studied. The classical way to implement the conditions on the derivative is using ghost nodes on the grid coupling this conditions with the general equation for the electrostatic potential.
The ghost nodes are virtual nodes external to the computational grid for which is not supposed to know the value of the unknown.
For the left side boundary we have that the Eq.(3.2.28) can be expressed as:

$$\frac{\partial \phi\left(r_i, z\right)}{\partial r} = 0 \rightarrow \frac{\phi_{k+1,l} - \phi_{k,l}}{r_{k+1} - r_k} + \frac{\phi_{k,l} - \phi_{k-1,l}}{r_k - r_{k-1}} = 0 \tag{4.1.44}$$

On this side of the cross section, the node $(k-1, l)$ is a ghost node and we can highlight the electrostatic potential on this node in order to obtain:

$$\phi_{k-1,l} = \phi_{k+1,l}\left(\frac{r_k - r_{k-1}}{r_{k+1} - r_k}\right) + \phi_{k,l}\left(1 - \frac{r_k - r_{k-1}}{r_{k+1} - r_k}\right) \tag{4.1.45}$$

Introducing Eq.(4.1.45) into Eq.(3.2.22) we obtain the Neumann condition applied using central finite differences scheme.
In the same way for the right boundary of the cross section, we have:

$$\frac{\partial \phi\left(r_e, z\right)}{\partial r} = 0 \rightarrow \frac{\phi_{k+1,l} - \phi_{k,l}}{r_{k+1} - r_k} + \frac{\phi_{k,l} - \phi_{k-1,l}}{r_k - r_{k-1}} = 0 \tag{4.1.46}$$

which means:

$$\phi_{k+1,l} = \phi_{k,l}\left(1 - \frac{r_{k+1} - r_k}{r_k - r_{k-1}}\right) + \phi_{k-1,l}\left(\frac{r_{k+1} - r_k}{r_k - r_{k-1}}\right) \tag{4.1.47}$$

With the same procedure we obtain the Neumann condition on the right boundary of the cross section.

4.1.6 Voltage Drive and Current Drive

The model can simulate the reaction of the conductive liquid to a certain kind of law $f(t)$ for the electrostatic potential assigned between the lower and the upper boundaries of the cross section.
It does not seem to be able to simulate an assigned trend $g(t)$ of the electric current; it is not possible to assign as boundary condition a given law for the electric current flowing through the conductive liquid.
In order to make it possible we have to consider the Eq.(3.1.14). Being the external electric field along z we can replace the divergence with the total derivative of the electrostatic potential with respect to z. We have:

$$\mathbf{J} = -\sigma \frac{\partial \phi}{\partial z} + \sigma \mathbf{U} \times \mathbf{B}_0 \tag{4.1.48}$$

Integrating over the surface in the plane $r - \theta$ we obtain the total current flowing in the conductive liquid:

$$\mathbf{I} = -\sigma \int_S \frac{\partial \phi}{\partial z} dS + \sigma \int_S \mathbf{U} \times \mathbf{B}_0 dS \tag{4.1.49}$$

In order to simplify the derivative of the electrostatic potential with respect of z component we proceed integrating along z:

$$\int_0^h \mathbf{I}\, dz = -\sigma \int_0^h \int_S \frac{\partial \phi}{\partial z}\, dS\, dz + \sigma \int_0^h \int_S \mathbf{U} \times \mathbf{B}_0\, dS\, dz \tag{4.1.50}$$

Due to the conservation of electric current and being the electrostatic potential just function of the z we have:

$$\mathbf{I} = -\frac{\sigma S}{h} \Delta\phi - \frac{\sigma}{h} \int_0^h \int_S \mathbf{U} \times \mathbf{B}_0\, dS\, dz \tag{4.1.51}$$

What we have found is the relation between the total electric current and the voltage applied to the upper boundary taking into account the back electromotive force. We can say that we can numerically impose a certain electric current of known law $I(t)$ through the following relation:

$$\phi(r,h,t) = -\frac{h}{\sigma S} I(t) - \frac{1}{S}\int_0^h \int_S \mathbf{U} \times \mathbf{B}_0 \; dS \; dz \tag{4.1.52}$$

where with $\phi(r,h,t)$ we intend the electrostatic potential at the upper boundary being zero its value at the lower boundary.

4.1.7 Iterative scheme

The solving algorithm uses in sequence all the relations presented in previous section. In order to have a clearer vision of the algorithm a flux diagram is presented, Figure 4.5.

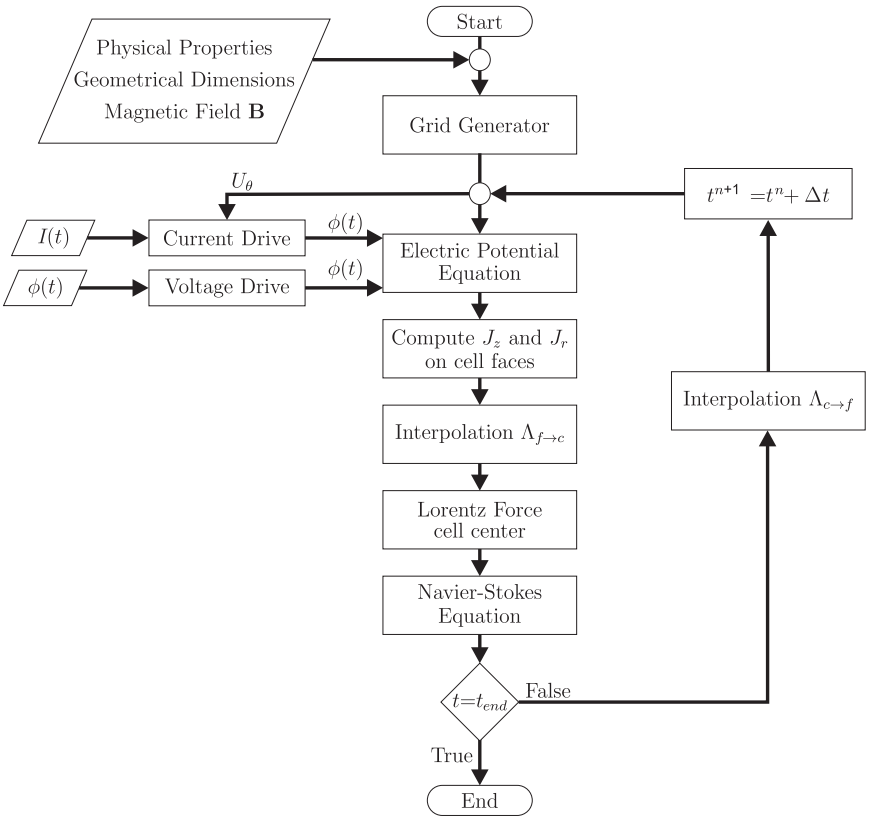

Figure 4.5: *Flux Diagram of the FDM model*

4.1.8 Conservation problems

The FDM shows problem of conservation of electric current. Figure (4.6) shows the total current flowing through the cross section along the axial direction z. It is evident that the current should be constant for each value of z because of the conservation of the electric current. The algorithm shows conservation errors of electric current near the armatures of the device. This is not acceptable because this conservation errors lead to an underestimation of the Lorentz force acting on the conductive liquid.
We then try to solve this problem with an alternative method. This method will be discussed in the next sections.

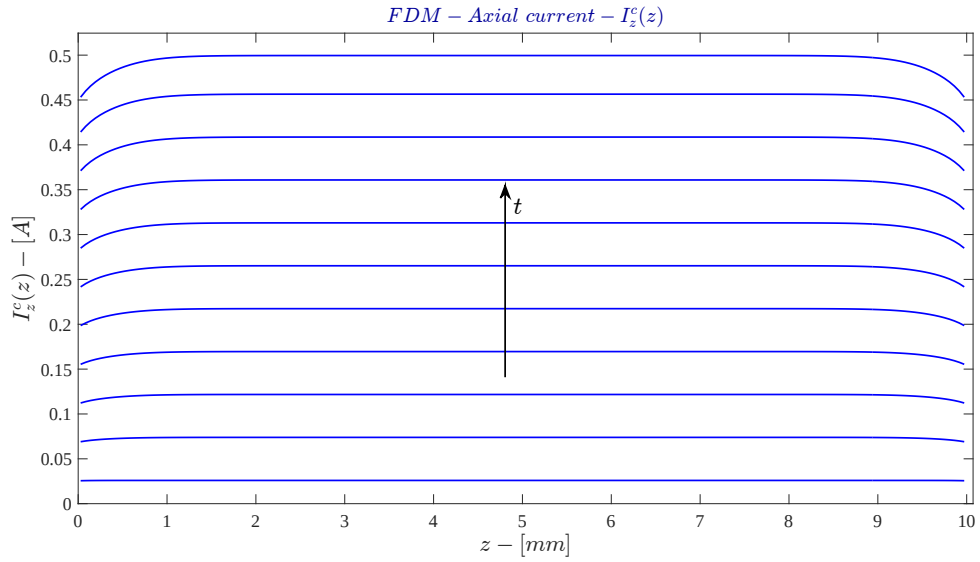

Figure 4.6: *FDM - Total axial electric current*

The radial component of the electric current, Figure(4.7) has no problem and it shows a perfect antisymmetric trend with null mean.

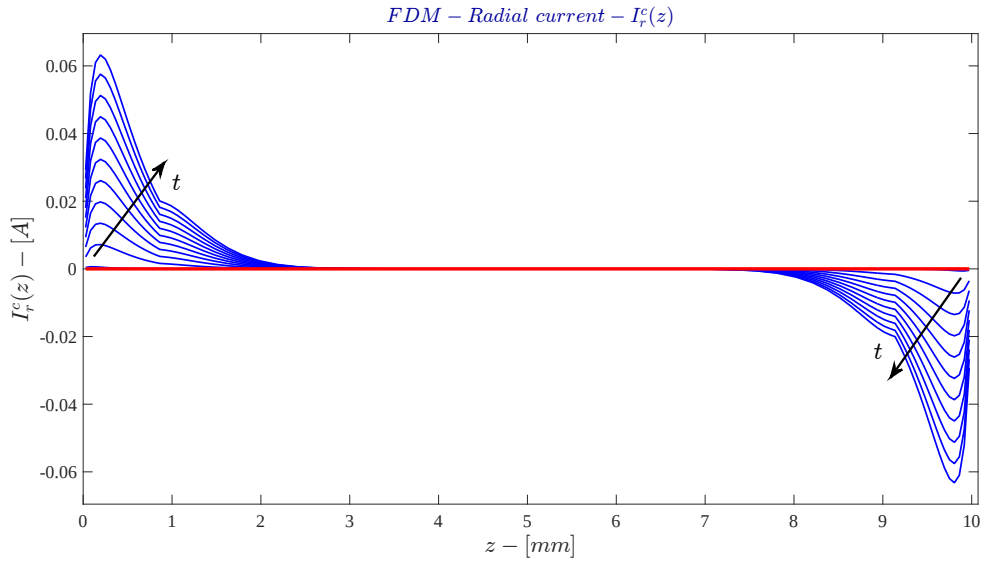

Figure 4.7: *FDM - Total radial electric current*

4.2 FDHM: Finite Differences Hybrid Model

The Finite Difference Hybrid Model is an alternative algorithm to solve the MHD equations. The difference with the FDM is in the way the electric part of the model is solved. Instead of solving the electrostatic potential equation, an electric network is created in order to obtain the distribution of the electrostatic potential and of the electric current inside the cross section of the device. The electric network is then solved applying the nodal analysis. This model has been inspired by [24], anyway this model solves numerically the Navier-Stokes equations instead of imposing a fixed velocity profile and it is set up to compute the transient between the state of null velocity to the state of completely developed MHD laminar flow. The same grid generator of the FDM is used in the FDHM. The cell centers become here the nodes of electric network while the cell faces are the branches.

4.2.1 Equivalent electric network

The equivalent electric network is made of radial and axial resistances and voltage generators.
The radial resistances link the nodes in the radial direction. Applying the conservation of the electric current along the radius on a sequence of cylindrical surface, a law for the density of electric current can be found:

$$\begin{cases} \dfrac{\partial(r\ J_r)}{\partial r} = 0 \\ J_r\left(r_1\right) = J_0 \end{cases} \quad \Rightarrow \quad J_r\left(r\right) = \frac{J_0\ r_1}{r} \tag{4.2.1}$$

Introducing first the laws linking the electric current to the electric current density and the voltage to the electric field:

$$I = \iint_S J_r\left(r\right)\ dS = \int_0^l \int_0^{2\pi} J_r r dz d\theta = 2\pi J_0 r l \tag{4.2.2}$$

$$\Delta\phi = -\int_{r_k}^{r_{k+1}} E_r dr = -\frac{1}{\sigma}\int_{r_k}^{r_{k+1}} \frac{J_0\ r_i}{r} dr = \frac{J_0\ r_i}{\sigma} \ln\left(\frac{r_k}{r_{k+1}}\right) \tag{4.2.3}$$

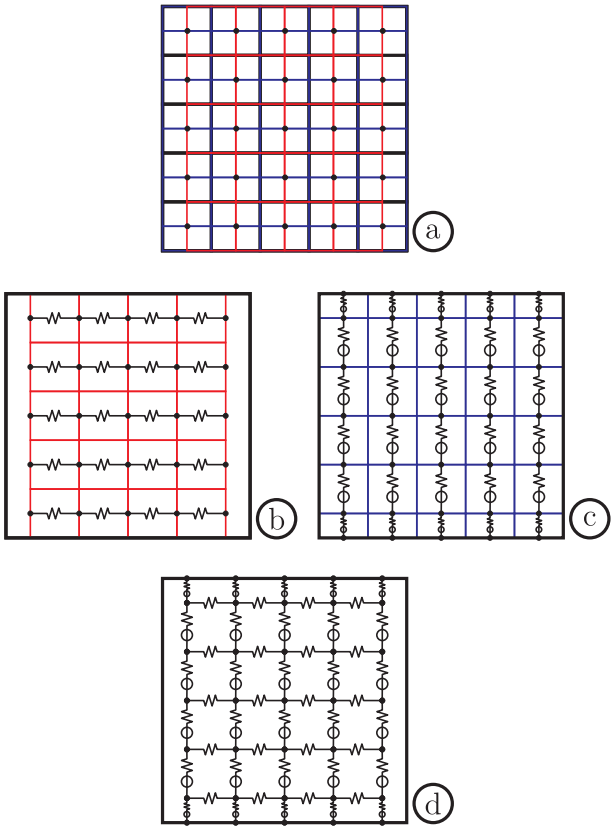

Figure 4.8: *Equivalent electric network.*
a) Nodes and cells
b) Electric radial resistances
c) Electric axial resistances and back electromotive voltage
b) Assembled electric network

and then the Ohm law, we obtain:

$$R_r = \frac{\Delta\phi}{I} = \frac{1}{2\pi\sigma} \frac{\ln\left(\frac{r_j}{r_{j+1}}\right)}{l} \tag{4.2.4}$$

The axial resistances link the nodes in direction parallel to z:

$$R_z = \frac{\Delta\phi}{I} = \frac{1}{\sigma} \frac{l}{\pi\left(r_k^2 - r_{k+1}^2\right)} \tag{4.2.5}$$

The voltage generators model the back electromotive voltage generated by the conductive liquid spinning in the magnetic field. Their values can be computed integrated the cross product between velocity and magnetic field over the length parallel to z. Using the Ohm Law for moving conductor we have:

$$\Delta\phi_{ind} = \int_0^{\delta z_l} \mathbf{U} \times \mathbf{B} dz = -U_\theta B\left(r\right) \delta z_l \tag{4.2.6}$$

4.2.2 Boundary Conditions

The FDHM does not need specific equations to impose the boundary conditions. The boundary conditions on the side of the cross section parallel to the z axis are imposed not taking into account any radial resistances that could bring electric current in the direction of the boundary. So, the nodes adjacent to vertical side of the cross section have just three branches: two axial branches and one radial branch towards the inside of the cross section.
The boundary conditions on the side of the cross section parallel to the r axis are applied imposing the same value of the electrostatic potential to all the nodes on the boundaries.

4.2.3 Voltage and Current drive

In the FDHM the voltage and current drive are realized with two different conditions on the nodes on the upper and lower boundaries.
In order to simulate the voltage drive the voltage on the boundaries is assumed to be known. The lower armature is set to a reference voltage while the nodes on the the upper armature are set to same value, in general, function of the time.
In the current drive it is necessary to control the current flowing through the conductive liquid and to have an equipotential surface on each armature. In order to satisfy these two constrains the nodes on each armature have been collapsed to only one node where to impose a net electric current.

4.2.4 Iterative scheme

The algorithm to solve the FDHM is presented in the following flux diagram.

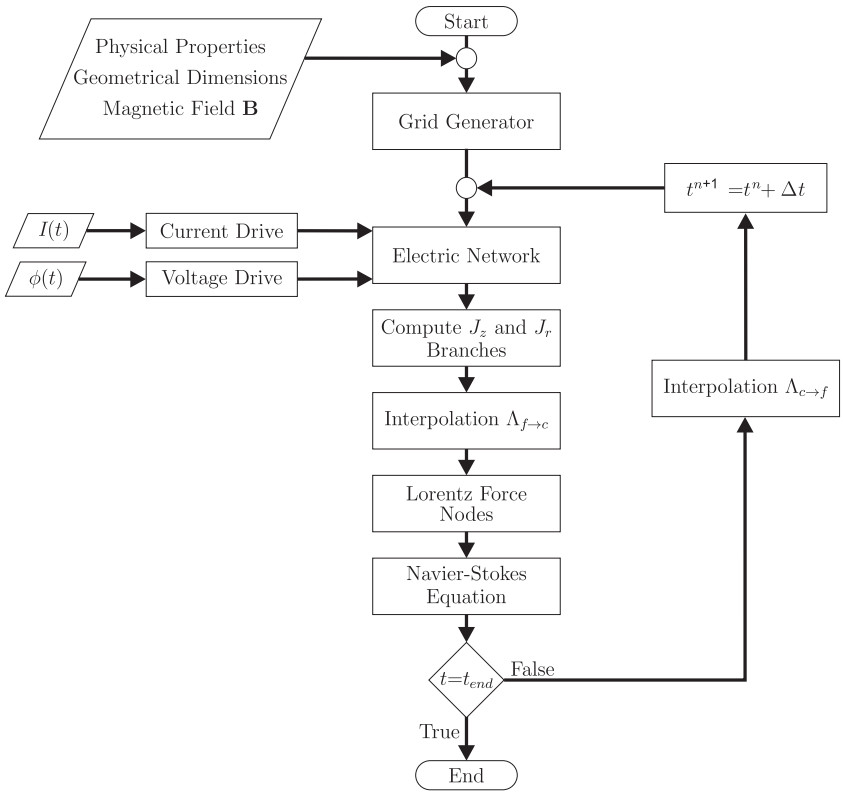

Figure 4.9: *Flux Diagram of the FDHM model*

4.2.5 FDHM performances

The FDHM appears to solve the conservation problem of the FDM algorithm, Figures (4.10)(4.11). The total axial electric current is now constant all over the cross section and equal to the supply value.

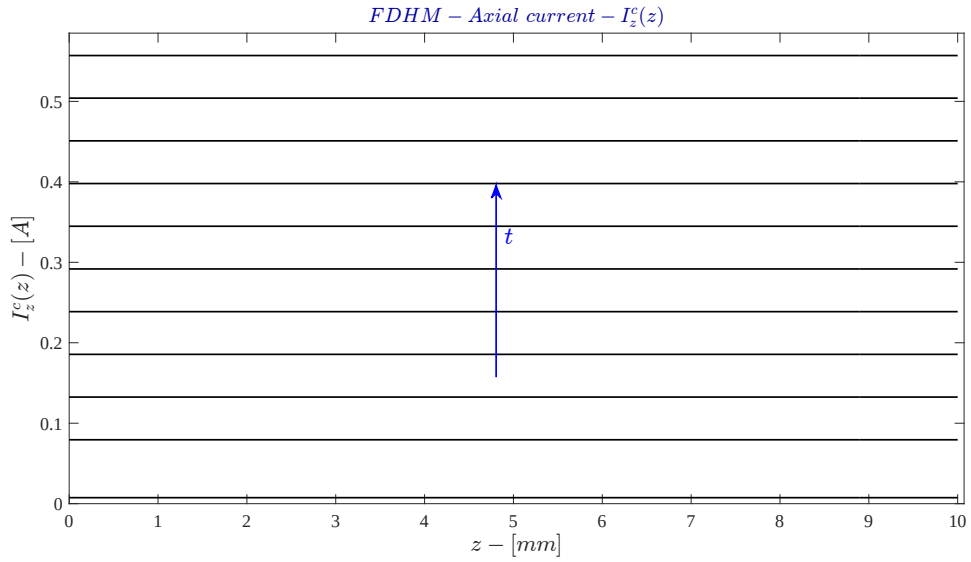

Figure 4.10: *FDHM - Total axial electric current*

The radial component of the electric current shows, as in FDM, an antisymmetric trend with null mean.

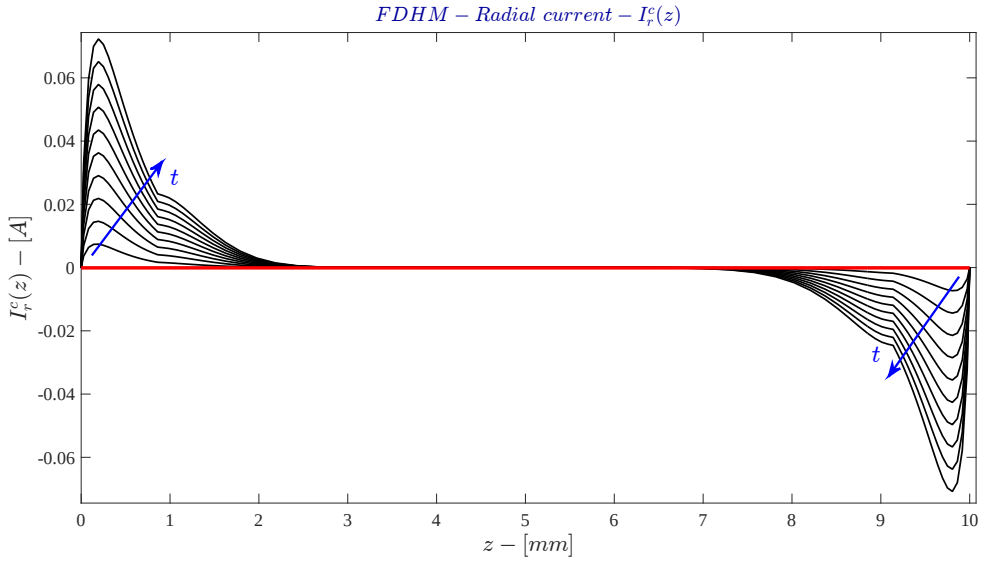

Figure 4.11: *FDHM - Total radial electric current*

The relative errors of the electric and fluid-dynamic part can be computed and they are respectively of the order of 10^{-10} and 10^{-5}.

The error of the electric problem is computed as the standard deviation of the difference between the commanded electric current and computed electric current flowing through the cross section.

$$Err_{el} = \sigma \left[I^c \left(z \right) \right] \tag{4.2.7}$$

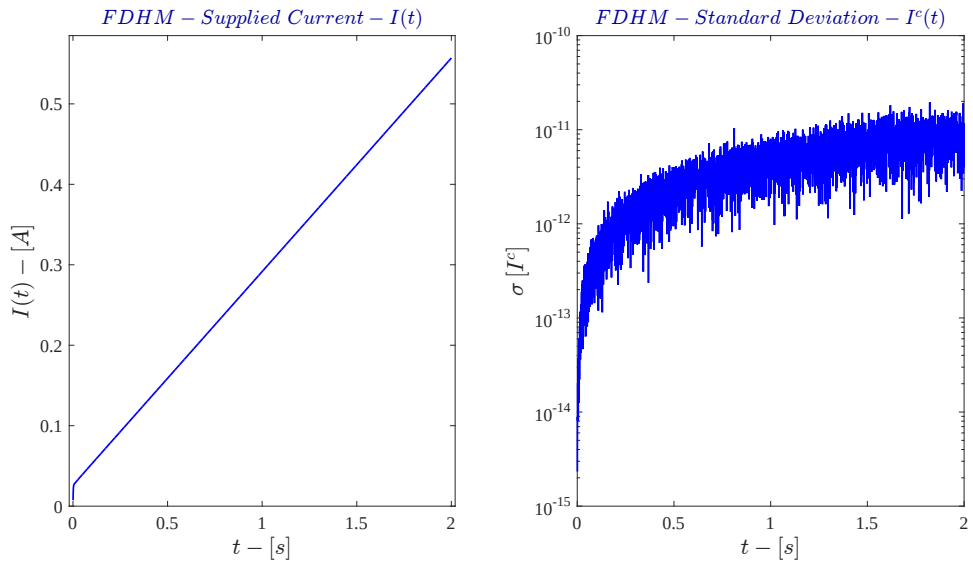

Figure 4.12: *FDHM - Error of the electric side of the MHD problem*

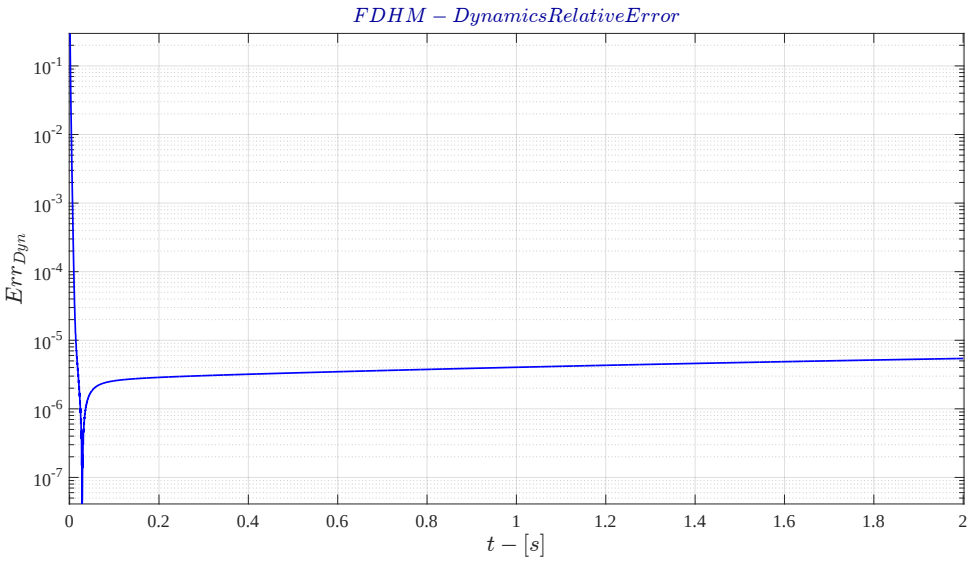

Figure 4.13: *FDHM - Error of the dynamic side of the MHD problem*

The error of the dynamic problem is computed as the difference between the absolute value of the torque computed with the numerical velocity distribution and the difference between the viscous shear stress moment and the moment of Lorentz force:

$$Err_{dyn} = \frac{|\dot{\Gamma}| - |M_{Lor} - M_{vis}|}{|\dot{\Gamma}|} \tag{4.2.8}$$

4.3 Conclusions

In this chapter two different numerical methods have been analysed in order to simulate the behaviour of an electrically conductive liquid spinning in an axial symmetric torus under the interaction of a magnetic field and an electric current. The first method, called FDM, shows problems of conservation of the electric current due to the numeric method adopted. For this reason an alternative method, called FDHM, has been set up and studied. The FDHM shows great accuracy in the estimation of both the dynamic and electric side of the MHD problem.

Chapter

5 Results and Discussion: FDHM

In this chapter several simulations based on the FDHM are presented in order to outline the performance of the device in study together with the performances of the numeric model itself.

5.1 Electric Current and Velocity Fields

The FDHM method developed and described in the previous section gives the possibility to visualize the distribution of the electric current flowing through the fluid and of the the velocity of the fluid in the cross section of the device. The axial electric current, Figure(5.1), appears to be forced to the boundaries of the cross section parallel to the z axis. The reason of this behaviour is the back-electromotive force, function of the velocity field, that pulls the electric current line towards the zones where the velocity of the fluid is lower.

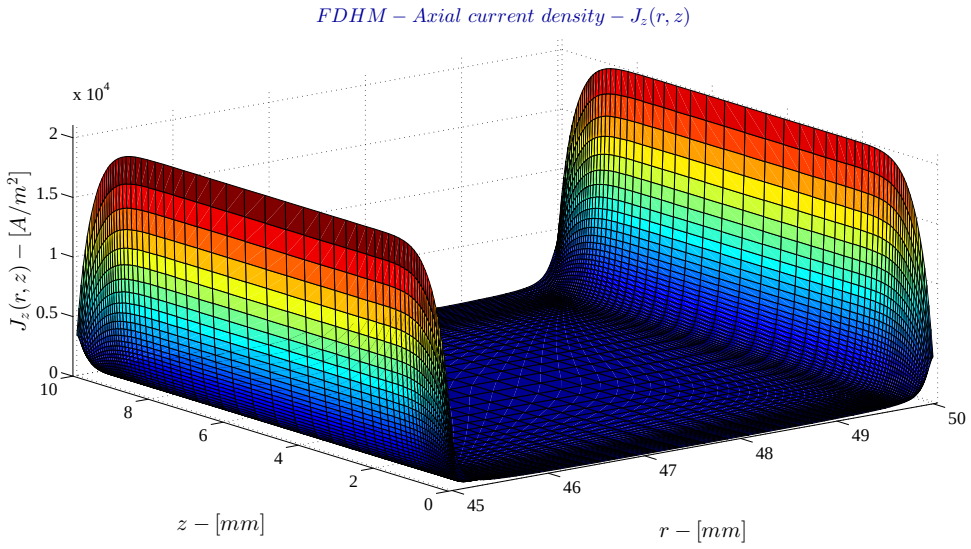

Figure 5.1: *FDHM - Axial electric current density*

For the same reason the radial electric current, Figure(5.2), shows an anti-symmetric behaviour in order to allow the electric charges to move from the equipotential armatures to the boundaries parallel to the z axis where the velocity of the fluid and so the back-electromotive force is lower. The velocity field computed by the FDHM, Figure(5.3), has a typical shape different from the classical hydrodynamic flux. It shows a strong gradient next to the boundaries parallel to the z axis. The reason of this resides in the strong concentration of the axial component of the electric current in those zones. The core zone of the flux shows a slight linear trend in the radial direction, increasing from the

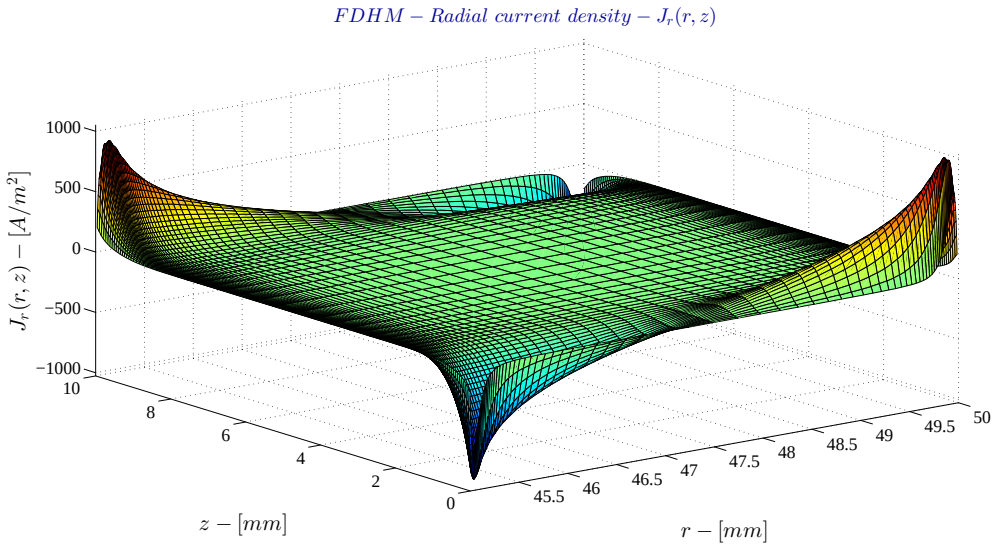

Figure 5.2: *FDHM - Radial electric current density*

inner radius to the outer radius. This typical trend is caused by the radial magnetic distribution that increase in the direction from the outer radius to the inner radius. These two opposite trends of the velocity and of the magnetic field generate an almost constant back electromotive force acting on the electric current.

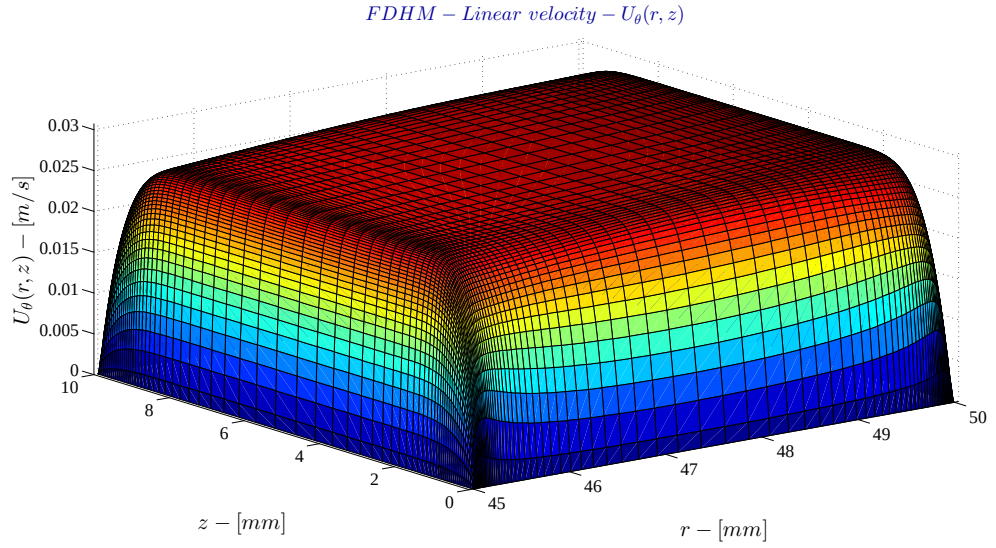

Figure 5.3: *FDHM - Linear velocity*

Figure(5.4) shows that the angular velocity in the core zone of the flux is constant; this helps to understand that the azimuthal velocity of the fluid in the core region varies linearly with the radius. This is consistent considering that the magnetic field varies linearly with the inverse of the radius.

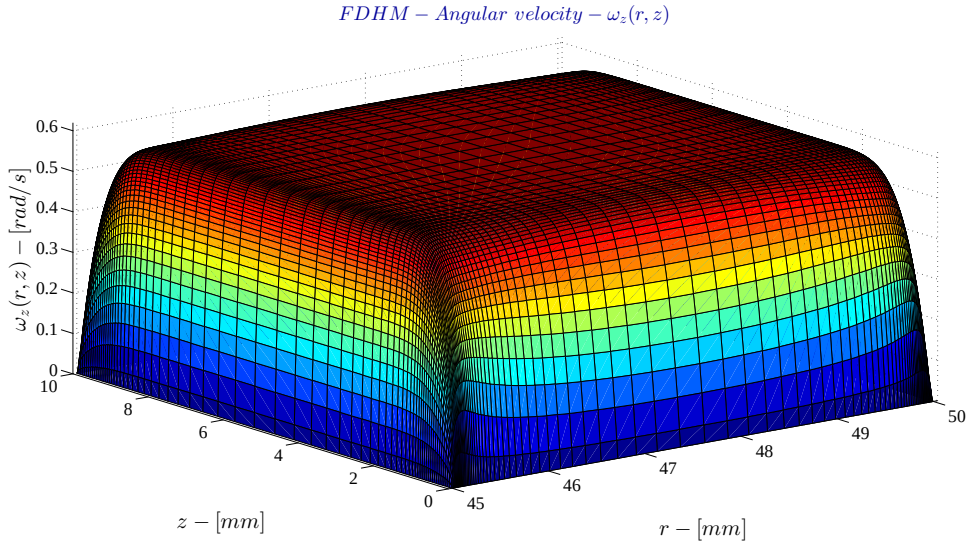

Figure 5.4: *FDHM - Angular velocity*

5.2 Torque-Current characteristic

Due to the presence of a liquid spinning the behaviour of this actuator appears to be different from the classical reaction wheels.

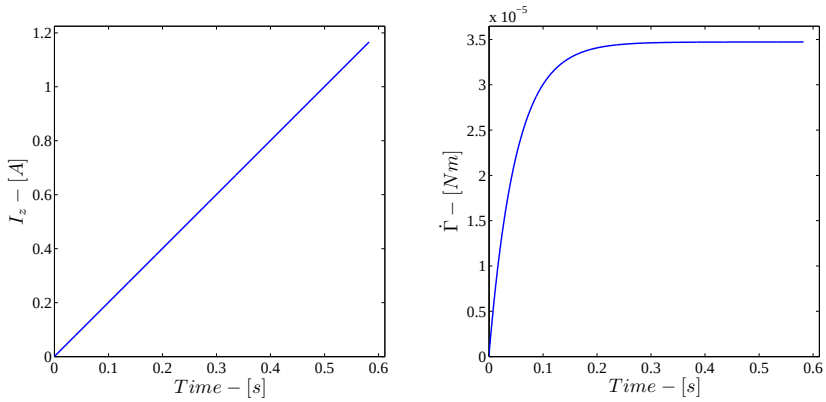

Figure 5.5: *FDHM - Torque*

In particular, the viscous shear leads to a different behaviour of the Torque-Current characteristic: while, for the classical reaction wheel, the torque provided is constant when the electric current fed to the device is constant, here, the torque is constant for a linear time-varying electric current, Figure (5.5). This comes directly from the nature of the model itself. It models a dumped system and the angular velocity of the liquid can be increased only providing an increasing torque acting on the liquid.

5.3 Current and Voltage drive

The FDHM is able to simulate both the current and voltage drive Figures (5.6)-(5.7).

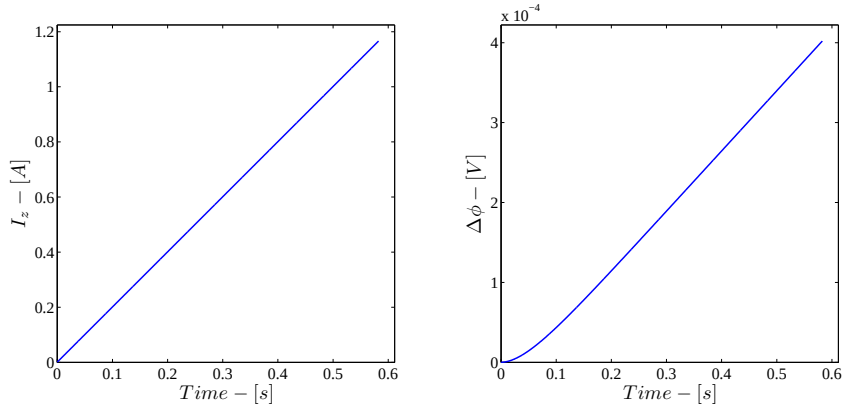

Figure 5.6: *FDHM - Current Drive*

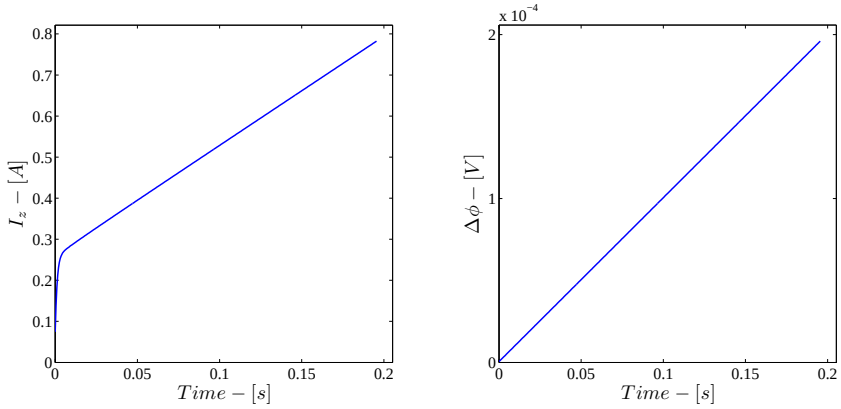

Figure 5.7: *FDHM - Voltage Drive*

The device appears to be characterized by non-linear effect in the neighbourhood of the null velocity. It can be seen by the trend of the electrostatic potential for the current drive and of the electric current in the case of voltage drive. The reason can be found in the modification of the velocity profile before than the fully developed MHD flow is reached.

5.4 Angular Momentum and Power Consumption

The FDHM can give information about power and angular momentum, Figures (5.8) - (5.9).
The power consumption of this devices is typically very low due to the high electric conductivity of the working fluid. The electrical resistance of the fluid at rest is of the order of 10^{-6} Ω; while the liquid increases its spin velocity the back electromotive force increases pulling the electric current to flow in narrows layers called Hartmann layers parallel to the z axis.

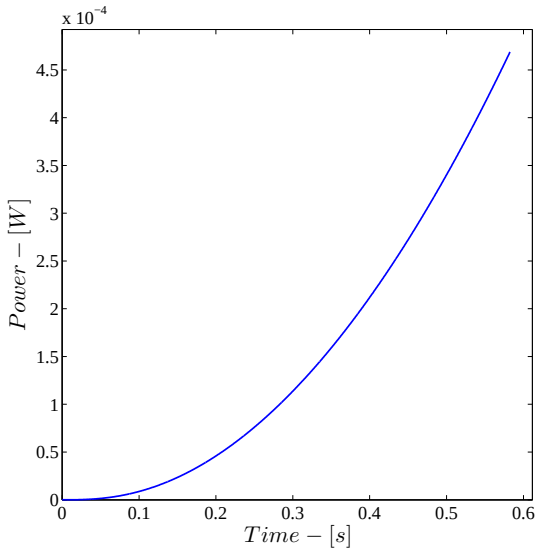

Figure 5.8: *FDHM - Power*

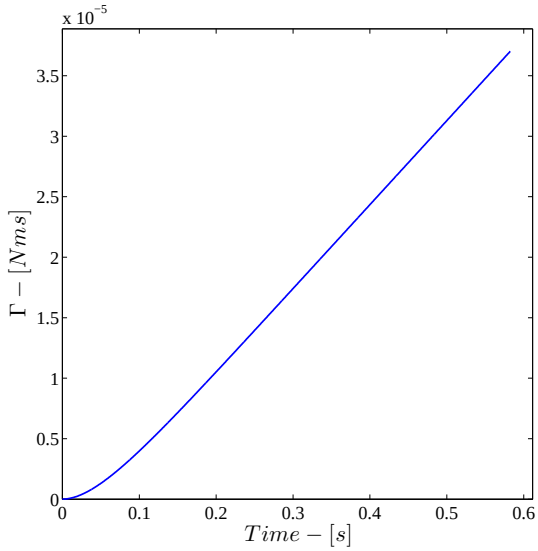

Figure 5.9: *FDHM - Angular Momentum* Γ

This leads to increasing values of the electrical resistance with increasing power consumption.
If the device is supplied with a linearly increasing electric current, the angular momentum has a linear trend with respect of the time, Figure (5.9). This is a direct consequence of the Torque-Current characteristic of this kind of device for which the torque provided is constant if the electric current is linear over the time.

5.5 Simulations

In order to test the accuracy of the FDHM and in order to understand the performances of the device, several simulations have been done.
The simulations have been computed varying the intensity of the magnetic field B_0, the electric conductivity of the liquid σ, the inner radius r_i and the height h of the the torus containing the liquid. Other parameter have been considered fixed, such as the outer radius r_e, the viscosity of the liquid μ and density ρ. The following table summarizes the grid of values of the simulations.
The results are provided in terms of physical quantities that will be described in the following subsections. The results are ordered according to electrical

	U.M.	Max Value	Min Value	N.points
Density - $\boldsymbol{\rho}$	$[kg/m^3]$	1000	1000	1
Viscosity - $\boldsymbol{\mu}$	$[Pa\ s]$	10^{-3}	10^{-3}	1
El. Conductivity - $\boldsymbol{\sigma}$	$[S/m]$	10^6	10	6
Magnetic Field - $\mathbf{B_0}$	$[T]$	0.8	0.2	4
Inner Radius - $\mathbf{r_i}$	$[mm]$	49	45	5
External Radius - $\mathbf{r_e}$	$[mm]$	50	50	1
Height - $\mathbf{h}$	$[mm]$	10	30	3

Table 5.1: *Values grid for the FDHM simulation*

conductivity of the the fluid simulated. In order to highlight the capabilities of the FDHM, the numeric error at the end of the each simulation of the dynamic and electric side of the problem are presented.
The results presented in the next sections refers only to liquid with electric conductivity $\sigma = 10\ S/m$, in 5.6, and $\sigma = 10^6\ S/m$ in 5.7. For all the intermediate values of electric conductivity the results are given in the Appendices: $\sigma = 10^2\ S/m$ in Appendix B, $\sigma = 10^3\ S/m$ in Appendix C, $\sigma = 10^4\ S/m$ in Appendix D, $\sigma = 10^5\ S/m$ in Appendix E. The results are discussed in 5.8.
For each electrical conductivity both the current drive and the voltage drive have been simulated. For the current drive an input of $a = 1A/s$ has been given, for the voltage drive $b = 10^{-3}V/s$.
The fluid has been considered at rest for $t = 0s$ and the simulations have been stopped when the torque reached the plateau.

5.5.1 Angular Momentum and Torque

The angular momentum Γ during the simulation is computed numerically. Each cell is considered as an infinitesimal hollow cylinder spinning at the center cell angular velocity. The angular momentum is then computed as follows:

$$\Gamma^n = \frac{\pi\rho}{2} \sum_{k=1}^{K} \sum_{l=1}^{L} \frac{u_{k,l}^n}{r_k} \left(z_{l+1/2} - z_{l-1/2}\right) \left(r_{k+1/2}^4 - r_{k-1/2}^4\right) \tag{5.5.1}$$

In order to increase the results readability, we decided not to plot the increasing angular momentum with the time, but the specific value of the angular momentum $\tilde{\Gamma}$ for an electric current of $I = 1A$. It has been computed dividing the angular momentum at the end of the simulation by the total electric

current flowing through the conductive liquid at the end of the simulation.

$$\tilde{\Gamma} = \left[\frac{\Gamma}{I^c}\right]_{EOS} \tag{5.5.2}$$

The torque provided is computed with a first order finite difference (same as Crank-Nicolson method) of the total angular moment:

$$\dot{\Gamma}^n = \frac{\Gamma^n - \Gamma^{n-1}}{dt} \tag{5.5.3}$$

where dt is the integration time step.

5.5.2 Characteristic Time

The characteristic time τ_c has been computed in the post-processing phase, finding the time when the provided torque is:

$$\dot{\Gamma}(t) = \left(1 - e^{-1}\right)\dot{\Gamma}_{max} \;\rightarrow\; \tau_c = t \tag{5.5.4}$$

The characteristic time is computed by interpolation in the case the previous relationship is not satisfied exactly in some of the time integration points.

5.5.3 Power

Because of the number of simulations and due to the fact that the power is constantly increasing with the time because of the increasing supplied electric current, the power plotted in the results is a specific value of the power. We can say it is an equivalent electric resistance.
The specific power $\tilde{P}$ is computed taking into account the total electric power at the end of the simulation, as the product between the voltage between the armatures and the total electric current flowing through the conductive liquid, divided by the the square of the total electric current:

$$\tilde{P} = \left[\frac{\Delta\phi\ I^c}{(I^c)^2}\right]_{EOS} = \left[\frac{\Delta\phi}{I^c}\right]_{EOS} \tag{5.5.5}$$

So, $\tilde{P}$ is an electric power over square electric current.

5.5.4 FDHM Errors

Together with the physical quantities just described, in the results can be read the numeric error of the solution of the electric and dynamic side of the problem for each simulation. The meaning of the errors is the same described in the equations Eq.(4.2.7) and Eq.(4.2.8).

5.6 Results: FDHM for $\sigma = 10\ S/m$

5.6.1 Current Drive

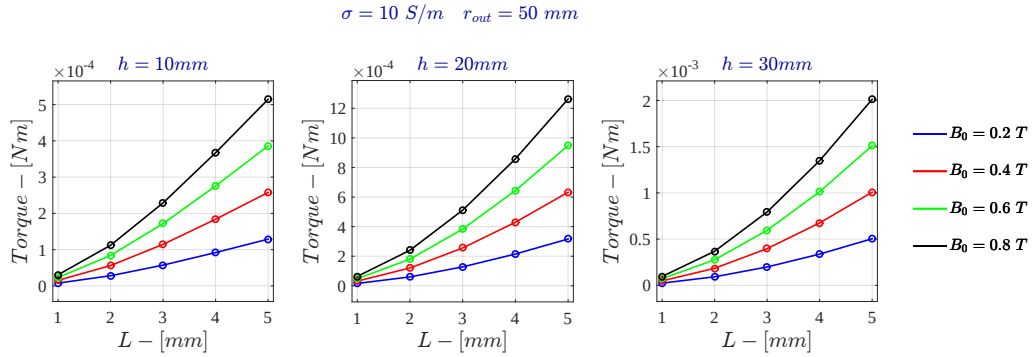

Figure 5.10: *Current Drive - Torque for* $\sigma = 10\ S/m$ *- FDHM*

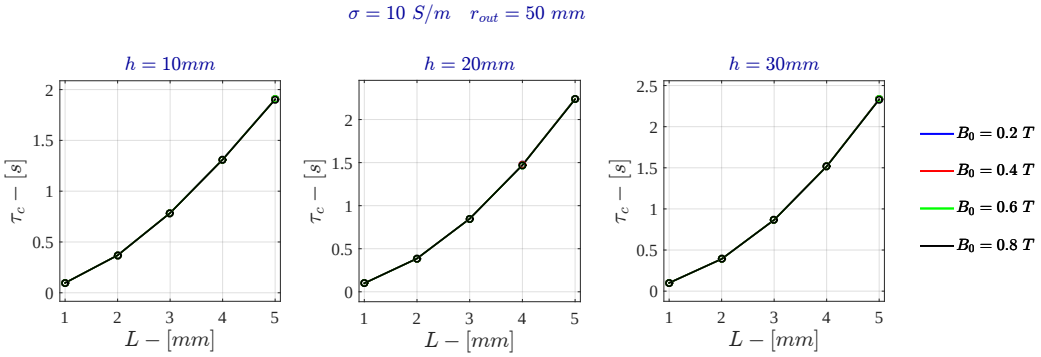

Figure 5.11: *Current Drive - Characteristic time for* $\sigma = 10\ S/m$ *- FDHM*

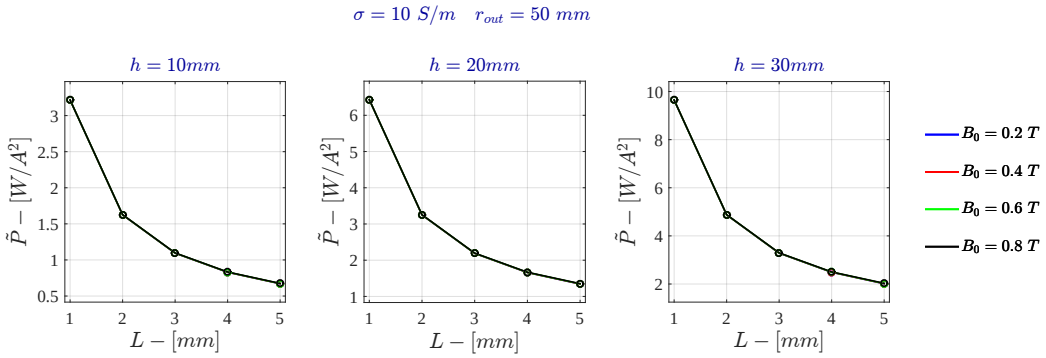

Figure 5.12: *Current Drive - Specific Power for* $\sigma = 10\ S/m$ *- FDHM*

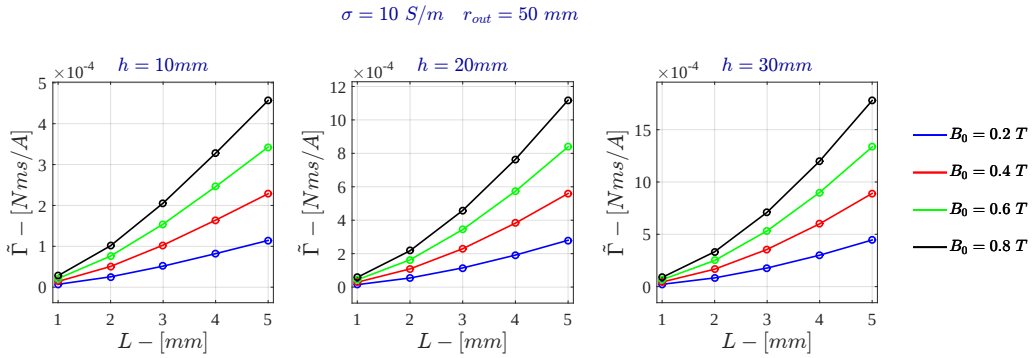

Figure 5.13: *Current Drive - Specific Angular Momentum for $\sigma = 10\ S/m$ - FDHM*

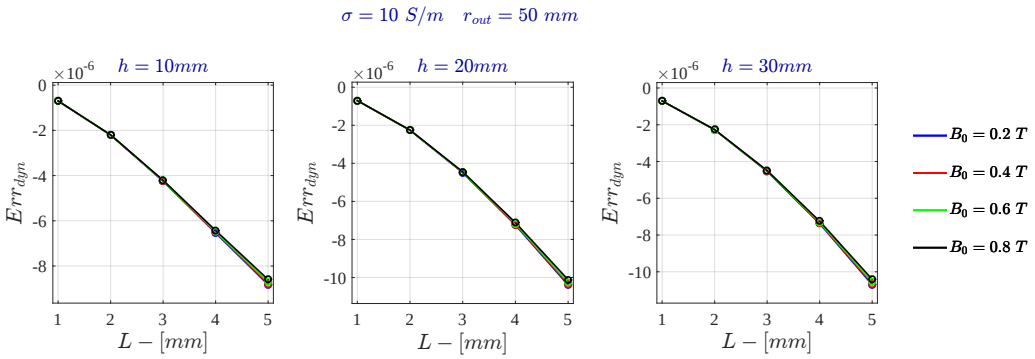

Figure 5.14: *Current Drive - Relative Dynamic Error for $\sigma = 10\ S/m$ - FDHM*

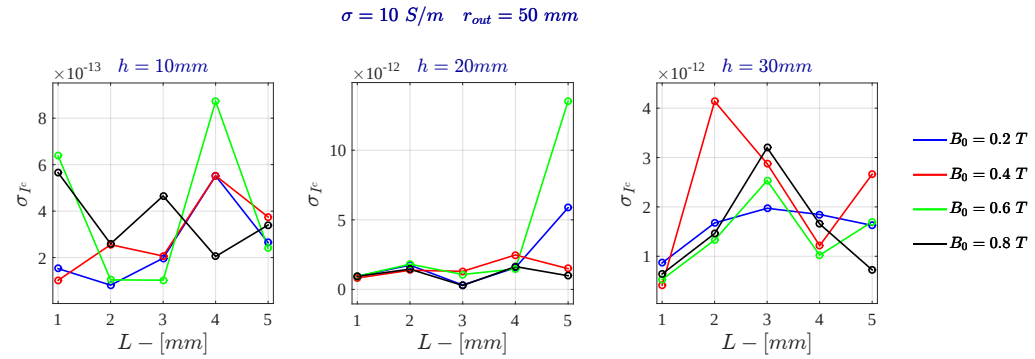

Figure 5.15: *Current Drive - Standard deviation of the electric current for $\sigma = 10\ S/m$ - FDHM*

5.6.2 Voltage Drive

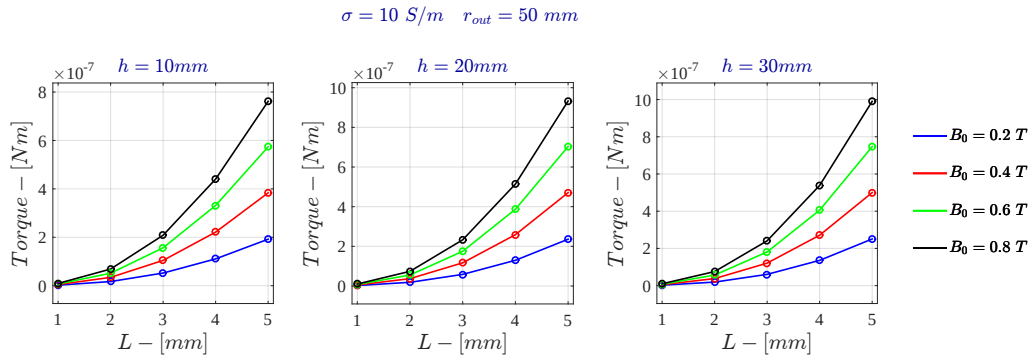

Figure 5.16: *Voltage Drive - Torque for* $\sigma = 10\ S/m$ *- FDHM*

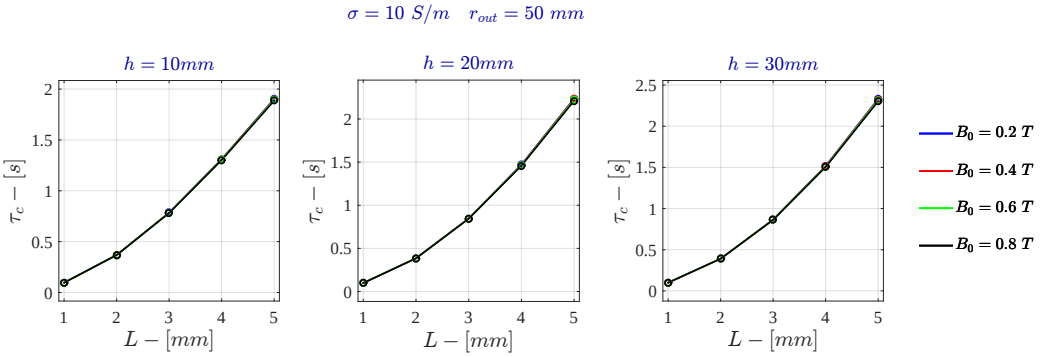

Figure 5.17: *Voltage Drive - Characteristic time for* $\sigma = 10\ S/m$ *- FDHM*

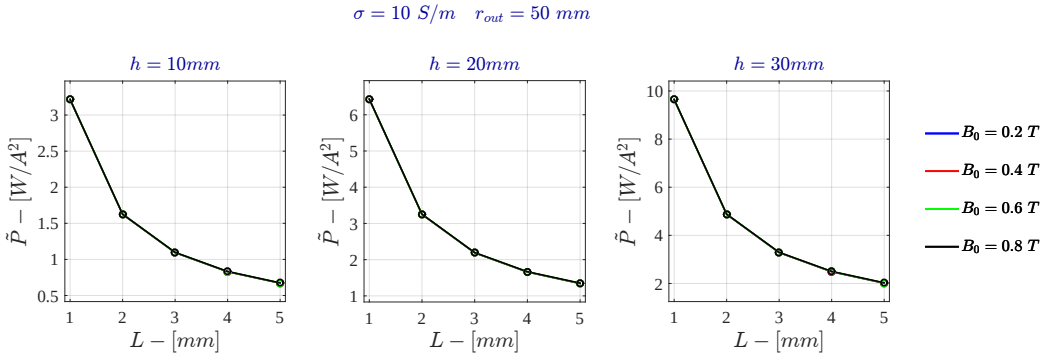

Figure 5.18: *Voltage Drive - Specific Power for* $\sigma = 10\ S/m$ *- FDHM*

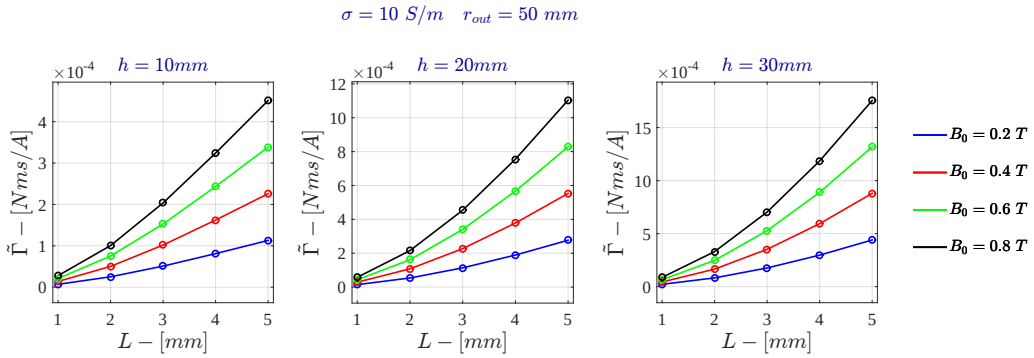

Figure 5.19: *Voltage Drive - Specific Angular Momentum for $\sigma = 10\ S/m$ - FDHM*

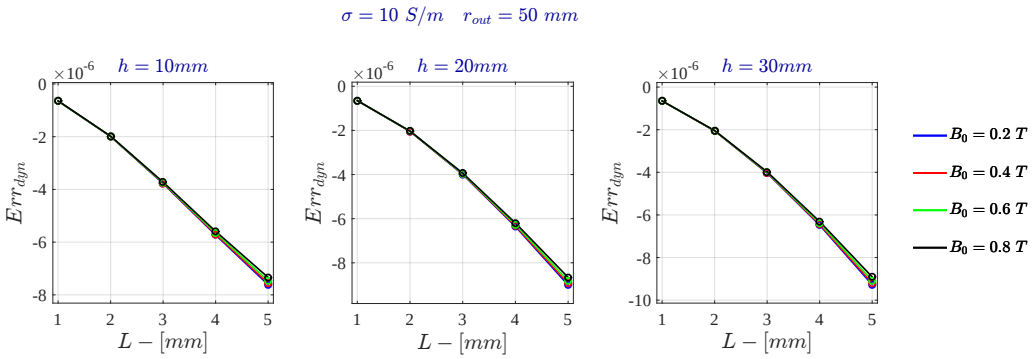

Figure 5.20: *Voltage Drive - Relative Dynamic Error for $\sigma = 10\ S/m$ - FDHM*

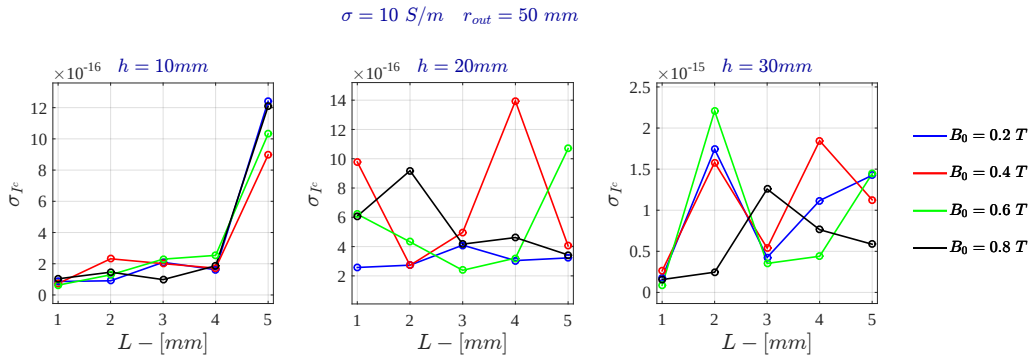

Figure 5.21: *Voltage Drive - Standard deviation of the electric current for $\sigma = 10\ S/m$ - FDHM*

5.7 Results: FDHM for $\sigma = 10^6\ S/m$

5.7.1 Current Drive

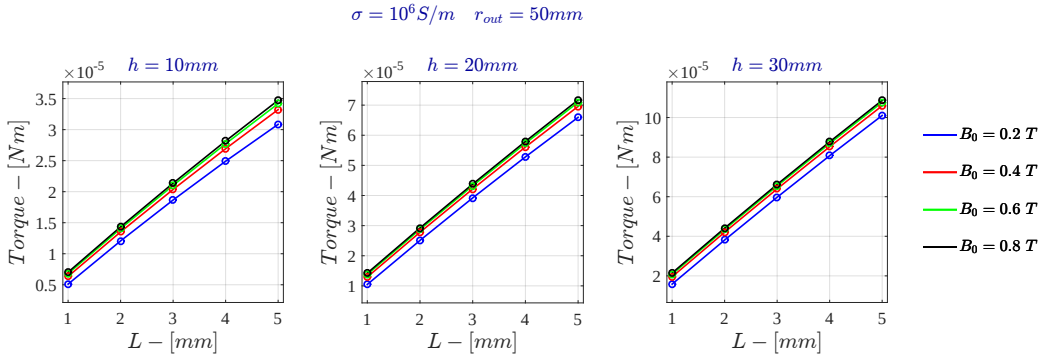

Figure 5.22: *Current Drive - Torque for* $\sigma = 10^6\ S/m$ *- FDHM*

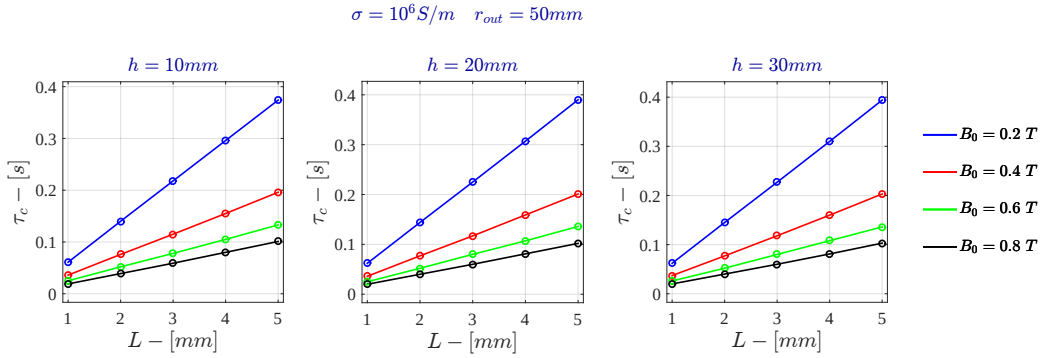

Figure 5.23: *Current Drive - Characteristic time for* $\sigma = 10^6\ S/m$ *- FDHM*

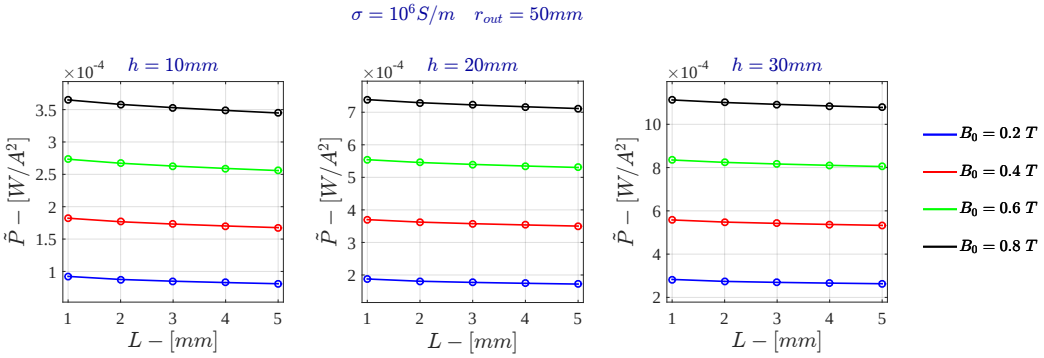

Figure 5.24: *Current Drive - Specific Power for* $\sigma = 10^6\ S/m$ *- FDHM*

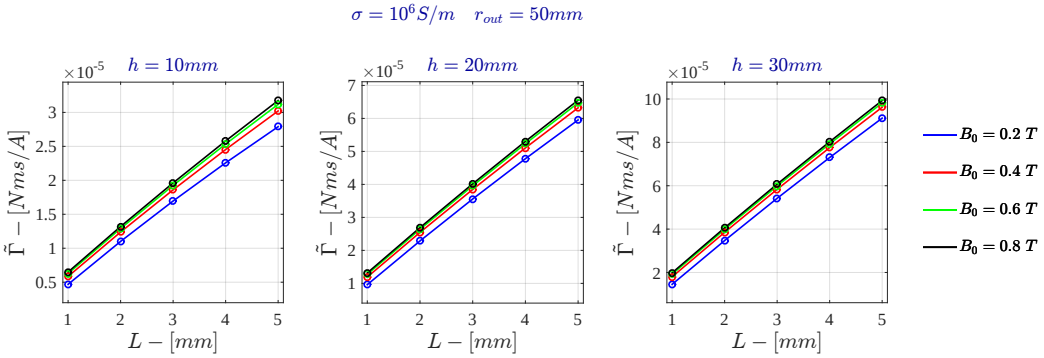

Figure 5.25: *Current Drive - Specific Angular Momentum for* $\sigma = 10^6\ S/m$ *- FDHM*

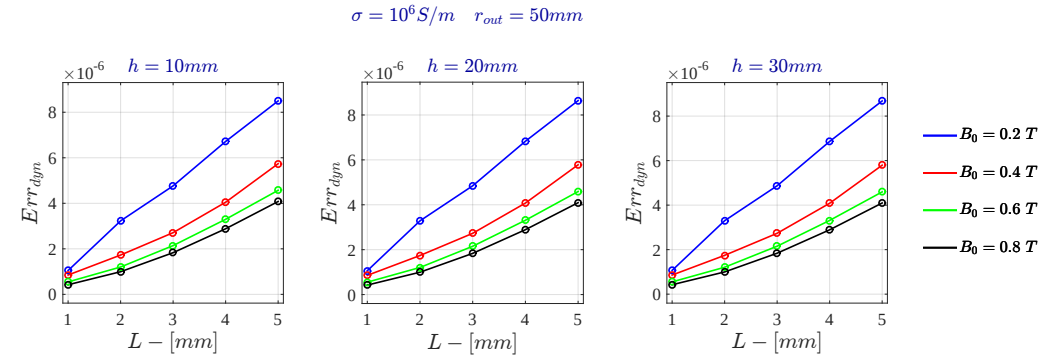

Figure 5.26: *Current Drive - Relative Dynamic Error for* $\sigma = 10^6\ S/m$ *- FDHM*

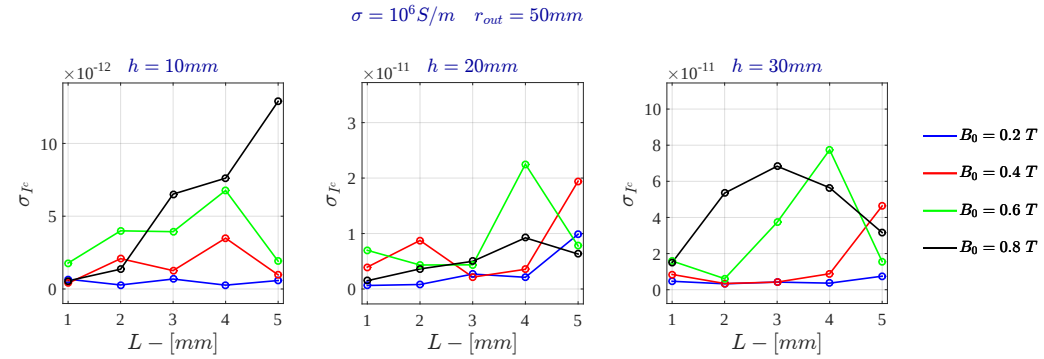

Figure 5.27: *Current Drive - Standard deviation of the electric current for* $\sigma = 10^6\ S/m$ *- FDHM*

5.7.2 Voltage Drive

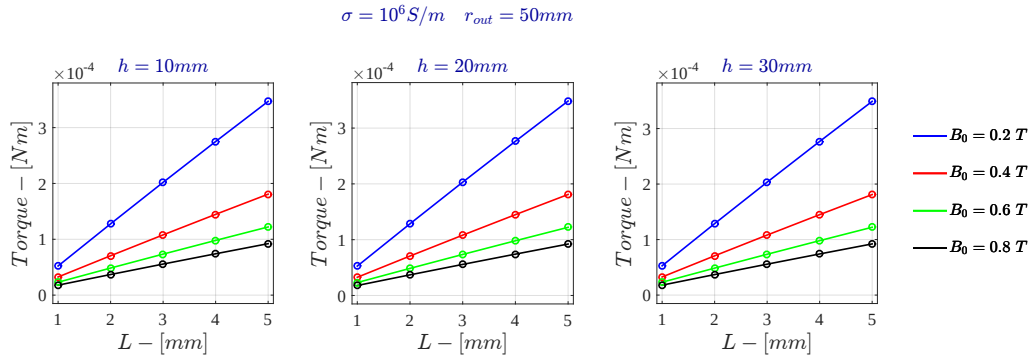

Figure 5.28: *Voltage Drive - Torque for* $\sigma = 10^6\ S/m$ *- FDHM*

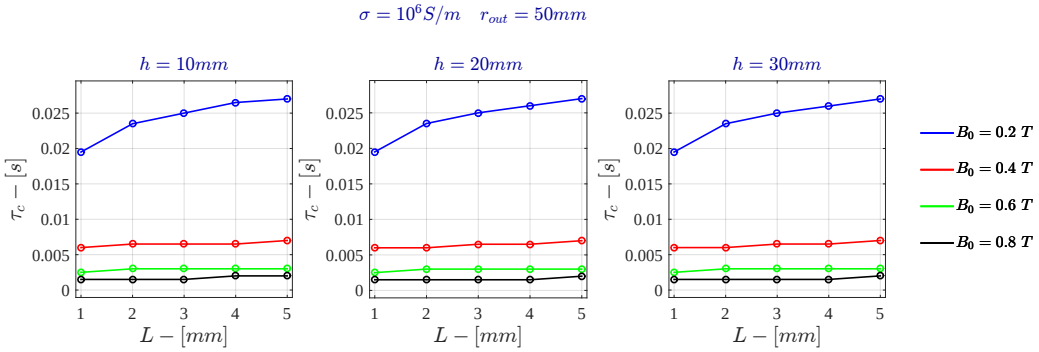

Figure 5.29: *Voltage Drive - Characteristic time for* $\sigma = 10^6\ S/m$ *- FDHM*

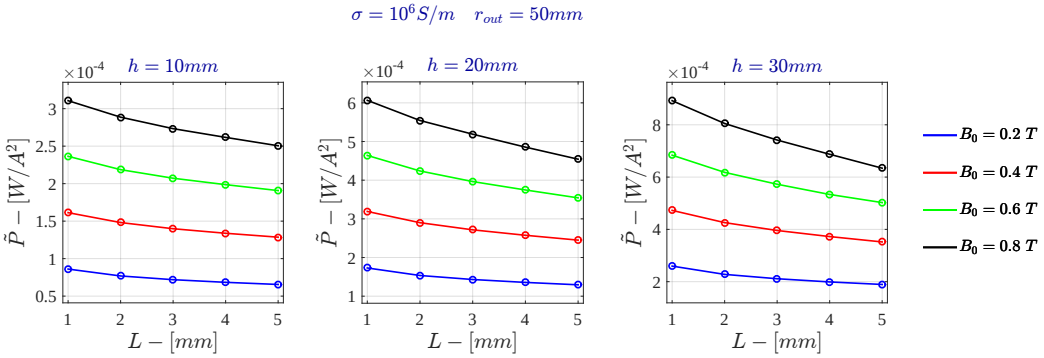

Figure 5.30: *Voltage Drive - Specific Power for* $\sigma = 10^6\ S/m$ *- FDHM*

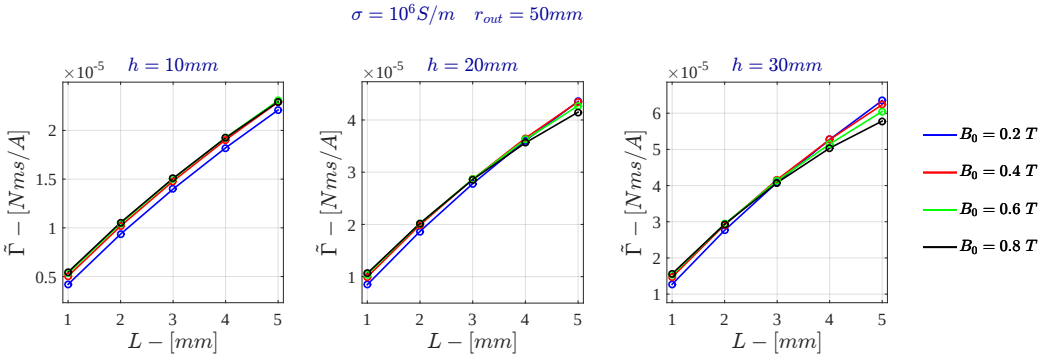

Figure 5.31: *Voltage Drive - Specific Angular Momentum for $\sigma = 10^6$ S/m - FDHM*

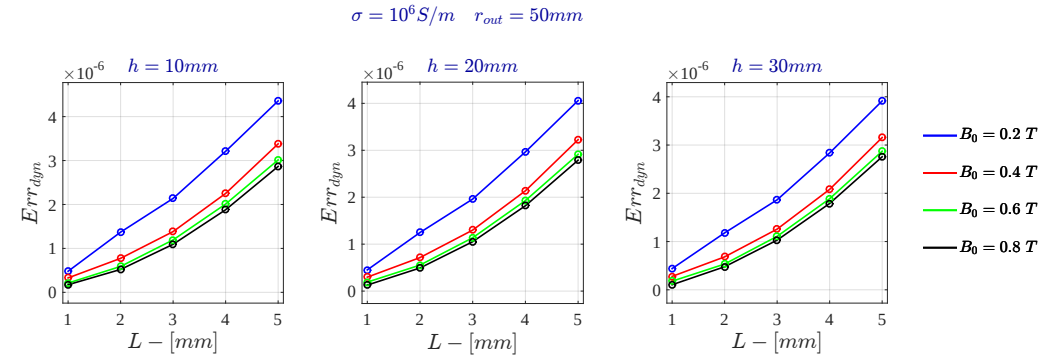

Figure 5.32: *Voltage Drive - Relative Dynamic Error for $\sigma = 10^6$ S/m - FDHM*

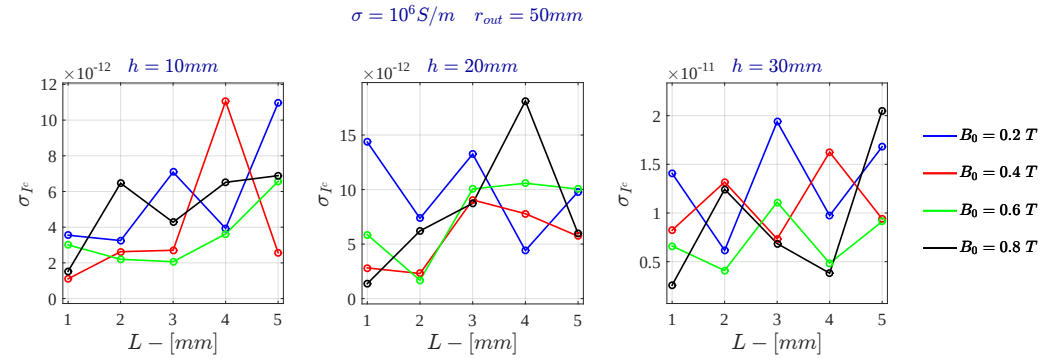

Figure 5.33: *Voltage Drive - Standard deviation of the electric current for $\sigma = 10^6$ S/m - FDHM*

5.8 Discussion

In this section we will discuss the plots present in the previous sections in order to highlight and justify the behaviour of the device and its sensitivity to the geometrical dimensions of the torus, the physical properties of the working fluid and the intensity of the magnetic field in both the case of current and voltage drive.
The torque provided by the device is highly dependent by the intensity of the magnetic field applied. In particular for increasing intensity of the magnetic field the torque increases. It is possible to see anyway two different trends according to the electrical conductivity of the working fluid.
For low electrical conductive fluid, Figure (5.10), the flow is almost biparabolic, and then quite different from a MHD flow at high Ha. The viscous shear is mainly linked with the overall dimensions of the cross section of the torus. So the torque provided increases for increasing height h and width L of the cross section because the viscous shear decreases. Being the viscous shear independent, in this case, by the magnetic field, the provided torque increases for increasing B_0 because the Lorentz force is proportional to the magnetic field applied.
For high electrical conductive fluid, Figure (5.22), the viscous shear is inversely proportional to the thickness of the Hartmann and Shercliff layers, which are proportional to $1/B_0$, and to the overall dimensions of the cross section. The torque provided increases for increasing height h and width L of the cross section. It increases for increasing intensity of the magnetic field but less than the case of low electrically conductive fluid. The reason resides in the fact that now, the viscous shear is proportional to the intensity of the magnetic field.
The torque provided in case of voltage drive is affected by the total electric current flowing through the liquid. Being the electric current influenced by the electric resistance of the fluid we can see in Figure (5.16) and Figure (5.28), that the torque is not proportional to the height h of the device. Furthermore for high electrically conductive liquids, Figure (5.28), the torque increases for decreasing intensity of the magnetic field; it is because the total electric current increases when the Hartmann layers become thicker and this has a major effects on the resulting Lorentz force than the intensity of the magnetic field.

The same cannot be said for low conductive fluid, Figure (5.10) and Figure (5.16), where the torque has the same trend, just scaled due to the different drive.
The characteristic time τ_c gives informations about the response of the system to a voltage or current input linear with the time, according to the specific drive.
For low conductive fluid, Figure (5.11) and Figure (5.17), the characteristic time is the same for both current and voltage drive. This is a proof of the fact that the flow is almost equivalent to classical Poiseuille flow and so not influenced by the magnetic field. In this this case, the characteristic time is mainly influenced by the moment of inertia of the spinning liquid, that increases for increasing height h and width L of the cross section.
For high conductive liquids, Figure (5.23) and Figure (5.29), on the contrary we have some differences. The system appears to have a faster response in the case of voltage drive than in the case of current drive. The reason is in the way the device manages the electric current. For current drive, the device has to distributed all the electric current given by the power supply to the fluid. This leads the system to be slower in the answer. On the contrary in the voltage drive the system chooses by itself the current according to the voltage applied and to the shape of the velocity profile. In Figure (5.6) and Figure (5.7) we can see that in the case of voltage drive the electric current increases faster in the first phase; this gives more Lorentz force to the liquid that tends faster to a fully developed laminar MHD flow than the case of current drive. For high electrically conductive fluids we can see that the characteristic time decreases for increasing intensity of the magnetic field, as the increasing viscous shear contributes to reach faster a fully developed laminar MHD flow.
The specific power $\tilde{P}$ has the meaning of equivalent electric resistance and it is computed using the voltage applied across the device and the total electric current.
For low conductive fluid, Figure (5.12) and Figure (5.18), there is no difference between voltage and current drive and the specific power $\tilde{P}$ can be considered as the classical electrical resistance of the fluid seen as simple electric conductor.
For high conductive fluid, Figure (5.24) and Figure (5.30), there are some little

differences and these are due to the different answer of the electric side of the system to the voltage or current drive. In Figure (5.6) and Figure (5.7) we can see that the voltage in the case of current drive and the current in the case of voltage drive have two different knees with opposite concavity. This influences the total electric power and as consequence the specific power, chosen as reference quantity.
The specific angular momentum $\tilde{\Gamma}$ is the angular momentum divided by the electric current flowing through the fluid. It has the meaning of how much angular momentum we can get from the device if the total current is $1/A$.
In the case of current drive in both the case of high and low conductive fluid, Figure (5.25) and Figure (5.13), we have that the specific angular momentum is numerically the same as the torque. The reason is the particular value of the current slope in time, $I = 1\ A$, that makes the specific angular momentum and torque numerically equivalent. In the case of voltage drive, Figure (5.19) and Figure (5.31), the behaviour of $\tilde{\Gamma}$ changes and it is due to the not constant electric current over the several simulation made. We will clarify better the behaviour of the angular momentum in the second phase of the project by means of a lumped parameter model.
Finally in the results can be found the computational errors made in the solution of the electric, Figures (5.15)-(5.27) and Figures (5.21)-(5.33), and the errors of the dynamic part of the problem, Figures (5.14)-(5.26) and Figures (5.20)-(5.32). The relative error in the solution of the dynamic part is of the order of 10^{-6} while the absolute error associated to the electric part is always less than 10^{-10}. They are all sufficiently low to consider the simulations trustworthy and it is also a proof of the accuracy of the FDHM over a wide range of input values.

Chapter

6 Methods and Procedures: Lumped Parameter Model

In this chapter, a Lumped Parameter Model similar to the model used for classical reaction wheels. The coefficients of the model are computed on the basis of two analytical solutions

6.1 Lumped Parameter Model

The lumped parameter model of a classical reaction wheel with rigid flywheel is well-known and it take into account the electric and dynamic phenomena happening while the flywheel spins. It has the following shape:

$$\begin{cases} I_z \dot{\omega}_w = K_I I \\ \Delta\phi = K_V \omega_w + R_{eq} I \end{cases} \tag{6.1.1}$$

The purpose of this chapter is to derive a lumped parameter model for the device in study. The model for the MHD reaction wheel is supposed to be very similar to the classical reaction wheel one. Some contributions need anyway to be added in order to take into account the viscous phenomena that are neglectable in the classical reaction wheel.
The Lumped Parameter Model (LPM) for MHD reaction wheel has the following shape:

$$\begin{cases} I_z c_\omega \dot{\omega}_w = -K_{vis} \omega_w + K_I I \\ \Delta\phi = K_V \omega_w + R_{eq} I \end{cases} \tag{6.1.2}$$

In the model the angular velocity ω_w of the fluid has the meaning of mean relative angular velocity between the fluid and the case of the reaction wheel. The model is similar to the model of a classical reaction wheel with an extra-term taking into account the viscous torque, proportional to the relative angular velocity ω_w. This term leads to a slight different behaviour of the Torque-Current characteristic: while, for the classical reaction wheel, the torque provided is constant when the electric current fed to the device is constant, here, the torque is constant if the electric current varies linearly over the time. This come directly from the nature of the device itself. It is modeled as a dumped system and the angular velocity of the liquid can be increased only providing an increasing torque acting on the liquid.
The first equation of (6.1.2) models the dynamic part of the problem stating that the provided torque is the resultant between the moment of the viscous shear and moment of the Lorentz force; the second equation of (6.1.2) models

the electric part of the problem stating that the applied voltage is equal to sum of the resistive voltage losses and the induced voltage generated by the electrically conductive liquid spinning through the magnetic field.
In the following two sections the coefficients of the dynamic and electric parts of the model will be derived [11].

6.2 Lumped Parameter Dynamic Model

In order to derive the dynamic part of the Lumped Parameter model we consider the Navier Stokes equation through an integral balance of moments along the z direction.

$$\int_V \rho r\hat{\mathbf{r}} \times \frac{\partial U_\theta}{\partial t}\hat{\boldsymbol{\theta}} dV = \int_V r\hat{\mathbf{r}} \times \left[J_z B\left(r\right)\right]\hat{\boldsymbol{\theta}} dV + \int_{S\perp r} \mu r\hat{\mathbf{r}} \times \left[r\frac{\partial}{\partial r}\left(\frac{U_\theta}{r}\right)\right]\hat{\boldsymbol{\theta}} dS + \int_{S\perp z} \mu r\hat{\mathbf{r}} \times \left[\frac{\partial U_\theta}{\partial z}\right]\hat{\boldsymbol{\theta}} dS \tag{6.2.1}$$

A stationary solution needs to be derived and used to obtain quantitative evaluation of the viscous shear at the boundaries together with an equivalent moment of inertia of the spinning liquid and the back electromotive force generated by the spinning liquid inside the superimposed magnetic field.
To compute the moment of the viscous shear, we consider the last term of right side of Eq.(6.2.1) and we obtain for the boundaries of the rectangular cross section:

$$M_{vis} = \int_{S\perp r} \mu r^2 \frac{\partial}{\partial r}\left(\frac{U_\theta}{r}\right) dS + \int_{S\perp z} \mu r \frac{\partial U_\theta}{\partial z} dS \tag{6.2.2}$$

where $S \perp r$ and $S \perp z$ are respectively the surfaces of the torus parallel to the z and r axes. For the terms on the right of the Eq.(6.2.2) a detailed expression can be given:

$$\begin{aligned}\int_{S\perp r} \mu r^2 \frac{\partial}{\partial r}\left(\frac{U_\theta}{r}\right) dS \; =& 2\pi\mu r_i^3 \int_0^h \left.\frac{\partial \omega_z(r,z)}{\partial r}\right|_{r=r_i} dz \\ &+ 2\pi\mu r_e^3 \int_0^h \left.\frac{\partial \omega_z(r,z)}{\partial r}\right|_{r=r_e} dz\end{aligned} \tag{6.2.3}$$

$$\begin{aligned}\int_{S\perp z} \mu r \frac{\partial U_\theta}{\partial z} dS \; =& 2\pi\mu \int_{r_i}^{r_e} r^3 \left.\frac{\partial \omega_z(r,z)}{\partial z}\right|_{z=0} dr \\ &+ 2\pi\mu \int_{r_i}^{r_e} r^3 \left.\frac{\partial \omega_z(r,z)}{\partial z}\right|_{z=h} dr\end{aligned} \tag{6.2.4}$$

The moment generated by the viscous shear can then be written as:

$$M_{vis} = K_{vis}\omega_w \tag{6.2.5}$$

where:

$$\begin{aligned}K_{vis} =& \frac{2\pi\mu r_i^3}{\omega_w} \int_0^h \left.\frac{\partial \omega_z(r,z)}{\partial r}\right|_{r=r_i} dz + \frac{2\pi\mu r_e^3}{\omega_w} \int_0^h \left.\frac{\partial \omega_z(r,z)}{\partial r}\right|_{r=r_e} dz \\ &+ \frac{2\pi\mu}{\omega_w} \int_{r_i}^{r_e} r^3 \left.\frac{\partial \omega_z(r,z)}{\partial z}\right|_{z=0} dr + \frac{2\pi\mu}{\omega_w} \int_{r_i}^{r_e} r^3 \left.\frac{\partial \omega_z(r,z)}{\partial z}\right|_{z=h} dr\end{aligned} \tag{6.2.6}$$

The term $\omega_z(r,z)\,\omega_w$ acquires the meaning of dimensionless angular velocity normalized with respect of the mean angular velocity.
The torque generated by the Lorentz Force can be derived from the first term of the right side of the (6.2.1). Introducing the shape of the radial magnetic field we have:

$$M_{Lor} = \int_V \mathbf{r} \times \hat{\theta}\,(J_z B_r)\, dV = B_0 r_i h I = K_I I \tag{6.2.7}$$

where:

$$K_I = B_0 r_i h \tag{6.2.8}$$

The term on the left side of the (6.2.1) represents the resulting torque acting on the conductive fluid, i.e. the time derivative of the angular moment. In order to have this term function of the only time derivative of the average relavite angular velocity of the fluid we start considering the angular moment in the reference frame of the spacecraft:

$$\Gamma = \int_V \rho r^2 \omega_z(r)\, \hat{\mathbf{z}} dV = \omega_w c_\omega I_z \hat{\mathbf{z}} \tag{6.2.9}$$

where:

$$c_\omega = \frac{2\pi\rho \int_{r_i}^{r_e} \int_0^h r^3 \omega_z(r,z)\, dr dz}{\omega_w I_z} \tag{6.2.10}$$

and I_z is the moment of inertia of a rigid hollow cylinder with the same dimensions of the cavity containing the liquid. In this way the time-derivative of the angular moment can be considered as:

$$\dot{\Gamma} = \dot{\omega}_w c_\omega I_z \tag{6.2.11}$$

due to invariance with respect of the time of the coefficient c_ω.

6.3 Lumped Parameter Electric Model

A formula for the lumped parameter electric model of the proposed MHD reaction wheel can be obtained by integrating over the volume the microscopic Ohm's Law for moving conductor and introducing the relative velocity between the liquid and the magnetic field considered stiffly linked to the boundaries:

$$\int_V E_z dz dS = \int_V \frac{J_z}{\sigma} dz dS + \int_V r\omega_z(r)\, B_r dz dS \tag{6.3.1}$$

Considering the electrostatic potential ϕ uniform over the surface and applying the conservation of the electric current we obtain:

$$\Delta\phi = I\frac{h}{\sigma S} + \frac{\int_V r\omega_z\left(r,z\right)B_r dzdS}{S} \tag{6.3.2}$$

where the coefficient of the electric current is the equivalent electric resistance of the conductive liquid:

$$R_{eq} = \frac{h}{\sigma S} \tag{6.3.3}$$

The second term on the right side of the (6.3.1) is the induced voltage that can be written as:

$$\Delta\phi_{ind} = K_V\omega_w \tag{6.3.4}$$

where:

$$K_V = 2\pi B_0 r_i \frac{\int_{r_i}^{r_e}\int_0^h r\omega_z\left(r,z\right)drdz}{\omega_w S} \tag{6.3.5}$$

6.4 Analytical solution for the angular and linear velocity

The principal problem to be solved to derive the LPM is to find an analytical solution for the angular and linear velocity of the conducting liquid. This step is necessary to compute the LPM coefficients which appear to be function of this distributions and because the LPM is referred to the average angular of the fluid.
In this paragraph two different solutions will be developed and then compared with the numerical solution provided by the FDHM model.

6.4.1 Monodimensional solution under the hypothesis of Low-Magnetic Reynolds

For convenience we proceed writing the whole set of equation in dimensionless variables. We obtain:

$$\nabla' \cdot \mathbf{b} = 0 \tag{6.4.1}$$

$$\nabla' \cdot \mathbf{j} = 0 \tag{6.4.2}$$

$$\mathbf{j} = \mathbf{e} + \mathbf{u} \times \mathbf{b} \tag{6.4.3}$$

$$\nabla' \times \mathbf{e} = 0 \tag{6.4.4}$$

$$\frac{\partial \mathbf{u}}{\partial \tau} = \frac{1}{Re}\Delta' \mathbf{u} + \frac{Ha^2}{Re}\mathbf{j} \times \mathbf{b} \tag{6.4.5}$$

$$s = \frac{r}{r_e} \tag{6.4.6}$$

$$\nabla' \cdot \mathbf{u} = 0 \tag{6.4.7}$$

in which the following substitutions have been done:

$$\mathbf{u} = \frac{\mathbf{U}}{U_0} \tag{6.4.8}$$

$$\mathbf{b} = \frac{\mathbf{B}}{B_0} \tag{6.4.9}$$

$$\mathbf{e} = \frac{\mathbf{E}}{B_0\ U_0} \tag{6.4.10}$$

$$\mathbf{j} = \frac{\mathbf{J}}{\sigma\ B_0\ U_0} \tag{6.4.11}$$

$$\tau = \frac{t\ U_0}{L} \tag{6.4.12}$$

$$\nabla' = L\ \nabla \tag{6.4.13}$$

The coefficients in Eq.(6.4.5) are the Hartmann Number, Ha defined as $B_0 L\sqrt{\sigma/\mu}$ and the Reynolds number, Re, defined as $\rho L U_0/\mu$. In Eqs.(6.4.8)-(6.4.13) U_0 has the meaning of average velocity of the fluid, B_0 is the magnetic field density at the outer radius and r_e is the outer radius of the liquid flywheel.
The main simplifying assumption adopted is to consider infinite the length of the annulus along the axis of symmetry. It implies the neglection of the boundary effects next to the two electric armatures and it implies moreover that all the derivative along z are considered neglectible. The superimposed magnetic field is assumed to be dependent just from the radial coordinate. This assumption together with the uniformity of the imposed electric field $\mathbf{e}$ makes the problem axially symmetric, i.e. all the derivative with respect of the

azimuthal direction can be neglected.

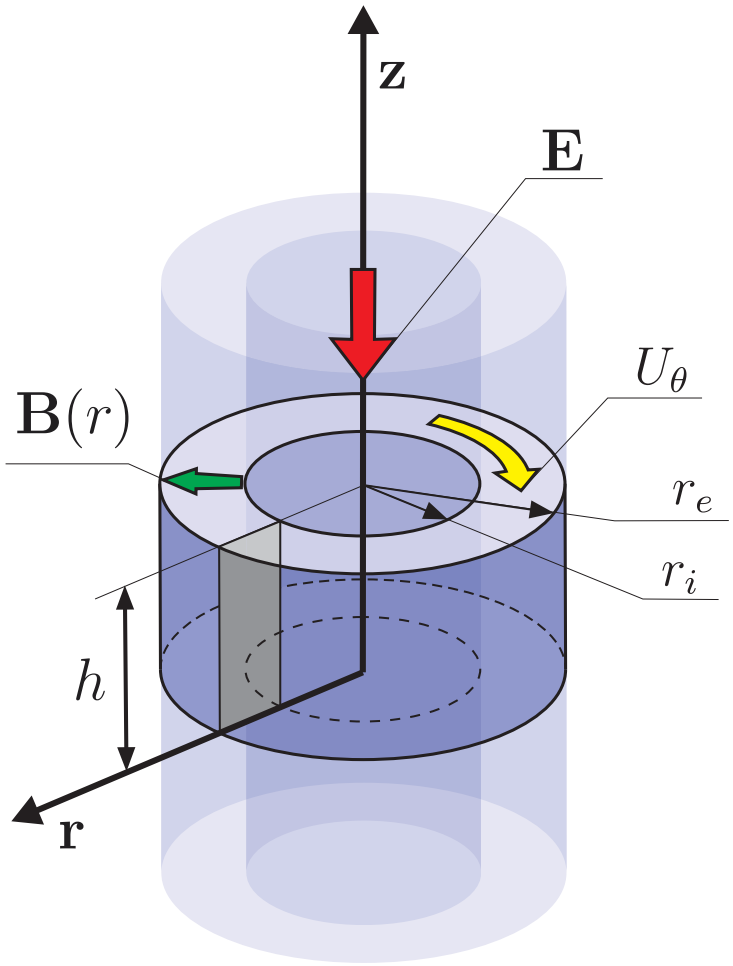

Figure 6.1: *Section of an infinite annulus with applied electric field* **E** *and radial magnetic field* $\mathbf{B}(r)$.

We start by analyzing the continuity equations of the magnetic flux density **b**, current density **j** and velocity **u**.
It is possible to simplify the continuity equations for the dimensionless magnetic flux density **b**, Eq.(6.4.1), the dimensionless electric current density **j**, Eq.(6.4.2), and the dimensionless velocity of the fluid **u**, Eq.(6.4.7). Introducing the expression of the divergence in cylindrical coordinates and simplifying we obtain:

$$\nabla \mathbf{b} = \frac{1}{s}\frac{\partial}{\partial s}(sb_r) + \frac{1}{s}\frac{\partial b_\theta}{\partial \theta} + \frac{\partial b_z}{\partial z} = \frac{\partial}{\partial s}(sb_r) = 0 \qquad (6.4.14)$$

$$\nabla \mathbf{j} = \frac{1}{s}\frac{\partial}{\partial s}(sj_r) + \frac{1}{s}\frac{\partial j_\theta}{\partial \theta} + \frac{\partial j_z}{\partial z} = \frac{\partial}{\partial s}(sj_r) = 0 \tag{6.4.15}$$

$$\nabla \mathbf{u} = \frac{1}{s}\frac{\partial}{\partial s}(su_r) + \frac{1}{s}\frac{\partial u_\theta}{\partial \theta} + \frac{\partial u_z}{\partial z} = \frac{\partial}{\partial s}(su_r) = 0 \tag{6.4.16}$$

with the following boundary condition at the outer radius:

$$\begin{aligned} & b_r(s_0, \tau) = 1 \\ s_0 = 1 \quad & j_r(s_0, \tau) = 0 \\ & u_r(s_0, \tau) = 0 \end{aligned} \tag{6.4.17}$$

Solving Eqs.(6.4.14)-(6.4.16) using Eqs.(6.4.17) we obtain:

$$b_r(s, \tau) = \frac{1}{s} \tag{6.4.18}$$

$$j_r(s, \tau) = 0 \tag{6.4.19}$$

$$u_r(s, \tau) = 0 \tag{6.4.20}$$

The axial component of the dimensionless velocity, u_z, can be studied taking into account the Eq.(6.4.5) along z:

$$\frac{\partial u_z}{\partial \tau} = \frac{\lambda^2}{Re}\left[\frac{1}{s}\frac{\partial}{\partial s}\left(s\frac{\partial u_z}{\partial s}\right)\right] + \frac{Ha^2}{Re} j_\theta b_r \tag{6.4.21}$$

Using the hypothesis of axial-symmetry it is possible to say that the component along θ of the current density j_θ is null both because of the radial distribution of the magnetic field and because of the uniformity of the electric field applied. This result leads the Eq. (6.4.21) to be a homogeneous PDE with homogeneous boundary condition due to the no-slip condition applied at the boundaries to the velocity field. Furthermore and without lack of generality we can impose that the fluid is at rest at the initial time $\tau = 0$. This problem gives a null

solution over the time for the u_z:

$$u_z(s,\tau) = 0 \tag{6.4.22}$$

Writing the Eq.(6.4.3) along the three directions of cylindrical reference frame and being the dimensionless velocity purely azimuthal and the magnetic flux density purely radial we have:

$$\begin{aligned} e_r &= j_r - u_\theta b_z + u_z b\theta = 0 \\ e_\theta &= j_\theta - u_z b_r + u_r bz = 0 \\ e_z &= j_z - u_r b_\theta + u_\theta b_r = j_z + u_\theta b_r \end{aligned} \tag{6.4.23}$$

The Eq.(6.4.4) describing the irrotationality of the applied electric field is solved taking into account the hypothesis that the component of the electric field along the z direction is uniform. In other words if we consider each armature equipotential we can see that the electric field along the z direction does not vary along the radial and azimuthal directions.
Finally we obtain the complete set of equation for magneto-fluid problems under the hypothesis of Low-Magnetic Reynolds reduced to the the following system of three equations:

$$b_r = \frac{1}{s} \tag{6.4.24}$$

$$j_z = e_z - u_\theta b_r \tag{6.4.25}$$

$$\frac{\partial u_\theta}{\partial \tau} = \frac{\lambda^2}{Re}\frac{\partial}{\partial s}\left[\frac{1}{s}\frac{\partial}{\partial s}\left(s u_\theta\right)\right] + \frac{Ha^2}{Re} j_z b_r \tag{6.4.26}$$

in which Eq.(6.4.24) is already solved and just Eqs.(6.4.25)-(6.4.26) are coupled. Starting from the hypothesis of Low-Magnetic Reynolds the same equations as in [25] has been found and we can use the same solution proposed in the paper.

Writing the Eq.(6.4.26) with the same symbology as in Reference [25] and introducing the Eq.(6.4.25) we have:

$$\frac{\partial u_\theta}{\partial \tau} = C_1 \left[\frac{\partial^2 u_\theta}{\partial s^2} + \frac{1}{s}\frac{\partial u_\theta}{\partial s} - \frac{n^2 u_\theta}{s^2} \right] + C_2 \frac{e_z}{s} \tag{6.4.27}$$

where:

$$\begin{aligned} C_1 &= \lambda^2/Re \qquad & C_2 &= Ha^2/Re \\ \lambda &= L/R \qquad & n^2 &= 1 + Ha^2/\lambda^2 \end{aligned} \tag{6.4.28}$$

In [25] two solutions are given: one steady-state solution and one time-dependent solution. Looking at the purpose to obtain a lumped parameter model we show more interest in the stationary solution in which the influence of the electric current and the shape of velocity profile can be easily uncoupled instead of considering the transient solution that gives a time dependent solution but by which is not possible to derive a lumped parameter model.
The steady-state solutions for the velocity and the angular velocity are:

$$U_\theta(r) = \frac{E_z}{B_0}\left[A_1 r - A_2 r^n - A_3 \frac{1}{r^n} \right] \tag{6.4.29}$$

$$\omega_z(r) = \frac{U_\theta(r)}{r} = \frac{E_z}{B_0}\left[A_1 - A_2 r^{n-1} - A_3 \frac{1}{r^{n+1}} \right] \tag{6.4.30}$$

where:

$$A_1 = \frac{1}{R} \quad A_2 = \frac{1-\beta^{n+1}}{(1-\beta^{2n})R^n} \quad A_3 = \frac{\beta^{n+1}(1-\beta^{n-1})R^n}{1-\beta^{2n}} \tag{6.4.31}$$

and

$$\beta = 1 - \lambda \tag{6.4.32}$$

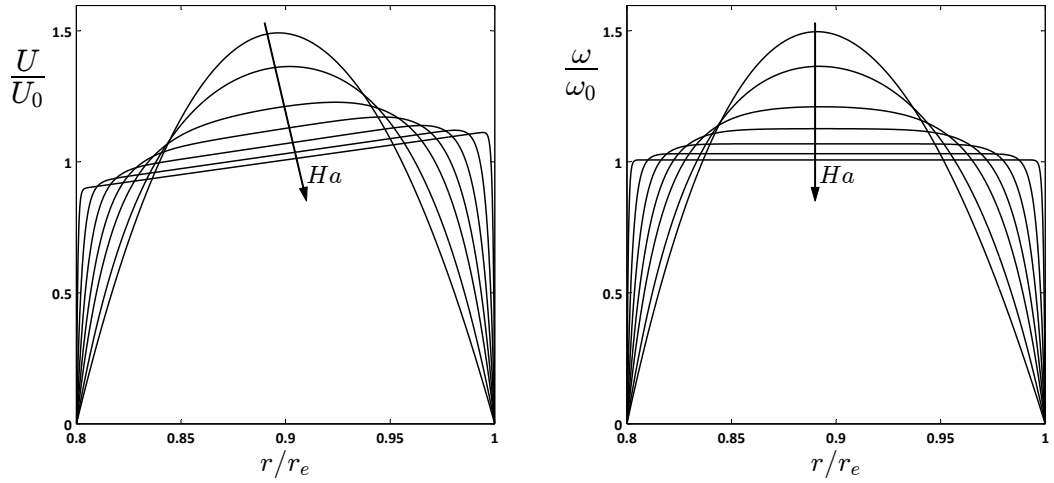

Figure 6.2: *Analytical solutions for dimensionless linear and angular velocities at different Hartmann Number Ha.*

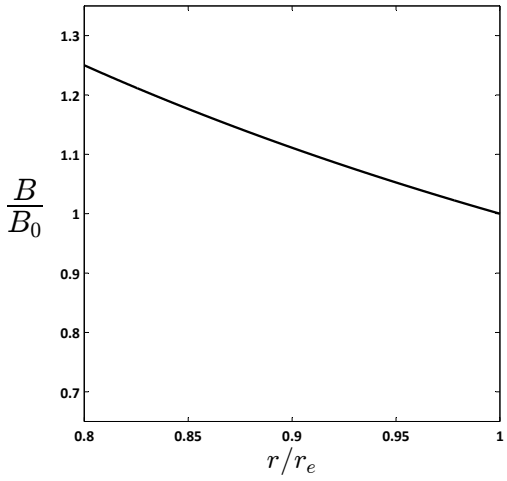

Figure 6.3: *Magnetic Field Density* **B** *normalized with respect of the Magnetic Field Density B_0 at the outer radius.*

The shape of the dimensional magnetic field B can be obtained from the Eqs.(6.4.9)-(6.4.24):

$$\mathbf{B}(r) = \frac{B_0 r_e}{r} \tag{6.4.33}$$

where B_0 is the value of the magnetic field at $r = r_e$. The solution is expressed in dimensional quantities. The coefficients n and β in Eq.(6.4.29) are function

of the physical property of the conductive fluid and of the dimension along the direction r of the cavity containing the fluid. The solution can be considered expressed in the reference frame of the spacecraft with the meaning of relative velocity between the liquid and the case. With respect of [25] this solution has been derived explicitly under the hypothesis of Low-Re_m and this can help to understand the range of validity of the solution.

6.4.2 Bi-dimensional solution extended to the cross-section

The first attempt is to find an asymptotic bi-dimensional analytical solution for the complete set of the MHD equations in cylindrical coordinates with radial magnetic field and axial electric current. Hunt and Baylis [12] already succeeded in finding this analytical solution but in the case of axial magnetic field and radial electric current. The same procedures can be followed to try to find a solution for the case in study.
The complete set of equations needs to be used:

$$\nabla \times \mathbf{E} = -\frac{\partial \mathbf{B}}{\partial t} \tag{6.4.34}$$

$$\nabla \cdot \mathbf{B} = 0 \tag{6.4.35}$$

$$\nabla \times \mathbf{H} = 4\pi \mathbf{J} \tag{6.4.36}$$

$$\nabla \cdot \mathbf{J} = 0 \tag{6.4.37}$$

$$J = \sigma(\mathbf{E} + \mathbf{V} \times \mathbf{B}) \tag{6.4.38}$$

$$-\nabla P_n + \nu\rho\Delta\mathbf{V} + \mathbf{J} \times \mathbf{B} = 0 \tag{6.4.39}$$

$$\nabla \cdot \mathbf{V} = 0 \tag{6.4.40}$$

Expanding the Eq.(6.4.38) and considering that:

$$\mathbf{E} = E_r\hat{r} + E_z\hat{z} = -\frac{\partial \phi}{\partial r}\hat{r} - \frac{\partial \phi}{\partial z}\hat{z} \tag{6.4.41}$$

we have:

$$J_r = -\sigma \frac{\partial \phi}{\partial r} \tag{6.4.42}$$

$$J_z = -\sigma \left(\frac{\partial \phi}{\partial z} + U_\theta \ \hat{\theta} \times \mathbf{B} \right) \tag{6.4.43}$$

Applying to Eq.(6.4.42) and Eq.(6.4.43) respectively the derivative with respect of z and r we obtain:

$$\frac{\partial J_r}{\partial z} = -\sigma \frac{\partial^2 \phi}{\partial r \partial z} \tag{6.4.44}$$

$$\frac{\partial J_z}{\partial r} = \sigma \left[-\frac{\partial^2 \phi}{\partial r \partial z} + \frac{\partial \left(U_\theta \ \hat{\theta} \times \mathbf{B} \right)}{\partial r} \right] \tag{6.4.45}$$

Taking now into account the Eq.(6.4.36) we have:

$$J_r = -\frac{1}{4\pi} \frac{\partial H_\theta}{\partial z} \tag{6.4.46}$$

$$J_z = \frac{1}{4\pi} \frac{1}{r} \frac{\partial (r H_\theta)}{\partial r} \tag{6.4.47}$$

Proceeding as before we obtain:

$$\frac{\partial J_r}{\partial z} = -\frac{1}{4\pi} \frac{\partial^2 H_\theta}{\partial z^2} \tag{6.4.48}$$

$$\frac{\partial J_z}{\partial r} = \frac{1}{4\pi} \left[\frac{1}{r} \frac{\partial H_\theta}{\partial r} + \frac{\partial^2 H_\theta}{\partial r^2} - \frac{H_\theta}{r^2} \right] \tag{6.4.49}$$

It is possible then to compare the Eq.(6.4.44) with Eq.(6.4.48):

$$\frac{\partial J_r}{\partial z} = -\sigma \frac{\partial^2 \phi}{\partial r \partial z} = -\frac{1}{4\pi} \frac{\partial^2 H_\theta}{\partial z^2} \tag{6.4.50}$$

and the Eq.(6.4.45) with Eq.(6.4.49):

$$\frac{\partial J_z}{\partial r} = \sigma \left[-\frac{\partial^2 \phi}{\partial r \partial z} + \frac{\partial \left(U_\theta \ \hat{\theta} \times \mathbf{B} \right)}{\partial r} \right] = \frac{1}{4\pi} \left[\frac{1}{r} \frac{\partial H_\theta}{\partial r} + \frac{\partial^2 H_\theta}{\partial r^2} - \frac{H_\theta}{r^2} \right] \quad (6.4.51)$$

Subtracting the Eq.(6.4.50) to the Eq.(6.4.51) we have:

$$\frac{1}{r} \frac{\partial H_\theta}{\partial r} + \frac{\partial^2 H_\theta}{\partial r^2} + \frac{\partial^2 H_\theta}{\partial z^2} - \frac{H_\theta}{r^2} - 4\pi\sigma \frac{\partial \left(U_\theta \ \hat{\theta} \times \mathbf{B} \right)}{\partial r} = 0 \quad (6.4.52)$$

Considering a perfect radial applied magnetic field with equation:

$$\mathbf{B} = B_0 \frac{r_i}{r} \quad (6.4.53)$$

The last term of Eq.(6.4.52) can be written as:

$$4\pi\sigma \frac{\partial \left(U_\theta \ \hat{\theta} \times \mathbf{B} \right)}{\partial r} = -4\pi\sigma B_0 r_i \left(\frac{1}{r} \frac{\partial U_\theta}{\partial r} - \frac{U_\theta}{r^2} \right) \quad (6.4.54)$$

We finally obtain:

$$\frac{\partial^2 H_\theta}{\partial r^2} + \frac{\partial^2 H_\theta}{\partial z^2} + \frac{1}{r} \frac{\partial H_\theta}{\partial r} - \frac{H_\theta}{r^2} + 4\pi\sigma B_0 r_i \left(\frac{1}{r} \frac{\partial U_\theta}{\partial r} - \frac{U_\theta}{r^2} \right) = 0 \quad (6.4.55)$$

The Navier stokes equation Eq.(6.4.39) along the θ direction is:

$$\mu \left[\frac{1}{r} \frac{\partial}{\partial r} \left(r \frac{\partial U_\theta}{\partial r} \right) + \frac{\partial^2 U_\theta}{\partial z^2} - \frac{U_\theta}{r^2} \right] + J_z \mathbf{B} = 0 \quad (6.4.56)$$

With the aid of the Eqs.(6.4.47),(6.4.53) the last term become:

$$J_z \mathbf{B} = B_0 r_i \left(\frac{1}{r} \frac{\partial H_\theta}{\partial r} + \frac{1}{r^2} H_\theta \right) \quad (6.4.57)$$

and then:

$$\frac{\partial^2 U_\theta}{\partial r^2} + \frac{\partial^2 U_\theta}{\partial z^2} + \frac{1}{r}\frac{\partial U_\theta}{\partial r} - \frac{U_\theta}{r^2} + \frac{B_0 r_i}{\mu}\left(\frac{1}{r}\frac{\partial H_\theta}{\partial r} + \frac{H_\theta}{r^2}\right) = 0 \tag{6.4.58}$$

What can be seen is that Eqs.(6.4.56) and (6.4.58) have similar shape. The first four terms of each equation have the same operators respectively applied to U_θ and H_θ. The last terms are different: they have different coefficient and different signes inside the brackets. The traditional technique is to add the two equations after having applied a non-dimensional substitution and then solve the equation in the variable resulting in the sum between U_θ and H_θ. In this case it is not possible because of the shape of the last term. We then try to find an approximated solution that will be compared with the results obtained from the FDHM.

6.4.3 Cartesian bi-dimensional solution

The axially-symmetric MHD problem extended to a torus with square section has different solution compared with the solution that can be obtained from the same problem in the cartesian form for a straight pipe.

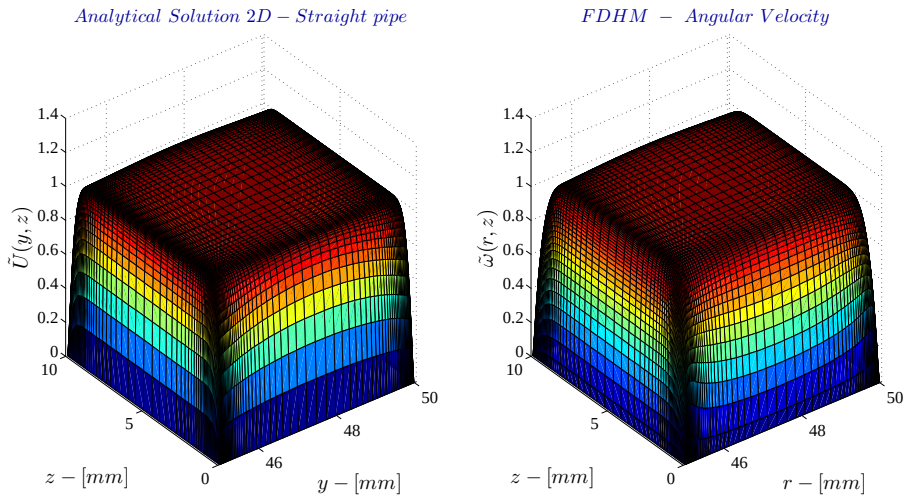

Figure 6.4: *Comparison between MHD velocity field in a straight pipe under trasverse magnetic field and MHD angular velocity for an axially-symmetric torus under a radial magnetic field.*

There are anyway some qualitative analogies. As can be seen in the results of the FDHM and in Figure (6.4), the angular velocity of the conductive liquid shows a rigid body-like behaviour of the liquid with constant angular velocity in core zone of the flux. Qualitatively this distribution can be compared with the linear velocity profile solution of the MHD problem in cartesian coordinates for a straight pipe with rectangular cross section.
The basic equations to solve the problem are, in dimensionless form [13]:

$$\nabla^2 b + Ha\frac{\partial u}{\partial y} = 0 \tag{6.4.59}$$

$$\nabla^2 u + Ha\frac{\partial b}{\partial y} = 0 \tag{6.4.60}$$

The two equations can be solved together with the Elsasser variables:

$$A = u + b, A' = u - b \tag{6.4.61}$$

Adding and subtracting Eq.(6.4.60) from the Eq.(6.4.59) we obtain:

$$\frac{\partial^2 A}{\partial y^2} + \frac{\partial^2 A}{\partial z^2} + Ha\frac{\partial A}{\partial y} = -1 \tag{6.4.62}$$

$$\frac{\partial^2 A'}{\partial y^2} + \frac{\partial^2 A'}{\partial z^2} - Ha\frac{\partial A'}{\partial y} = -1 \tag{6.4.63}$$

The boundary conditions to be applied are no slip condition at all walls, $u = 0$, and considering the boundaries electrically insulating, the induced magnetic field vanishes at the boundaries, $b = 0$. If the boundaries is called Γ, it means that:

$$A = A' = 0 \ \text{ on } \ \Gamma \tag{6.4.64}$$

Moreover it can be said by symmetry that:

$$A'(y) = A(-y) = 0 \tag{6.4.65}$$

so that it is sufficient to determine A for the solution of the problem. The solution is obtained by expanding the unknown A into a Fourier series as:

$$A\left(y,z\right)=A'\left(-y,z\right)=\sum_{i=1,3,5}^{\infty}a_i\left(y\right)\cos\left(\lambda_i z\right) \tag{6.4.66}$$

where we satisfy the boundary conditions at $z=\pm d$ with:

$$\lambda_i=\frac{i\pi}{2d} \tag{6.4.67}$$

Using the Eq.(6.4.61), for the dimensionless linear velocity u and the dimensionless induced magnetic field b, we have:

$$u\left(y,z\right)=\sum_{i=1,3,5}^{\infty}u_i\left(y\right)\cos\left(\lambda_i z\right) \tag{6.4.68}$$

$$b\left(y,z\right)=\sum_{i=1,3,5}^{\infty}b_i\left(y\right)\cos\left(\lambda_i z\right) \tag{6.4.69}$$

Inserting Eq.(6.4.66) into Eq.(6.4.62) and using orthogonality of trigonometric functions yields:

$$\frac{\partial^2 a_i}{\partial y^2}-\lambda_i^2 a_i+Ha\frac{\partial a_i}{\partial y}=-2\frac{\sin\left(\lambda_i z\right)}{\lambda_i d}=-k_i \tag{6.4.70}$$

whose solution is:

$$a_i\left(y\right)=\frac{k_i}{\lambda_i^2}+C_{i_1}\cosh\exp-p_{i_1}y+C_{i_2}\exp-p_{i_2}y \tag{6.4.71}$$

where:

$$p_{i_{1,2}}=\frac{1}{2}\left(Ha\mp\sqrt{Ha^2+4\lambda_i^2}\right) \tag{6.4.72}$$

In order to obtain the coefficient of the Eqs.(6.4.67),(6.4.68) we can use the symmetry of the problem and Eq.(6.4.61):

$$u_i(y) = \frac{a_i(y) + a_i(-y)}{2} = \\ = \frac{k_i}{\lambda_i^2} + C_{i_1}\cosh(p_{i_1}y) - C_{i_2}\cosh(-p_{i_2}y) \tag{6.4.73}$$

$$b_i(y) = \frac{a_i(y) - a_i(-y)}{2} = \\ = -C_{i_1}\cosh(p_{i_1}y) - C_{i_2}\cosh(-p_{i_2}y) \tag{6.4.74}$$

which correspond to the Fourier modes for velocity and magnetic field. Both vanish at the Hartmann walls, $u_i(1) = b_i(1) = 0$, so that the coefficients are determined. We express the Fourier modes for velocity and induced field in Eqs.(6.4.67),(6.4.68) as:

$$u_i(y) = \frac{k_i}{\lambda_i^2}\left[1 - \frac{f_i(y)}{f_i(1)}\right] \tag{6.4.75}$$

$$b_i(y) = \frac{k_i}{\lambda_i^2}\left[\frac{g_i(y)}{f_i(1)}\right] \tag{6.4.76}$$

where:

$$f_i(y) = \alpha_{i_2}\cosh(p_{i_1}y) - \alpha_{i_1}\cosh(p_{i_2}y) \tag{6.4.77}$$

$$g_i(y) = \alpha_{i_2}\sinh(p_{i_1}y) - \alpha_{i_1}\sinh(p_{i_2}y) \tag{6.4.78}$$

and:

$$\alpha_{i_{1,2}} = \sinh\left(p_{i_{1,2}}\right) \tag{6.4.79}$$

The solution $u(y,z)$ found will now be taken as it was the angular velocity profile ω_z instead of the linear velocity profile. To do this, the dimensionless y axis will be renamed r. We then have:

$$\omega_z(r,z) = \sum_{i=1,3,5}^{\infty} \frac{k_i}{\lambda_i^2} \left[1 - \frac{f_i\left(\frac{2r}{r_e + r_i}\right)}{f_i(1)} \right] \cos\left(\lambda_i \frac{2z}{h}\right) \tag{6.4.80}$$

6.5 Conclusions

In this chapter a Lumped Parameter Model, LPM, has been proposed. The numerical values of the coefficients of the LPM can be computed analytically on the basis of two different analytical solutions: a mono-dimensional analytical solution and a bi-dimensional analytical solution. The expression of each coefficient is given in closed form function of the geometry of the torus, of the physical properties of the fluid and function of the intensity of the magnetic field. It is not known a priori the precision of the coefficients computed with both the solutions. In the next chapter the LPM is then compared with the results obtained with the FDHM.

Chapter

7 Results and Discussion: Comparison between LPM and FDHM

In this chapter, a comparison between the FDHM and the LPM is shown in order to understand the precision of the estimation of the LPM coefficients based on both the analytical solutions.

7.1 Simulations

In order to test the accuracy of the lumped parameter model several simulation have been done with the FDHM. The aim is to compare the value of the coefficients obtained through the LPM with the ones obtained numerically with the FDHM. The analysis will be done with all the coefficients and extended to other two quantities: the torque provided by the device and the characteristic time of the torque. The torque and the characteristic time will be studied for both the voltage and current drive: the device will be supplied respectively with a voltage or current trend linear over the time.
The LPM will be tested with the monodimensional analytical solution and the bidimensional cartesian solution obtained in the previous chapter.
The simulations have been computed varying the intensity of the magnetic field B_0, the electric conductivity of the liquid σ, the inner radius r_i and the height h of the the torus containing the liquid. Other parameter have been considered fixed, such as the outer radius r_e, the viscosity of the liquid μ and its density ρ. The relative errors between the LPM and the FDHM are shown in order to highlight the accuracy of the solution computed by the LPM. The following table summarizes the grid of values of the simulations.

	U.M.	Max Value	Min Value	N.points
Density - $\boldsymbol{\rho}$	$[kg/m^3]$	1000	1000	1
Viscosity - $\boldsymbol{\mu}$	$[Pa\ s]$	10^{-3}	10^{-3}	1
El. Conductivity - $\boldsymbol{\sigma}$	$[S/m]$	10^6	10	6
Magnetic Field - $\mathbf{B_0}$	$[T]$	0.8	0.2	4
Inner Radius - $\mathbf{r_i}$	$[mm]$	49	45	5
External Radius - $\mathbf{r_e}$	$[mm]$	50	50	1
Height - $\mathbf{h}$	$[mm]$	10	30	3

Table 7.1: *Values grid for the LPM simulation*

The results presented in the next sections refers only to liquid with electric conductivity $\sigma = 10\ S/m$ and $\sigma = 10^6\ S/m$. For all the intermediate values of electric conductivity the results are given in the Appendices: $\sigma = 10^2\ S/m$ in Appendix F, $\sigma = 10^3\ S/m$ in Appendix G, $\sigma = 10^4\ S/m$ in Appendix H, $\sigma = 10^5\ S/m$ in Appendix I.

7.2 Coefficient of the viscous shear moment

The coefficient of the viscous shear moment for the LPM based on the Monodimensional analytical solution can be expressed as:

$$K_{vis} = \frac{2\pi\mu r_i^3 h}{\omega_w}\frac{d\omega_z(r)}{dr}\bigg|_{r=r_i} + \frac{2\pi\mu r_e^3 h}{\omega_w}\frac{d\omega_z(r)}{dr}\bigg|_{r=r_e} \tag{7.2.1}$$

The derivatives present in Eq.(7.2.1) can be computed analytically.
In the bidimensional LPM all the boundaries need to be taken into account. The coefficient of viscous shear moment is computes as:

$$\begin{aligned} K_{vis} =& \frac{2\pi\mu r_i^3}{\omega_w}\int_0^h \frac{\partial\omega_z(r,z)}{\partial r}\bigg|_{r=r_i} dz + \frac{2\pi\mu r_e^3}{\omega_w}\int_0^h \frac{\partial\omega_z(r,z)}{\partial r}\bigg|_{r=r_e} dz \\ &+ \frac{2\pi\mu}{\omega_w}\int_{r_i}^{r_e} r^3\frac{\partial\omega_z(r,z)}{\partial z}\bigg|_{z=0} dr + \frac{2\pi\mu}{\omega_w}\int_{r_i}^{r_e} r^3\frac{\partial\omega_z(r,z)}{\partial z}\bigg|_{z=h} dr \end{aligned} \tag{7.2.2}$$

The K_{vis} obtained with the Eq.(7.2.1) and Eq.(7.5.3) need to be compared with the numerical K_{vis} obtained with the FDHM. The numerical K_{vis} is obtained evaluating the velocity profile and its derivative with respect of r and z at the boundaries and then multiplying each values for the elementary surface it is referred to:

$$\begin{aligned} K_{vis_{FDHM}} =& \frac{2\mu\pi}{\omega_w}\sum_{l=1}^{L}\left(z_{l+1/2} - z_{l-1/2}\right)\left[r_i\frac{\partial\omega_z(r_i,z_l)}{\partial r} + r_e\frac{\partial\omega_z(r_e,z_l)}{\partial r}\right] \\ &+ \frac{\mu\pi}{\omega_w}\sum_{k=1}^{K}\left(r_{k+1/2}^2 - r_{k-1/2}^2\right)\left[\frac{\partial\omega_z(r_k,0)}{\partial r} + \frac{\partial\omega_z(r_k,h)}{\partial r}\right] \end{aligned} \tag{7.2.3}$$

where N e M are the number of intervals of the FDHM computational grid along z and r.

7.3 Coefficient of the Lorentz Force moment

For both the mono-dimensional and bi-dimensional LPM, the coefficient of the Lorentz Force moment K_I can be expressed as:

$$K_I = B_0 r_i h \tag{7.3.1}$$

The same coefficient can be computed for the FDHM data. The numerical K_I is calculated as:

$$K_{I_{FDHM}} = \frac{\pi \sum_{l=1}^{L} \sum_{k=1}^{K} J_{z_{k,l}} B_{r_{k,l}} \left(z_{l+1/2} - z_{l-1/2}\right) \left(r_{k+1/2}^2 - r_{k-1/2}^2\right)}{I} \tag{7.3.2}$$

For the current drive I is the electric current fed to the system. In the voltage drive the electric current is not know a priori, so it is taken as the average current flowing through the device. This current is computed as:

$$I = \frac{1}{L} \sum_{l=1}^{L} \tilde{I}_{z_l}^c = \frac{1}{L} \sum_{l=1}^{L} \sum_{k=1}^{K} I_{z_{k,l}}^c \tag{7.3.3}$$

So $I_{z_{k,l}}^c$ comes directly from the nodal analysis in the FDHM and it is the average of the electric currents in the branches.

7.4 Coefficient of the moment of inertia

The coefficient c_ω represents the difference between the moment of inertia of a rigid flywheel with the same dimensions of the torus containing the liquid and the liquid spinning in the torus. In the LPM, with the mono-dimensional solution, we have:

$$c_\omega = \frac{2\pi\rho h \int_{r_i}^{r_e} r^3 \omega_z(r)\, dr}{\omega_w I_z} \tag{7.4.1}$$

In the bidimensional LPM, the coefficient c_ω is computed as:

$$c_\omega = \frac{2\pi\rho \int_{r_i}^{r_e} \int_0^h r^3 \omega_z(r,z)\, dr dz}{\omega_w I_z} \tag{7.4.2}$$

In the FDHM the c_ω is computed as:

$$c_\omega = \frac{\pi\rho \sum_{k=1}^{K} \sum_{l=1}^{L} \omega_{z_{k,l}} \left(r_{k+1/2}^4 - r_{k+1/2}^4 \right) \left(z_{l+1/2} - z_{l-1/2} \right)}{2\omega_w I_z} \tag{7.4.3}$$

7.5 Coefficient of Induced Voltage

The coefficient of the induced voltage calculated in the LPM with the monodimensional solution is:

$$K_V = \frac{2\pi B_0 h \int_{r_i}^{r_e} r\omega_z(r)\, dr}{\omega_w S} \tag{7.5.1}$$

where S is the surface perpendicular to z. In the bidimensional LPM, the coefficient K_V is computed as:

$$K_V = \frac{2\pi B_0 \int_{r_i}^{r_e} \int_0^h r\omega_z(r,z)\, dr dz}{\omega_w S} \tag{7.5.2}$$

The coefficient K_V for the FDHM can be computed as:

$$K_{V_{FDHM}} = \frac{B_0 r_i \sum_{l=1}^{L} \sum_{k=1}^{K} \omega_{z_{k,l}} \left(z_{l+1/2} - z_{l-1/2} \right)}{\omega_w} \tag{7.5.3}$$

7.6 Current Drive

In the case of electric current drive we will solve the dynamic part of the LPM for a generic law for the electric current:

$$\dot{\omega} + \frac{K_{vis}}{I_z'}\omega = \frac{K_I}{I_z'} I \tag{7.6.1}$$

with general initial condition:

$$\omega(t_0) = \omega_w \tag{7.6.2}$$

The solution for ω is:

$$\omega(t) = e^{-\frac{K_{vis}}{I'_z}t}\left[\omega_w + \int_0^t \frac{K_I}{I'_z}\, I\,(t)\; e^{\frac{K_{vis}}{I'_z}t}\, dt\right] \tag{7.6.3}$$

If we now apply a linear law to the electric current:

$$I\,(t) = at \tag{7.6.4}$$

the solution (7.6.3) becomes:

$$\omega\,(t) = \frac{K_I}{K_{vis}}at - \frac{I'_z K_I a}{K_{vis}^2}\left[\,1 - e^{-\frac{K_{vis}t}{I'_z}}\,\right] \tag{7.6.5}$$

and the torque provided is:

$$T = I'_z\dot{\omega} = I'_z\frac{K_I}{K_{vis}}a\left[1 - e^{-\frac{K_{vis}t}{I'_z}}\right] \tag{7.6.6}$$

The (7.6) shows that the reaction of the system has a characteristic time:

$$\tau_I = \frac{I'_z}{K_{vis}} \tag{7.6.7}$$

and the torque provided becomes constant for a linear electric current:

$$T_\infty = \lim_{t\to\infty} T\,(t) = I'_z\; a\frac{K_I}{K_{vis}} \tag{7.6.8}$$

The angular momentum generated by the device is computed as:

$$\Gamma\,(t) = I_z c_\omega \omega\,(t) \tag{7.6.9}$$

where $\omega\,(t)$ is computed by the Eq.(7.6.5) for a given time t. The power consumption of the device for a linear current law is:

$$P\,(t) = (K_V\omega\,(t) + R_{eq}at)\,at \tag{7.6.10}$$

The quantities $\tilde{\Gamma}$ and $\tilde{P}$ are intended as specific power and specific angular momentum for an electric current of $1A$. They are computed as:

$$\tilde{\Gamma} = \frac{I_z c_\omega \omega\left(t_{EOS}\right)}{a t_{EOS}} \tag{7.6.11}$$

$$\tilde{P} = \frac{K_V \omega\left(t_{EOS}\right) + R_{eq} a t_{EOS}}{a t_{EOS}} \tag{7.6.12}$$

The specific power and the specific angular momentum in the $FDHM$ are computed as:

$$\tilde{\Gamma}_{FDHM} = \frac{\Gamma_{EOS}}{I_{EOS}} \tag{7.6.13}$$

$$\tilde{P}_{FDHM} = \frac{P_{EOS}}{I_{EOS}^2} \tag{7.6.14}$$

where I_{EOS}, Γ_{EOS} and P_{EOS} are the total electric current, the power consumption and the angular momentum computed numerically with the FDHM data and the relative to the end of the simulation (EOS). The simulations have been conducted with a current slope $a = 1A/s$.

7.7 Voltage Drive

In the case the device is voltage driven we need to consider both the equations of the LPM. Putting them together through the electric current we obtain:

$$\dot{\omega} \; + \frac{1}{I_z'}\left(K_{vis} + \frac{K_I K_V}{R_{eq}}\right)\omega = \frac{K_I}{R_{eq} I_z'} V \tag{7.7.1}$$

with general initial condition:

$$\omega\left(t_0\right) = \omega_w \tag{7.7.2}$$

The solution for ω is:

$$\omega(t) = e^{-\frac{1}{I_z'}\left(K_{vis} + \frac{K_I K_V}{R_{eq}}\right)t}\left[\omega_w + \int_0^t \frac{K_I}{R_{eq} I_z'}\, V\left(t\right)\; e^{-\frac{1}{I_z'}\left(K_{vis} + \frac{K_I K_V}{R_{eq}}\right)t}\, dt\right] \tag{7.7.3}$$

Considering now a linear law for the voltage:

$$V(t) = bt \tag{7.7.4}$$

the solution (7.7.3) becomes:

$$\begin{aligned} \omega(t) \; &= \frac{K_I}{K_I K_V + K_{vis} R_{eq}} \; bt \; + \\ &- \; \frac{I'_z K_I R_{eq} b}{\left(K_I K_V + K_{vis} R_{eq}\right)^2} \left[1 - e^{-\frac{K_I K_V + K_{vis} R_{eq}}{I'_z R_{eq}} t}\right] \end{aligned} \tag{7.7.5}$$

and the torque provided is:

$$T = I'_z \dot{\omega} = I'_z \frac{K_I}{K_I K_V + K_{vis} R_{eq}} \; b \left[1 - e^{-\frac{K_I K_V + K_{vis} R_{eq}}{I'_z R_{eq}} t}\right] \tag{7.7.6}$$

The (7.7.6) shows that the reaction of the system has a characteristic time:

$$\tau_V = \frac{I'_z R_{eq}}{K_I K_V + K_{vis} R_{eq}} \tag{7.7.7}$$

and the torque provided becomes constant for a linear voltage:

$$T_\infty = \lim_{t \to \infty} T(t) = I'_z \; b \; \frac{K_I}{K_I K_V + K_{vis} R_{eq}} \tag{7.7.8}$$

The torque generated in the FDHM is read as the final value obtained during the simulation.
The angular momentum generated by the device is computed as:

$$\Gamma(t) = I_z c_\omega \omega(t) \tag{7.7.9}$$

where $\omega(t)$ is computed by the Eq.(7.7.5) for a given time t. The power consumption of the device for a linear current law is:

$$P(t) = \frac{\left(bt - K_V \omega(t)\right) bt}{R_{eq}} \tag{7.7.10}$$

The quantities $\tilde{\Gamma}$ and $\tilde{P}$ are intended as specific power and specific angular momentum for an electric current of $1A$. They are computed as:

$$\tilde{\Gamma} = R_{eq} \frac{I_z c_\omega \omega \left(t_{EOS}\right)}{b t_{EOS} - K_V \omega \left(t_{EOS}\right))} \tag{7.7.11}$$

$$\tilde{P} = \frac{b t_{EOS}}{R_{eq} b t_{EOS} - R_{eq} K_V \omega \left(t_{EOS}\right)} \tag{7.7.12}$$

The specific power and the specific angular momentum in the $FDHM$ are computed as:

$$\tilde{\Gamma}_{FDHM} = \frac{\Gamma_{EOS}}{I_{EOS}} \tag{7.7.13}$$

$$\tilde{P}_{FDHM} = \frac{P_{EOS}}{I_{EOS}^2} \tag{7.7.14}$$

where I_{EOS}, Γ_{EOS} and P_{EOS} are the total electric current, the power consumption and the angular momentum computed numerically with the FDHM data and the relative to the end of the simulation (EOS). The simulations have been conducted with a voltage slope $b = 10^{-3} V/s$.

7.8 Results: Monodimensional LPM - $\sigma = 10 S/m$

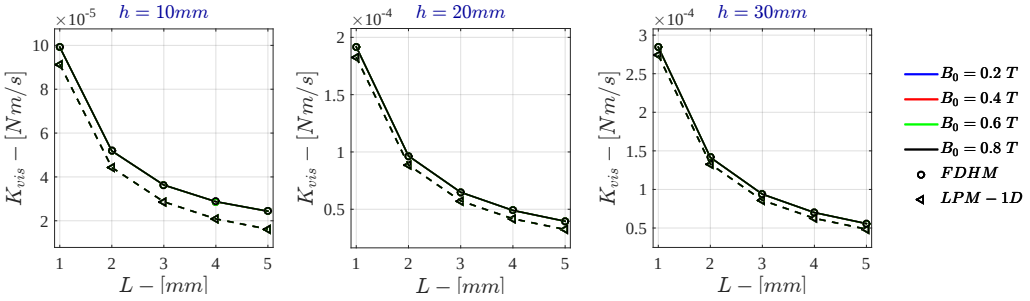

Figure 7.1: *K_{vis} for $\sigma = 10\ S/m$ - $r_{out} = 50mm$ - Monodimensional LPM*

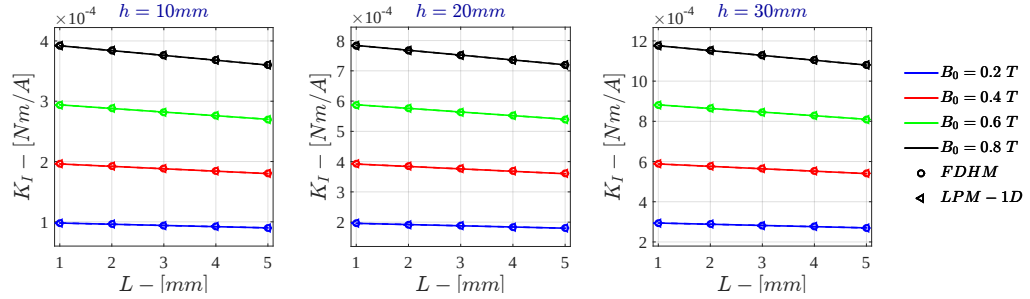

Figure 7.2: *Monodimensional LPM*
K_I for $\sigma = 10\ S/m$ - $r_{out} = 50mm$

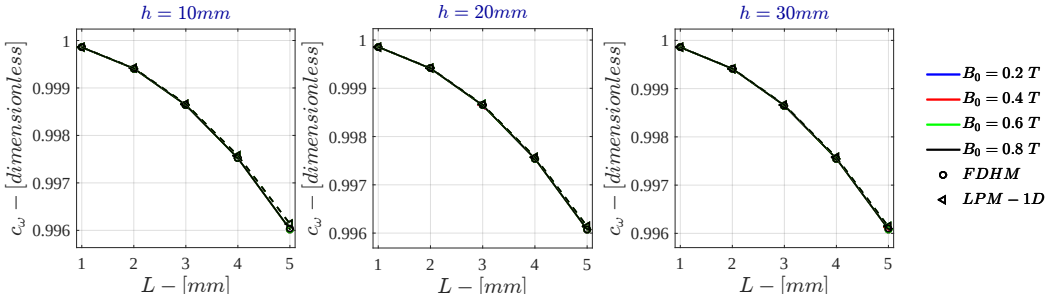

Figure 7.3: *Monodimensional LPM*
c_ω for $\sigma = 10\ S/m$ - $r_{out} = 50mm$

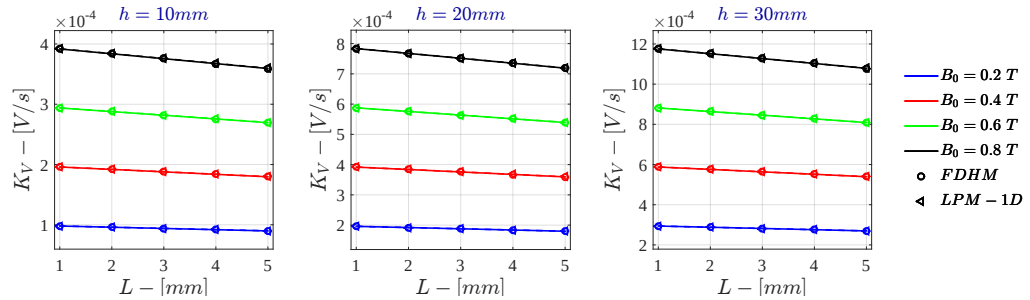

Figure 7.4: *Monodimensional LPM*
K_V for $\sigma = 10\ S/m$ - $r_{out} = 50mm$

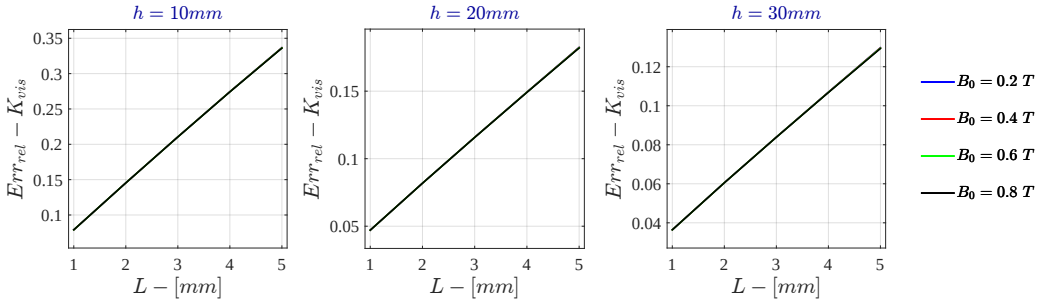

Figure 7.5: *Monodimensional LPM*
Relative Error - K_{vis} for $\sigma = 10\ S/m$ - $r_{out} = 50mm$

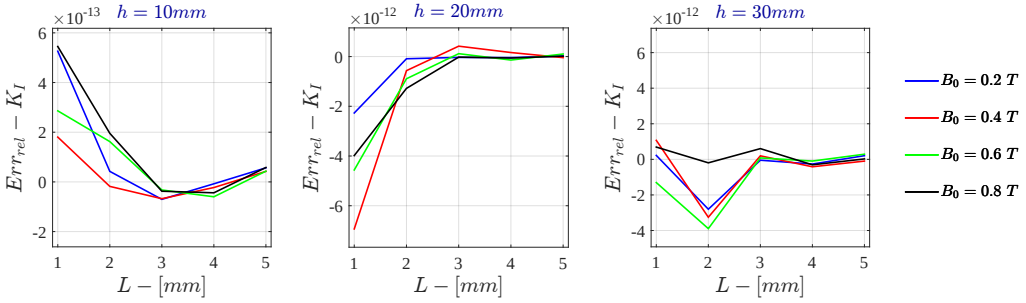

Figure 7.6: *Monodimensional LPM*
Relative Error - K_I for $\sigma = 10\ S/m$ - $r_{out} = 50mm$

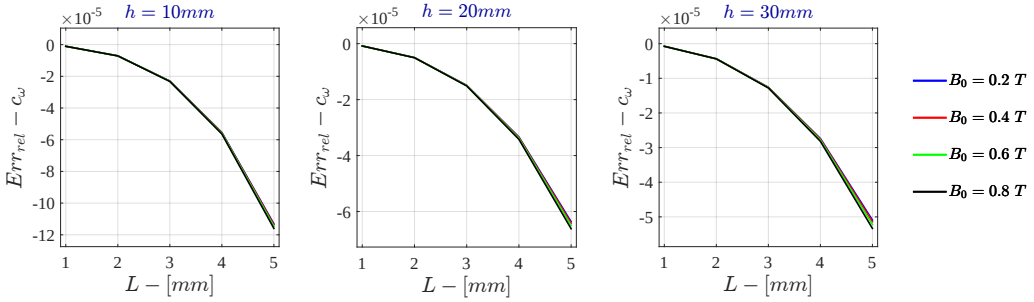

Figure 7.7: *Monodimensional LPM*
Relative Error - c_ω for $\sigma = 10\ S/m$ - $r_{out} = 50mm$

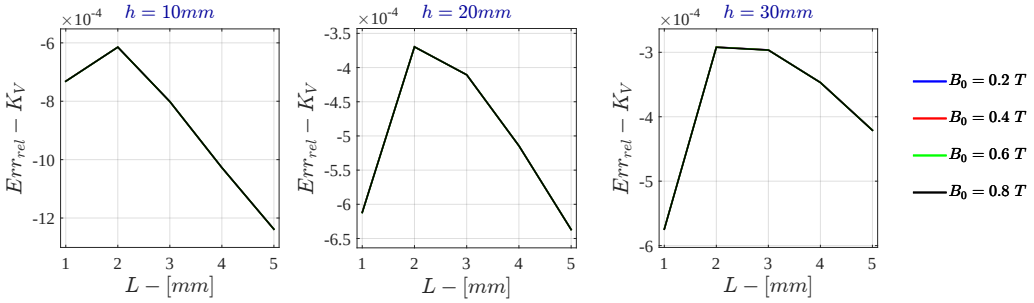

Figure 7.8: *Monodimensional LPM*
Relative Error - K_V for $\sigma = 10\ S/m$ - $r_{out} = 50mm$

7.8.1 Current Drive

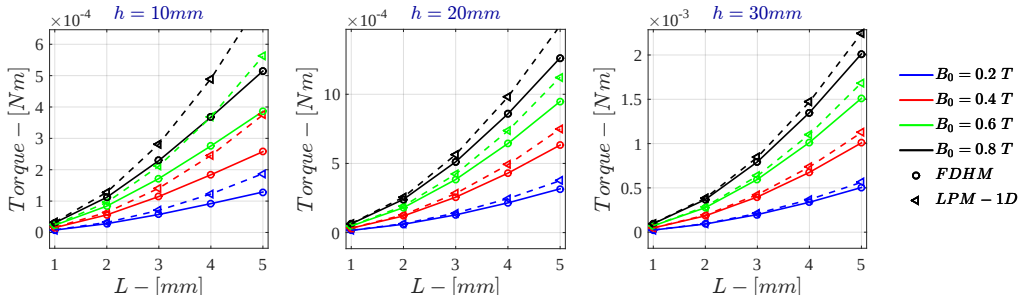

Figure 7.9: *Monodimensional LPM - Current Drive* $\dot{\Gamma}$ *for* $\sigma = 10\ S/m$ - $r_{out} = 50mm$

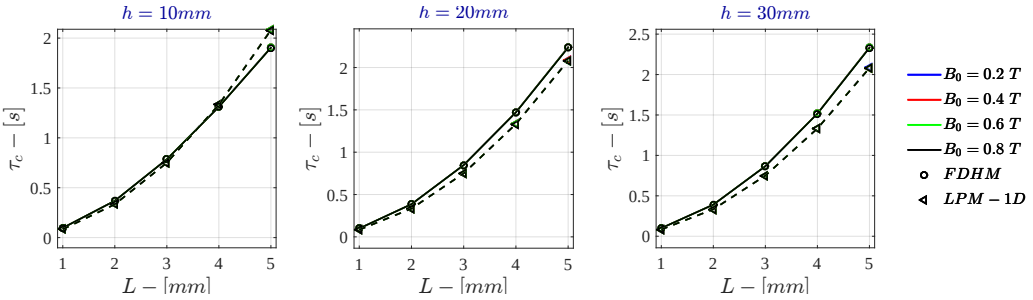

Figure 7.10: *Monodimensional LPM - Current Drive* τ_c *for* $\sigma = 10\ S/m$ - $r_{out} = 50mm$

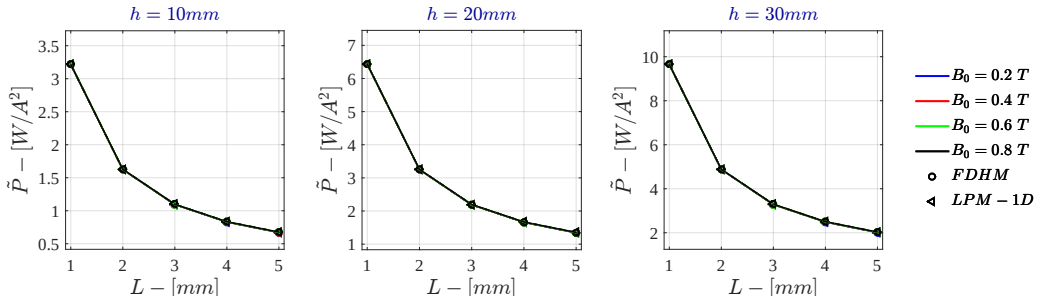

Figure 7.11: *Monodimensional LPM - Current Drive* $\tilde{P}$ *for* $\sigma = 10\ S/m$ - $r_{out} = 50mm$

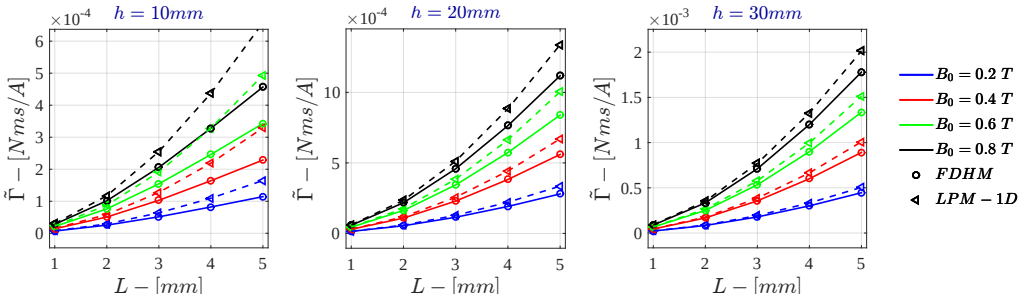

Figure 7.12: *Monodimensional LPM - Current Drive* $\tilde{\Gamma}$ *for* $\sigma = 10\ S/m$ - $r_{out} = 50mm$

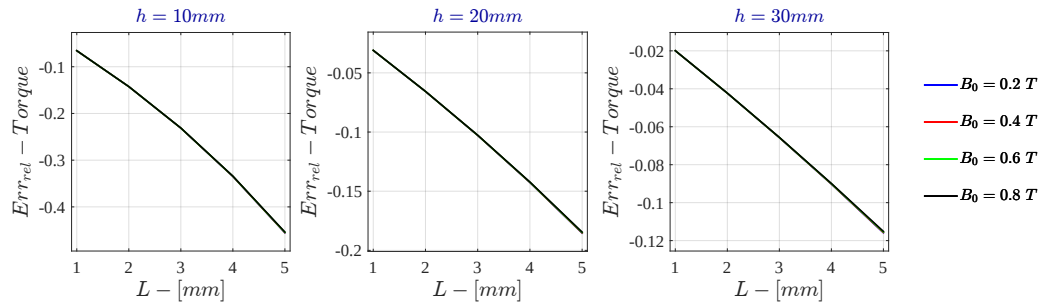

Figure 7.13: *Monodimensional LPM - Current Drive Relative Error - $\dot{\Gamma}$ for $\sigma = 10\ S/m$ - $r_{out} = 50mm$*

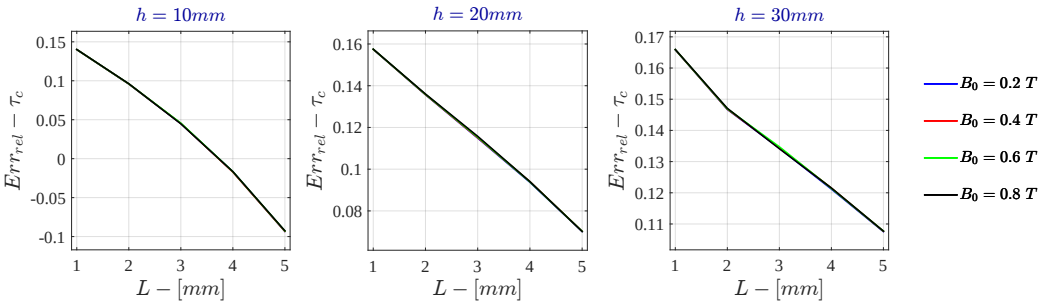

Figure 7.14: *Monodimensional LPM - Current Drive Relative Error - τ_c for $\sigma = 10\ S/m$ - $r_{out} = 50mm$*

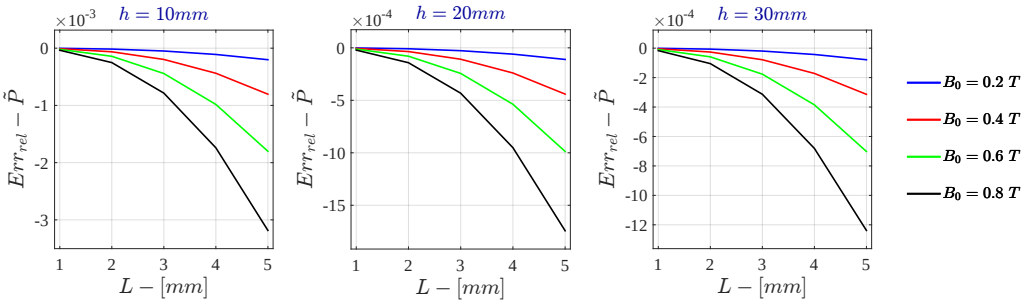

Figure 7.15: *Monodimensional LPM - Current Drive Relative Error - $\tilde{P}$ for $\sigma = 10\ S/m$ - $r_{out} = 50mm$*

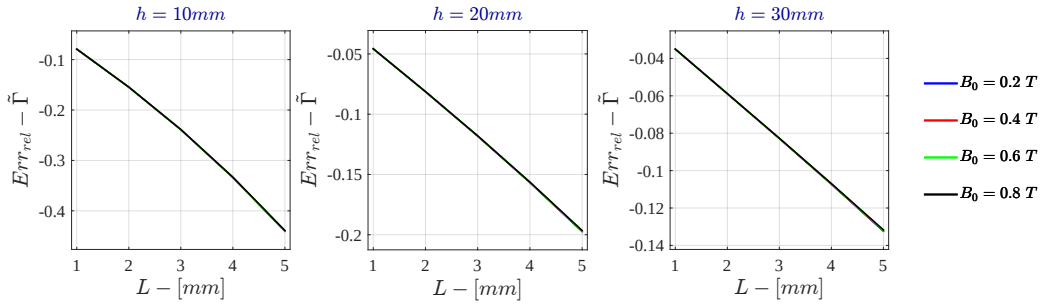

Figure 7.16: *Monodimensional LPM - Current Drive Relative Error - $\tilde{\Gamma}$ for $\sigma = 10\ S/m$ - $r_{out} = 50mm$*

7.8.2 Voltage Drive

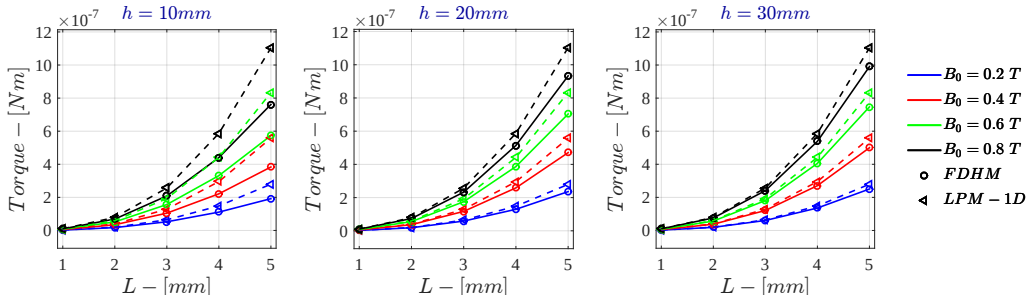

Figure 7.17: *Monodimensional LPM - Voltage Drive* $\dot{\Gamma}$ *for* $\sigma = 10\ S/m$ - $r_{out} = 50mm$

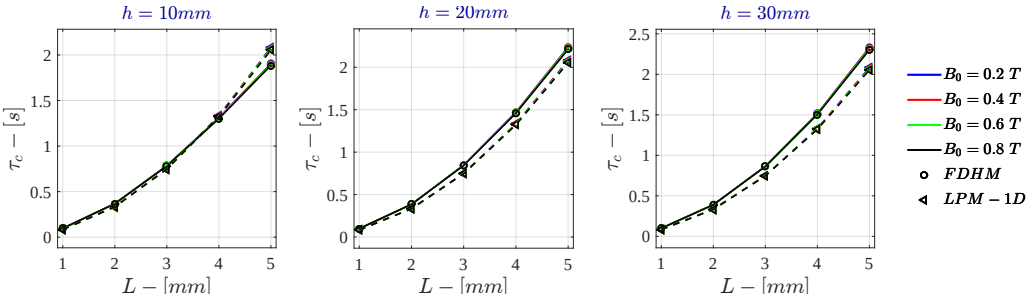

Figure 7.18: *Monodimensional LPM - Voltage Drive* τ_c *for* $\sigma = 10\ S/m$ - $r_{out} = 50mm$

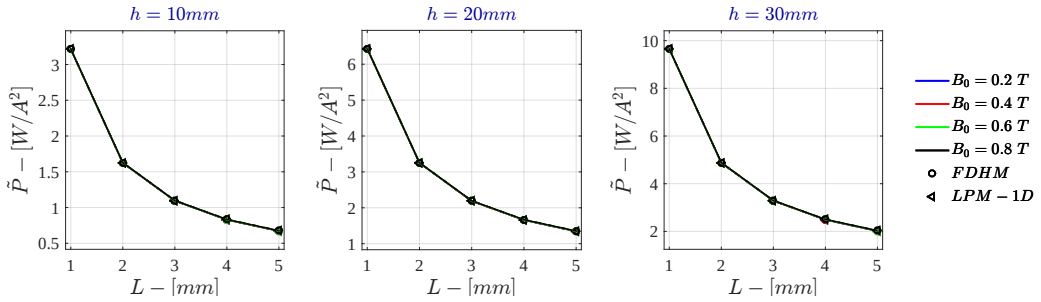

Figure 7.19: *Monodimensional LPM - Voltage Drive* $\tilde{P}$ *for* $\sigma = 10\ S/m$ - $r_{out} = 50mm$

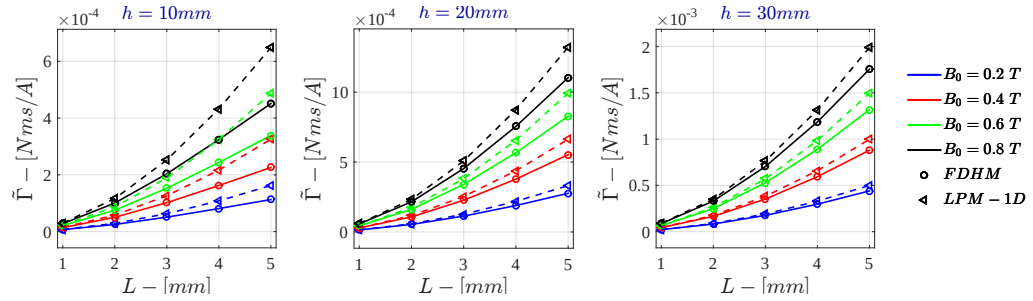

Figure 7.20: *Monodimensional LPM - Voltage Drive* $\tilde{\Gamma}$ *for* $\sigma = 10\ S/m$ - $r_{out} = 50mm$

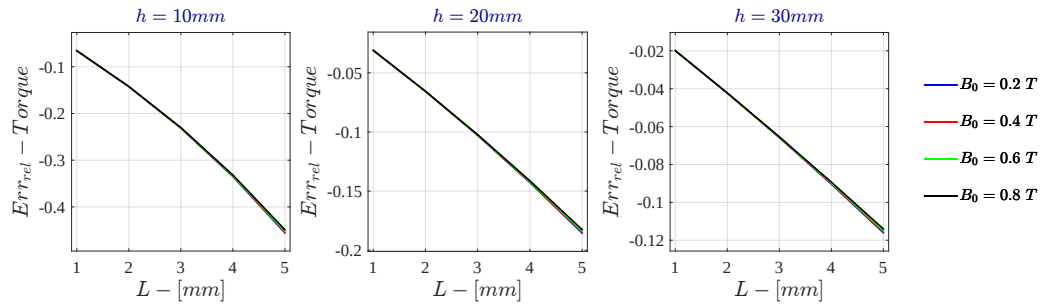

Figure 7.21: *Monodimensional LPM - Voltage Drive Relative Error - $\dot{\Gamma}$ for $\sigma = 10\ S/m$ - $r_{out} = 50mm$*

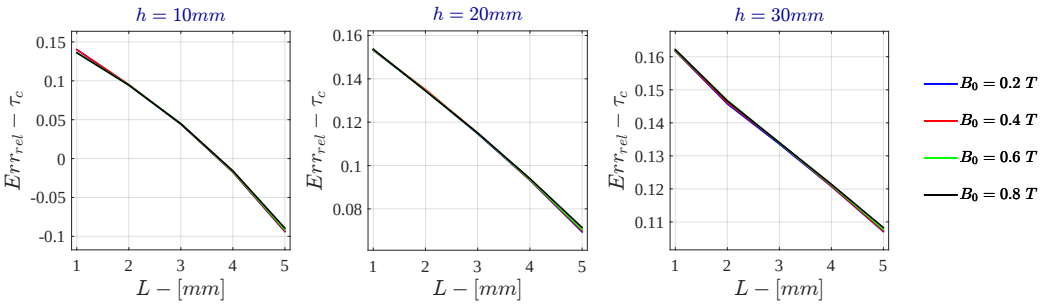

Figure 7.22: *Monodimensional LPM - Voltage Drive Relative Error - τ_c for $\sigma = 10\ S/m$ - $r_{out} = 50mm$*

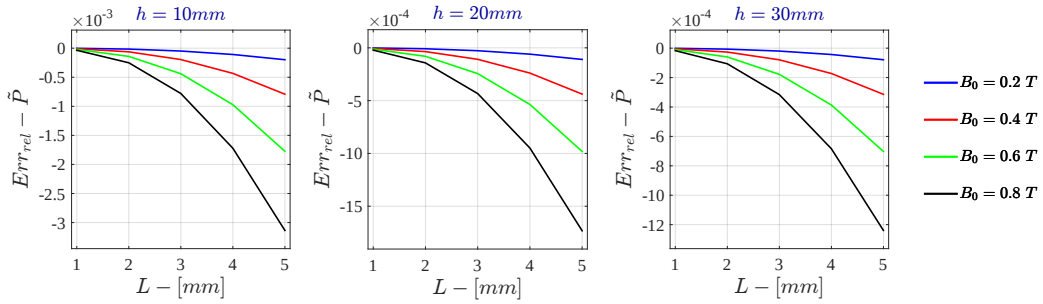

Figure 7.23: *Monodimensional LPM - Voltage Drive Relative Error - $\tilde{P}$ for $\sigma = 10\ S/m$ - $r_{out} = 50mm$*

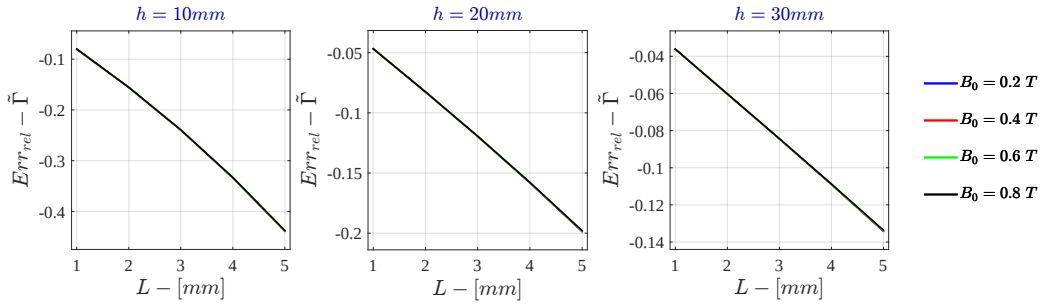

Figure 7.24: *Monodimensional LPM - Voltage Drive Relative Error - $\tilde{\Gamma}$ for $\sigma = 10\ S/m$ - $r_{out} = 50mm$*

7.9 Results: Bidimensional LPM - $\sigma = 10 S/m$

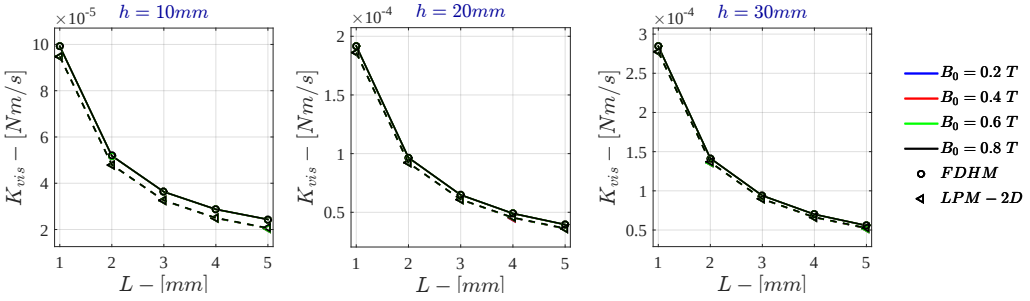

Figure 7.25: *Bidimensional LPM*
K_{vis} *for* $\sigma = 10\ S/m$ - $r_{out} = 50mm$

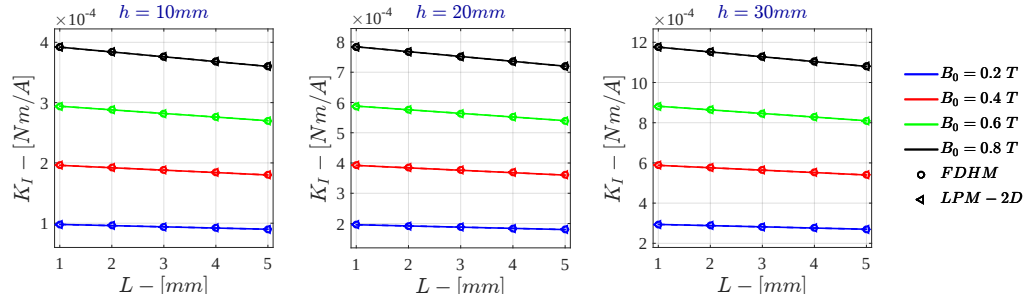

Figure 7.26: *Bidimensional LPM*
K_I *for* $\sigma = 10\ S/m$ - $r_{out} = 50mm$

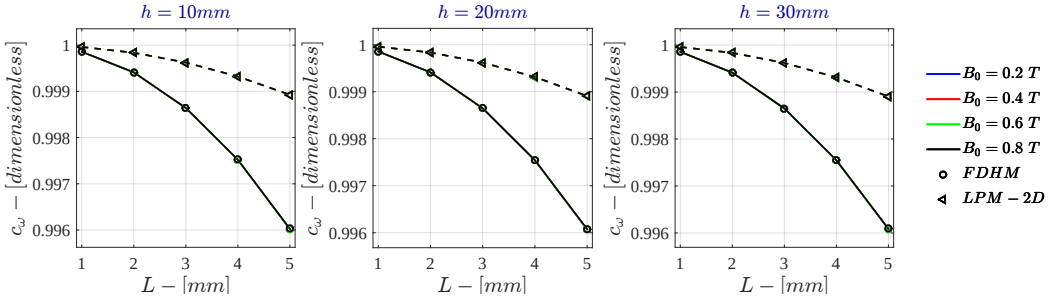

Figure 7.27: *Bidimensional LPM*
c_ω *for* $\sigma = 10\ S/m$ - $r_{out} = 50mm$

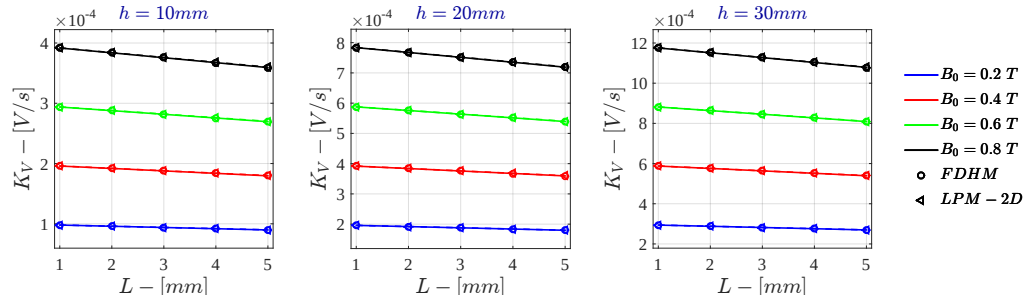

Figure 7.28: *Bidimensional LPM*
K_V *for* $\sigma = 10\ S/m$ - $r_{out} = 50mm$

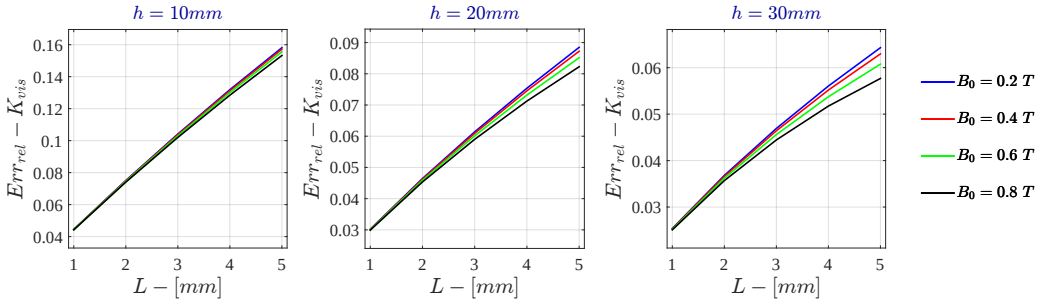

Figure 7.29: *Bidimensional LPM*
Relative Error - K_{vis} for $\sigma = 10\ S/m$ - $r_{out} = 50mm$

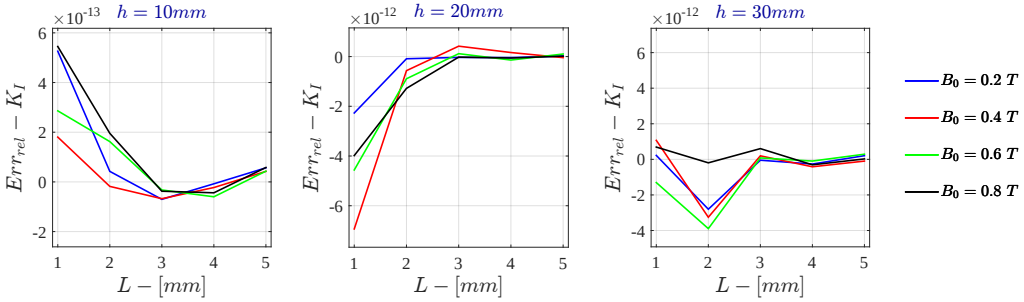

Figure 7.30: *Bidimensional LPM*
Relative Error - K_I for $\sigma = 10\ S/m$ - $r_{out} = 50mm$

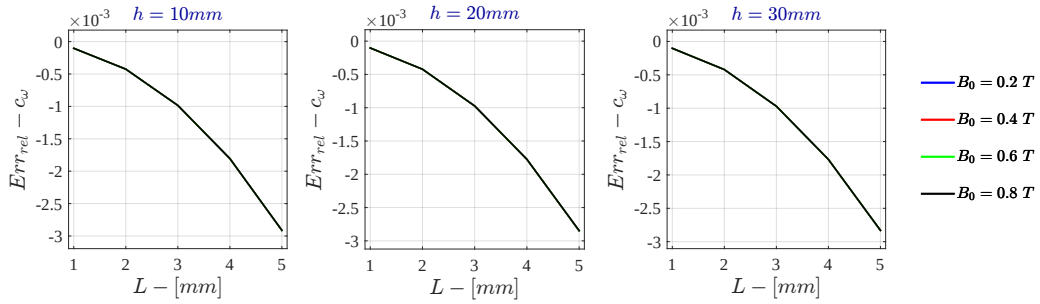

Figure 7.31: *Bidimensional LPM*
Relative Error - c_ω for $\sigma = 10\ S/m$ - $r_{out} = 50mm$

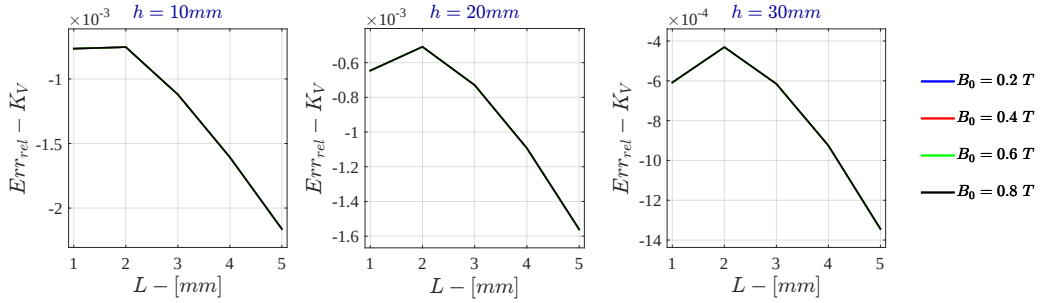

Figure 7.32: *Bidimensional LPM*
Relative Error - K_V for $\sigma = 10\ S/m$ - $r_{out} = 50mm$

7.9.1 Current Drive

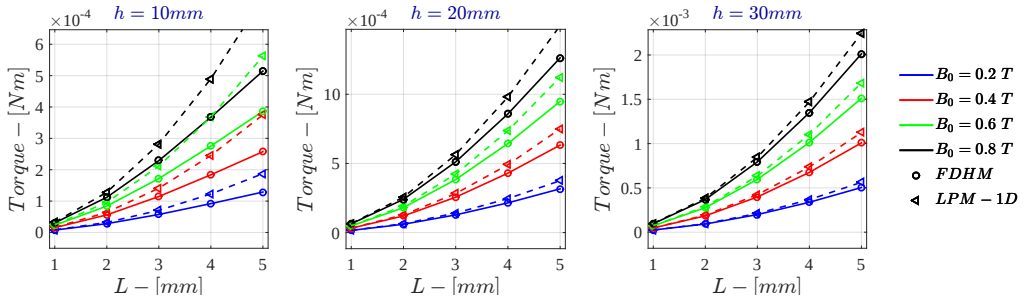

Figure 7.33: *Bidimensional LPM - Current Drive* $\dot{\Gamma}$ *for* $\sigma = 10\ S/m$ - $r_{out} = 50mm$

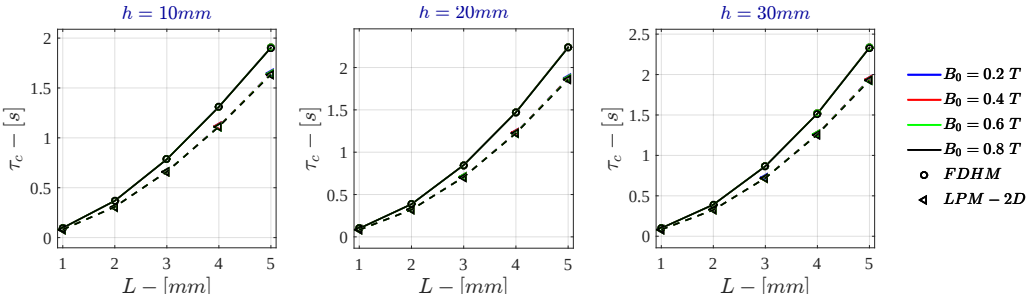

Figure 7.34: *Bidimensional LPM - Current Drive* τ_c *for* $\sigma = 10\ S/m$ - $r_{out} = 50mm$

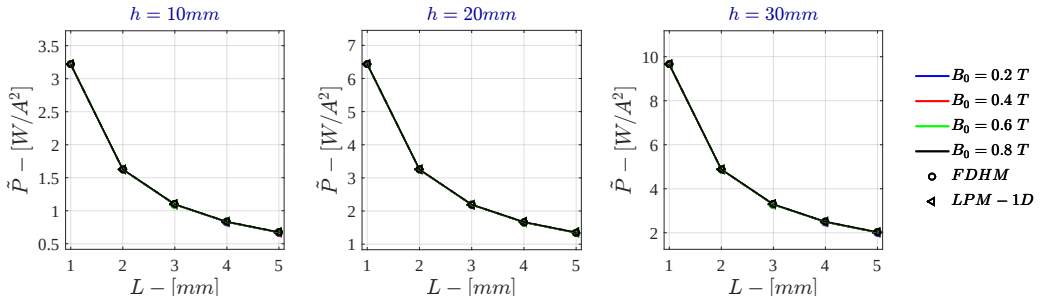

Figure 7.35: *Bidimensional LPM - Current Drive* $\tilde{P}$ *for* $\sigma = 10\ S/m$ - $r_{out} = 50mm$

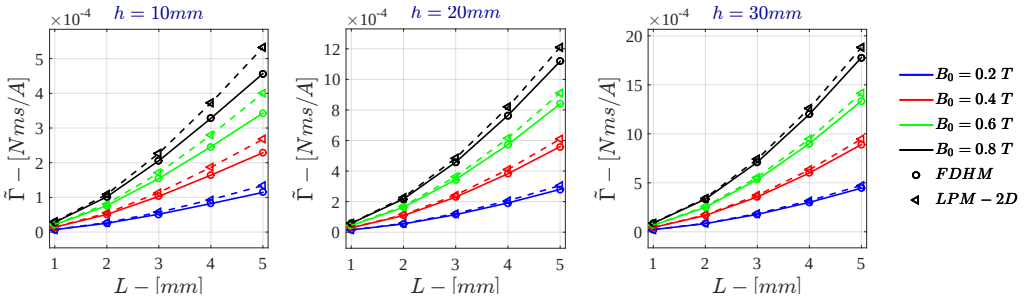

Figure 7.36: *Bidimensional LPM - Current Drive* $\tilde{\Gamma}$ *for* $\sigma = 10\ S/m$ - $r_{out} = 50mm$

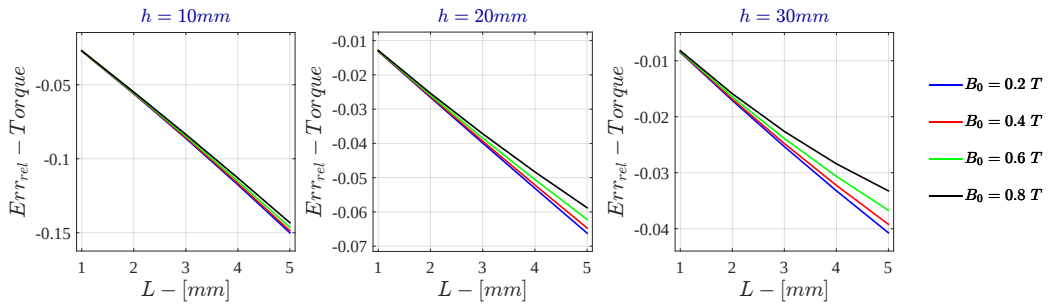

Figure 7.37: *Bidimensional LPM - Current Drive*
Relative Error - $\dot{\Gamma}$ for $\sigma = 10\ S/m$ - $r_{out} = 50mm$

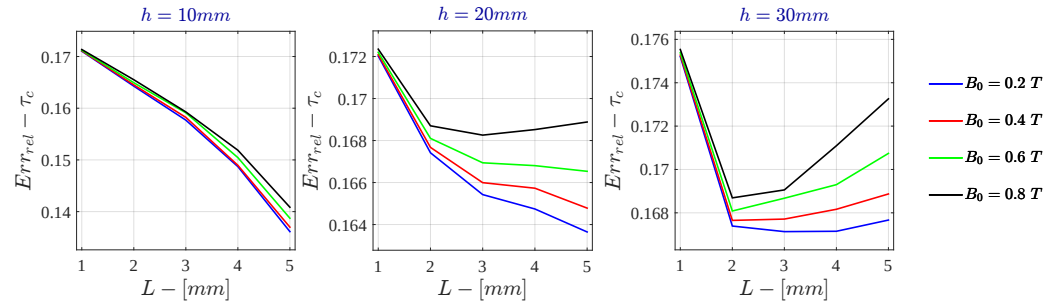

Figure 7.38: *Bidimensional LPM - Current Drive*
Relative Error - τ_c for $\sigma = 10\ S/m$ - $r_{out} = 50mm$

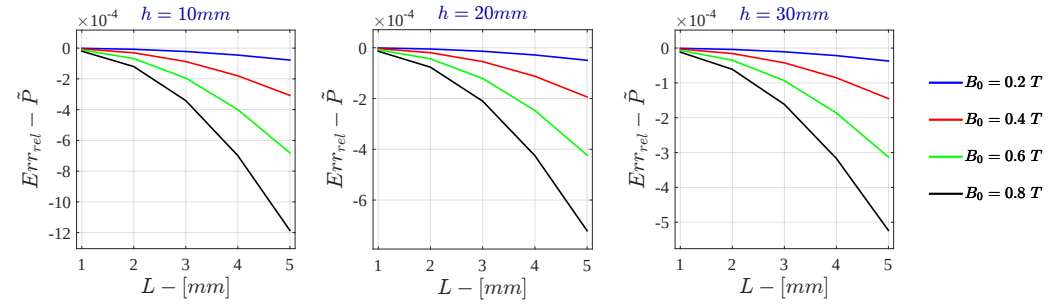

Figure 7.39: *Bidimensional LPM - Current Drive*
Relative Error - $\tilde{P}$ for $\sigma = 10\ S/m$ - $r_{out} = 50mm$

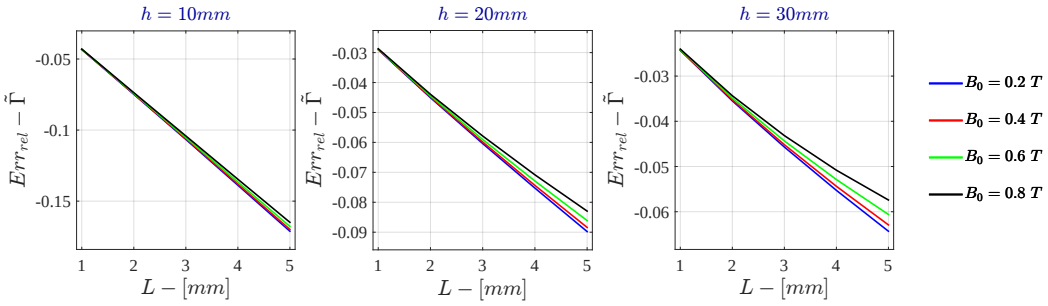

Figure 7.40: *Bidimensional LPM - Current Drive*
Relative Error - $\tilde{\Gamma}$ for $\sigma = 10\ S/m$ - $r_{out} = 50mm$

7.9.2 Voltage Drive

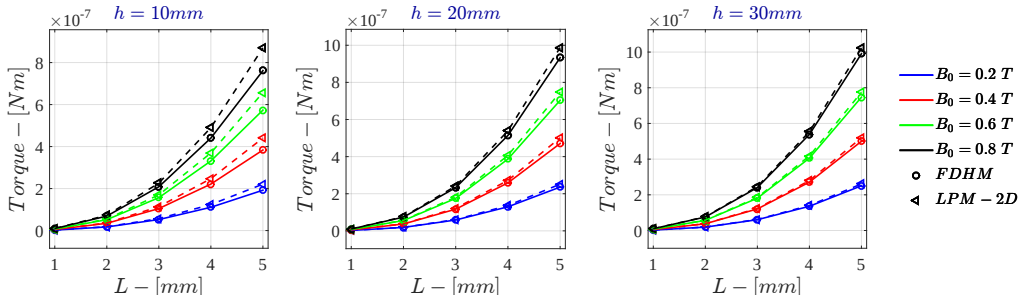

Figure 7.41: *Bidimensional LPM - Voltage Drive* $\dot{\Gamma}$ *for* $\sigma = 10\ S/m$ *-* $r_{out} = 50mm$

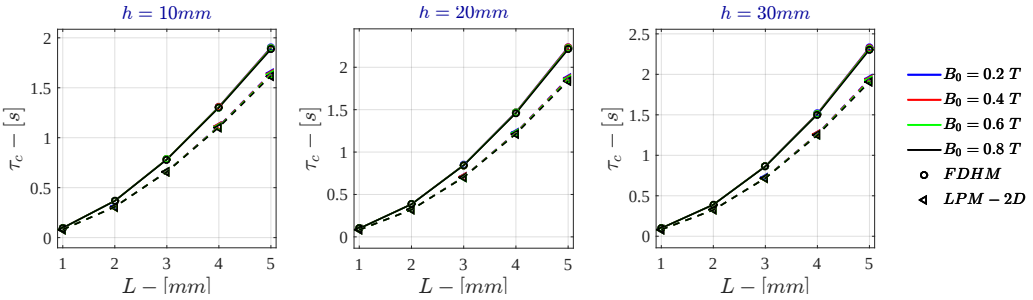

Figure 7.42: *Bidimensional LPM - Voltage Drive* τ_c *for* $\sigma = 10\ S/m$ *-* $r_{out} = 50mm$

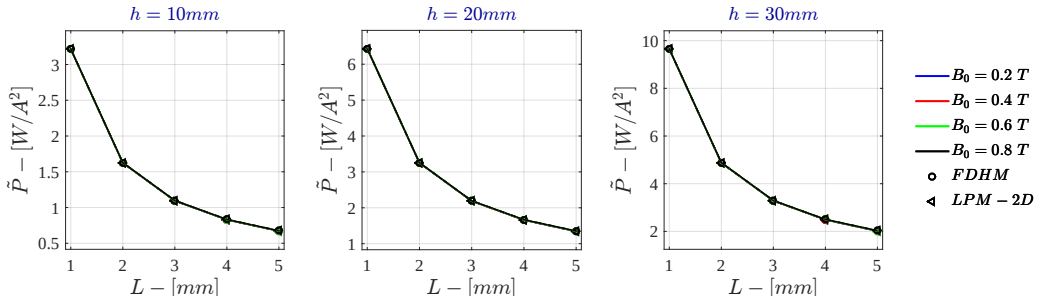

Figure 7.43: *Bidimensional LPM - Voltage Drive* $\tilde{P}$ *for* $\sigma = 10\ S/m$ *-* $r_{out} = 50mm$

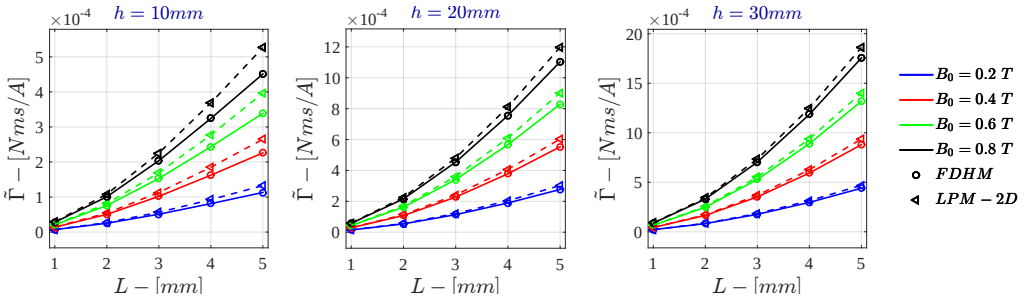

Figure 7.44: *Bidimensional LPM - Voltage Drive* $\tilde{\Gamma}$ *for* $\sigma = 10\ S/m$ *-* $r_{out} = 50mm$

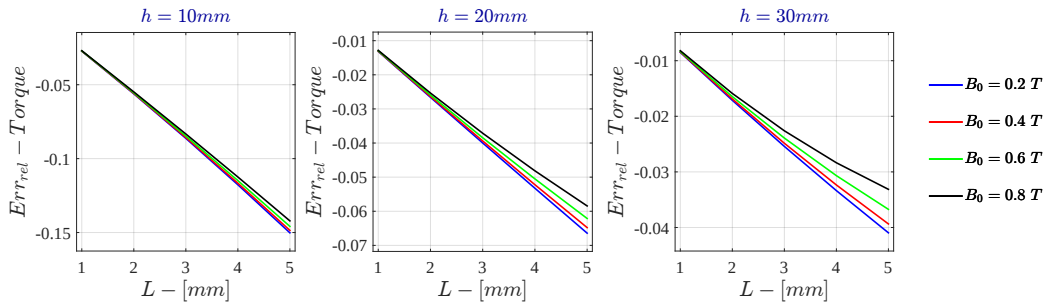

Figure 7.45: *Bidimensional LPM - Voltage Drive*
Relative Error - $\dot{\Gamma}$ for $\sigma = 10\ S/m$ - $r_{out} = 50mm$

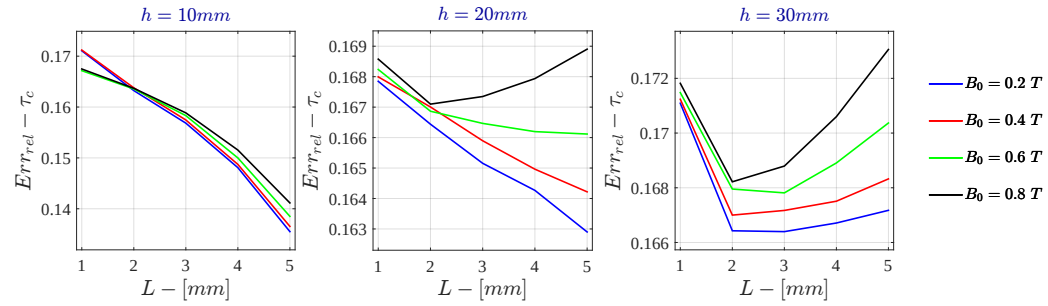

Figure 7.46: *Bidimensional LPM - Voltage Drive*
Relative Error - τ_c for $\sigma = 10\ S/m$ - $r_{out} = 50mm$

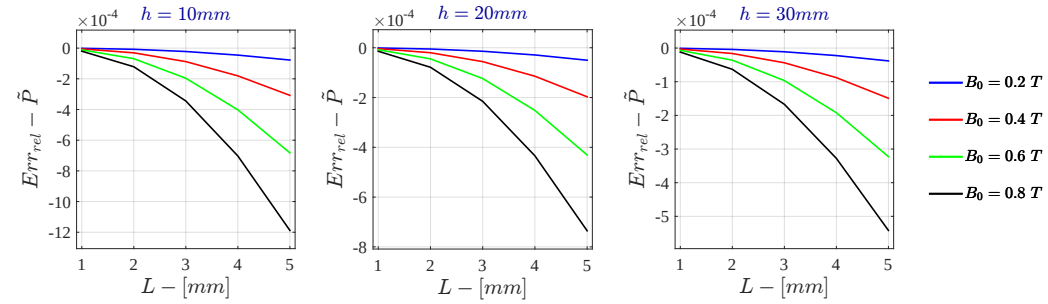

Figure 7.47: *Bidimensional LPM - Voltage Drive*
Relative Error - $\tilde{P}$ for $\sigma = 10\ S/m$ - $r_{out} = 50mm$

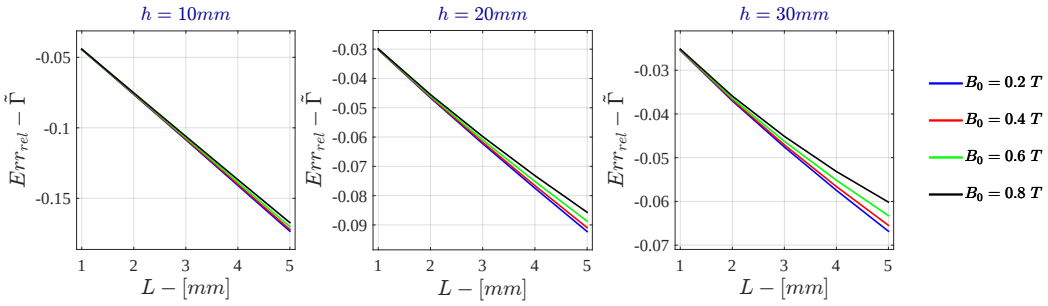

Figure 7.48: *Bidimensional LPM - Voltage Drive*
Relative Error - $\tilde{\Gamma}$ for $\sigma = 10\ S/m$ - $r_{out} = 50mm$

7.10 Results: Monodimensional LPM - $\sigma = 10^6 S/m$

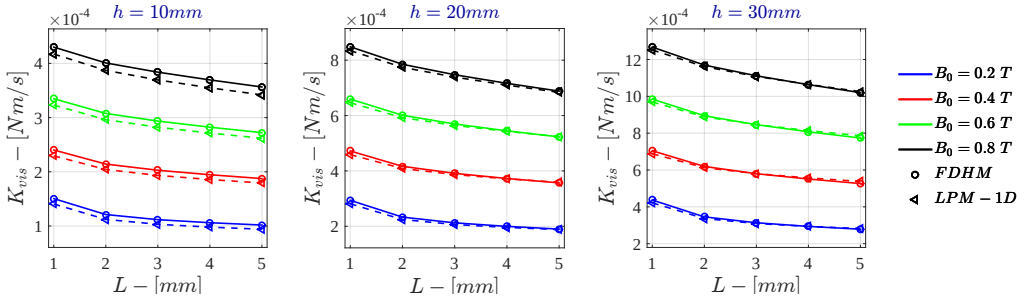

Figure 7.49: *K_{vis} for $\sigma = 10^6$ S/m - $r_{out} = 50mm$ - Monodimensional LPM*

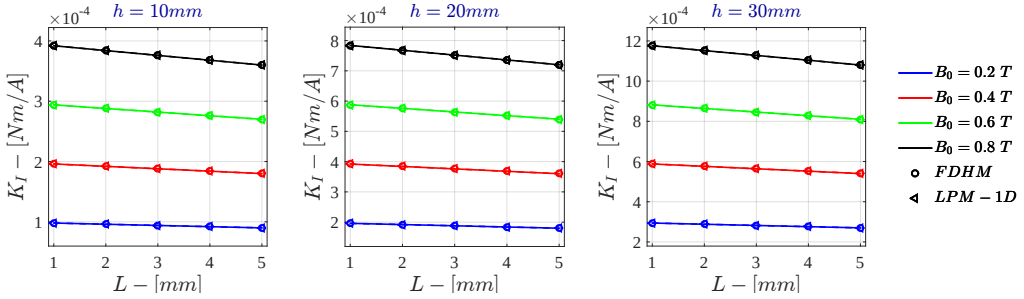

Figure 7.50: *Monodimensional LPM*
K_I for $\sigma = 10^6$ S/m - $r_{out} = 50mm$

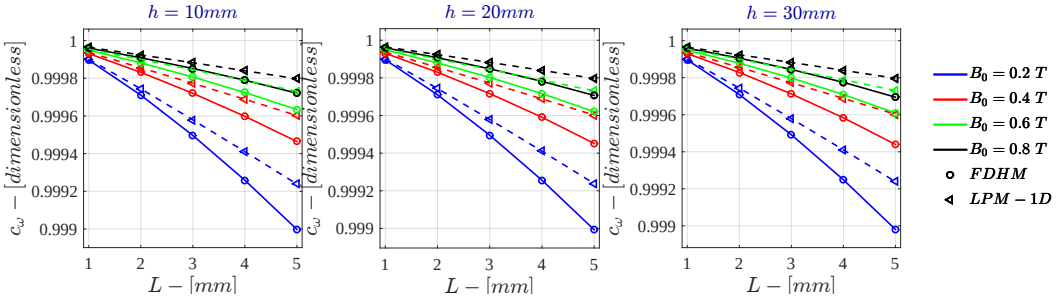

Figure 7.51: *Monodimensional LPM*
c_ω for $\sigma = 10^6$ S/m - $r_{out} = 50mm$

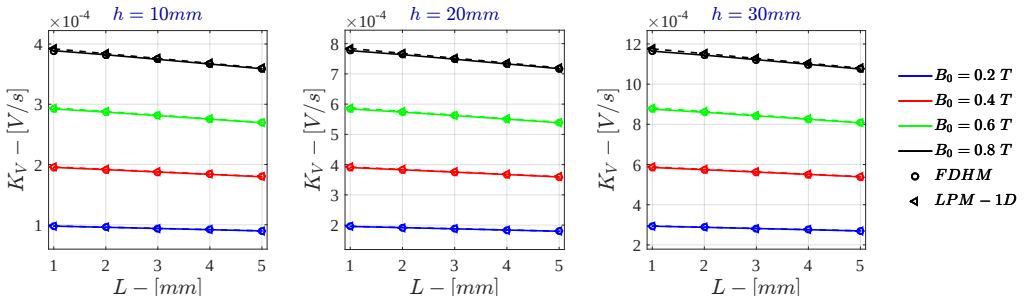

Figure 7.52: *Monodimensional LPM*
K_V for $\sigma = 10^6$ S/m - $r_{out} = 50mm$

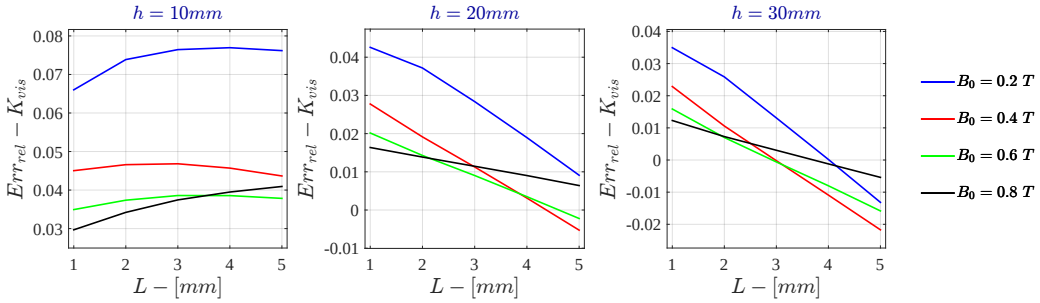

Figure 7.53: *Monodimensional LPM*
Relative Error - K_{vis} for $\sigma = 10^6\ S/m$ - $r_{out} = 50mm$

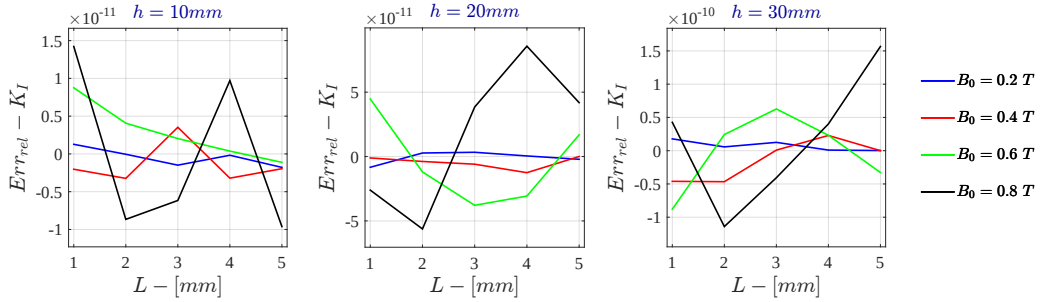

Figure 7.54: *Monodimensional LPM*
Relative Error - K_I for $\sigma = 10^6\ S/m$ - $r_{out} = 50mm$

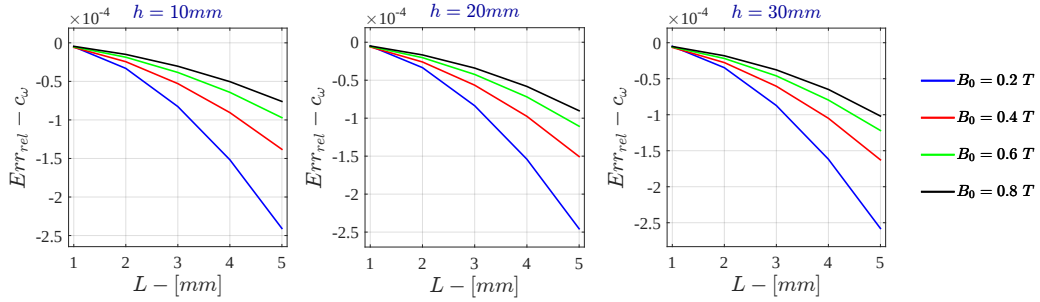

Figure 7.55: *Monodimensional LPM*
Relative Error - c_ω for $\sigma = 10^6\ S/m$ - $r_{out} = 50mm$

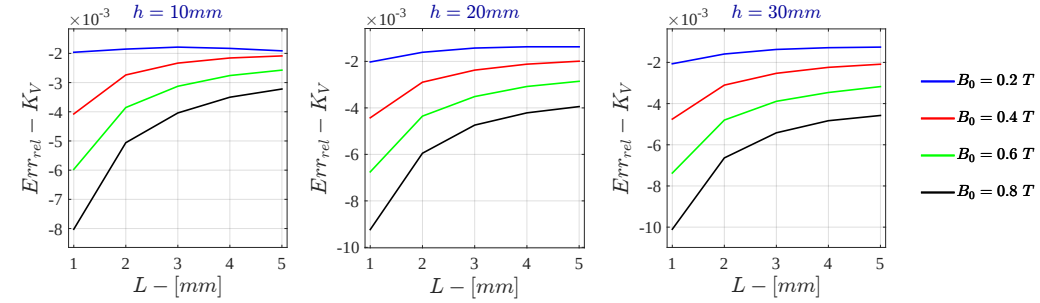

Figure 7.56: *Monodimensional LPM*
Relative Error - K_V for $\sigma = 10^6\ S/m$ - $r_{out} = 50mm$

7.10.1 Current Drive

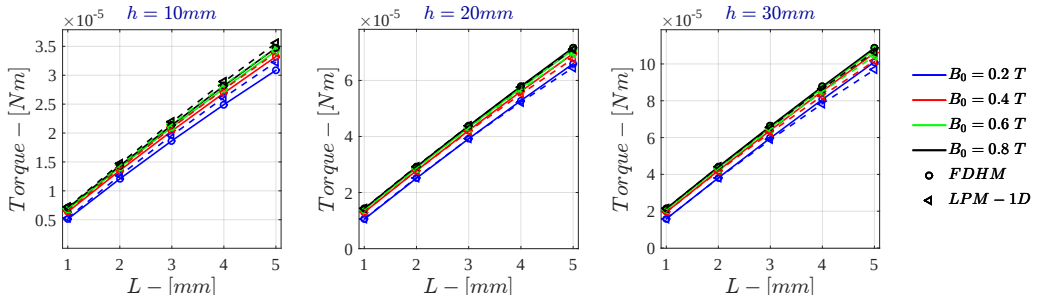

Figure 7.57: *Monodimensional LPM - Current Drive* $\dot{\Gamma}$ *for* $\sigma = 10^6\ S/m$ - $r_{out} = 50mm$

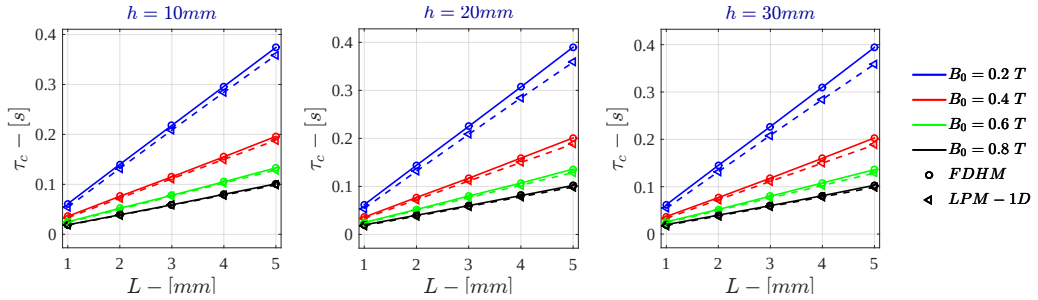

Figure 7.58: *Monodimensional LPM - Current Drive* τ_c *for* $\sigma = 10^6\ S/m$ - $r_{out} = 50mm$

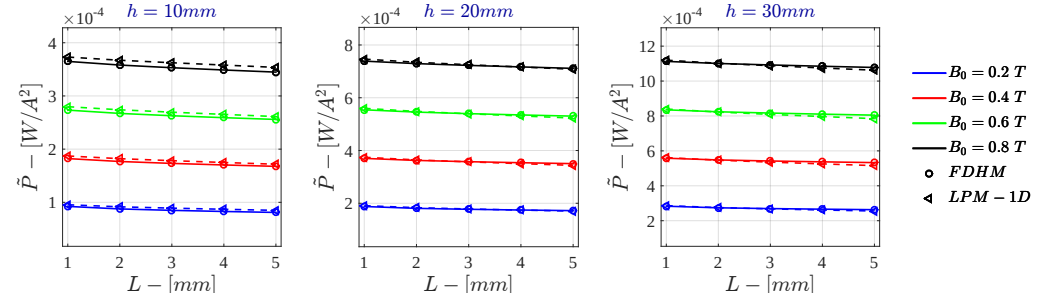

Figure 7.59: *Monodimensional LPM - Current Drive* $\tilde{P}$ *for* $\sigma = 10^6\ S/m$ - $r_{out} = 50mm$

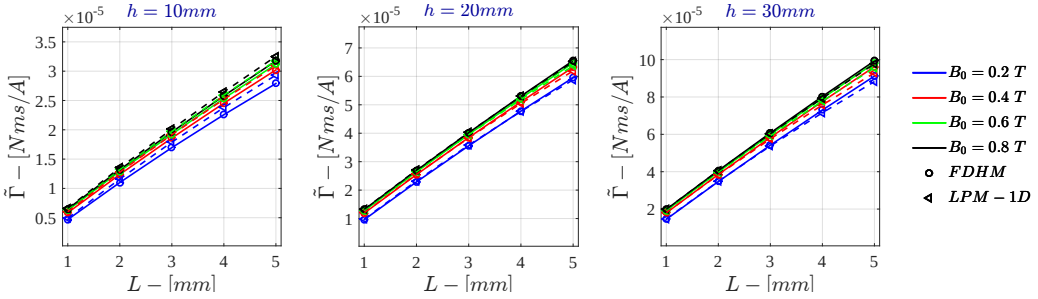

Figure 7.60: *Monodimensional LPM - Current Drive* $\tilde{\Gamma}$ *for* $\sigma = 10^6\ S/m$ - $r_{out} = 50mm$

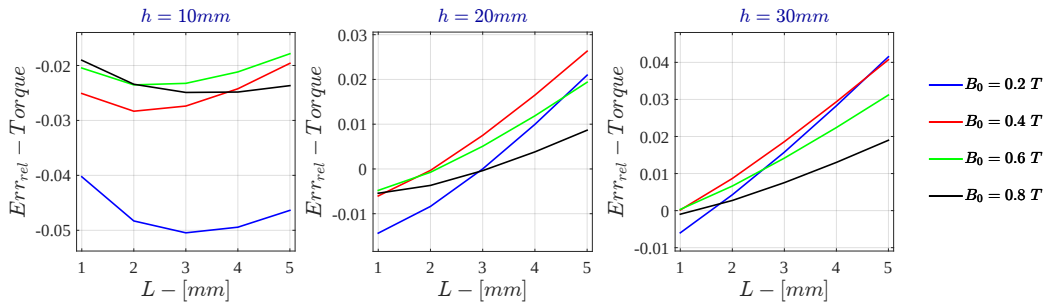

Figure 7.61: *Monodimensional LPM - Current Drive Relative Error - $\dot{\Gamma}$ for $\sigma = 10^6$ S/m - $r_{out} = 50mm$*

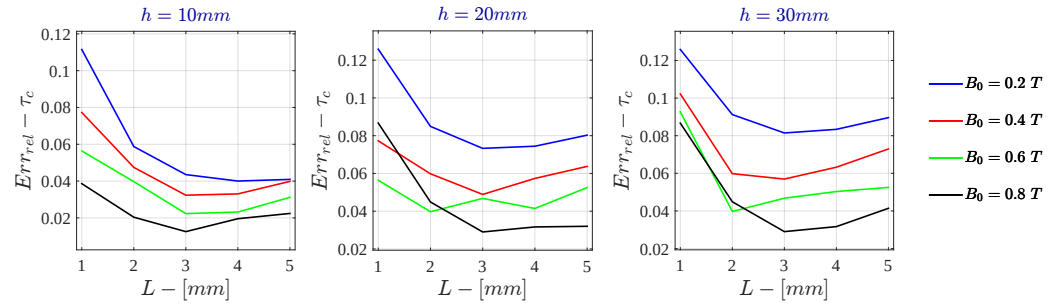

Figure 7.62: *Monodimensional LPM - Current Drive Relative Error - τ_c for $\sigma = 10^6$ S/m - $r_{out} = 50mm$*

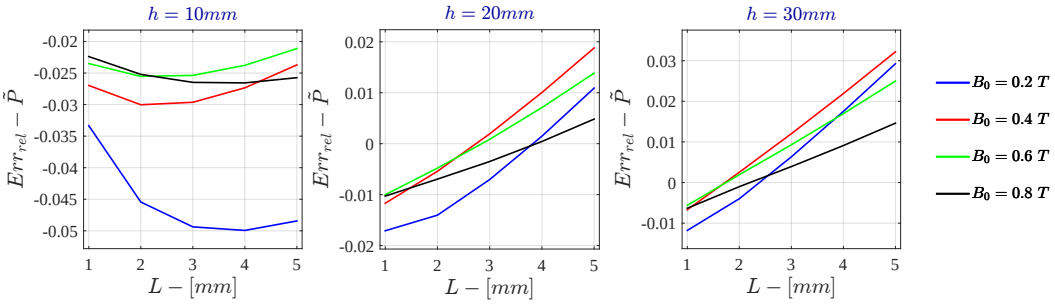

Figure 7.63: *Monodimensional LPM - Current Drive Relative Error - $\tilde{P}$ for $\sigma = 10^6$ S/m - $r_{out} = 50mm$*

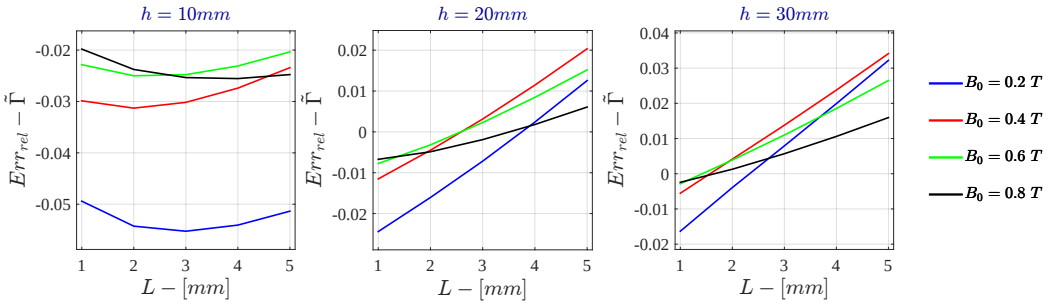

Figure 7.64: *Monodimensional LPM - Current Drive Relative Error - $\tilde{\Gamma}$ for $\sigma = 10^6$ S/m - $r_{out} = 50mm$*

7.10.2 Voltage Drive

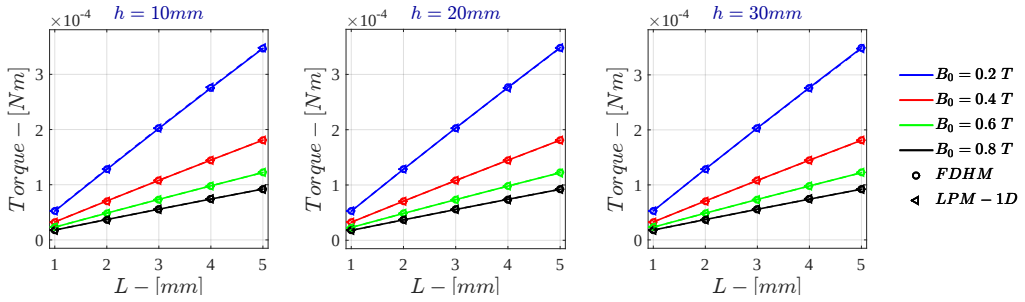

Figure 7.65: *Monodimensional LPM - Voltage Drive* $\dot{\Gamma}$ *for* $\sigma = 10^6\ S/m$ - $r_{out} = 50mm$

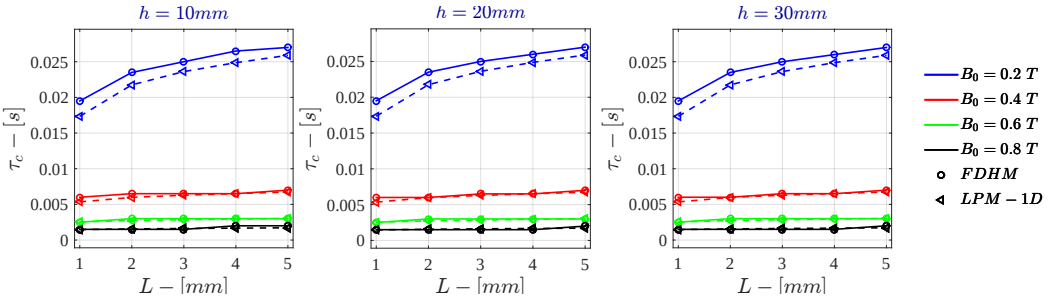

Figure 7.66: *Monodimensional LPM - Voltage Drive* τ_c *for* $\sigma = 10^6\ S/m$ - $r_{out} = 50mm$

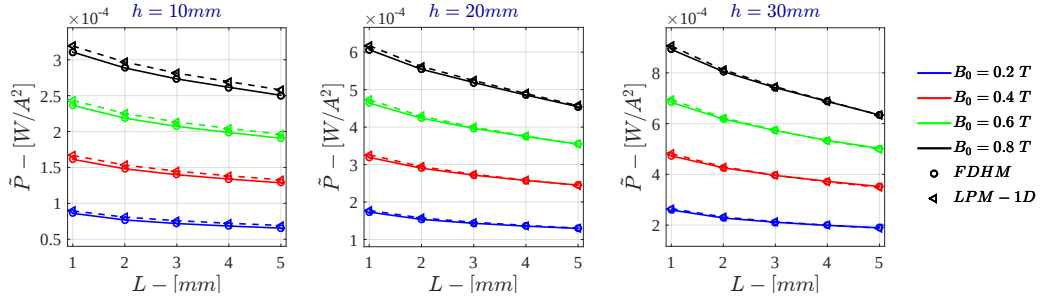

Figure 7.67: *Monodimensional LPM - Voltage Drive* $\tilde{P}$ *for* $\sigma = 10^6\ S/m$ - $r_{out} = 50mm$

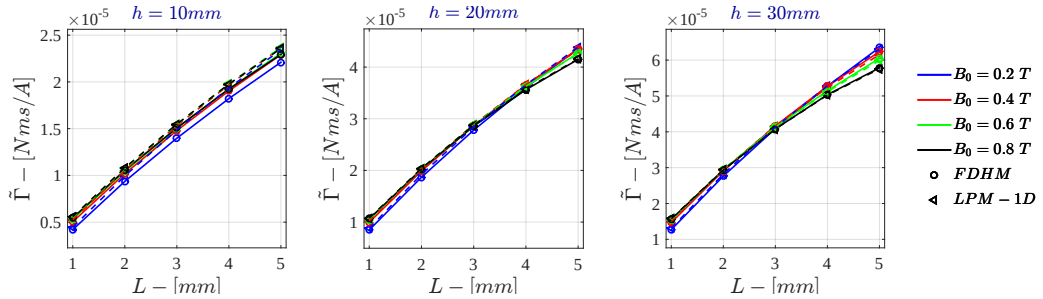

Figure 7.68: *Monodimensional LPM - Voltage Drive* $\tilde{\Gamma}$ *for* $\sigma = 10^6\ S/m$ - $r_{out} = 50mm$

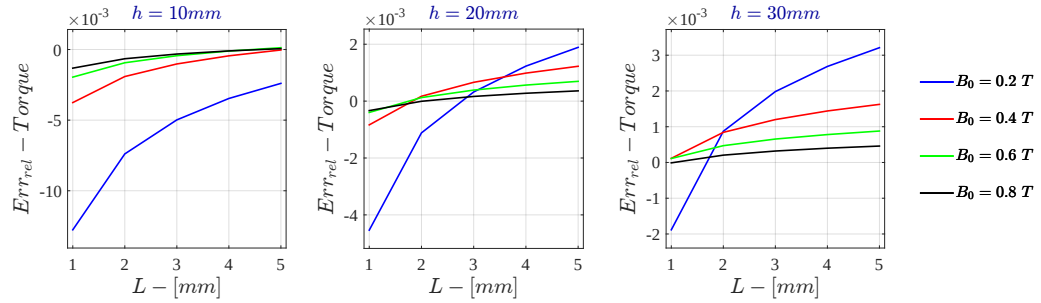

Figure 7.69: *Monodimensional LPM - Voltage Drive*
Relative Error - $\dot{\Gamma}$ for $\sigma = 10^6$ S/m - $r_{out} = 50mm$

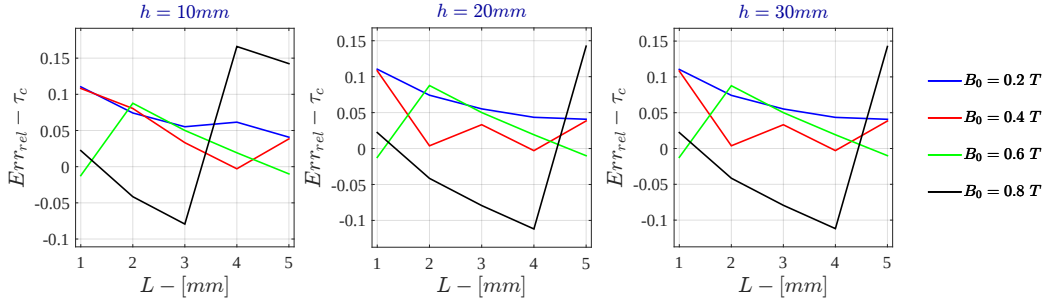

Figure 7.70: *Monodimensional LPM - Voltage Drive*
Relative Error - τ_c for $\sigma = 10^6$ S/m - $r_{out} = 50mm$

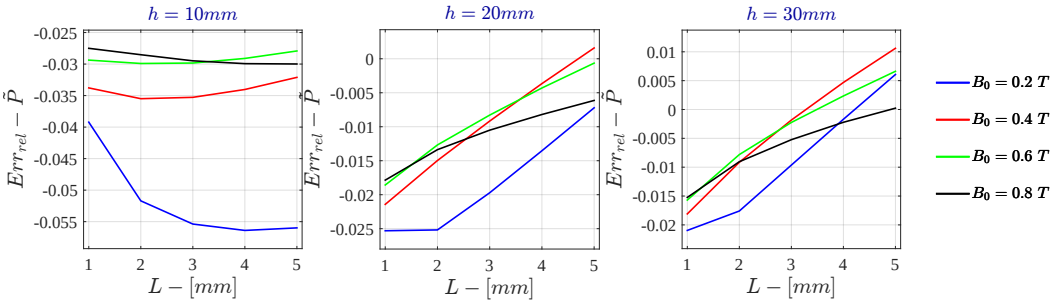

Figure 7.71: *Monodimensional LPM - Voltage Drive*
Relative Error - $\tilde{P}$ for $\sigma = 10^6$ S/m - $r_{out} = 50mm$

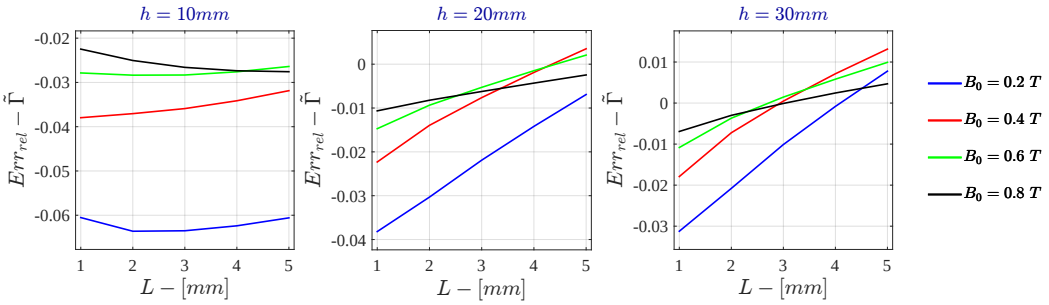

Figure 7.72: *Monodimensional LPM - Voltage Drive*
Relative Error - $\tilde{\Gamma}$ for $\sigma = 10^6$ S/m - $r_{out} = 50mm$

7.11 Results: Bidimensional LPM - $\sigma = 10^6 S/m$

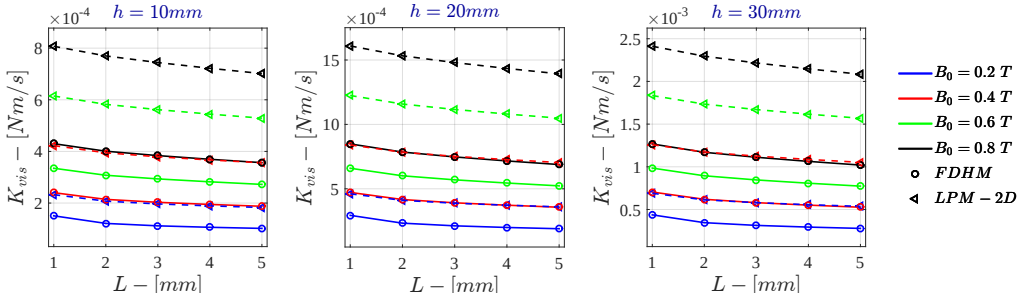

Figure 7.73: *Bidimensional LPM*
K_{vis} *for* $\sigma = 10^6\ S/m$ - $r_{out} = 50mm$

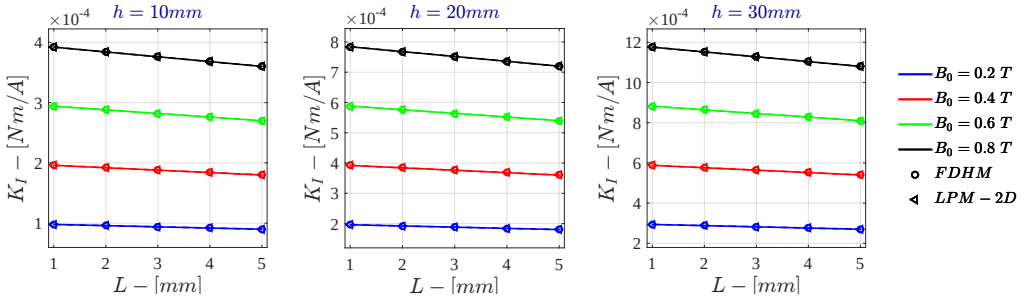

Figure 7.74: *Bidimensional LPM*
K_I *for* $\sigma = 10^6\ S/m$ - $r_{out} = 50mm$

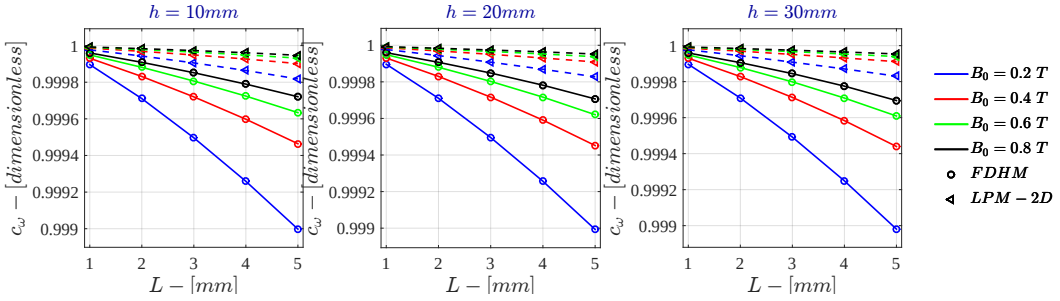

Figure 7.75: *Bidimensional LPM*
c_ω *for* $\sigma = 10^6\ S/m$ - $r_{out} = 50mm$

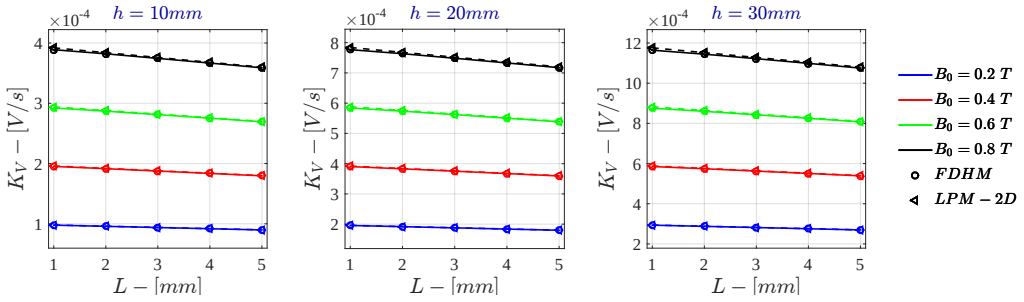

Figure 7.76: *Bidimensional LPM*
K_V *for* $\sigma = 10^6\ S/m$ - $r_{out} = 50mm$

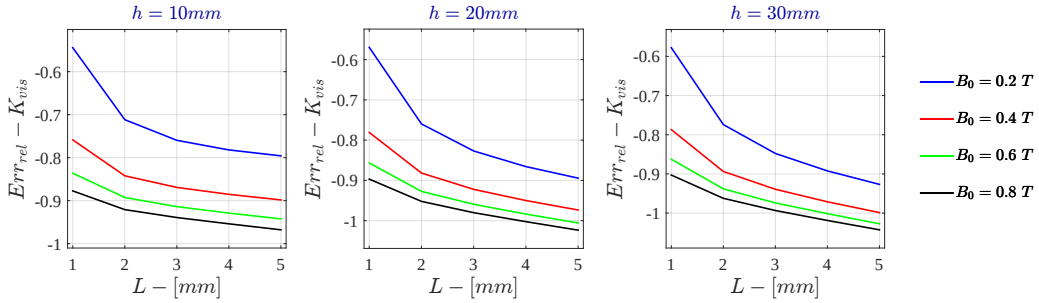

Figure 7.77: *Bidimensional LPM*
Relative Error - K_{vis} for $\sigma = 10^6\ S/m$ - $r_{out} = 50mm$

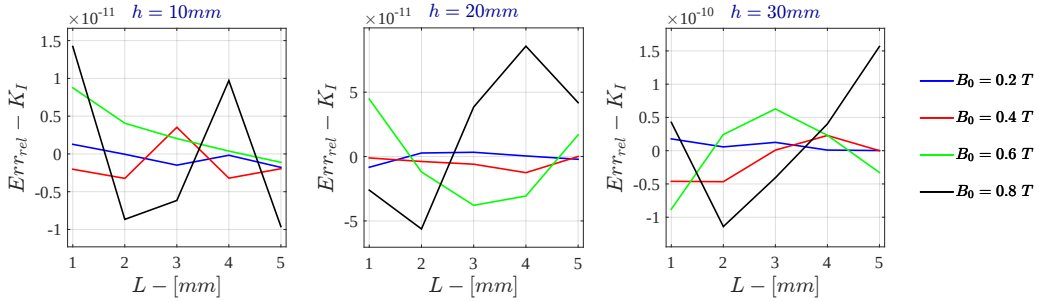

Figure 7.78: *Bidimensional LPM*
Relative Error - K_I for $\sigma = 10^6\ S/m$ - $r_{out} = 50mm$

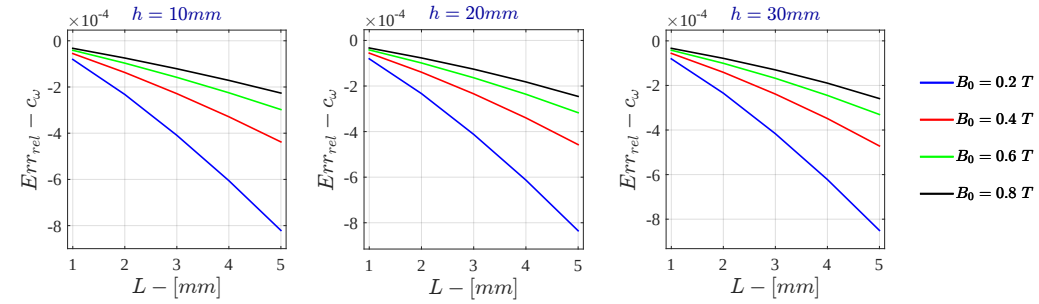

Figure 7.79: *Bidimensional LPM*
Relative Error - c_ω for $\sigma = 10^6\ S/m$ - $r_{out} = 50mm$

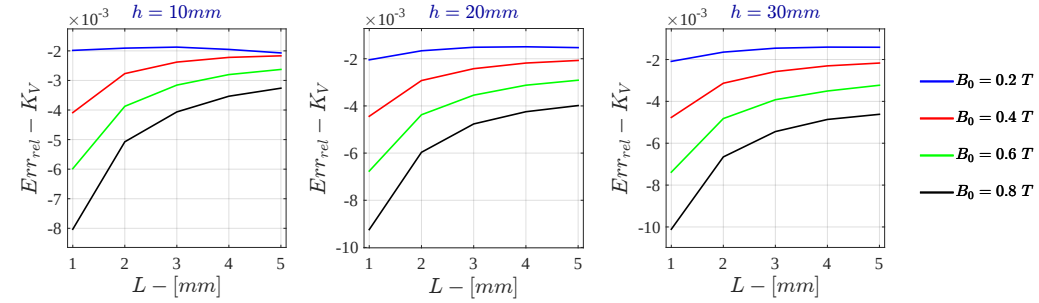

Figure 7.80: *Bidimensional LPM*
Relative Error - K_V for $\sigma = 10^6\ S/m$ - $r_{out} = 50mm$

7.11.1 Current Drive

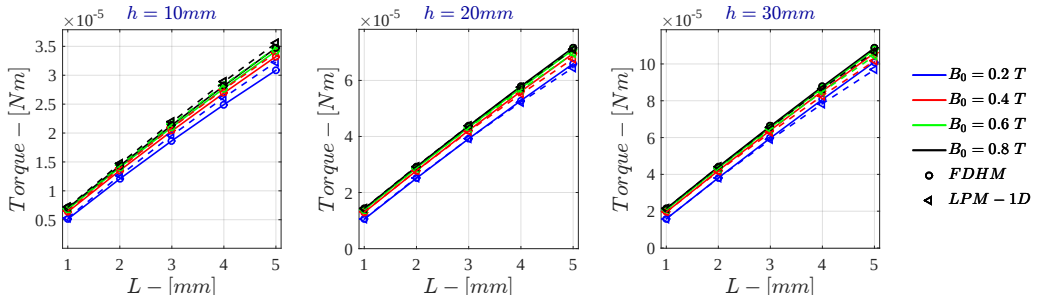

Figure 7.81: *Bidimensional LPM - Current Drive* $\dot{\Gamma}$ *for* $\sigma = 10^6\ S/m$ *-* $r_{out} = 50mm$

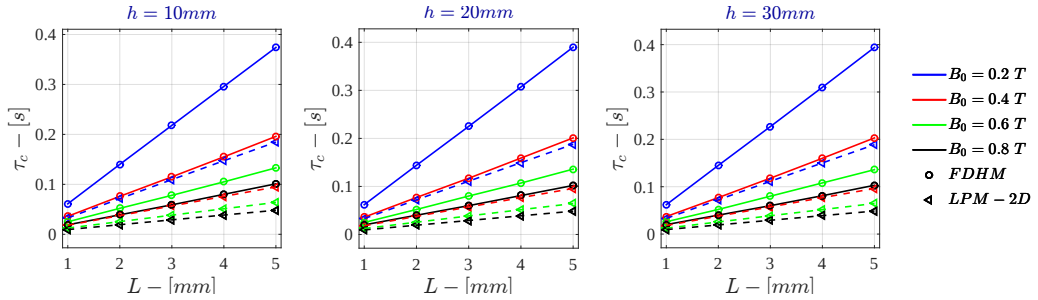

Figure 7.82: *Bidimensional LPM - Current Drive* τ_c *for* $\sigma = 10^6\ S/m$ *-* $r_{out} = 50mm$

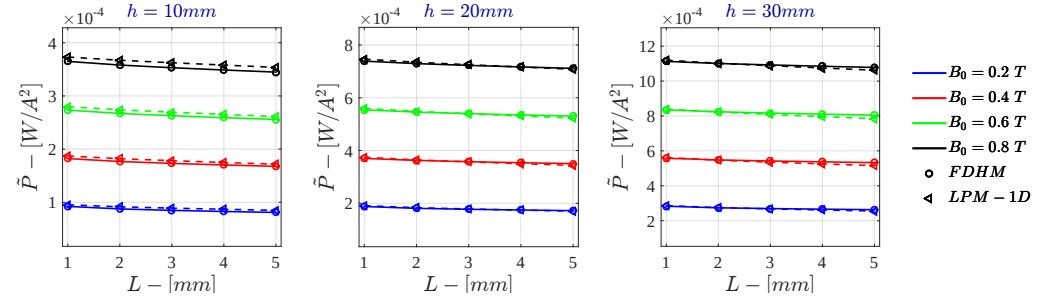

Figure 7.83: *Bidimensional LPM - Current Drive* $\tilde{P}$ *for* $\sigma = 10^6\ S/m$ *-* $r_{out} = 50mm$

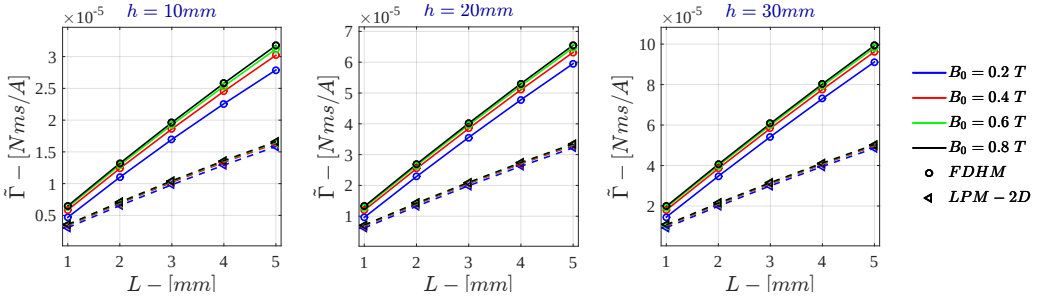

Figure 7.84: *Bidimensional LPM - Current Drive* $\tilde{\Gamma}$ *for* $\sigma = 10^6\ S/m$ *-* $r_{out} = 50mm$

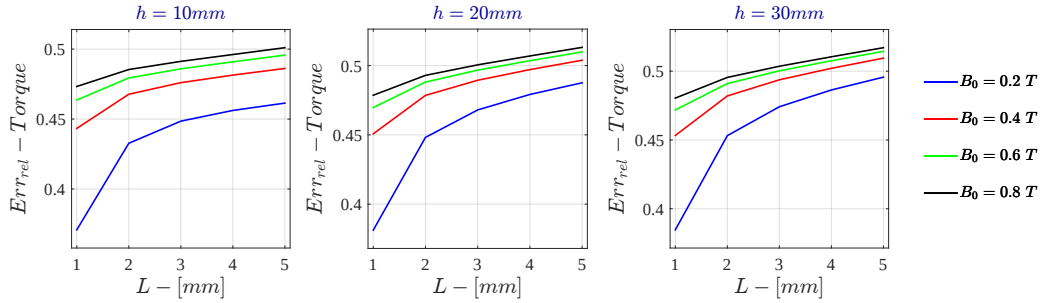

Figure 7.85: *Bidimensional LPM - Current Drive*
Relative Error - $\dot{\Gamma}$ for $\sigma = 10^6$ S/m - $r_{out} = 50mm$

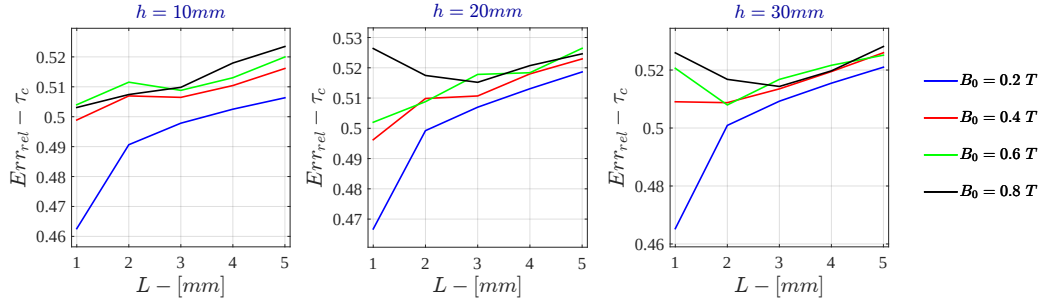

Figure 7.86: *Bidimensional LPM - Current Drive*
Relative Error - τ_c for $\sigma = 10^6$ S/m - $r_{out} = 50mm$

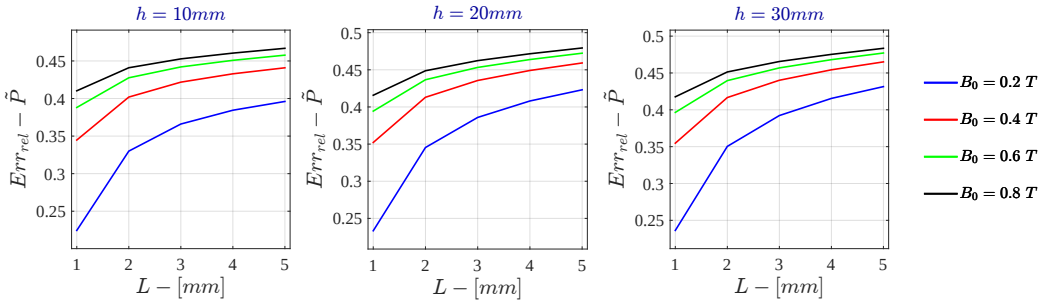

Figure 7.87: *Bidimensional LPM - Current Drive*
Relative Error - $\tilde{P}$ for $\sigma = 10^6$ S/m - $r_{out} = 50mm$

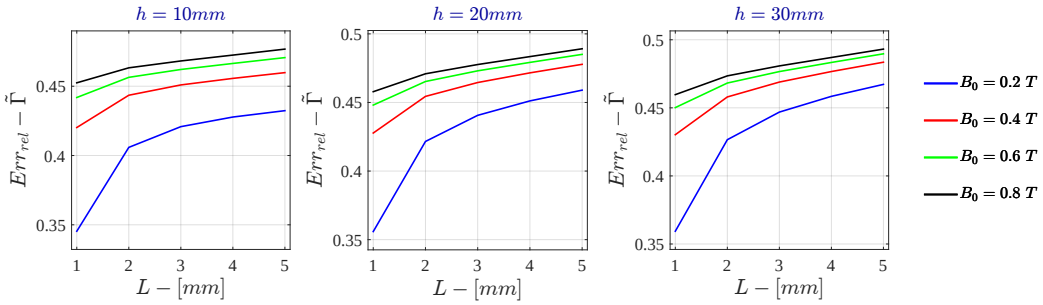

Figure 7.88: *Bidimensional LPM - Current Drive*
Relative Error - $\tilde{\Gamma}$ for $\sigma = 10^6$ S/m - $r_{out} = 50mm$

7.11.2 Voltage Drive

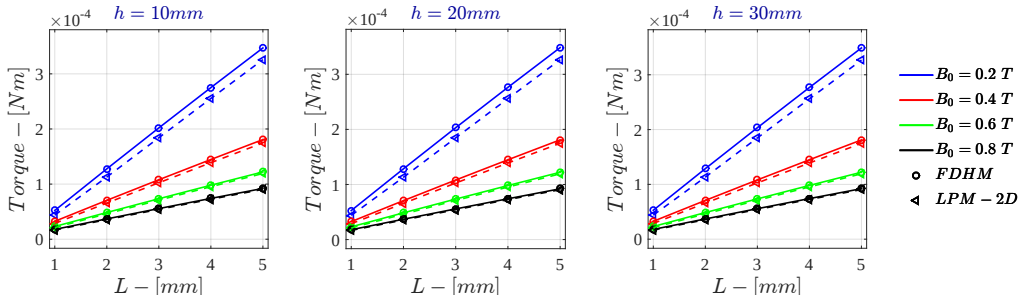

Figure 7.89: *Bidimensional LPM - Voltage Drive* $\dot{\Gamma}$ *for* $\sigma = 10^6\ S/m$ - $r_{out} = 50mm$

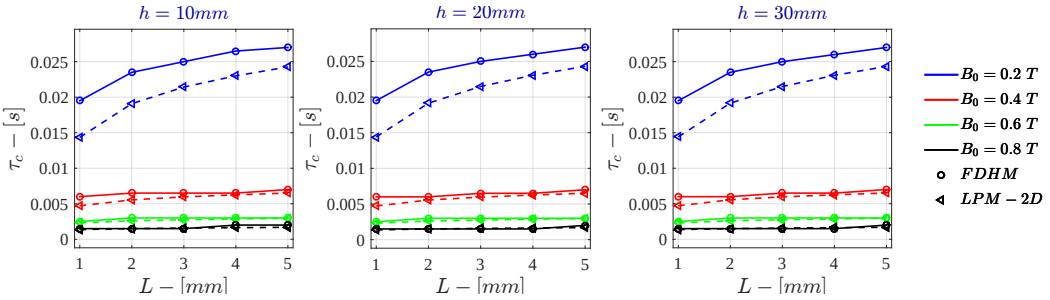

Figure 7.90: *Bidimensional LPM - Voltage Drive* τ_c *for* $\sigma = 10^6\ S/m$ - $r_{out} = 50mm$

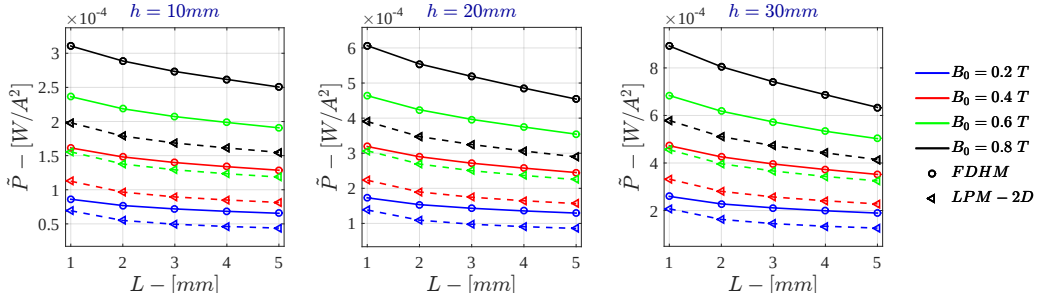

Figure 7.91: *Bidimensional LPM - Voltage Drive* $\tilde{P}$ *for* $\sigma = 10^6\ S/m$ - $r_{out} = 50mm$

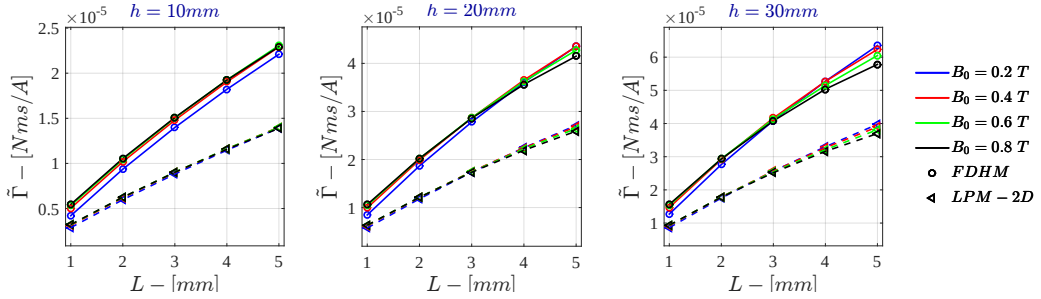

Figure 7.92: *Bidimensional LPM - Voltage Drive* $\tilde{\Gamma}$ *for* $\sigma = 10^6\ S/m$ - $r_{out} = 50mm$

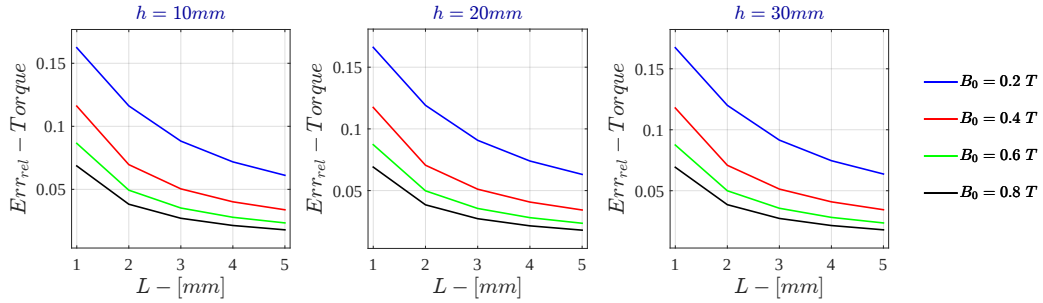

Figure 7.93: *Bidimensional LPM - Voltage Drive*
Relative Error - $\dot{\Gamma}$ for $\sigma = 10^6$ S/m - $r_{out} = 50mm$

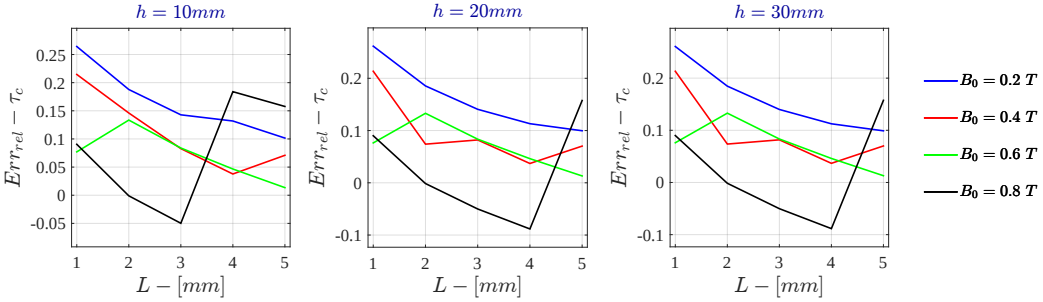

Figure 7.94: *Bidimensional LPM - Voltage Drive*
Relative Error - τ_c for $\sigma = 10^6$ S/m - $r_{out} = 50mm$

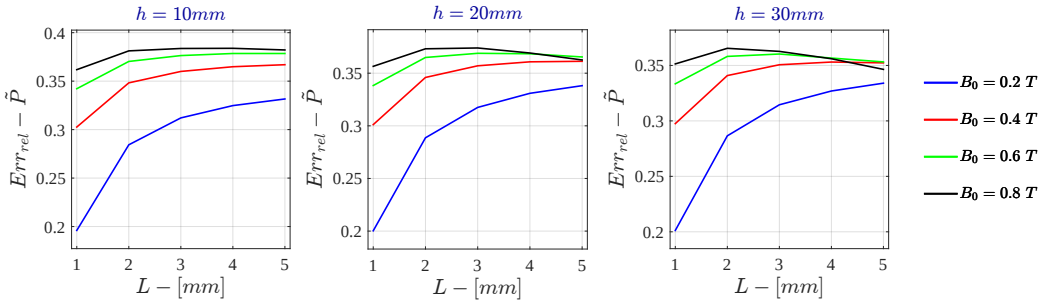

Figure 7.95: *Bidimensional LPM - Voltage Drive*
Relative Error - $\tilde{P}$ for $\sigma = 10^6$ S/m - $r_{out} = 50mm$

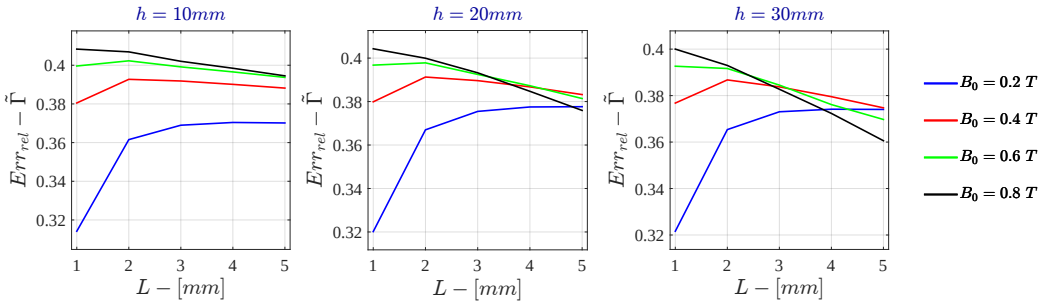

Figure 7.96: *Bidimensional LPM - Voltage Drive*
Relative Error - $\tilde{\Gamma}$ for $\sigma = 10^6$ S/m - $r_{out} = 50mm$

7.12 Discussion

Figures (7.1) and (7.5) show the inability of the mono-dimensional analytical solution to give good results in the estimation of K_{vis} if the electric conductivity of the liquid is low. The reason resides on the fact that the Shercliff and Hartmann layers are of the same magnitude if the electrical conductivity of the liquid is low. So, as the mono-dimensional solution neglects the viscous shear on the armatures of the device, the computed K_{vis} is underestimated.
On the other hand, in Figures (7.49) and (7.53) the mono-dimensional solution shows its ability to compute the K_{vis} for high conductive liquid; the reason of the improvement is in the fact that the Hartmann layers are a bit less than 2 order of magnitude thinner than the Shercliff layers, so the neglection of the influence of the Shercliff layers does not affect the estimation of K_{vis}.
For both high and low electrically conductive liquids the error in the estimation of K_{vis} decreases for increasing height and decreasing radial dimension of the torus and for decreasing magnetic field.
The coefficient K_{vis} computed on the basis of the bi-dimensional solution shows better accuracy for low electrically conductive liquids than for high electrically conductive liquids. For low electrically conductive liquids, the accuracy of the K_{vis} based on the bi-dimensional solution is furthermore more accurate than the one based on the mono-dimensional solution; the opposite trend can be read for high electrically conductive liquids. The error in the estimation of K_{vis} increases for decreasing height and decreasing radial dimension of the torus and for decreasing magnetic field.
The computed coefficient of Lorentz force moment, K_I, is directly influenced neither by the analytical solution used nor by the electric conductivity of the liquid. Figures (7.2)-(7.54) show actually the precision of the FDHM model, being the K_I given in closed form.
The errors regarding the coefficient K_I are not directly affected by the particular analytical solution used.
The neglection of the Shercliff layers does not affect the estimation of c_ω for both high and low electrically conductive liquids. The reason resides in the presence of the not derived value of the angular velocity in the formula for the computation of c_ω and it seems to be quite accurate for both high and low

electrically conductive liquids. The coefficient is anyway overestimated due to the neglection of the Shercliff layers. The error in the estimation of c_ω increases for decreasing height and increasing radial dimension of the torus and for decreasing magnetic field.
Figures (7.27)-(7.79) show that the estimation of c_ω based on the bi-dimensional solution is more precise for high electrically conductive liquid than for low electrically conductive liquid, so following the same trend of the c_ω based on the mono-dimensional solution. The error in this case is for both high and low electrically conductive liquids higher than the c_ω estimated with the mono-dimensional solution.
As for the computation of the c_ω, here the neglection of the Shercliff layers does not affect the estimation of K_V for both high and low electrically conductive liquids. The coefficient is anyway overestimated due to the neglection of the Shercliff layers. The error in the estimation of K_V increase for decreasing height and increasing radial dimension of the torus and for decreasing magnetic field. The error in the estimation of K_V increases for decreasing height and increasing radial dimension of the torus and for decreasing magnetic field.
The K_V based on the bi-dimensional solution has accuracy comparable with the one computed with the mono-dimensional solution with same trend with respect of the height and radial dimension of the torus and the intensity of the magnetic field.
The precision torque $\dot{\Gamma}$ computed with both the monodimensional and bidimensional solutions is mainly affected by the estimation error of the K_{vis} being the c_ω and K_I quite accurate. The monodimensional solution is able to computed with sufficient accuracy the torque provided by the device in the case a high conductive liquid is used, the bidimensional solution guarantees good performances for low conductive liquids. The comparison between the predictions in the case of current and voltage drive shows that The torque $\dot{\Gamma}$ for Voltage Drive is more accurate than the one computed for the Current Drive. The reason resides in the weight the K_{vis} has in in (7.7.8). The error of the K_{vis} is reduced by the low value of the electrical resistance of the fluid and so, the estimated torque appears to be close to the one derived from the FDHM simulations.
About the characteristic time it can be seen that the error between the characteristic time computed by the FDHM and the LPM is not the result of the

propagation error of each coefficient used to compute τ_c. A further analysis of the time evolution of the coefficients c_ω and K_{vis} made with the results obtained with the FDHM, shows how these coefficients, considered constant in the LPM, are function of the velocity, Figures(7.97) (7.98) (7.99).

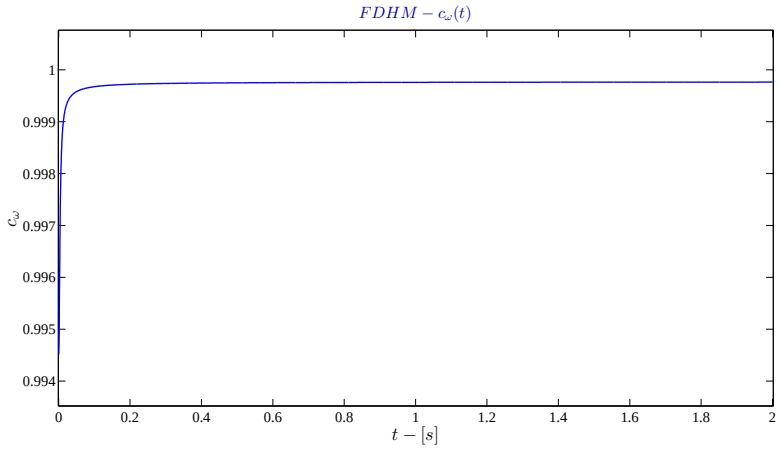

Figure 7.97: *Evolution of* c_ω

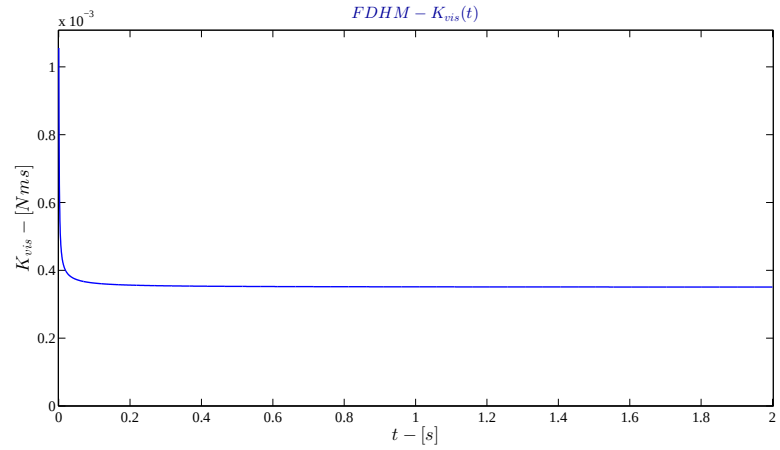

Figure 7.98: *Evolution of* K_{vis}

This analysis highlights how the device is affected by non-linear effect in the neighbourhood of null angular velocity. This, in some way, resize the hypothetical advantage not to have jump of torque around the zero crossing [3].
Furthermore, it is evident from the previous results that the characteristic time is smaller in case of Voltage drive because of the role played by the electrical resistance, supposed to be little for this kind of device.

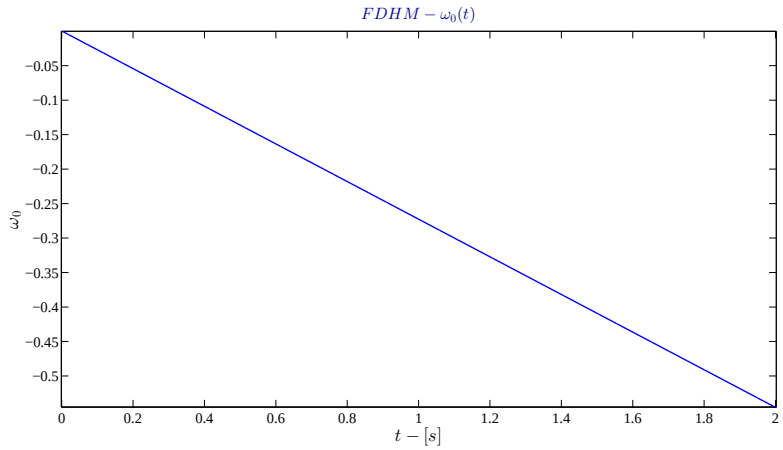

Figure 7.99: *Evolution of* ω_w

The error on the characteristic time influences the estimated power consumption and the estimated angular momentum.

Chapter

8 Performances analysis.

In this chapter, a performance analysis has been conducted by means of the LPM. The possibility to use liquid metal or an ideal liquid to be designed as been evaluated.

8.1 Liquid Metal

Considering mercury as conductive fluid with the following physical properties:

$$\begin{aligned} \sigma_{Hg} &= 1.04 \cdot 10^6 \ S/m \\ \rho_{Hg} &= 1.36 \cdot 10^4 \ Kg/m^3 \\ \mu_{Hg} &= 1.50 \cdot 10^{-3} \ Pa/s \end{aligned} \tag{8.1.1}$$

the coefficients of the lumped parameter model together with the torque and the power consumption are presented in Figures(8.1)-(8.4). All the values plotted in the following figure are calculated for a torus with rectangular cross section whose height is equal to $h = 1cm$. The symbols on the y axis of Fig.(8.3) and Fig.(8.4) have the following meaning:

$$\tilde{T} = \frac{\dot{\Gamma}}{ah} = \frac{1}{h}\left(I_z c_\omega \ \frac{K_I}{K_{vis}}\right) \tag{8.1.2}$$

$$\tilde{P} = \frac{P}{hI^2} = \frac{1}{h}\left(\frac{K_V K_I}{K_{vis}} + R_{eq}\right) \tag{8.1.3}$$

where P is the power consumption of the actuator for an electric current with value of 1 A. All the following values are obtained by means of the LPM based on the mono-dimensional solution with the value of K_vis computed by the bi-dimensional solution.

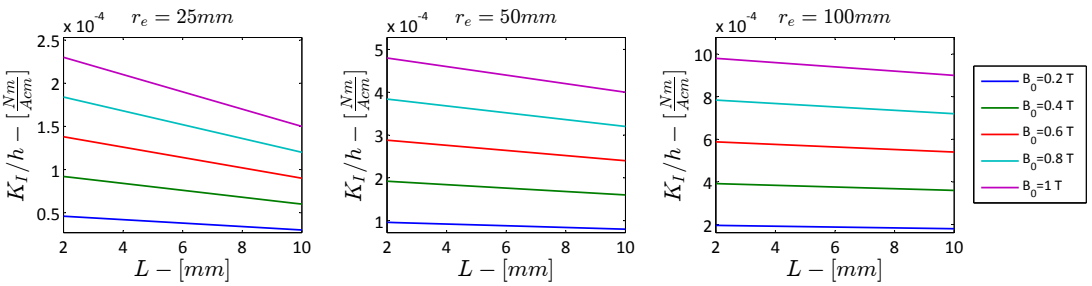

Figure 8.1: *K_I function of L for $B_0 = 0.2 \div 1.0$ and 3 different outer radii $r_e = 25, 50, 100mm$. Liquid: Mercury (Hg).*

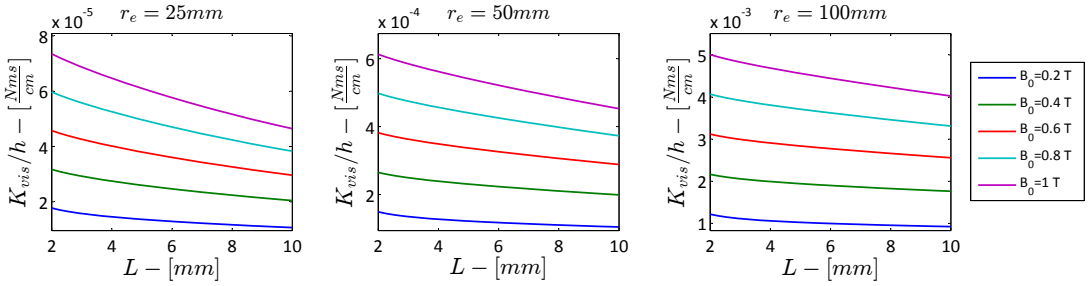

Figure 8.2: *K_{vis} function of L for $B_0 = 0.2 \div 1.0$ and 3 different outer radii $r_e = 25, 50, 100mm$. Liquid: Mercury (Hg).*

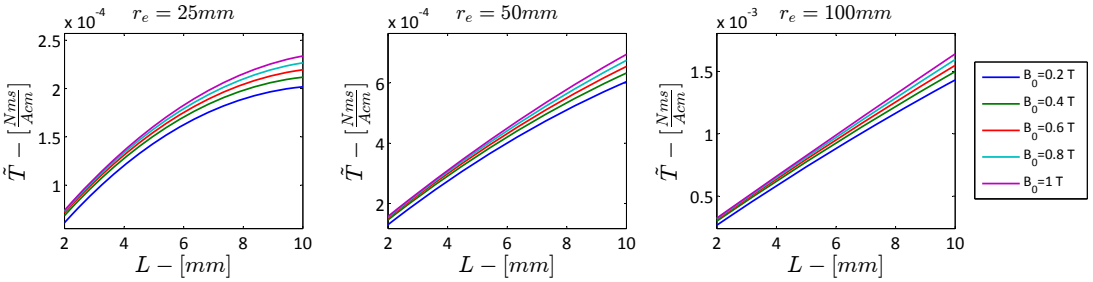

Figure 8.3: *Torque function of L for $B_0 = 0.2 \div 1.0$ and 3 different outer radii $r_e = 25, 50, 100mm$. Liquid: Mercury (Hg).*

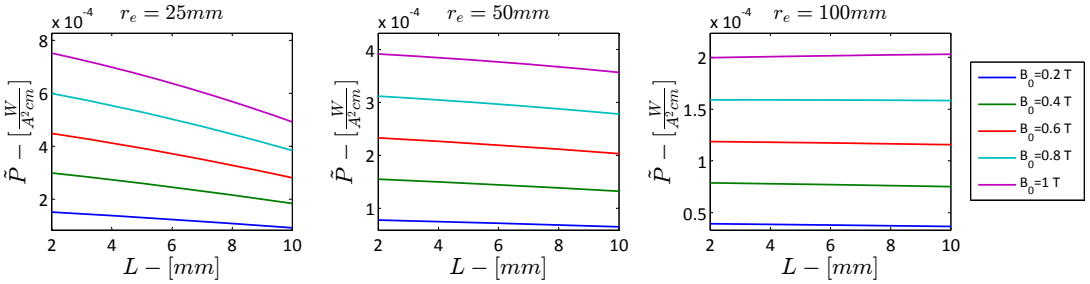

Figure 8.4: *Power consumption function of L for $B_0 = 0.2 \div 1.0$ and 3 different outer radii $r_e = 25, 50, 100mm$. Liquid: Mercury (Hg).*

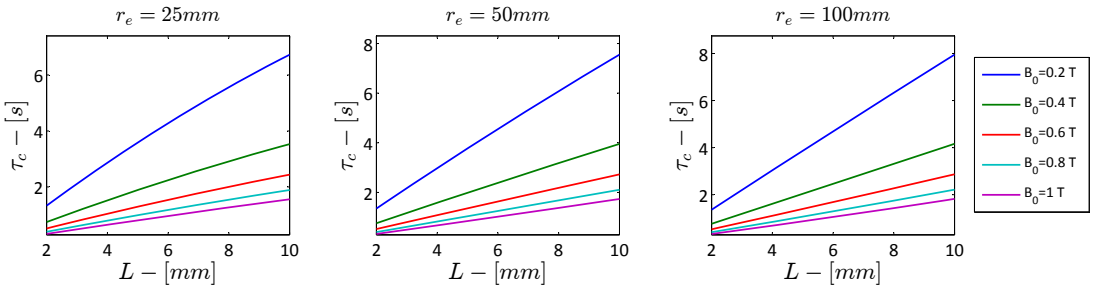

Figure 8.5: *Characteristic time function of L for $\sigma = 10 \div 10^6$ S/m and 3 different outer radii $r_e = 25, 50, 100mm$. $B_0 = 1.0$ T. $\rho = 1000$ Kg/m^3.*

In Figure(8.2) it is possible to see that the influence of the viscosity is not neglectable and it influences the overall performance of the device. The high value of the K_{vis} is proportional to the electrical conductivity of the fluid due to the coupling between the induced voltage and the velocity profile.
The high values of K_{vis} compared to the values of K_I lead to a low level of torque provided by the actuator. Furthermore the torque is limited in time by the total current that can be fed by the power subsystem.

8.2 Ideal Liquid

In order to understand the influence of the electric conductivity on the performances of the device, the values of K_{vis} have been computed for different electrical conductivities of the liquid together with the power consumption $\tilde{P}$ and the generated torque $\tilde{T}$. The values are calculated for a liquid with density $\rho = 1000$ Kg/m^3 and viscosity $\mu = 10^{-3}$ $Pa\ s$; the magnetic field is set to $B_0 = 1$ T.

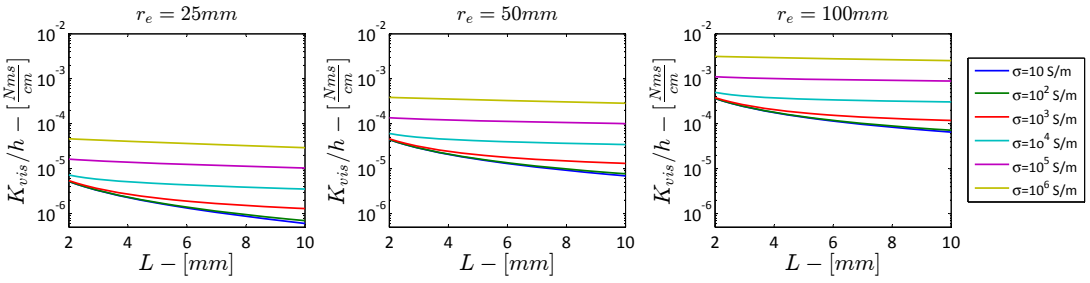

Figure 8.6: *K_{vis} function of L for $\sigma = 10 \div 10^6$ S/m and 3 different outer radii $r_e = 25, 50, 100mm$. $B_0 = 1.0$ T. $\rho = 1000$ Kg/m^3.*

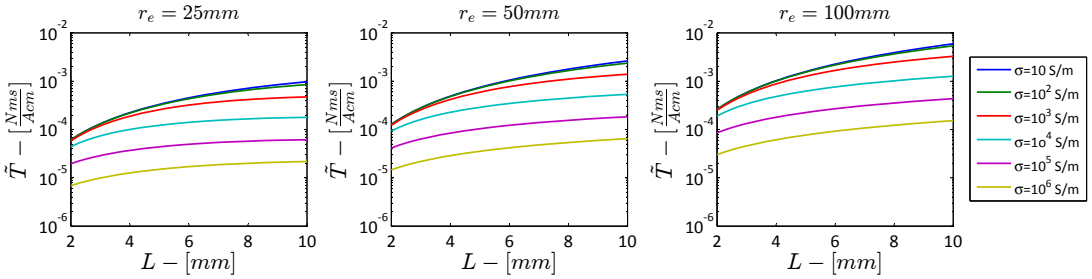

Figure 8.7: *Torque function of L for $\sigma = 10 \div 10^6$ S/m and 3 different outer radii $r_e = 25, 50, 100mm$. $B_0 = 1.0$ T. $\rho = 1000$ Kg/m^3.*

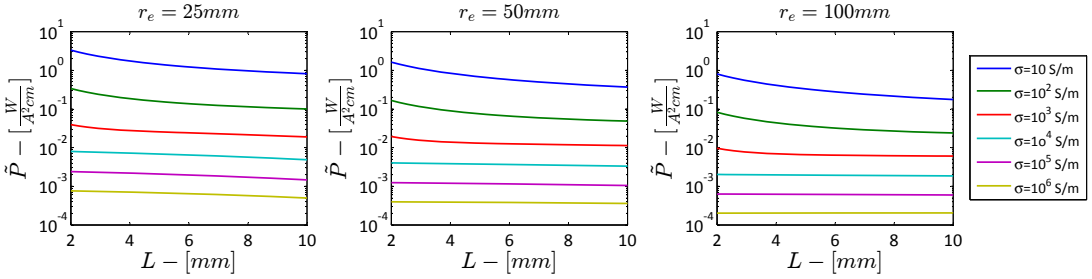

Figure 8.8: *Power consumption function of L for $\sigma = 10 \div 10^6$ S/m and 3 different outer radii $r_e = 25, 50, 100mm$. $B_0 = 1.0$ T. $\rho = 1000$ Kg/m^3.*

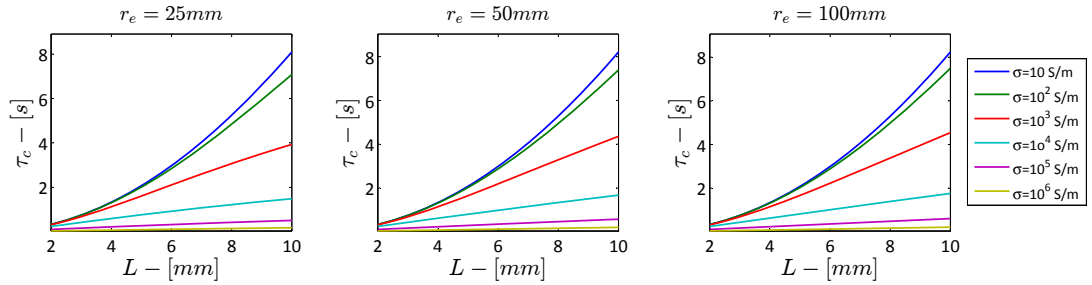

Figure 8.9: *Characteristic time function of L for $\sigma = 10 \div 10^6$ S/m and 3 different outer radii $r_e = 25, 50, 100mm$. $B_0 = 1.0$ T. $\rho = 1000$ Kg/m^3.*

From Figures(8.6) and (8.7) it is possible to see the improving in the performances for low conducting fluid. Due to the low coupling between the velocity

and the magnetic field, the generated torque for a low conductive fluid become bigger of about two orders of magnitude with respect to an high conductive fluid. As expected, the power consumption has an opposite trend but its maximum value is anyway around $1W$ if an electric current of $1A$ is applied, Figure(8.8).
For high conductive fluids the estimation of the parameters is expected to be quite accurate due to the fact that the length of the boundary layers on the upper and bottom walls scale as $\delta_{Sh} \sim 1/\sqrt{Ha}$ while the boundary layers on the lateral surfaces scale as $\delta_{Ha} \sim 1/Ha$. For high Ha these two characteristic length can differ of one order of magnitude, then the error due to the neglection of the Shercliff layers, next to the armatures, is low.
On the other side the prediction of K_{vis} and the available torque could be regarded as not accurate for very low conductive fluid due to the reason that the Shercliff layers on the upper and bottom surface of the torus are in this case of the same order of magnitude as the Hartmann layers on the lateral walls of the torus. Anyway the density of an hypothetical low conductive fluid is expected to be low if compared with the density of a liquid metal. This implies that in order to have the same moment of inertia for low conductive fluid, we need to increase the height of the cross section if the working fluid has low electric conductivity. This implies again that the viscous shear on the top and bottom boundaries could be neglectable with respect of the viscous shear acting on the lateral cylindrical surfaces of the device.

8.3 Comparison with commercial reaction wheels designed for Cubesats

In this section, in order exploits the performances of the proposed Liquid Wheel, a comparison with three commercial reaction wheels designed for Cubesats will be presented. The sizing of the Liquid Wheel has been made with the purpose to have a final mass of conductive liquid comparable with the overall mass of the commercial classical reaction wheels taken as example. Furthermore the dimensions of the simulated Liquid Wheel have been made suitable for the Cubesat Standard. The three reaction wheels are available at www.isispace.nl and represent three different classes of reaction wheels ac-

cording to the torque provided. The selected working fluid for the simulated Liquid Wheel is Mercury, even if the advantage to use an *ad-hoc* conductive liquid has been commented and proved in the dedicated section of this chapter. The comparison is shown in the table 8.1.

	CubeWheel S	CubeWheel M	CubeWheel L
Weight	55 g	130 g	200 g
Lenght	28 mm	46 mm	57 mm
Width	31 mm	46 mm	57 mm
Height	26 mm	31.5 mm	31.5 mm
Torque	0.23 mNm	1.0 mNm	2.3 mNm
Angular Momentum	1.7 mNms	10 mNms	30 mNms
Power	< 600 mW	< 1000 mW	< 2200 mW
	MHD Wheel S	MHD Wheel M	MHD Wheel L
Weight (Liquid)	64 g	124 g	181 g
Outer Radius	45 mm	45 mm	45 mm
Inner Radius	43 mm	41 mm	39 mm
Height	10 mm	10 mm	10 mm
Torque(@1A/s)	0.18 mNm	0.36 mNm	0.53 mNm
Angular Momentum(@1A)	0.18 mNms	0.36 mNms	0.53 mNms
Power(@1A)	0.55 mW	0.54 mW	0.52 mW

Table 8.1: *Comparison between classical Reaction Wheels for Cubesats and Liquid Wheels*

The values listed in table 8.1 show that the proposed actuator, even providing a torque slightly smaller than the classical reaction wheels, is characterized by a power consumption that is three orders of magnitude less than the classical reaction wheels. The power consumption proposed do not take into account the efficiency of the power board that have to drive the actuator, but shows only the power consumption of the Liquid Wheel across its electric armatures. The angular momentum provided by the Liquid Wheel is computed for a current of $1A$. In general the possibility to increase the current supplied to the actuator, leads to a proportional increase of the provided angular momentum. But this aspect is constrained by the capability of the power board.
What is evident in the numbers proposed is that the Liquid Wheel can provide comparable performances of small reaction wheels, similar to the ones in table 8.1. As the required torque or angular momentum increase the performance of the classical reaction become hard to meet by a Liquid Wheel.
Even if in paragraph 7.12 it has been shown that the behaviour of the Liquid

wheel is characterized by non-linearities in the vicinity of the null angular velocity, the Liquid Wheel in this zone is not characterized by discontinue torque, as for the classical reaction wheels. This aspect, together to the possibility to provide a clean torque, not influenced by ripple or mechanical noise, still represent positive aspects of the proposed actuator.

8.4 Conclusions

In this chapter the possibility to use an ideal electrically conductive liquid with low electric conductivity is evaluated. The results show that this can be a good solution in order to improve the performances of the device in terms of provided torque. Unfortunately such kind of liquid is not yet available. It should be the a non aqueous solution of electrolytes in order to avoid the the electrolysis phenomena and so the generation of hydrogen (H_2) and oxygen (O).

Chapter

8 Conclusions

A novel actuator for spacecraft attitude control with liquid flywheel has been studied. Two different configurations of the device with didtributed magnetic field have been studied on the base of the optimization of dimensionless moment of inertia and the minimization of the viscous shear.

In order to estimate the performances of this actuator, a 2-dimensional Finite Differences Hybrid Model (FDHM) has been developed on the base of the MHD set equation under the hypothesis of low Magnetic Reynolds. The model solves numerically the time dependent axially symmetric problem of a conductive liquid rotating in a torus with rectangular cross section due to the interaction of a radial magnetic field and an axial electric field. The electric side of the problem has been solved by means of the node method applied to a network of electric resistances and voltage generators representing the back electromotive voltage induced by the spinning liquid through the magnetic field. The fluid-dynamics side of the problem has been solved using a Crank-Nicolson method over a non uniform and collocated grid. The grid generator has been written to be sensitive to the Hartmann number of the problem.

The FDHM has shown great accuracy over a wide range of geometrical and physical quantities and the analysis of the results has helped a deeper understanding of the device and its performances related to the dimension of the torus, the intensity of the magnetic field, the conductivity of the working fluid and the different drive chosen.

A Lumped Parameter Model (LPM) has been then derived using two stationary mono and bi-dimensional analytical solution of the MHD set of equations under the hypothesis of low Magnetic Reynolds. The LPM has been compared with the results obtained with the FDHM, showing good agreement in the estimation of the coefficients of the model.

The possibility to use an ideal fluid different from liquid metal has been evaluated by means of the LPM. Due to the low coupling between the velocity and

the magnetic field, the generated torque of a device using a low conductive fluid is about two orders of magnitude bigger than a device using a high conductive fluid. As expected, the power consumption has an opposite trend.

Appendix

A The Crank-Nicolson Method

The Crank-Nicolson method is a well-known finite difference method for the numerical integration of the heat equation and closely related partial differential equations.
It is an implicit second-order method in time, it can be written as an implicit Runge-Kutta method, and it is numerically stable. The method was developed by John Crank and Phyllis Nicolson in the mid 20th century.
Considerind a $1D$ partial differential equation:

$$\frac{\partial u}{\partial t} = F\left(u,\, x,\, \frac{\partial u}{\partial x},\, \frac{\partial^2 u}{\partial x^2}\right) \tag{A.0.1}$$

the time derivative on the left hand side can be replaced with a forward finite difference:

$$\left.\frac{\partial u}{\partial t}\right|_{j,n} \approx \frac{u_j^{n+1} - u_j^n}{\Delta t}. \tag{A.0.2}$$

The Crank-Nicolson method appears to be a combination of the forwards and backwards Euler method at two different steps in time, n an $n+1$.

$$\frac{u_i^{n+1} - u_i^n}{\Delta t} = \frac{1}{2}\left[F_i^{n+1}\left(u,\, x,\, \frac{\partial u}{\partial x},\, \frac{\partial^2 u}{\partial x^2}\right) + F_i^n\left(u,\, x,\, \frac{\partial u}{\partial x},\, \frac{\partial^2 u}{\partial x^2}\right)\right] \tag{A.0.3}$$

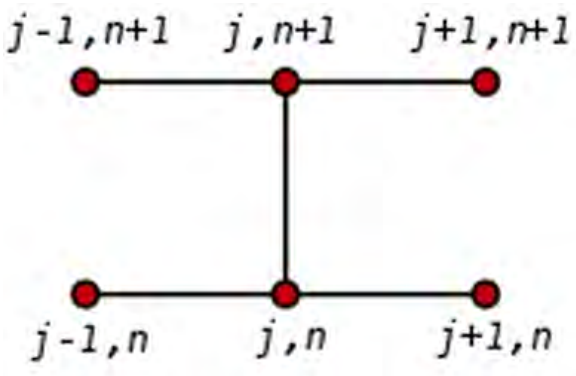

Figure A.1: *Crank-Nicolson stencil for a* $1D$ *problem*

As the quantities defined at the time step $n+1$ are unknown, in order to update the solution at the time $n+1$, as algebraic system must be solved:

$$u^{n+1} = Au^n + B \tag{A.0.4}$$

The shape of the matrix A depends on the studied partial differential equation and on the chosen finite difference scheme used to approximate the spatial part of the partial differential equation. The vector B is not null if the source term of the differential equation is not equal to zero.

Appendix

B

Results: FDHM for $\sigma = 10^2\ S/m$

B.1 Current Drive

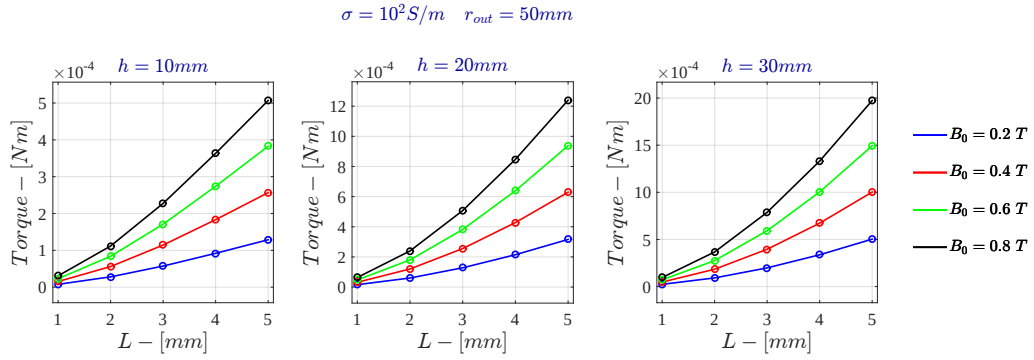

Figure B.1: *Current Drive - Torque for* $\sigma = 10^2$ *S/m - FDHM*

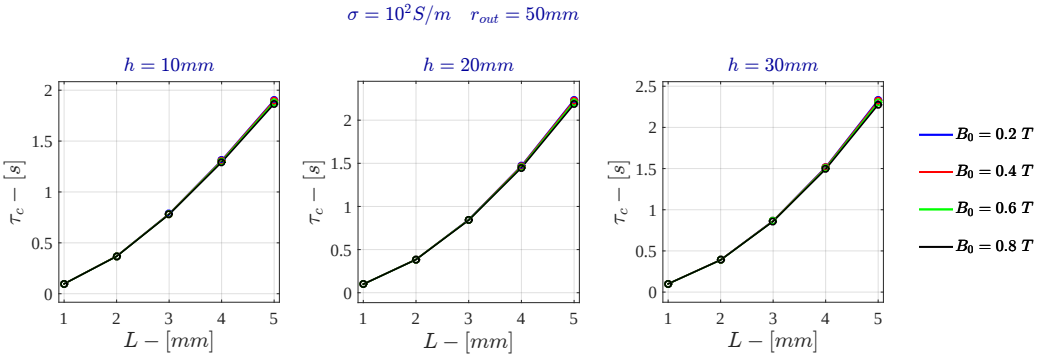

Figure B.2: *Current Drive - Characteristic time for* $\sigma = 10^2$ *S/m - FDHM*

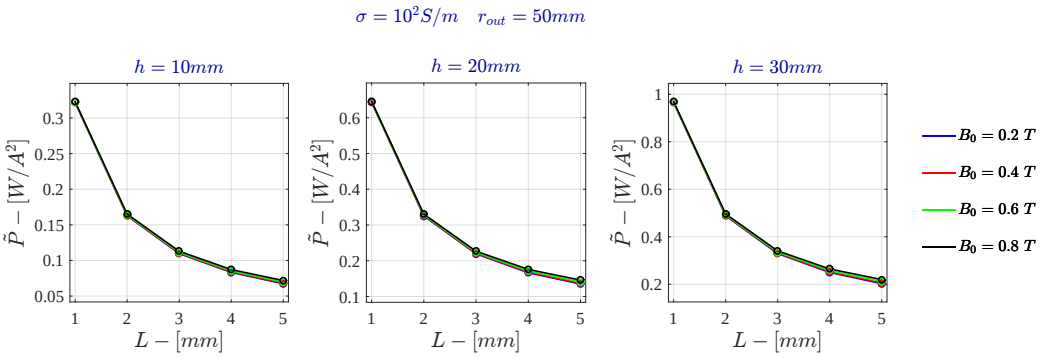

Figure B.3: *Current Drive - Specific Power for* $\sigma = 10^2$ *S/m - FDHM*

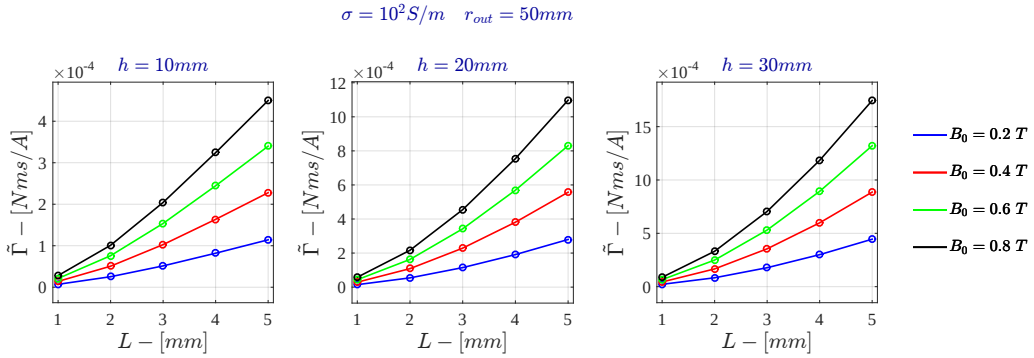

Figure B.4: *Current Drive - Specific Angular Momentum for* $\sigma = 10^2\ S/m$ *- FDHM*

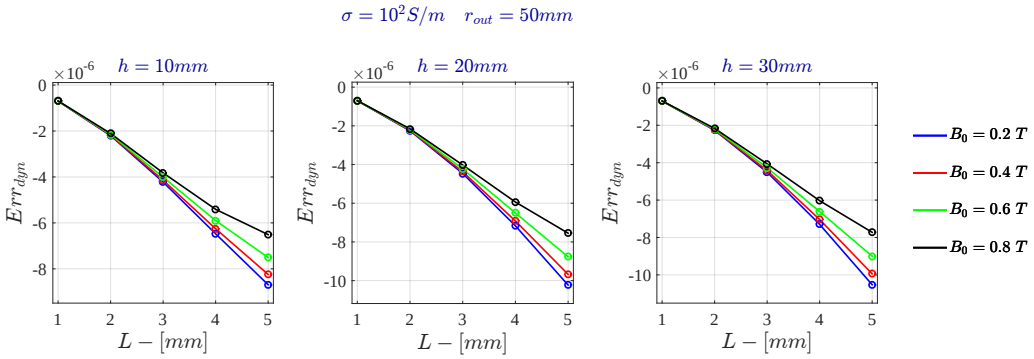

Figure B.5: *Current Drive - Relative Dynamic Error for* $\sigma = 10^2\ S/m$ *- FDHM*

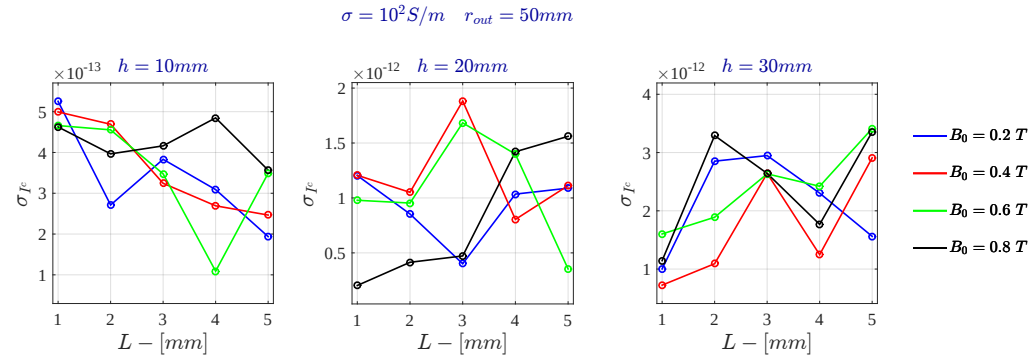

Figure B.6: *Current Drive - Standard deviation of the electric current for* $\sigma = 10^2\ S/m$ *- FDHM*

B.2 Voltage Drive

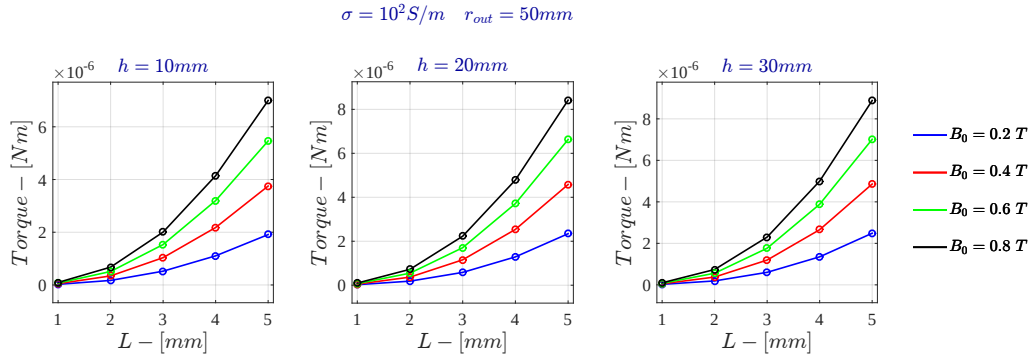

Figure B.7: *Voltage Drive - Torque for* $\sigma = 10^2\ S/m$ *- FDHM*

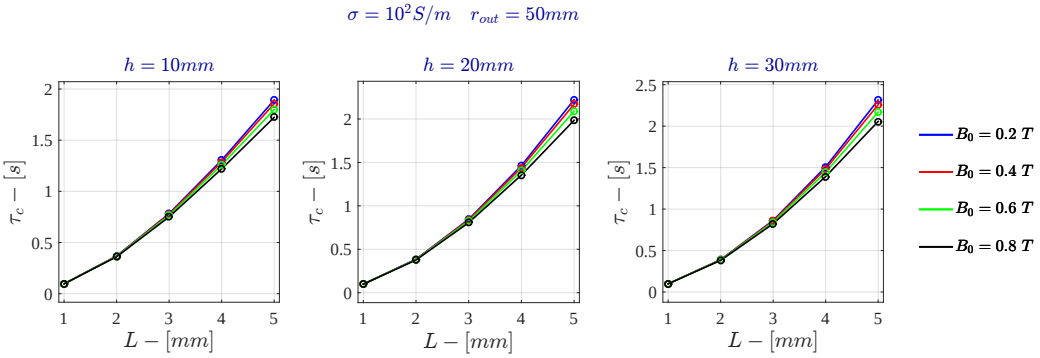

Figure B.8: *Voltage Drive - Characteristic time for* $\sigma = 10^2\ S/m$ *- FDHM*

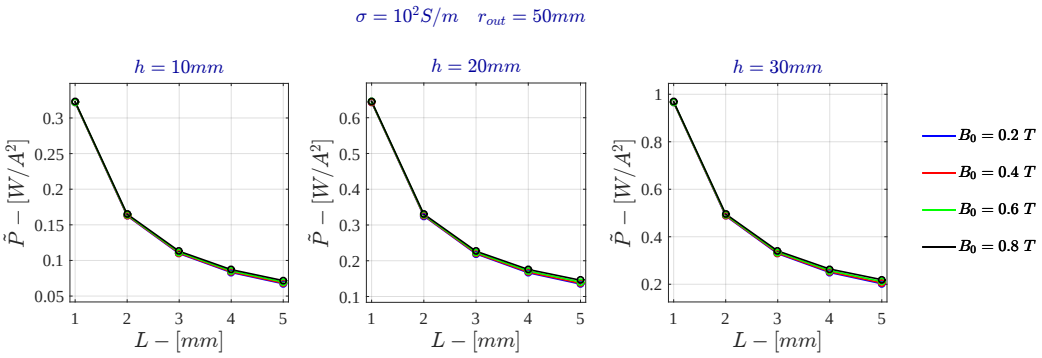

Figure B.9: *Voltage Drive - Specific Power for* $\sigma = 10^2\ S/m$ *- FDHM*

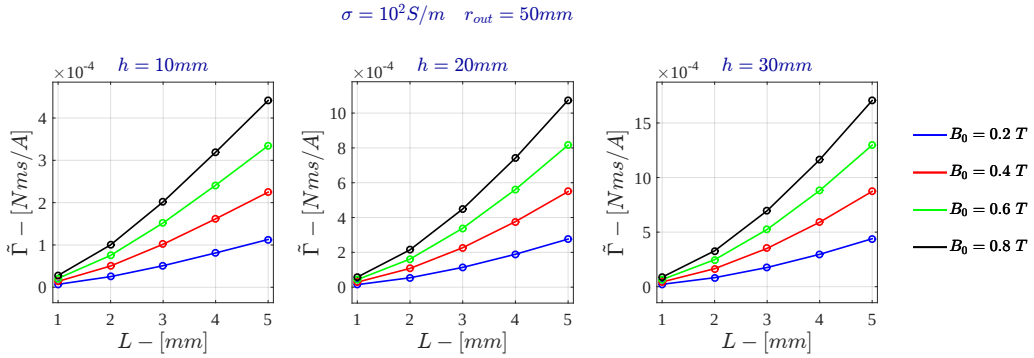

Figure B.10: *Voltage Drive - Specific Angular Momentum for* $\sigma = 10^2\ S/m$ *- FDHM*

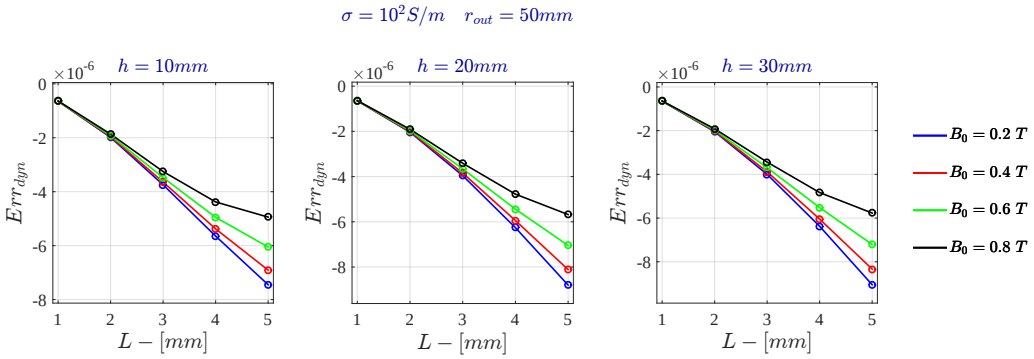

Figure B.11: *Voltage Drive - Relative Dynamic Error for* $\sigma = 10^2\ S/m$ *- FDHM*

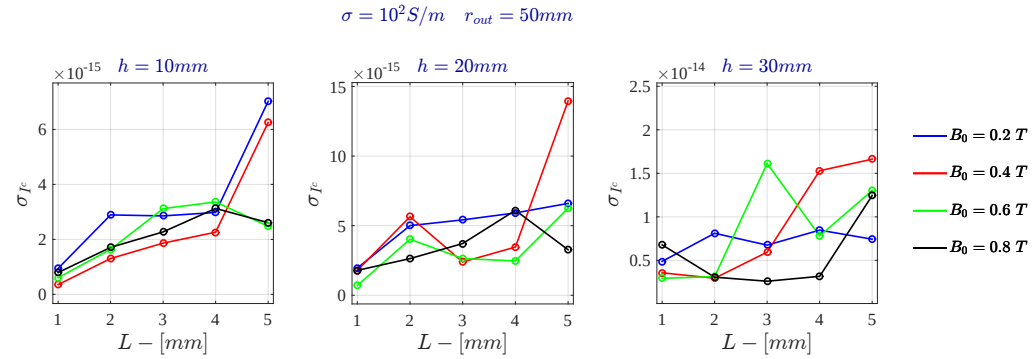

Figure B.12: *Voltage Drive - Standard deviation of the electric current for* $\sigma = 10^2\ S/m$ *- FDHM*

Appendix

C

Results: FDHM for $\sigma = 10^3\ S/m$

C.1 Current Drive

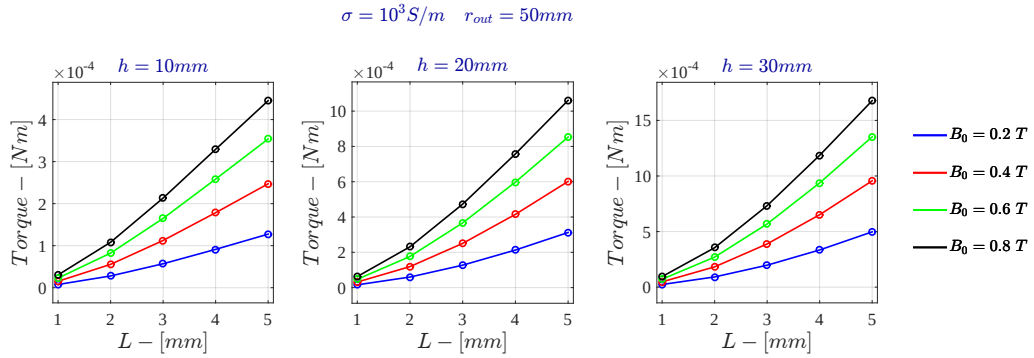

Figure C.1: *Current Drive - Torque for* $\sigma = 10^3\ S/m$ *- FDHM*

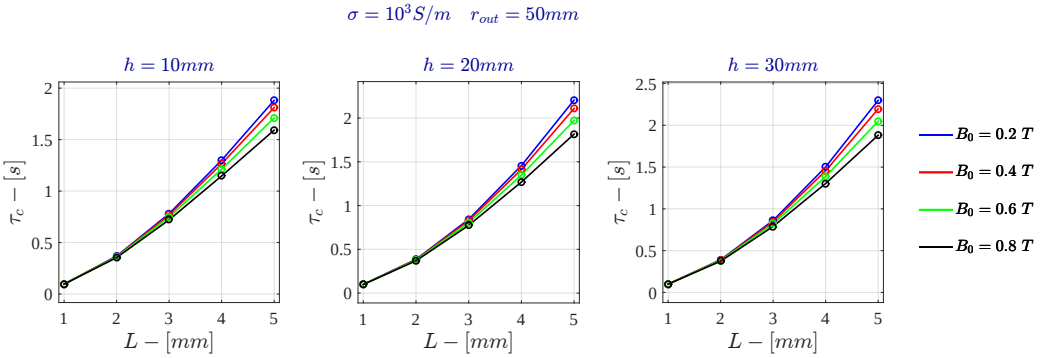

Figure C.2: *Current Drive - Characteristic time for* $\sigma = 10^3\ S/m$ *- FDHM*

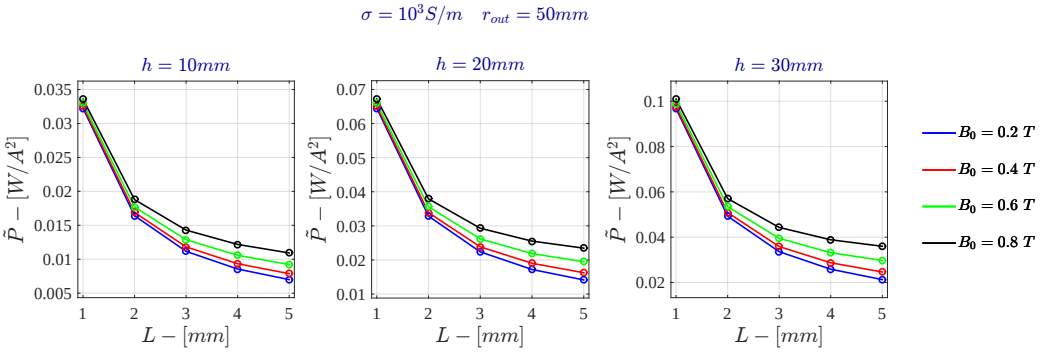

Figure C.3: *Current Drive - Specific Power for* $\sigma = 10^3\ S/m$ *- FDHM*

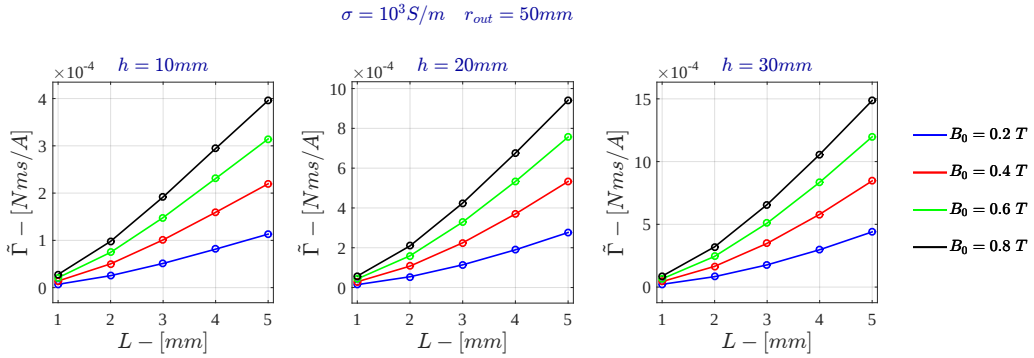

Figure C.4: *Current Drive - Specific Angular Momentum for* $\sigma = 10^3\ S/m$ *- FDHM*

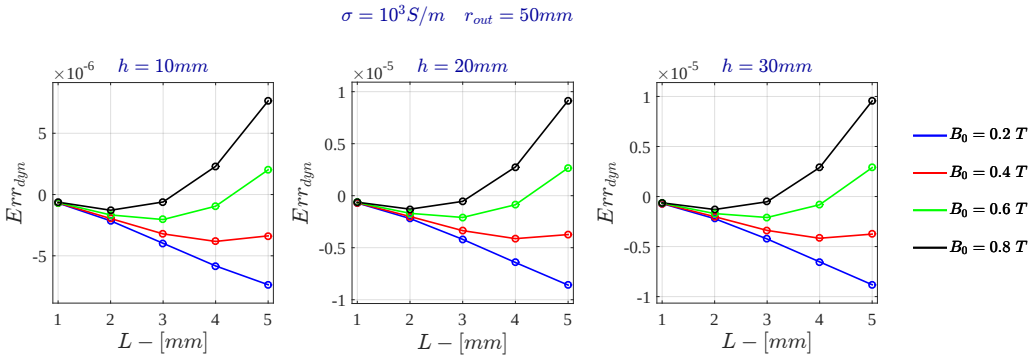

Figure C.5: *Current Drive - Relative Dynamic Error for* $\sigma = 10^3\ S/m$ *- FDHM*

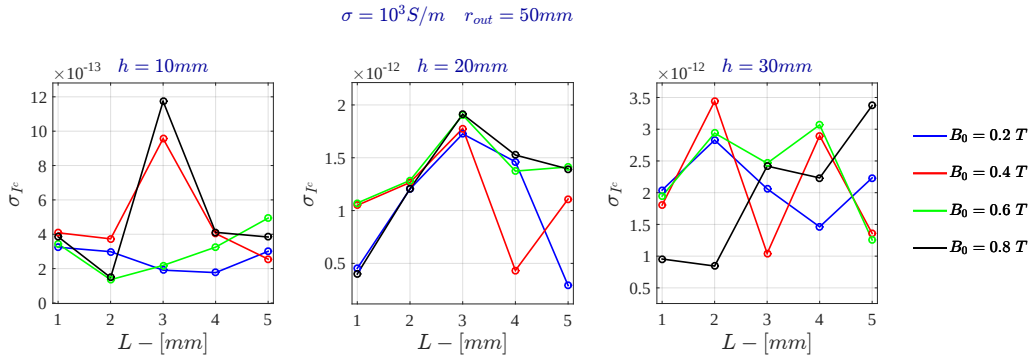

Figure C.6: *Current Drive - Standard deviation of the electric current for* $\sigma = 10^3\ S/m$ *- FDHM*

C.2 Voltage Drive

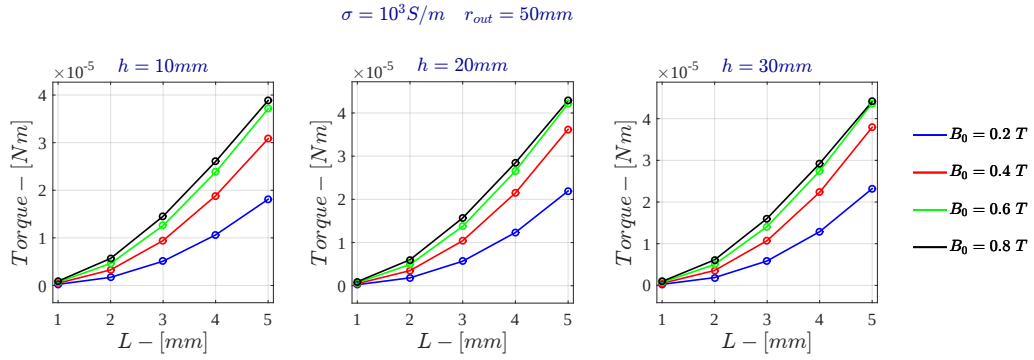

Figure C.7: *Voltage Drive - Torque for* $\sigma = 10^3$ *S/m - FDHM*

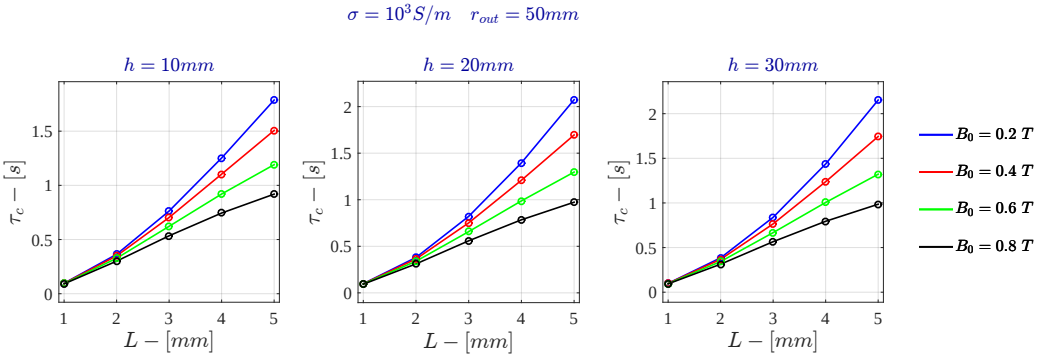

Figure C.8: *Voltage Drive - Characteristic time for* $\sigma = 10^3$ *S/m - FDHM*

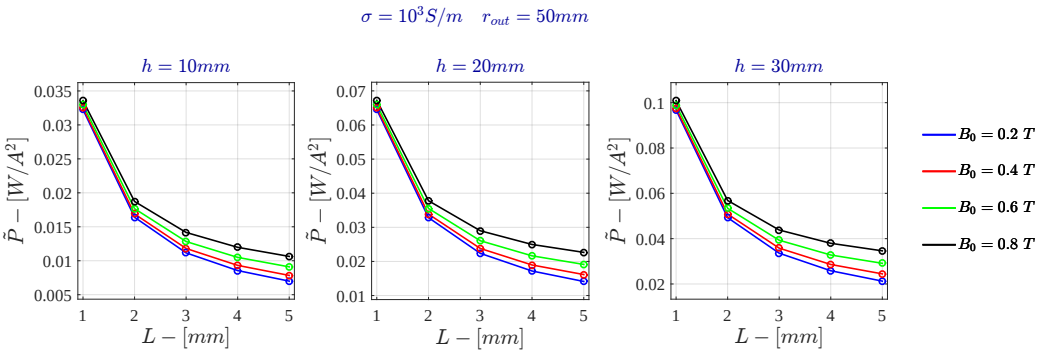

Figure C.9: *Voltage Drive - Specific Power for* $\sigma = 10^3$ *S/m - FDHM*

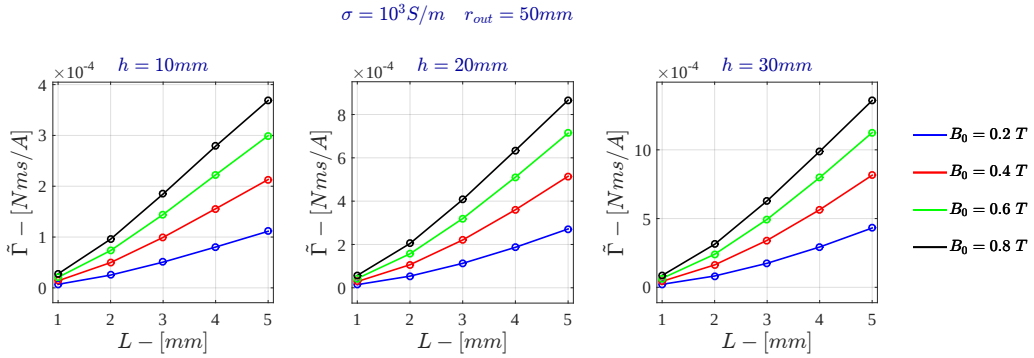

Figure C.10: *Voltage Drive - Specific Angular Momentum for* $\sigma = 10^3\ S/m$ *- FDHM*

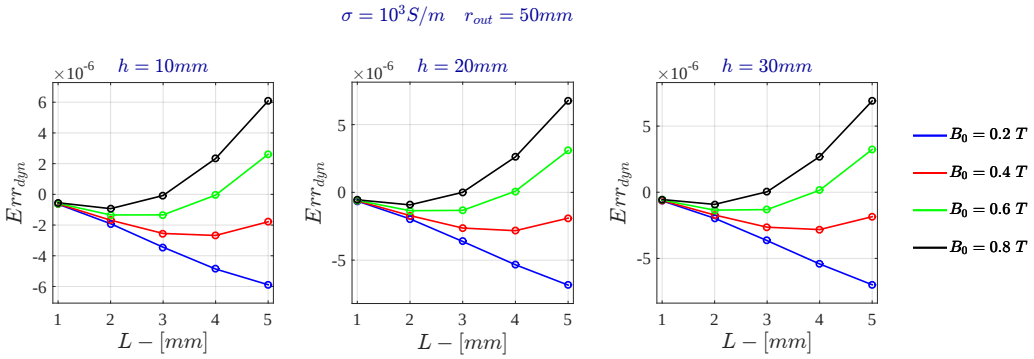

Figure C.11: *Voltage Drive - Relative Dynamic Error for* $\sigma = 10^3\ S/m$ *- FDHM*

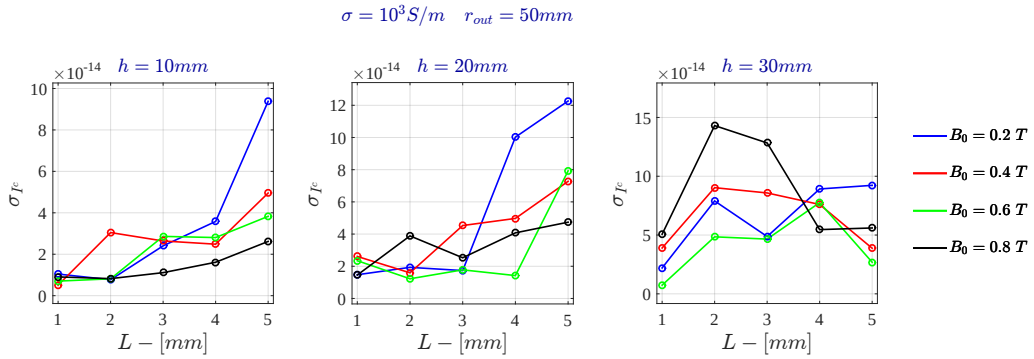

Figure C.12: *Voltage Drive - Standard deviation of the electric current for* $\sigma = 10^3\ S/m$ *- FDHM*

Appendix

D

Results: FDHM for $\sigma = 10^4\ S/m$

D.1 Current Drive

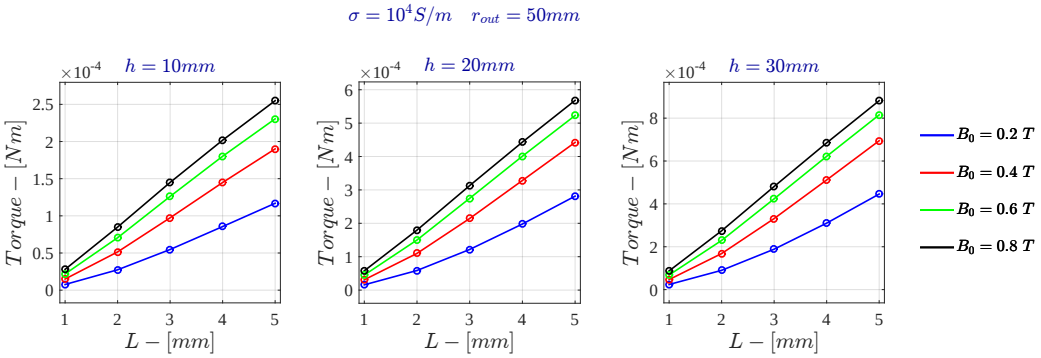

Figure D.1: *Current Drive - Torque for* $\sigma = 10^4$ S/m *- FDHM*

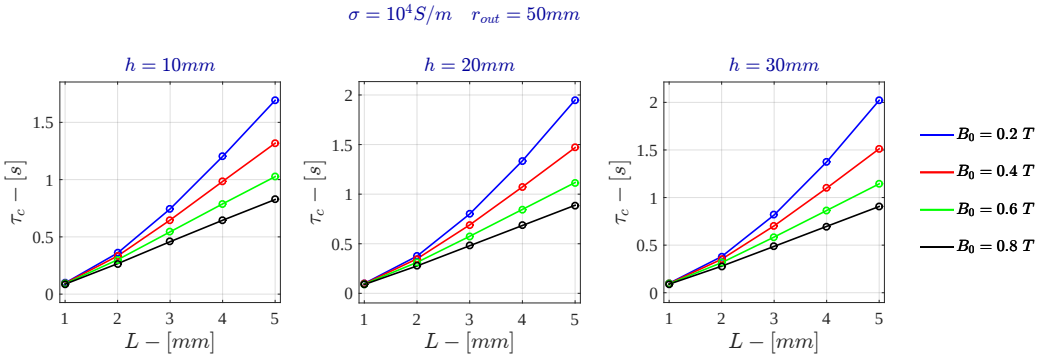

Figure D.2: *Current Drive - Characteristic time for* $\sigma = 10^4$ S/m *- FDHM*

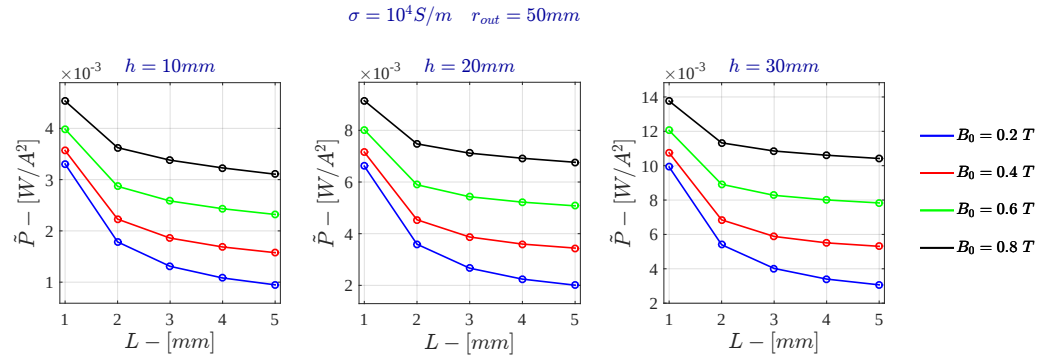

Figure D.3: *Current Drive - Specific Power for* $\sigma = 10^4$ S/m *- FDHM*

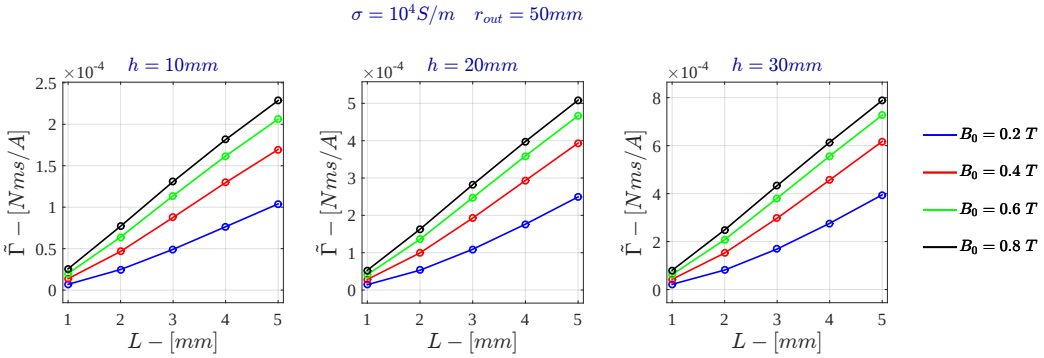

Figure D.4: *Current Drive - Specific Angular Momentum for* $\sigma = 10^4\ S/m$ *- FDHM*

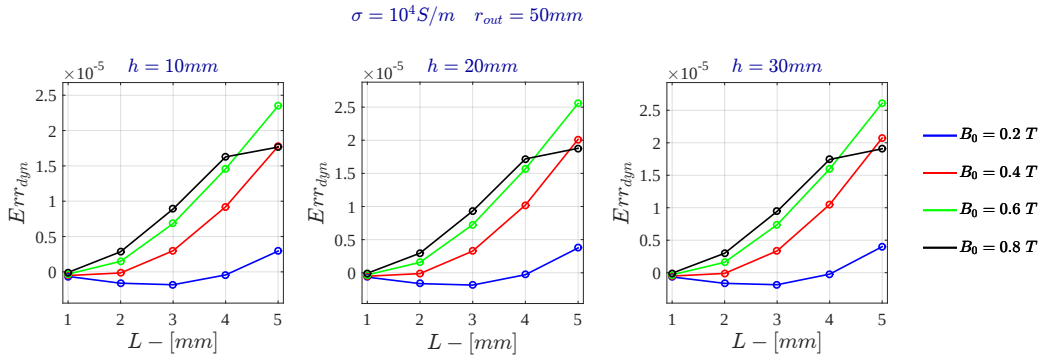

Figure D.5: *Current Drive - Relative Dynamic Error for* $\sigma = 10^4\ S/m$ *- FDHM*

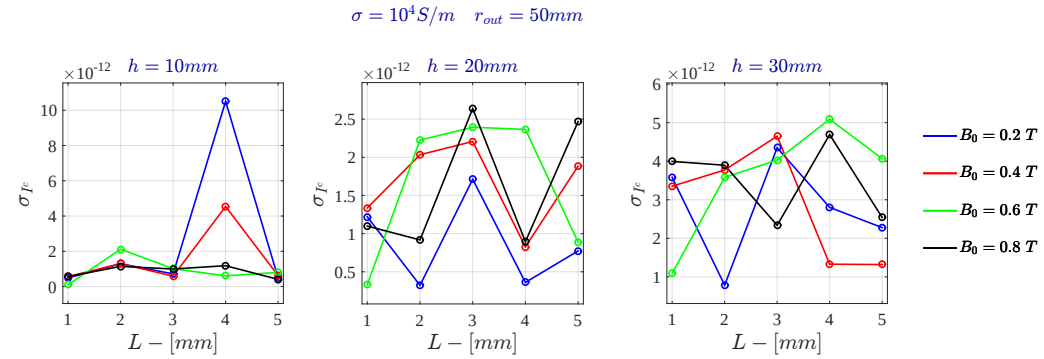

Figure D.6: *Current Drive - Standard deviation of the electric current for* $\sigma = 10^4\ S/m$ *- FDHM*

D.2 Voltage Drive

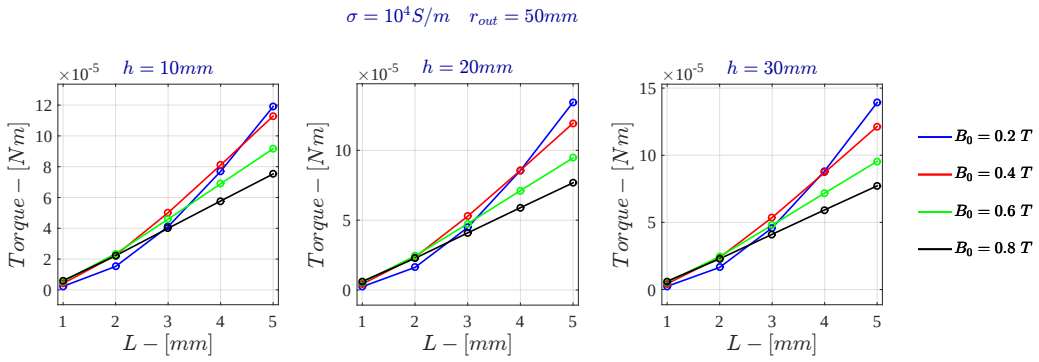

Figure D.7: *Voltage Drive - Torque for* $\sigma = 10^4\ S/m$ *- FDHM*

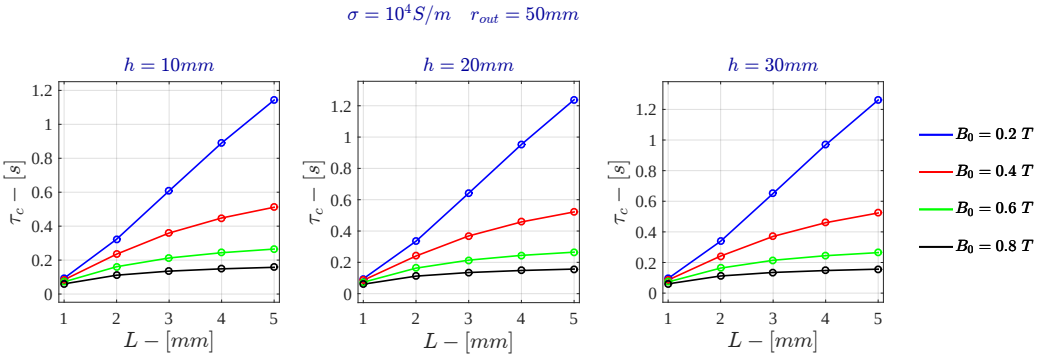

Figure D.8: *Voltage Drive - Characteristic time for* $\sigma = 10^4\ S/m$ *- FDHM*

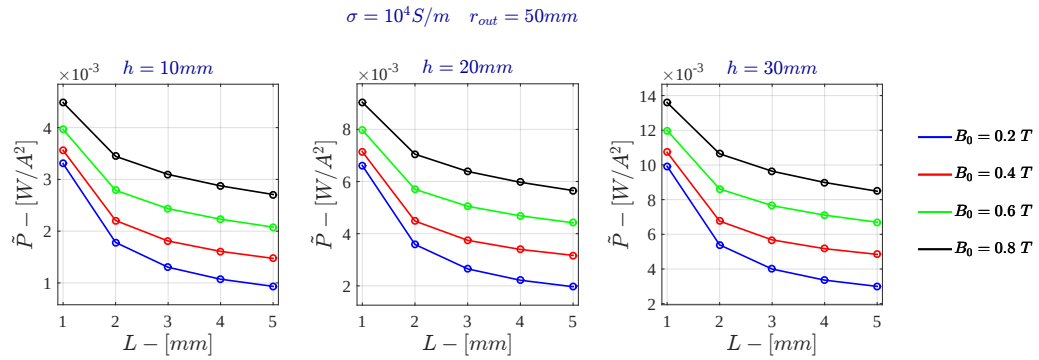

Figure D.9: *Voltage Drive - Specific Power for* $\sigma = 10^4\ S/m$ *- FDHM*

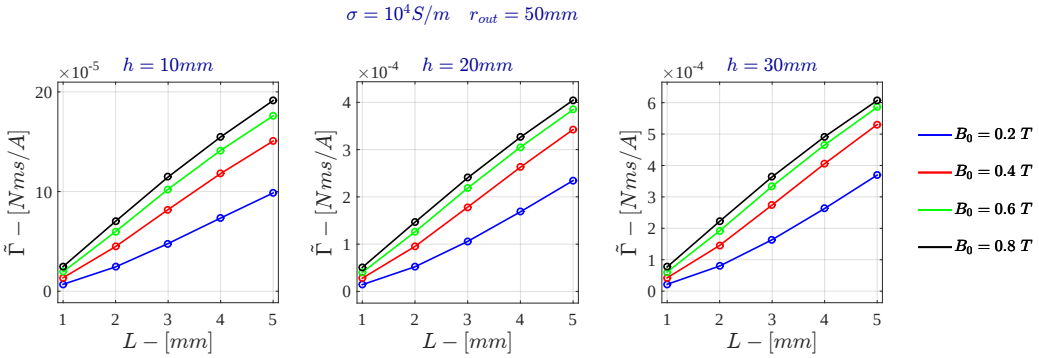

Figure D.10: *Voltage Drive - Specific Angular Momentum for* $\sigma = 10^4\ S/m$ *- FDHM*

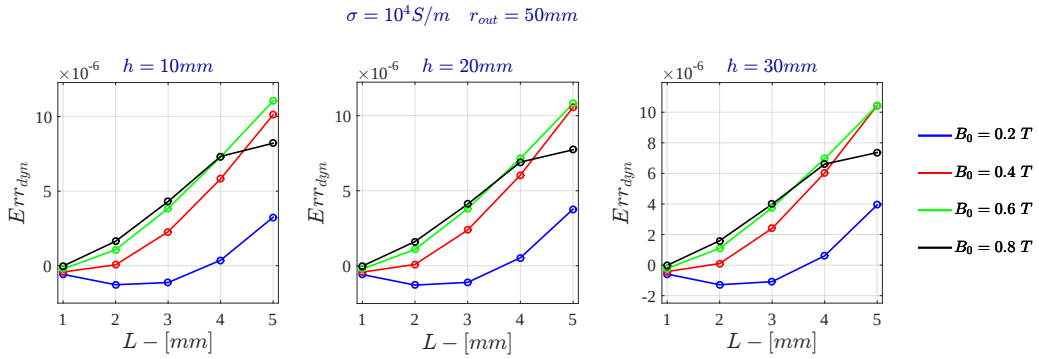

Figure D.11: *Voltage Drive - Relative Dynamic Error for* $\sigma = 10^4\ S/m$ *- FDHM*

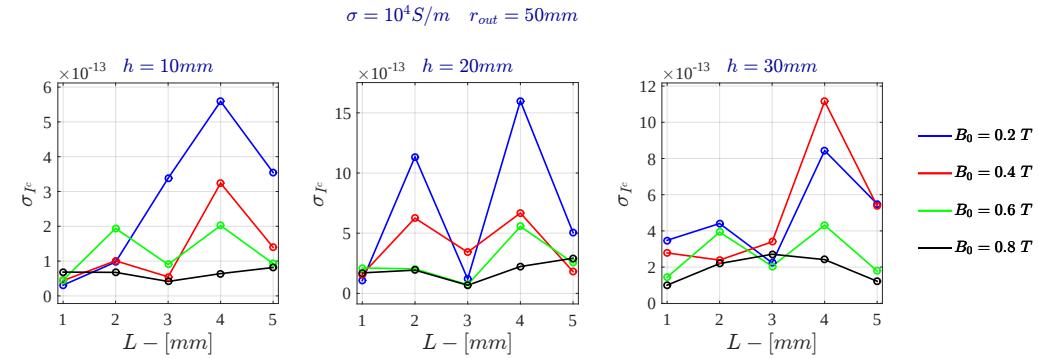

Figure D.12: *Voltage Drive - Standard deviation of the electric current for* $\sigma = 10^4\ S/m$ *- FDHM*

Appendix

E

Results: FDHM for $\sigma = 10^5\ S/m$

E.1 Current Drive

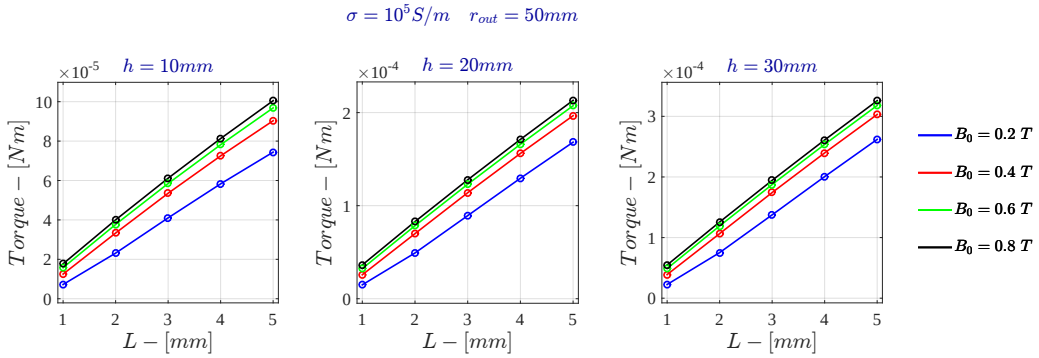

Figure E.1: *Current Drive - Torque for* $\sigma = 10^5\ S/m$ *- FDHM*

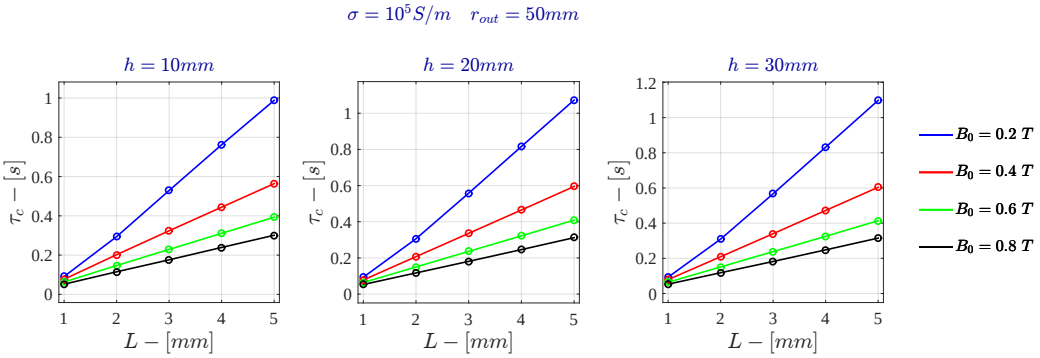

Figure E.2: *Current Drive - Characteristic time for* $\sigma = 10^5\ S/m$ *- FDHM*

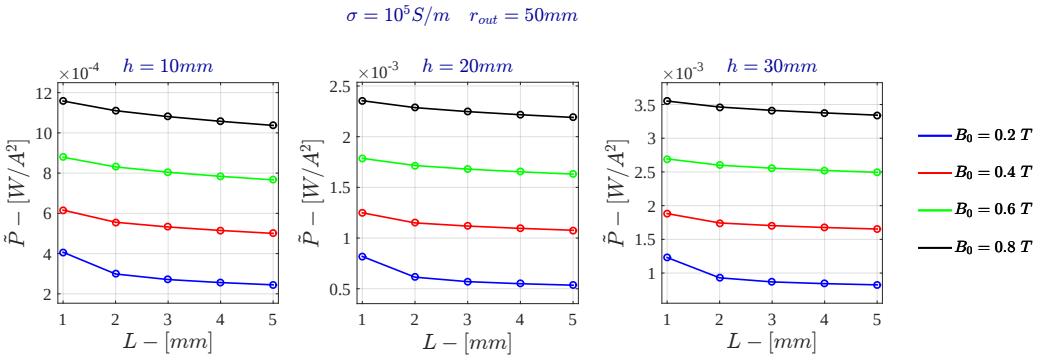

Figure E.3: *Current Drive - Specific Power for* $\sigma = 10^5\ S/m$ *- FDHM*

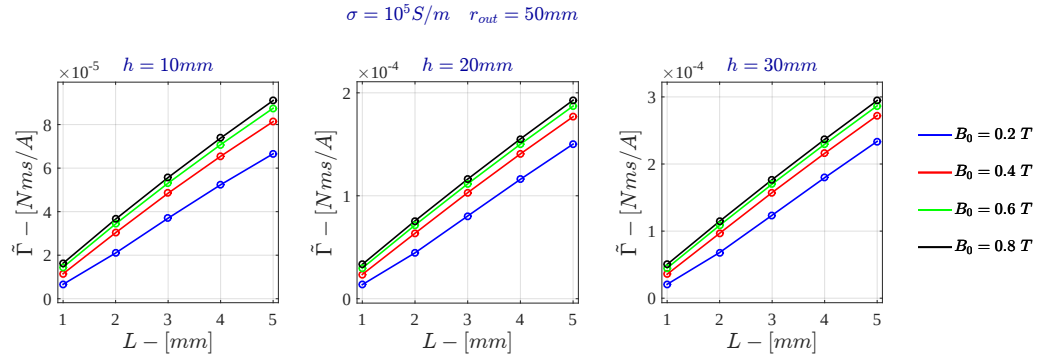

Figure E.4: *Current Drive - Specific Angular Momentum for* $\sigma = 10^5\ S/m$ *- FDHM*

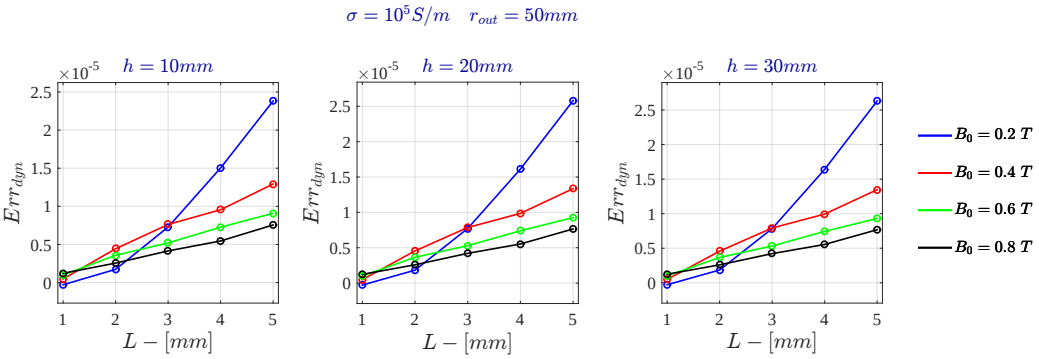

Figure E.5: *Current Drive - Relative Dynamic Error for* $\sigma = 10^5\ S/m$ *- FDHM*

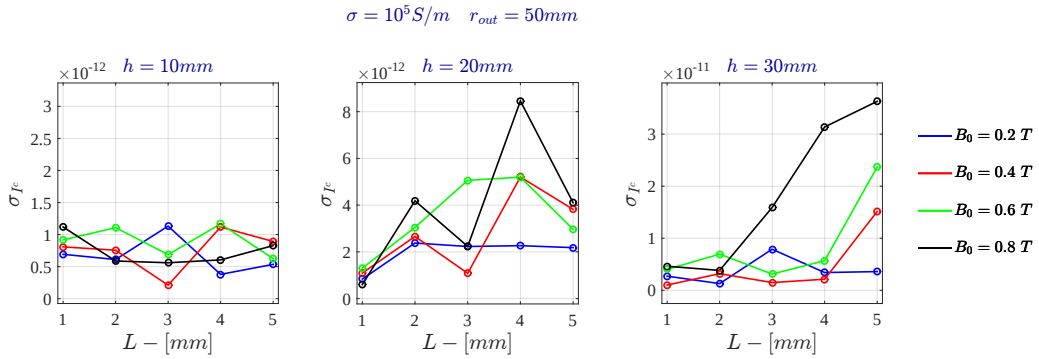

Figure E.6: *Current Drive - Standard deviation of the electric current for* $\sigma = 10^5\ S/m$ *- FDHM*

E.2 Voltage Drive

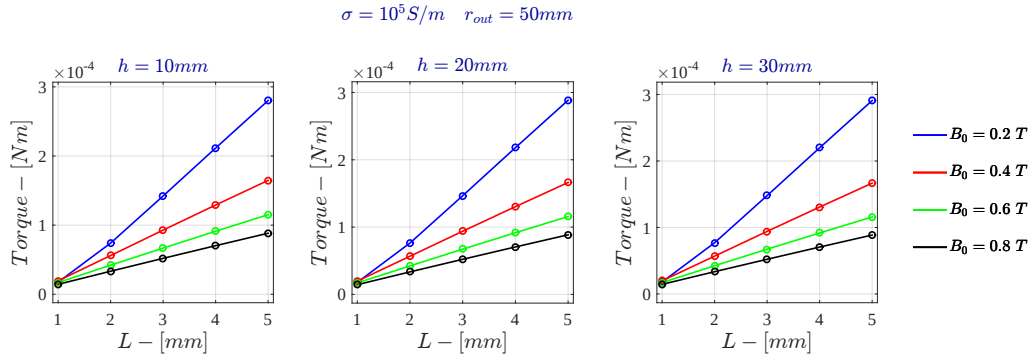

Figure E.7: *Voltage Drive - Torque for* $\sigma = 10^5\ S/m$ *- FDHM*

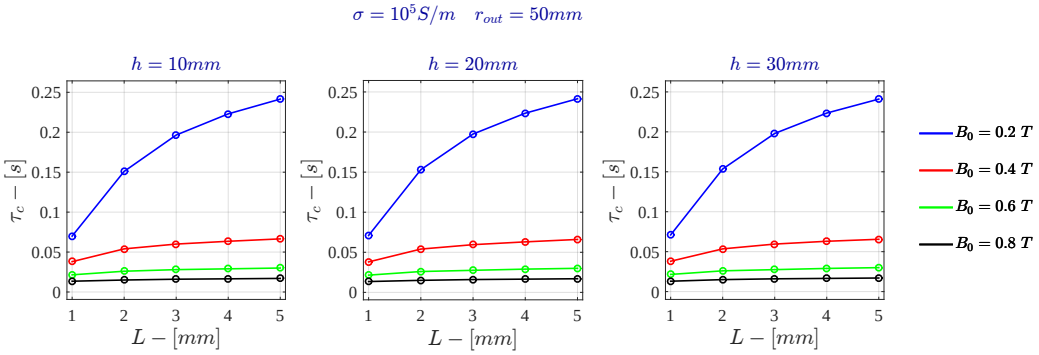

Figure E.8: *Voltage Drive - Characteristic time for* $\sigma = 10^5\ S/m$ *- FDHM*

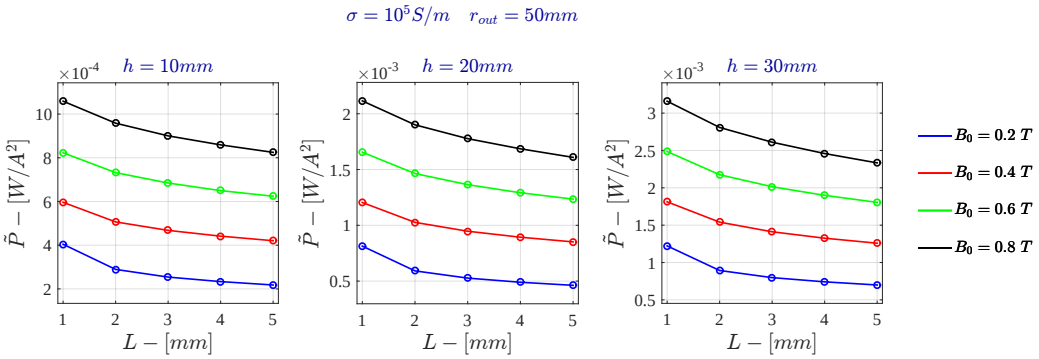

Figure E.9: *Voltage Drive - Specific Power for* $\sigma = 10^5\ S/m$ *- FDHM*

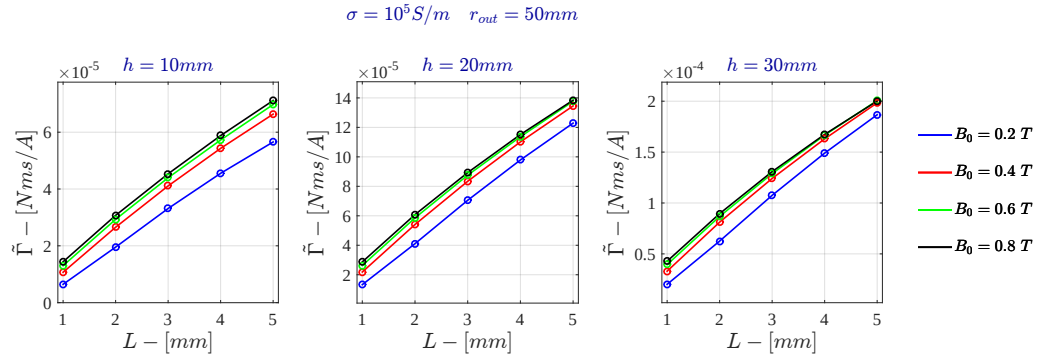

Figure E.10: *Voltage Drive - Specific Angular Momentum for* $\sigma = 10^5\ S/m$ *- FDHM*

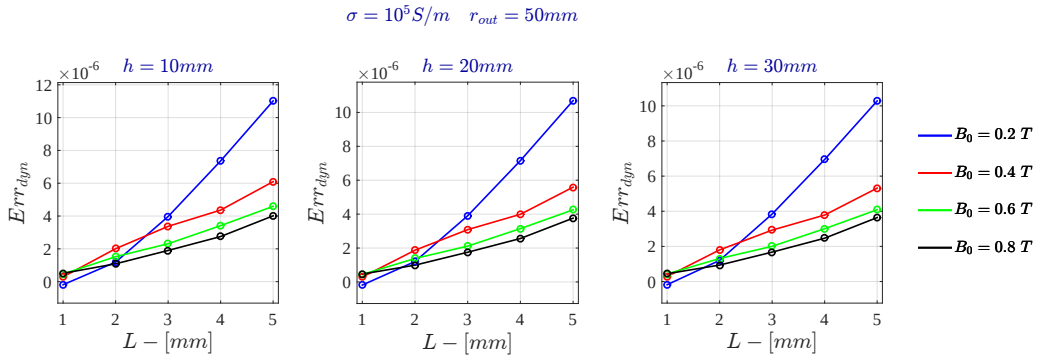

Figure E.11: *Voltage Drive - Relative Dynamic Error for* $\sigma = 10^5\ S/m$ *- FDHM*

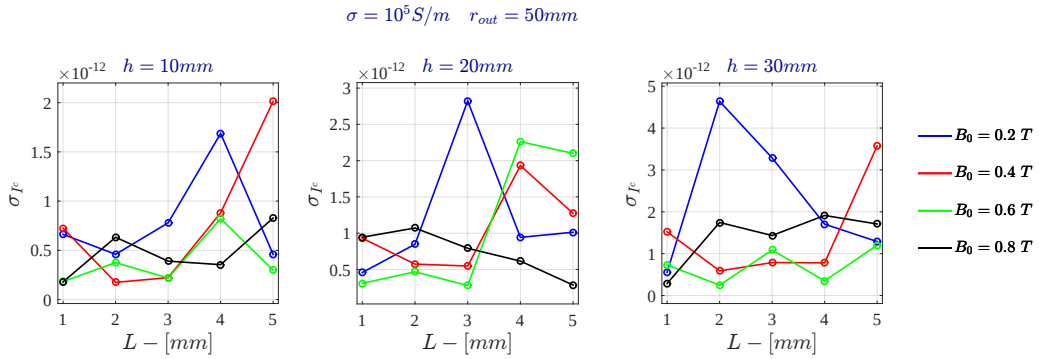

Figure E.12: *Voltage Drive - Standard deviation of the electric current for* $\sigma = 10^5\ S/m$ *- FDHM*

Appendix

F

Comparison between FDHM and LPM: $\sigma = 10^2\ S/m$

F.1 Monodimensional LPM - $\sigma = 10^2 S/m$

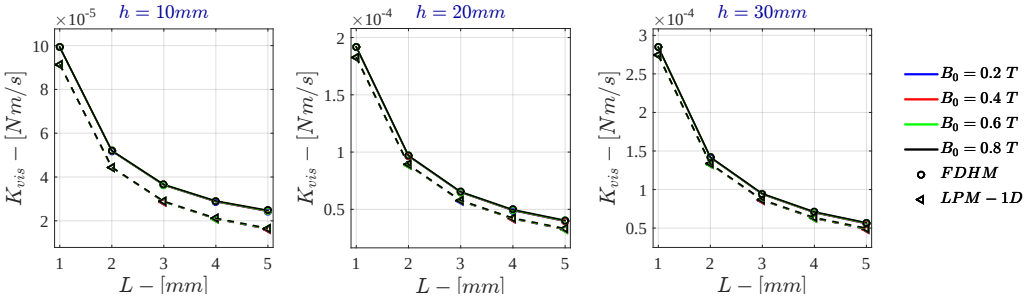

Figure F.1: *K_{vis} for $\sigma = 10^2$ S/m - $r_{out} = 50mm$ - Monodimensional LPM*

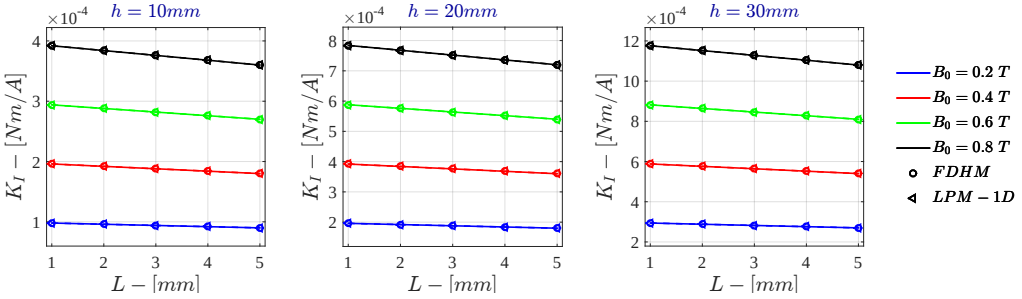

Figure F.2: *Monodimensional LPM*
K_I for $\sigma = 10^2$ S/m - $r_{out} = 50mm$

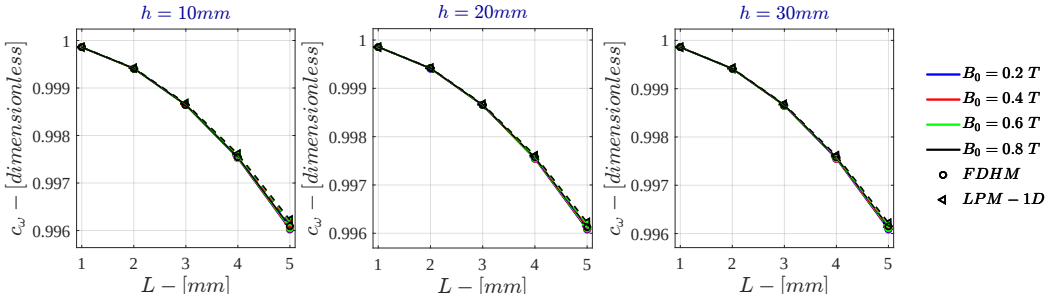

Figure F.3: *Monodimensional LPM*
c_ω for $\sigma = 10^2$ S/m - $r_{out} = 50mm$

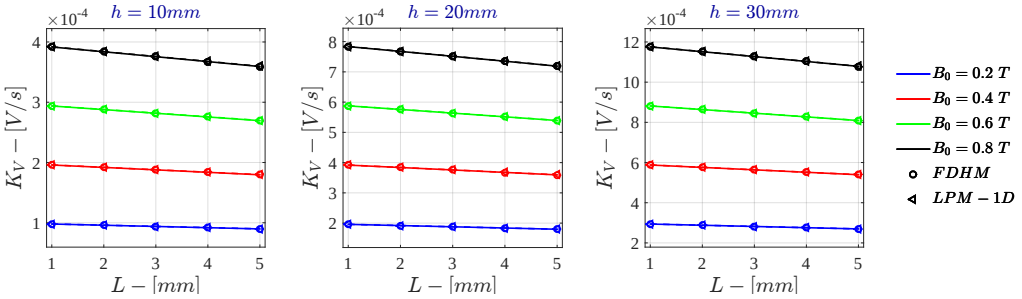

Figure F.4: *Monodimensional LPM*
K_V for $\sigma = 10^2$ S/m - $r_{out} = 50mm$

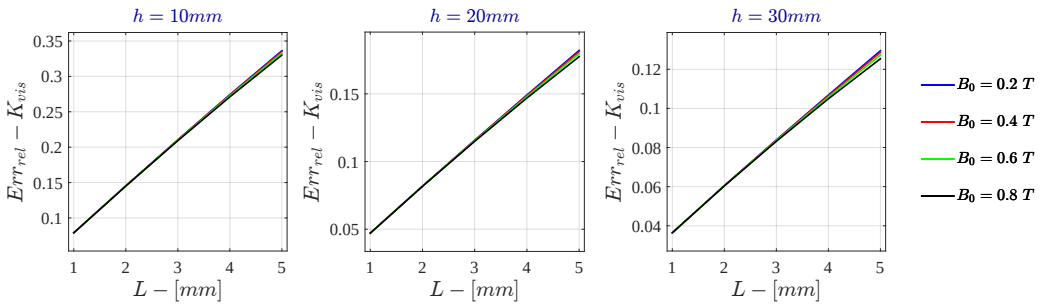

Figure F.5: *Monodimensional LPM*
Relative Error - K_{vis} for $\sigma = 10^2\ S/m$ - $r_{out} = 50mm$

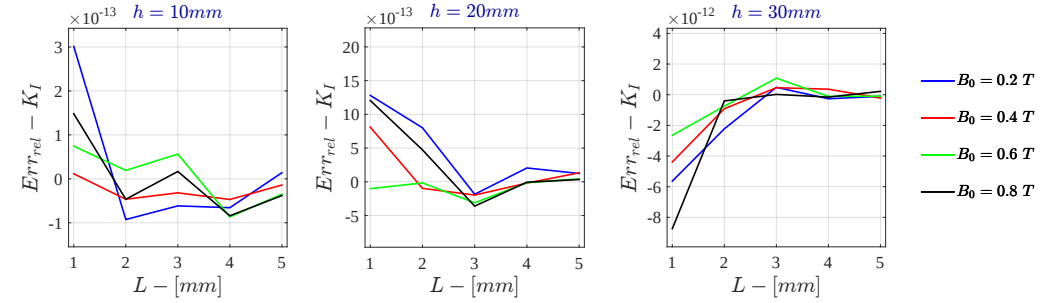

Figure F.6: *Monodimensional LPM*
Relative Error - K_I for $\sigma = 10^2\ S/m$ - $r_{out} = 50mm$

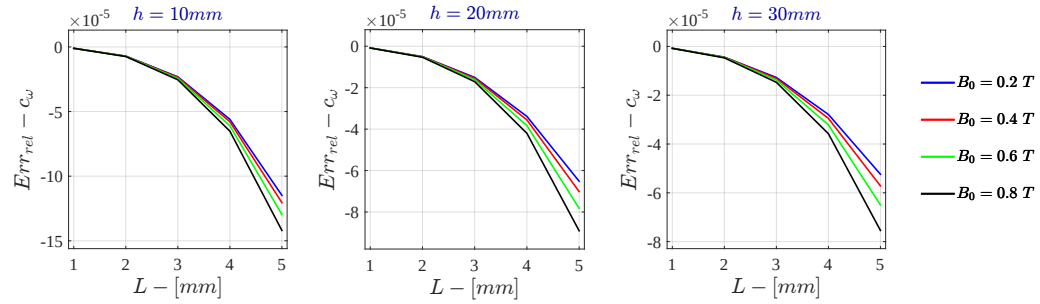

Figure F.7: *Monodimensional LPM*
Relative Error - c_ω for $\sigma = 10^2\ S/m$ - $r_{out} = 50mm$

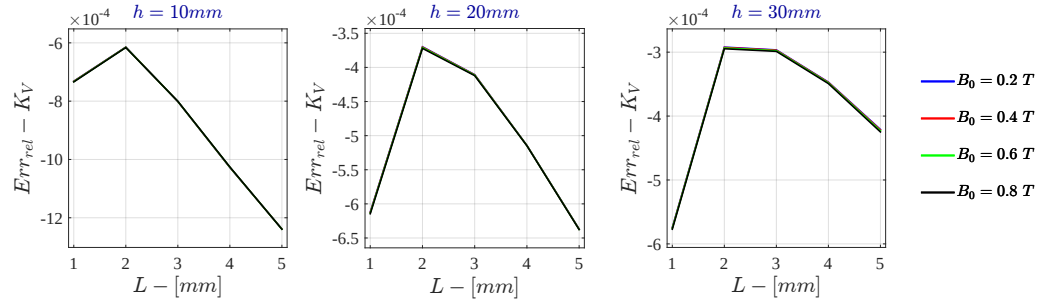

Figure F.8: *Monodimensional LPM*
Relative Error - K_V for $\sigma = 10^2\ S/m$ - $r_{out} = 50mm$

F.1.1 Current Drive

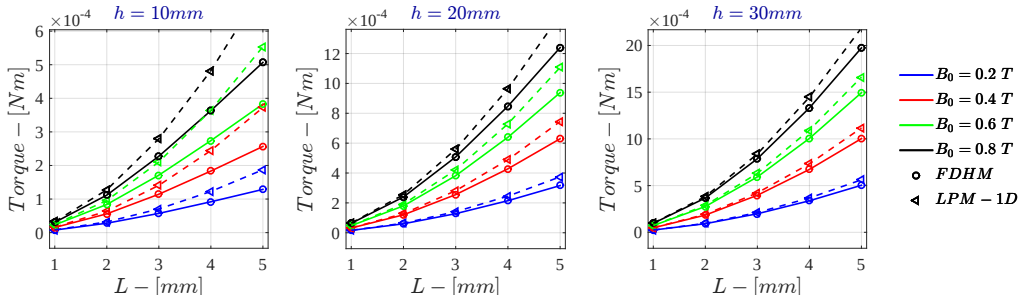

Figure F.9: *Monodimensional LPM - Current Drive* $\dot{\Gamma}$ *for* $\sigma = 10^2$ S/m - $r_{out} = 50mm$

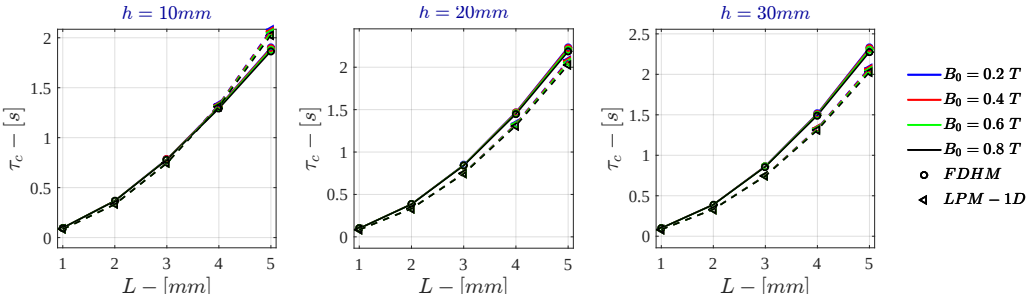

Figure F.10: *Monodimensional LPM - Current Drive* τ_c *for* $\sigma = 10^2$ S/m - $r_{out} = 50mm$

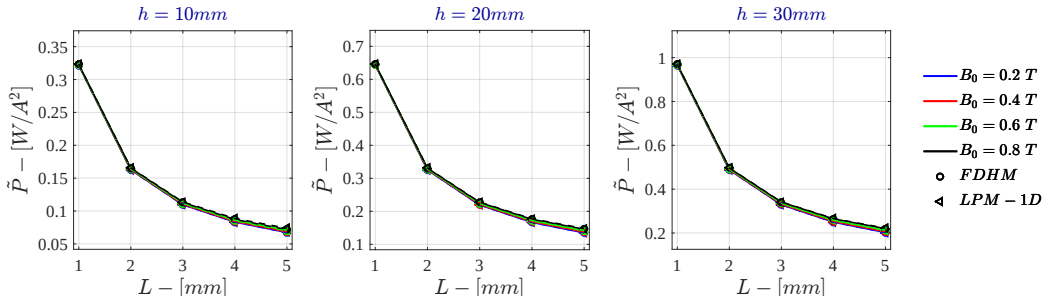

Figure F.11: *Monodimensional LPM - Current Drive* $\tilde{P}$ *for* $\sigma = 10^2$ S/m - $r_{out} = 50mm$

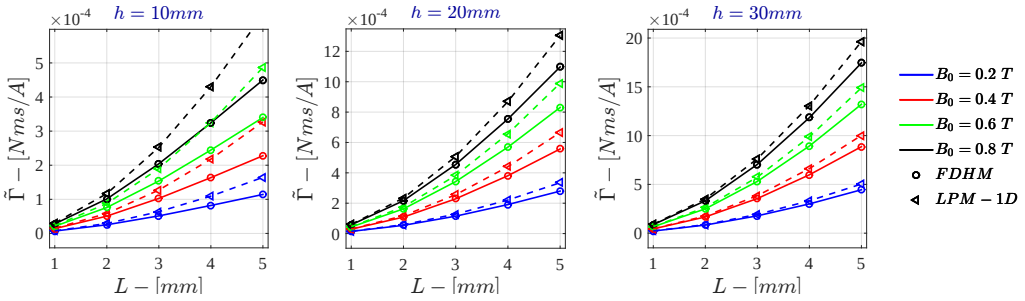

Figure F.12: *Monodimensional LPM - Current Drive* $\tilde{\Gamma}$ *for* $\sigma = 10^2$ S/m - $r_{out} = 50mm$

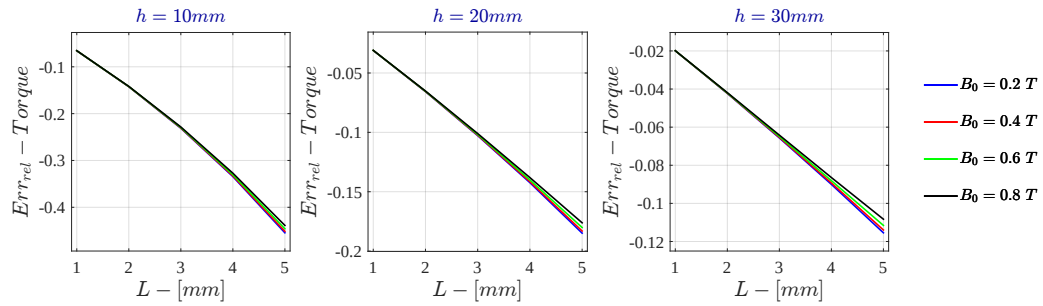

Figure F.13: *Monodimensional LPM - Current Drive Relative Error -* $\dot{\Gamma}$ *for* $\sigma = 10^2\ S/m$ *-* $r_{out} = 50mm$

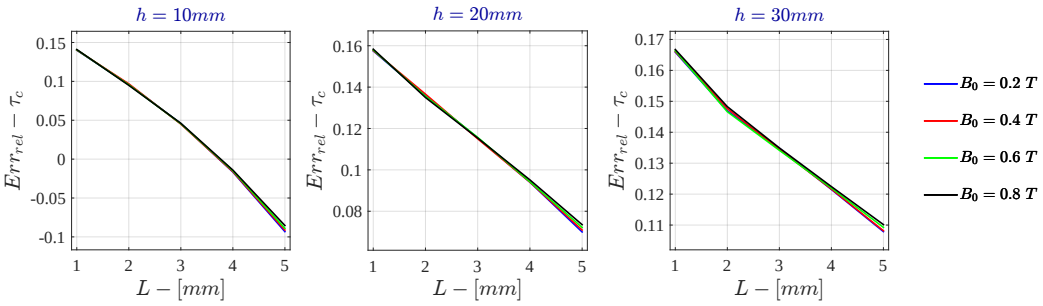

Figure F.14: *Monodimensional LPM - Current Drive Relative Error -* τ_c *for* $\sigma = 10^2\ S/m$ *-* $r_{out} = 50mm$

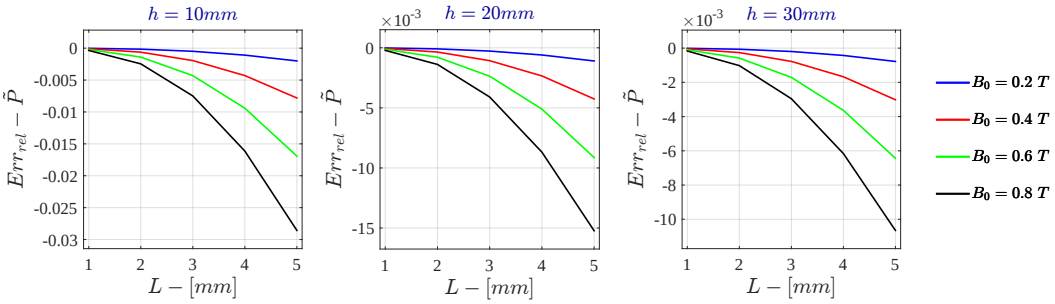

Figure F.15: *Monodimensional LPM - Current Drive Relative Error -* $\tilde{P}$ *for* $\sigma = 10^2\ S/m$ *-* $r_{out} = 50mm$

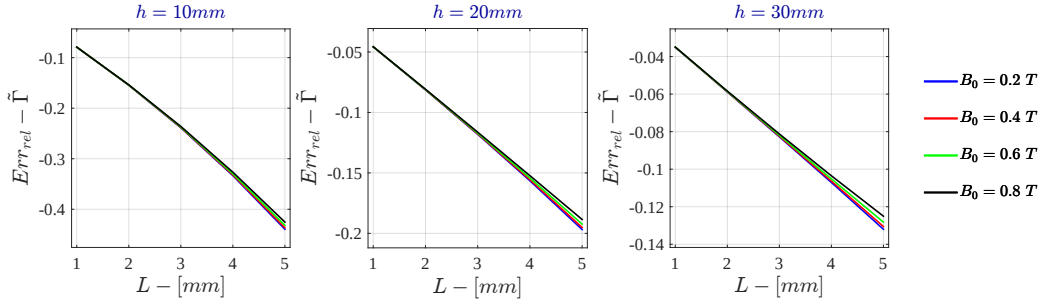

Figure F.16: *Monodimensional LPM - Current Drive Relative Error -* $\tilde{\Gamma}$ *for* $\sigma = 10^2\ S/m$ *-* $r_{out} = 50mm$

F.1.2 Voltage Drive

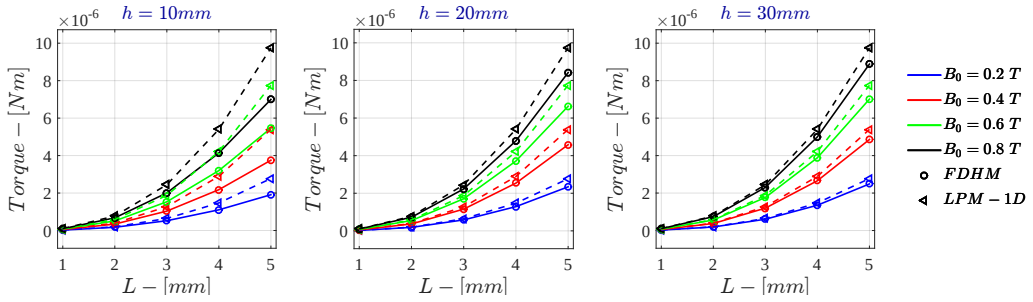

Figure F.17: *Monodimensional LPM - Voltage Drive* $\dot{\Gamma}$ *for* $\sigma = 10^2$ *S/m -* $r_{out} = 50mm$

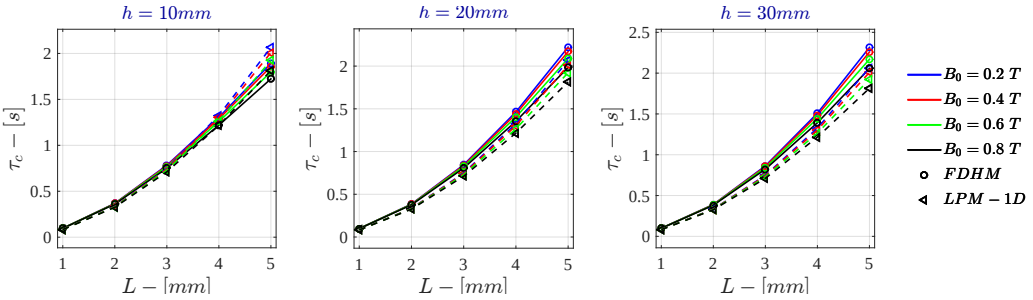

Figure F.18: *Monodimensional LPM - Voltage Drive* τ_c *for* $\sigma = 10^2$ *S/m -* $r_{out} = 50mm$

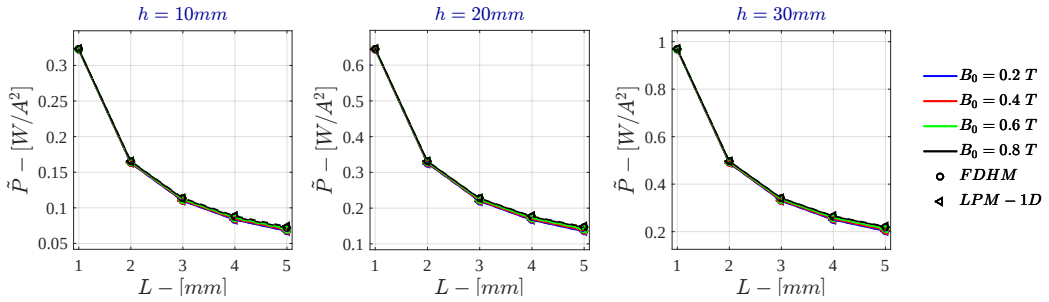

Figure F.19: *Monodimensional LPM - Voltage Drive* $\tilde{P}$ *for* $\sigma = 10^2$ *S/m -* $r_{out} = 50mm$

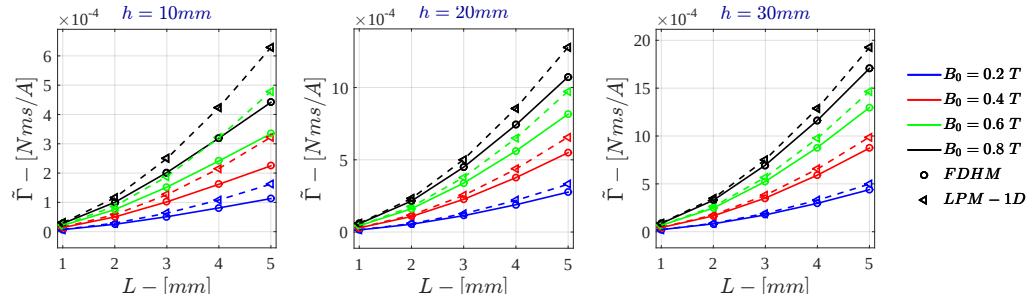

Figure F.20: *Monodimensional LPM - Voltage Drive* $\tilde{\Gamma}$ *for* $\sigma = 10^2$ *S/m -* $r_{out} = 50mm$

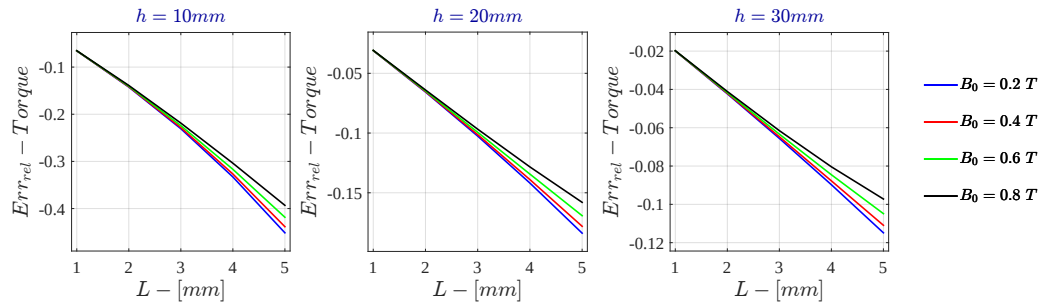

Figure F.21: *Monodimensional LPM - Voltage Drive*
Relative Error - $\dot{\Gamma}$ for $\sigma = 10^2$ S/m - $r_{out} = 50mm$

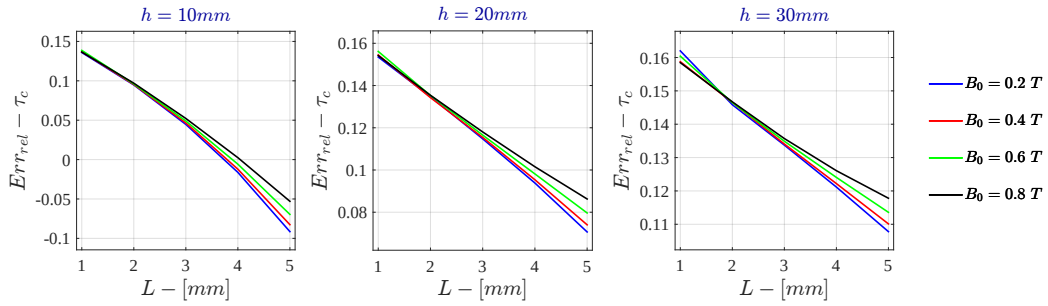

Figure F.22: *Monodimensional LPM - Voltage Drive*
Relative Error - τ_c for $\sigma = 10^2$ S/m - $r_{out} = 50mm$

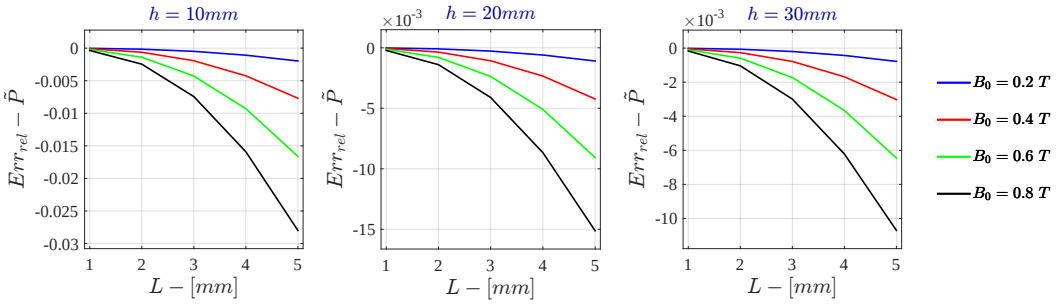

Figure F.23: *Monodimensional LPM - Voltage Drive*
Relative Error - $\tilde{P}$ for $\sigma = 10^2$ S/m - $r_{out} = 50mm$

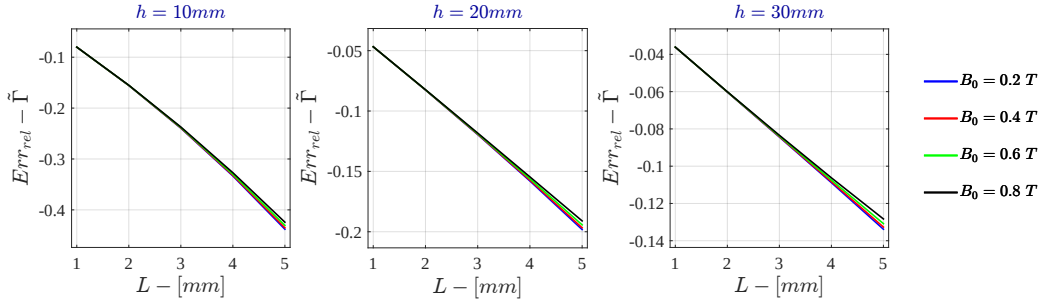

Figure F.24: *Monodimensional LPM - Voltage Drive*
Relative Error - $\tilde{\Gamma}$ for $\sigma = 10^2$ S/m - $r_{out} = 50mm$

F.2 Bidimensional LPM - $\sigma = 10^2 S/m$

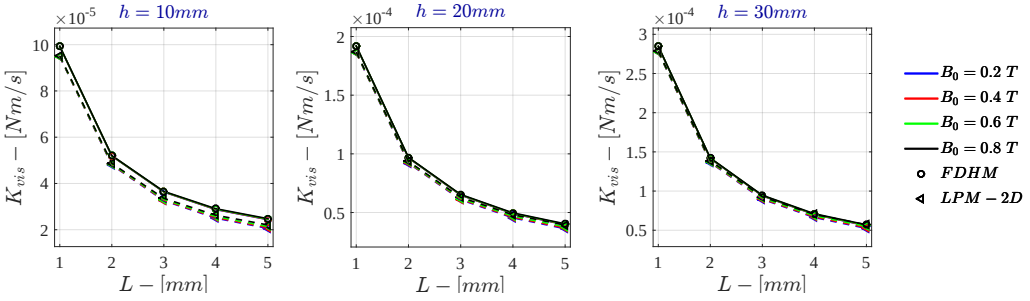

Figure F.25: *Bidimensional LPM* K_{vis} *for* $\sigma = 10^2\ S/m$ - $r_{out} = 50mm$

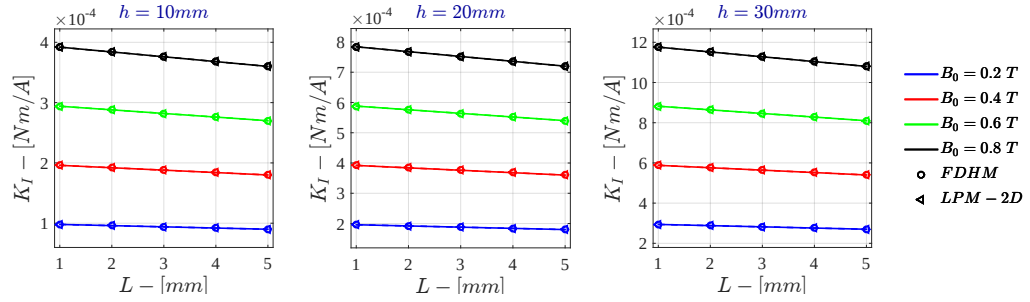

Figure F.26: *Bidimensional LPM* K_I *for* $\sigma = 10^2\ S/m$ - $r_{out} = 50mm$

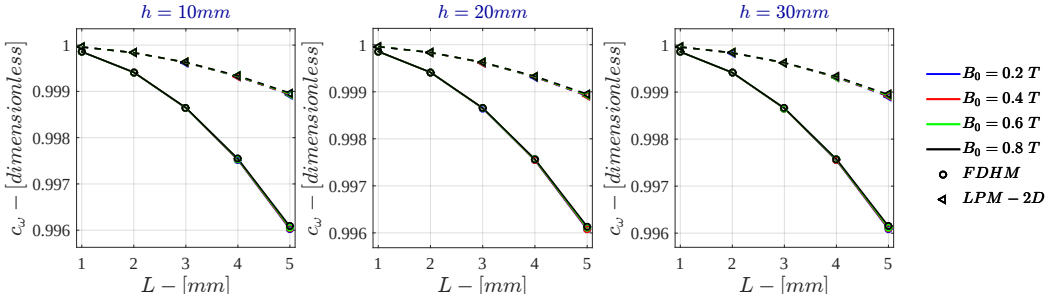

Figure F.27: *Bidimensional LPM* c_ω *for* $\sigma = 10^2\ S/m$ - $r_{out} = 50mm$

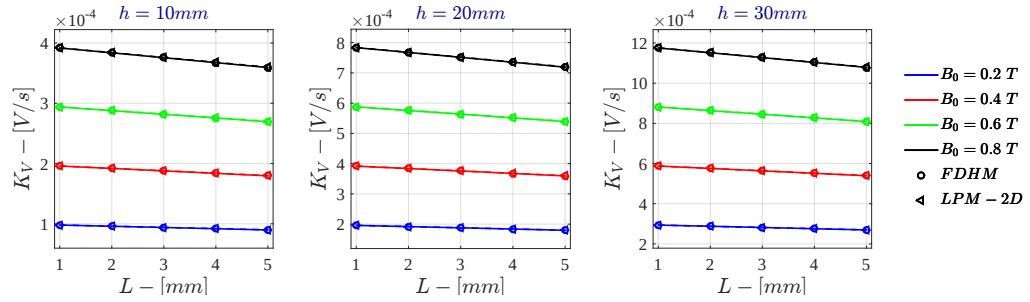

Figure F.28: *Bidimensional LPM* K_V *for* $\sigma = 10^2\ S/m$ - $r_{out} = 50mm$

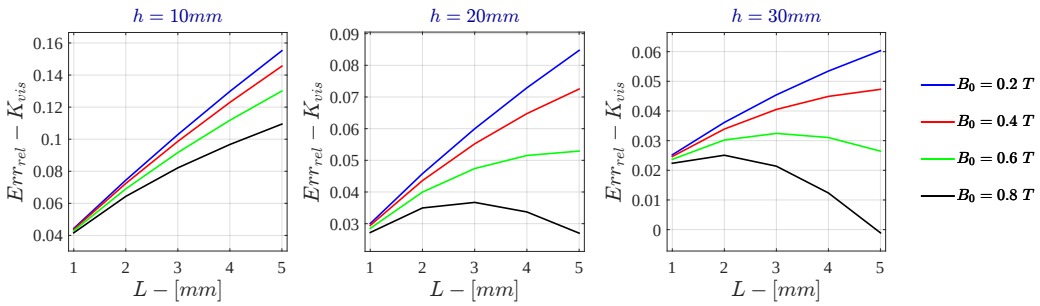

Figure F.29: *Bidimensional LPM*
Relative Error - K_{vis} for $\sigma = 10^2\ S/m$ - $r_{out} = 50mm$

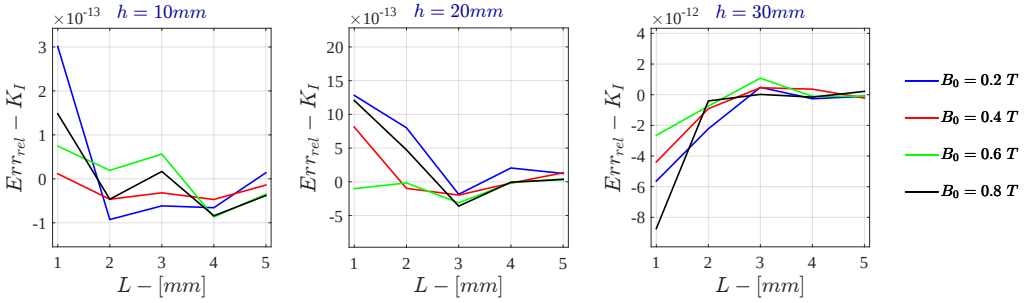

Figure F.30: *Bidimensional LPM*
Relative Error - K_I for $\sigma = 10^2\ S/m$ - $r_{out} = 50mm$

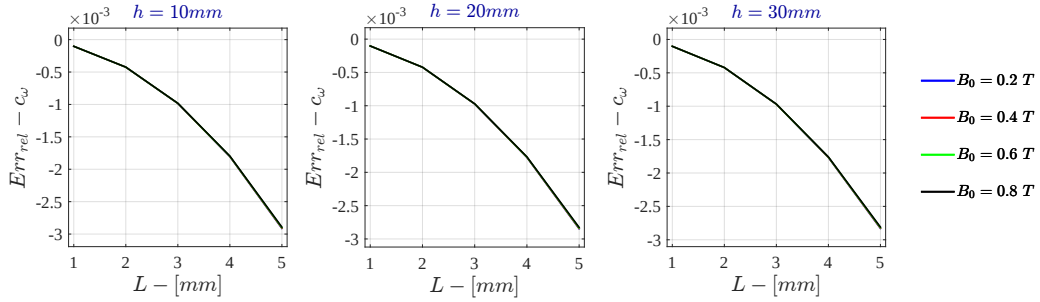

Figure F.31: *Bidimensional LPM*
Relative Error - c_ω for $\sigma = 10^2\ S/m$ - $r_{out} = 50mm$

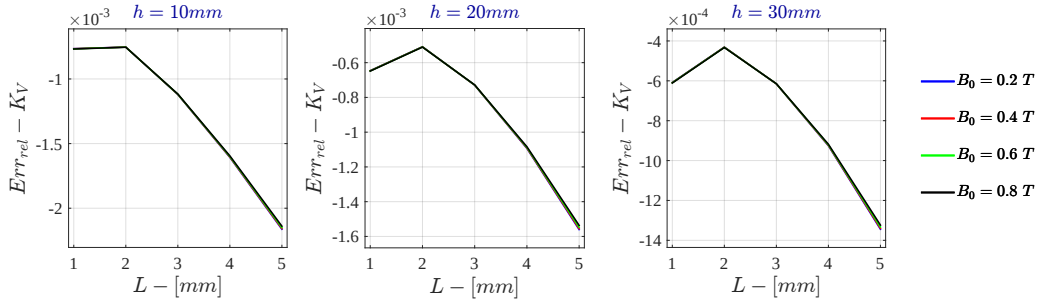

Figure F.32: *Bidimensional LPM*
Relative Error - K_V for $\sigma = 10^2\ S/m$ - $r_{out} = 50mm$

F.2.1 Current Drive

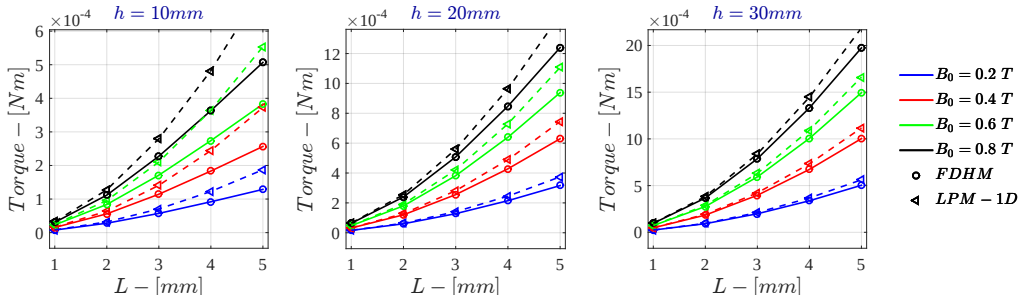

Figure F.33: *Bidimensional LPM - Current Drive* $\dot{\Gamma}$ *for* $\sigma = 10^2$ S/m - $r_{out} = 50mm$

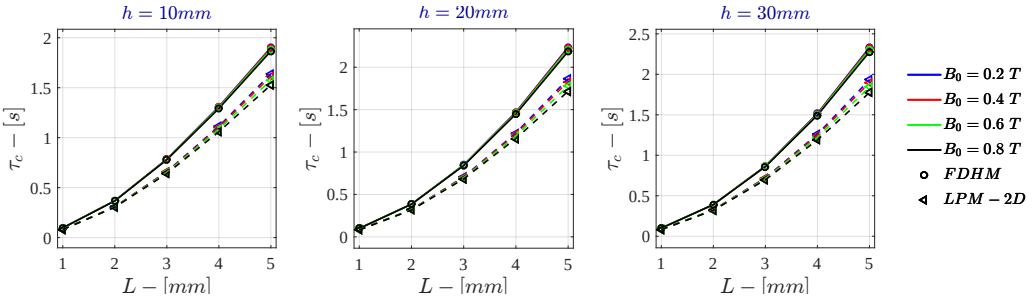

Figure F.34: *Bidimensional LPM - Current Drive* τ_c *for* $\sigma = 10^2$ S/m - $r_{out} = 50mm$

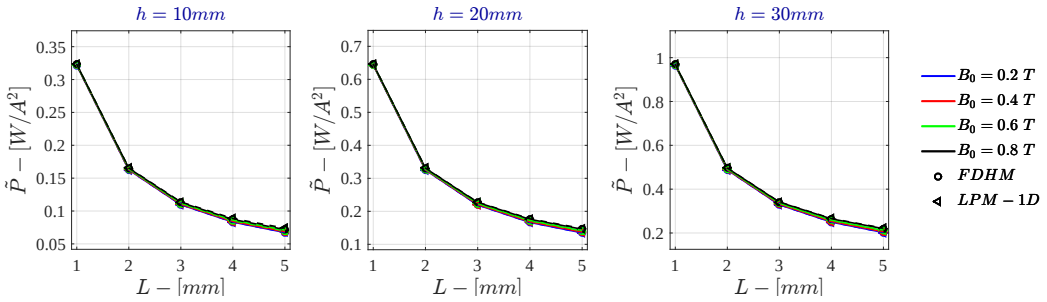

Figure F.35: *Bidimensional LPM - Current Drive* $\tilde{P}$ *for* $\sigma = 10^2$ S/m - $r_{out} = 50mm$

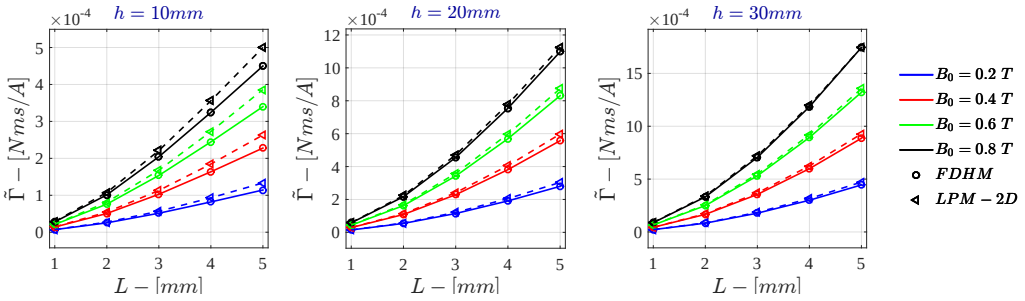

Figure F.36: *Bidimensional LPM - Current Drive* $\tilde{\Gamma}$ *for* $\sigma = 10^2$ S/m - $r_{out} = 50mm$

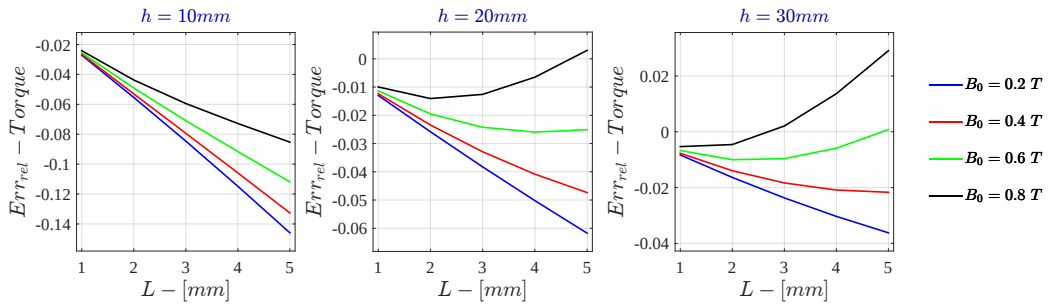

Figure F.37: *Bidimensional LPM - Current Drive Relative Error -* $\dot{\Gamma}$ *for* $\sigma = 10^2$ S/m *-* $r_{out} = 50mm$

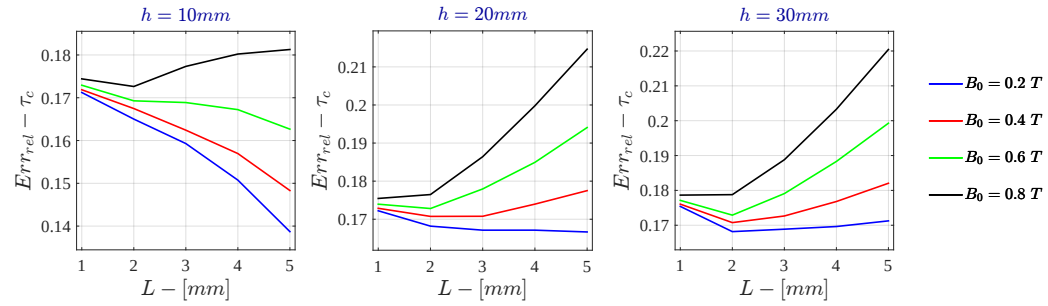

Figure F.38: *Bidimensional LPM - Current Drive Relative Error -* τ_c *for* $\sigma = 10^2$ S/m *-* $r_{out} = 50mm$

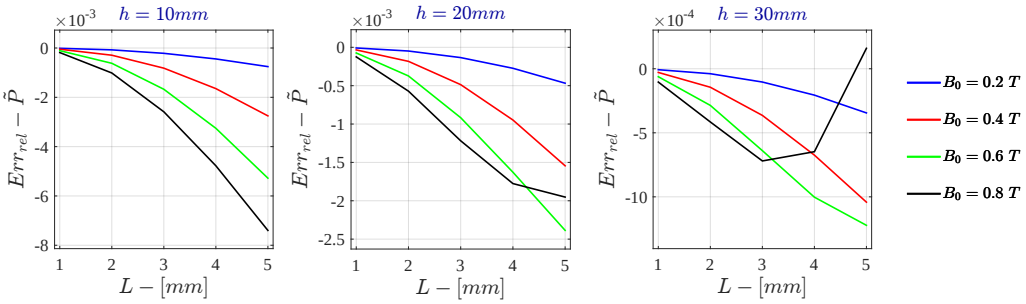

Figure F.39: *Bidimensional LPM - Current Drive Relative Error -* $\tilde{P}$ *for* $\sigma = 10^2$ S/m *-* $r_{out} = 50mm$

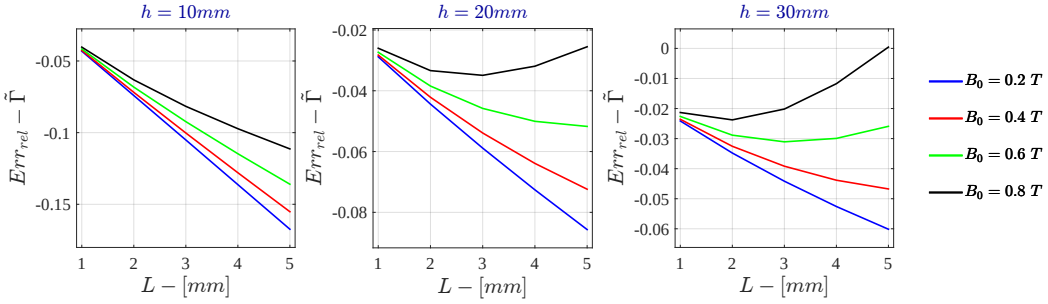

Figure F.40: *Bidimensional LPM - Current Drive Relative Error -* $\tilde{\Gamma}$ *for* $\sigma = 10^2$ S/m *-* $r_{out} = 50mm$

F.2.2 Voltage Drive

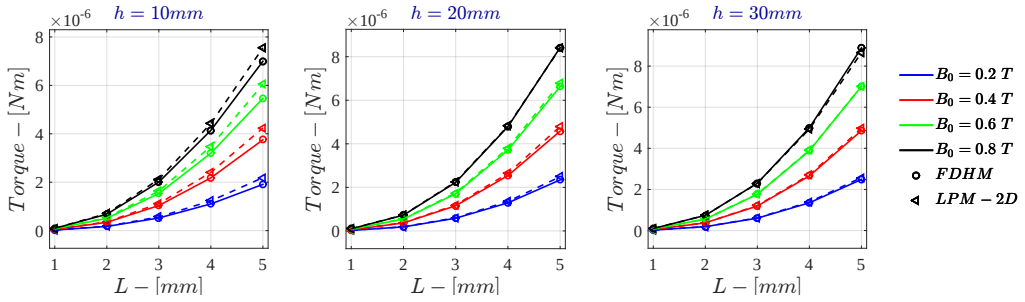

Figure F.41: *Bidimensional LPM - Voltage Drive* $\dot{\Gamma}$ *for* $\sigma = 10^2$ S/m - $r_{out} = 50mm$

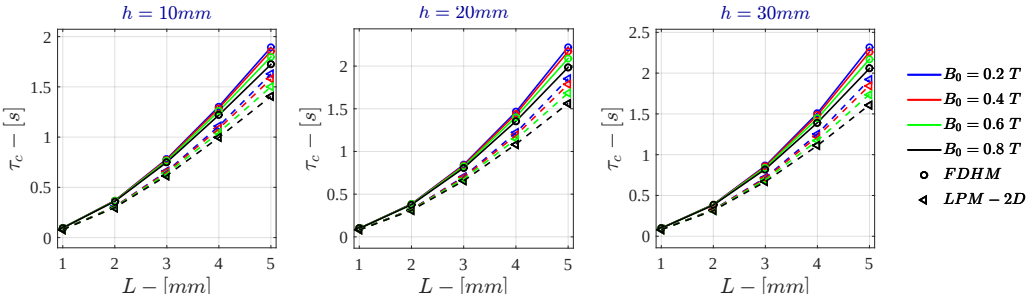

Figure F.42: *Bidimensional LPM - Voltage Drive* τ_c *for* $\sigma = 10^2$ S/m - $r_{out} = 50mm$

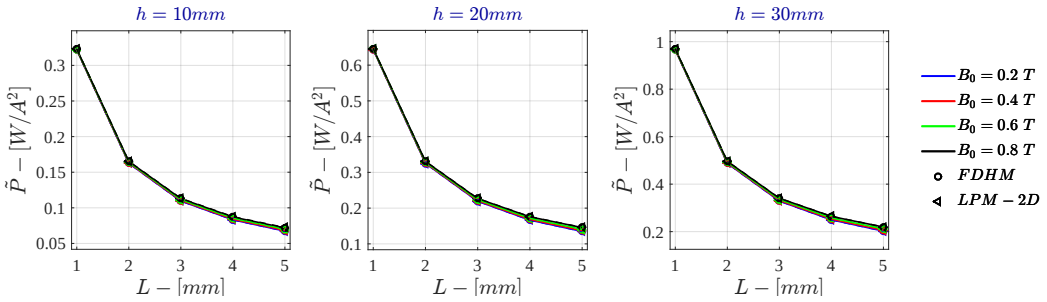

Figure F.43: *Bidimensional LPM - Voltage Drive* $\tilde{P}$ *for* $\sigma = 10^2$ S/m - $r_{out} = 50mm$

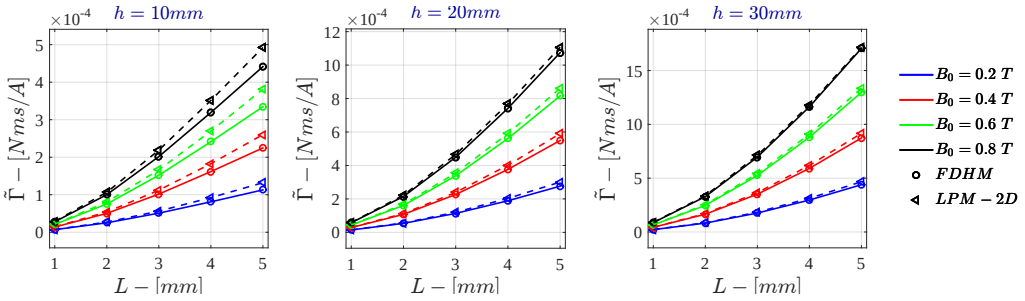

Figure F.44: *Bidimensional LPM - Voltage Drive* $\tilde{\Gamma}$ *for* $\sigma = 10^2$ S/m - $r_{out} = 50mm$

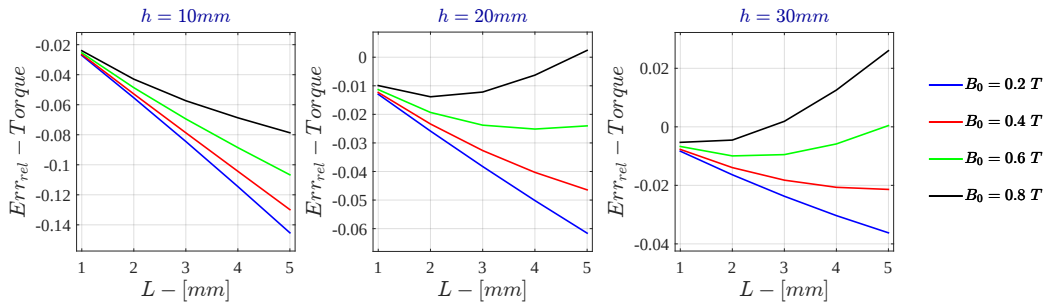

Figure F.45: *Bidimensional LPM - Voltage Drive Relative Error - $\dot{\Gamma}$ for $\sigma = 10^2$ S/m - $r_{out} = 50mm$*

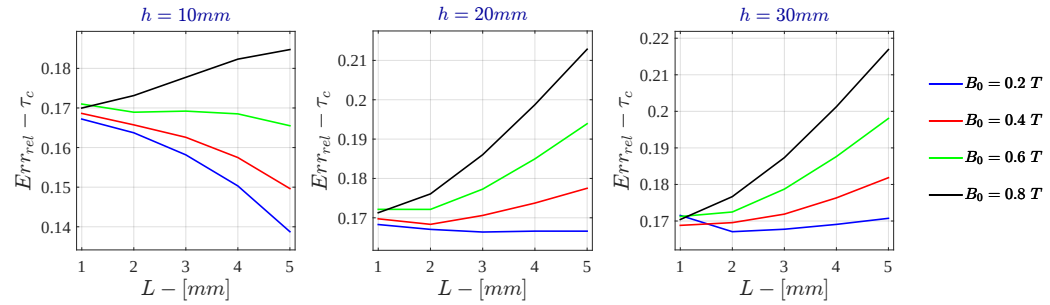

Figure F.46: *Bidimensional LPM - Voltage Drive Relative Error - τ_c for $\sigma = 10^2$ S/m - $r_{out} = 50mm$*

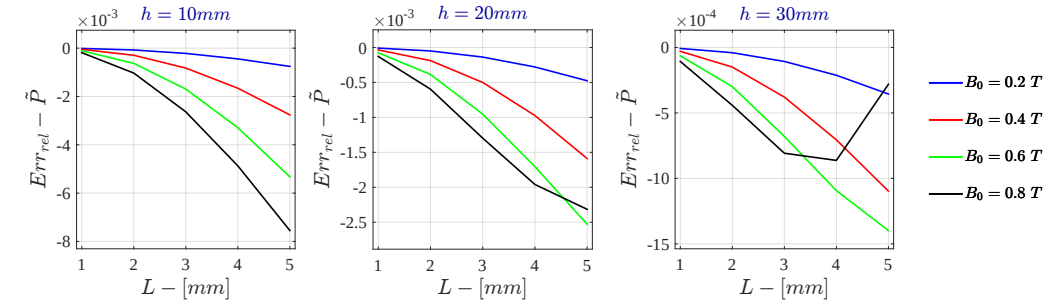

Figure F.47: *Bidimensional LPM - Voltage Drive Relative Error - $\tilde{P}$ for $\sigma = 10^2$ S/m - $r_{out} = 50mm$*

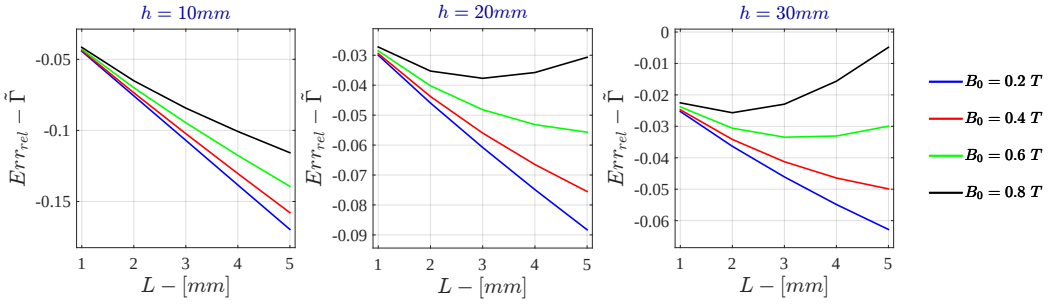

Figure F.48: *Bidimensional LPM - Voltage Drive Relative Error - $\tilde{\Gamma}$ for $\sigma = 10^2$ S/m - $r_{out} = 50mm$*

Appendix

G

Comparison between FDHM and LPM: $\sigma = 10^3\ S/m$

G.1 Monodimensional LPM - $\sigma = 10^3 S/m$

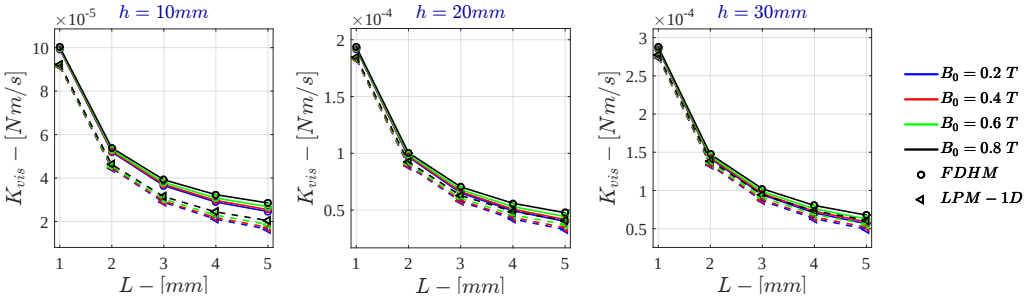

Figure G.1: K_{vis} *for* $\sigma = 10^3\ S/m$ - $r_{out} = 50mm$ - *Monodimensional LPM*

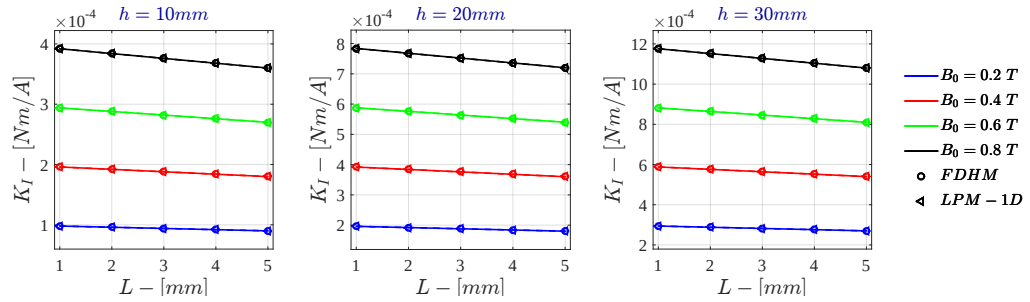

Figure G.2: *Monodimensional LPM*
K_I *for* $\sigma = 10^3\ S/m$ - $r_{out} = 50mm$

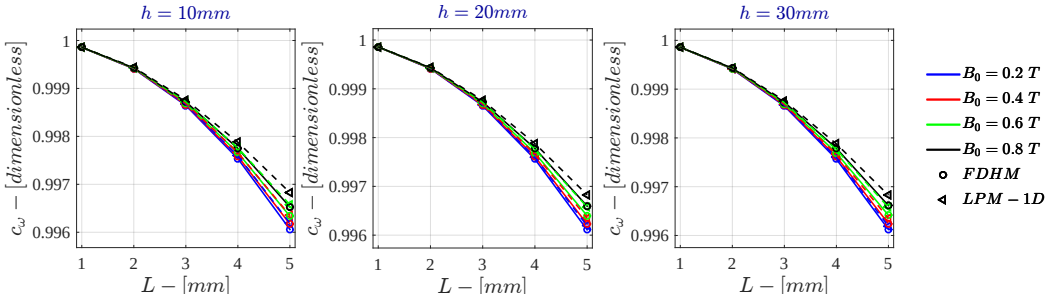

Figure G.3: *Monodimensional LPM*
c_ω *for* $\sigma = 10^3\ S/m$ - $r_{out} = 50mm$

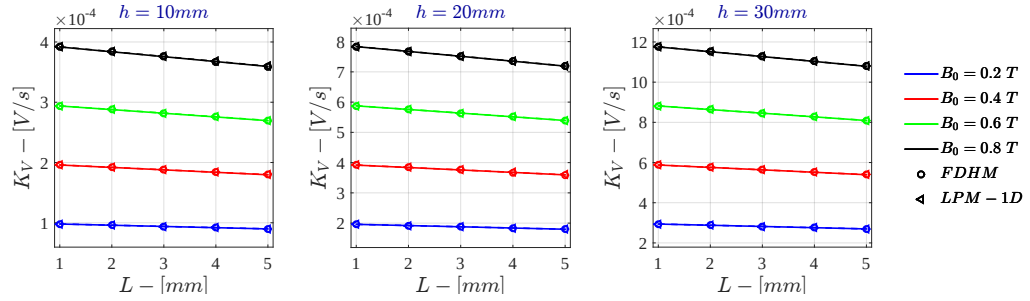

Figure G.4: *Monodimensional LPM*
K_V *for* $\sigma = 10^3\ S/m$ - $r_{out} = 50mm$

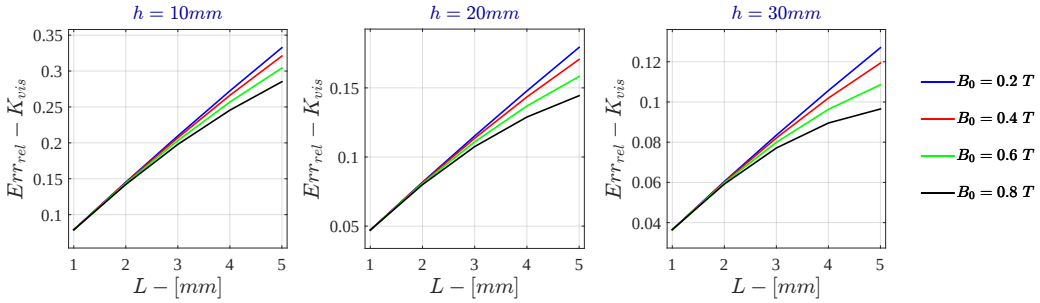

Figure G.5: *Monodimensional LPM*
Relative Error - K_{vis} for $\sigma = 10^3$ S/m - $r_{out} = 50mm$

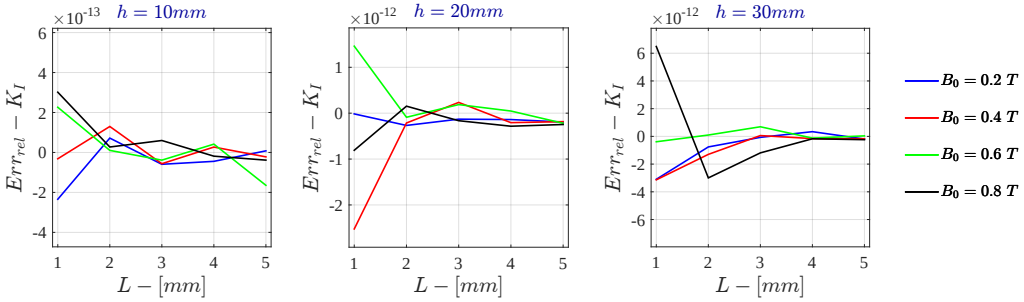

Figure G.6: *Monodimensional LPM*
Relative Error - K_I for $\sigma = 10^3$ S/m - $r_{out} = 50mm$

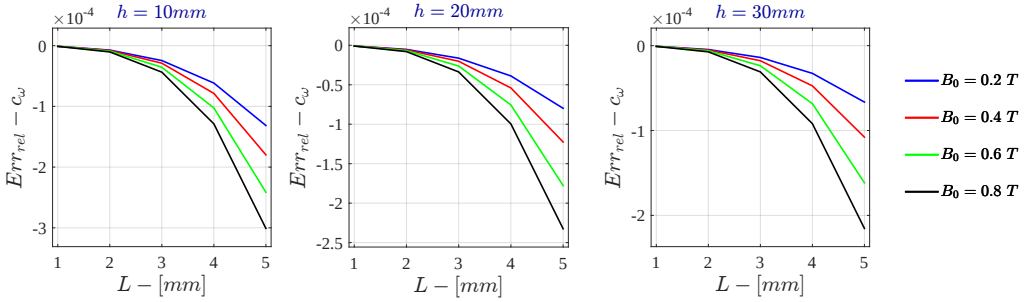

Figure G.7: *Monodimensional LPM*
Relative Error - c_ω for $\sigma = 10^3$ S/m - $r_{out} = 50mm$

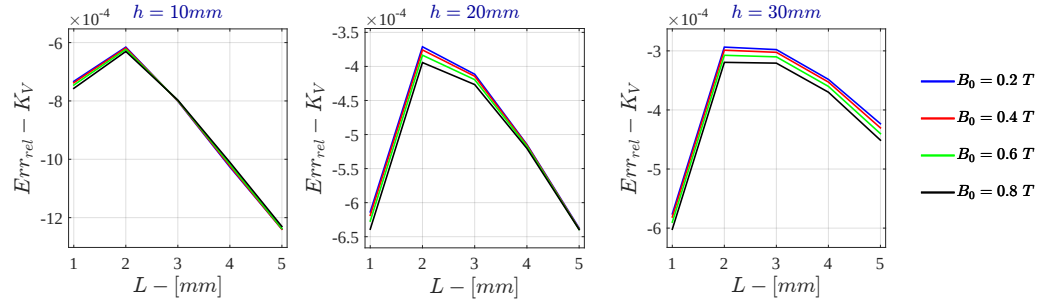

Figure G.8: *Monodimensional LPM*
Relative Error - K_V for $\sigma = 10^3$ S/m - $r_{out} = 50mm$

G.1.1 Current Drive

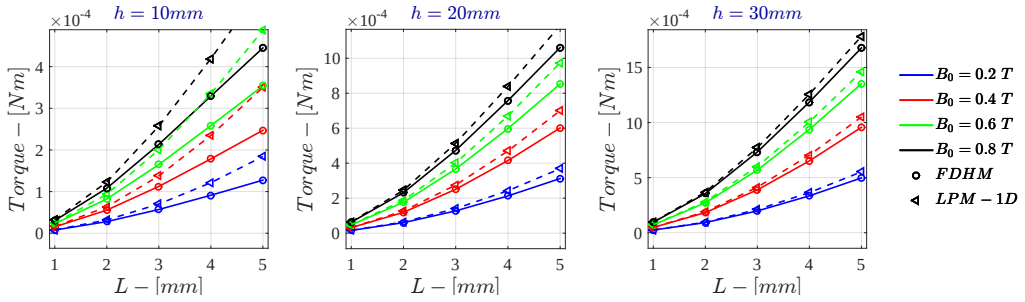

Figure G.9: *Monodimensional LPM - Current Drive* $\dot{\Gamma}$ *for* $\sigma = 10^3\ S/m$ *-* $r_{out} = 50mm$

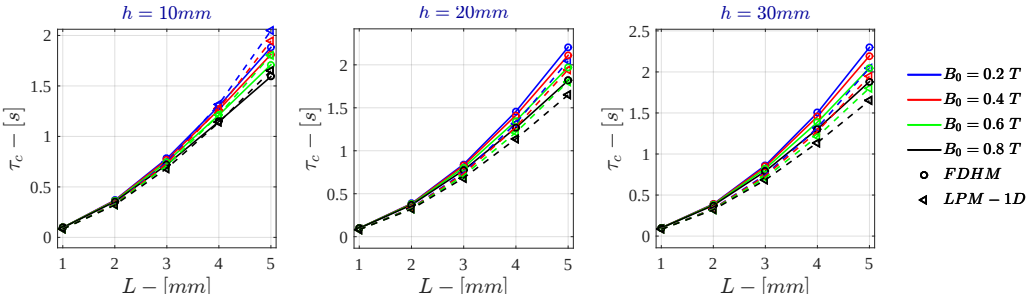

Figure G.10: *Monodimensional LPM - Current Drive* τ_c *for* $\sigma = 10^3\ S/m$ *-* $r_{out} = 50mm$

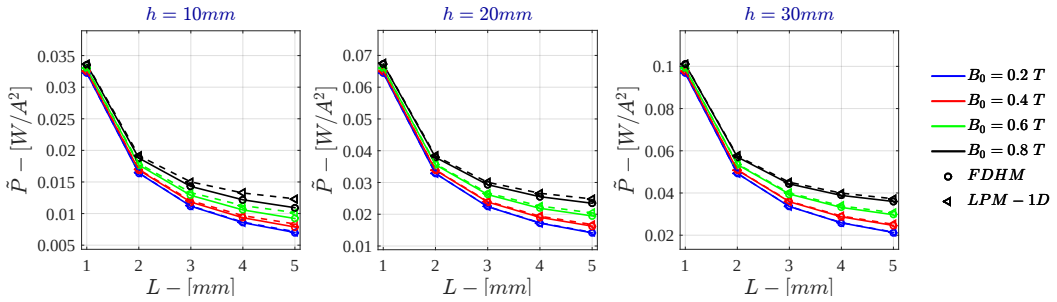

Figure G.11: *Monodimensional LPM - Current Drive* $\tilde{P}$ *for* $\sigma = 10^3\ S/m$ *-* $r_{out} = 50mm$

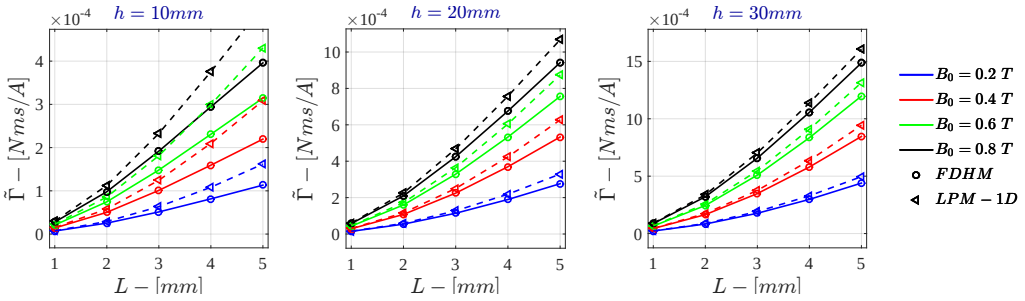

Figure G.12: *Monodimensional LPM - Current Drive* $\tilde{\Gamma}$ *for* $\sigma = 10^3\ S/m$ *-* $r_{out} = 50mm$

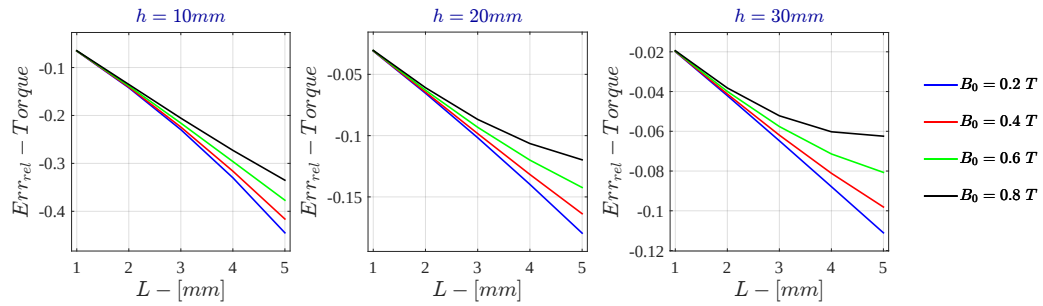

Figure G.13: *Monodimensional LPM - Current Drive Relative Error -* $\dot{\Gamma}$ *for* $\sigma = 10^3$ S/m *-* $r_{out} = 50mm$

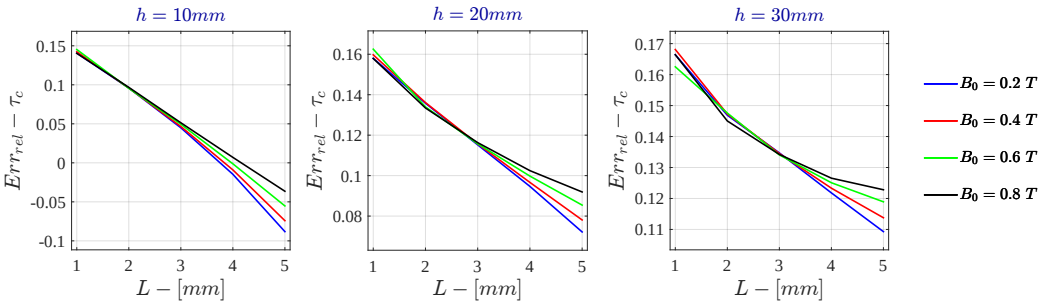

Figure G.14: *Monodimensional LPM - Current Drive Relative Error -* τ_c *for* $\sigma = 10^3$ S/m *-* $r_{out} = 50mm$

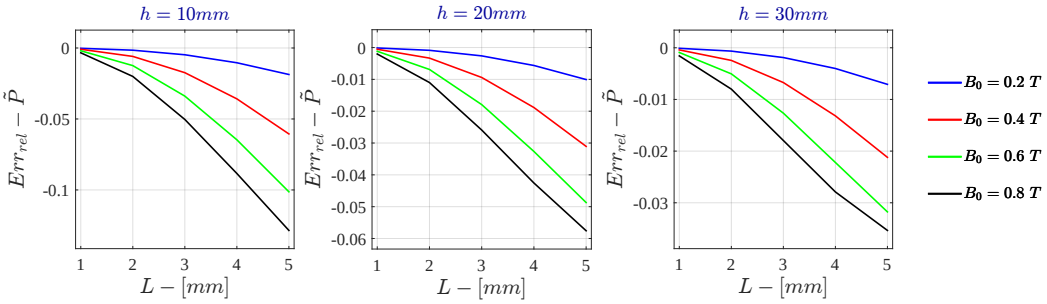

Figure G.15: *Monodimensional LPM - Current Drive Relative Error -* $\tilde{P}$ *for* $\sigma = 10^3$ S/m *-* $r_{out} = 50mm$

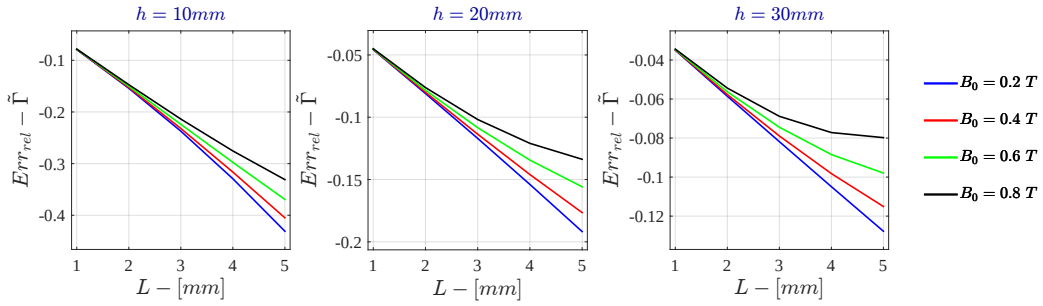

Figure G.16: *Monodimensional LPM - Current Drive Relative Error -* $\tilde{\Gamma}$ *for* $\sigma = 10^3$ S/m *-* $r_{out} = 50mm$

G.1.2 Voltage Drive

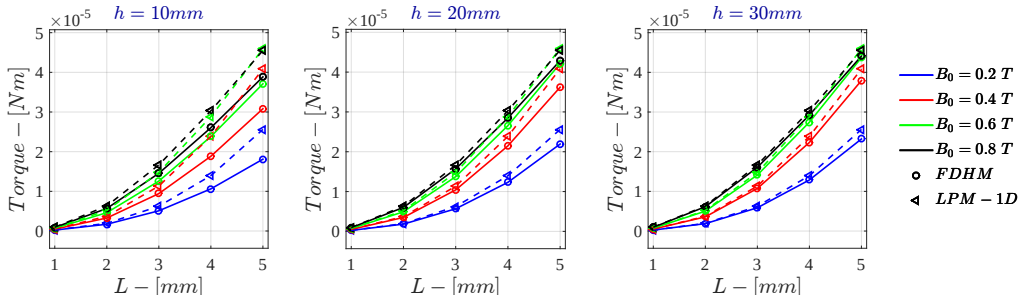

Figure G.17: *Monodimensional LPM - Voltage Drive* $\dot{\Gamma}$ *for* $\sigma = 10^3\ S/m$ *-* $r_{out} = 50mm$

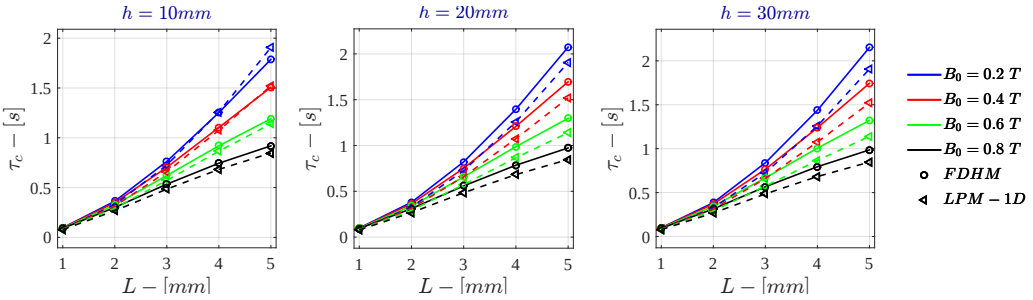

Figure G.18: *Monodimensional LPM - Voltage Drive* τ_c *for* $\sigma = 10^3\ S/m$ *-* $r_{out} = 50mm$

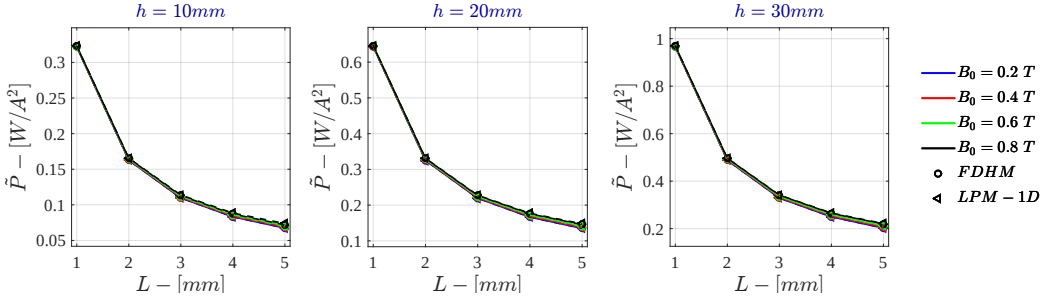

Figure G.19: *Monodimensional LPM - Voltage Drive* $\tilde{P}$ *for* $\sigma = 10^3\ S/m$ *-* $r_{out} = 50mm$

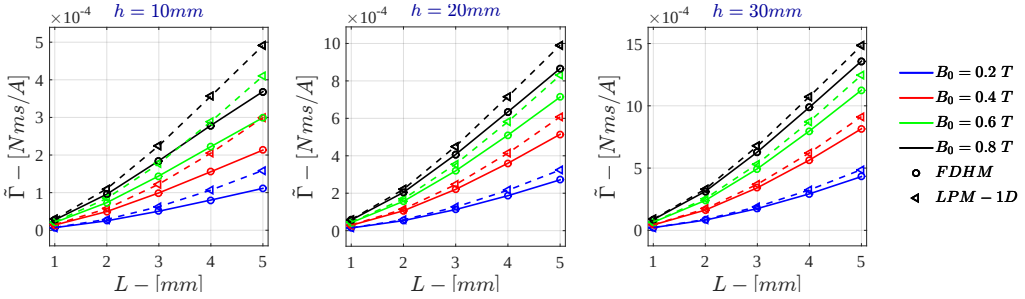

Figure G.20: *Monodimensional LPM - Voltage Drive* $\tilde{\Gamma}$ *for* $\sigma = 10^3\ S/m$ *-* $r_{out} = 50mm$

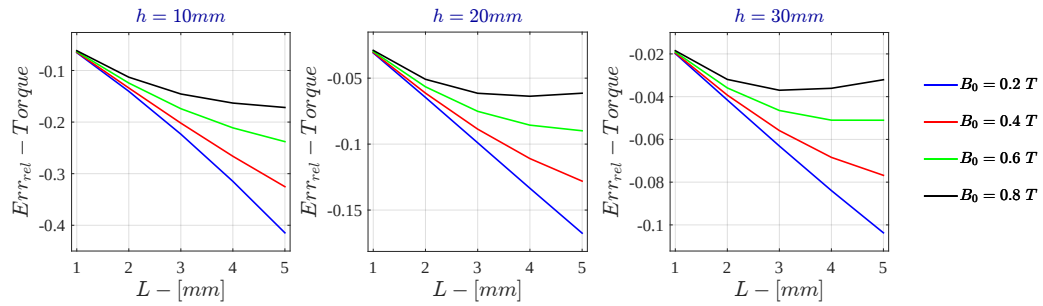

Figure G.21: *Monodimensional LPM - Voltage Drive*
Relative Error - $\dot{\Gamma}$ *for* $\sigma = 10^3$ S/m *-* $r_{out} = 50mm$

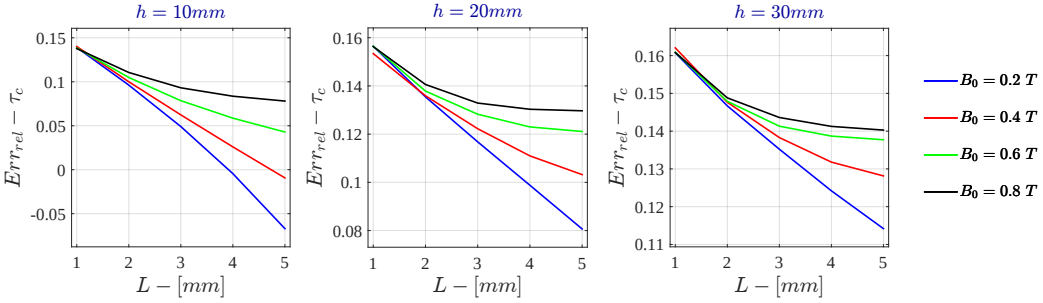

Figure G.22: *Monodimensional LPM - Voltage Drive*
Relative Error - τ_c *for* $\sigma = 10^3$ S/m *-* $r_{out} = 50mm$

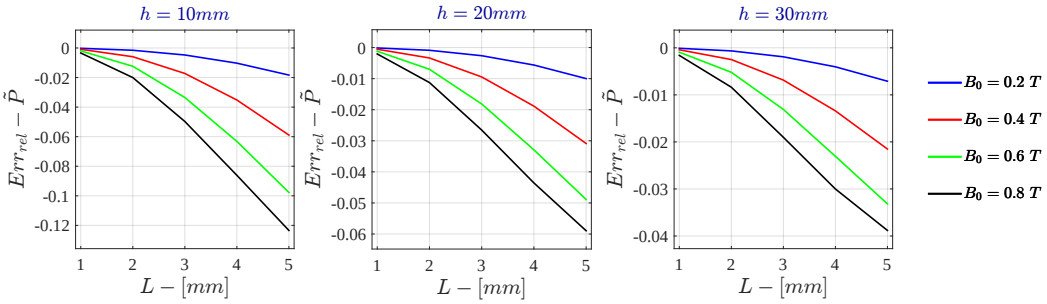

Figure G.23: *Monodimensional LPM - Voltage Drive*
Relative Error - $\tilde{P}$ *for* $\sigma = 10^3$ S/m *-* $r_{out} = 50mm$

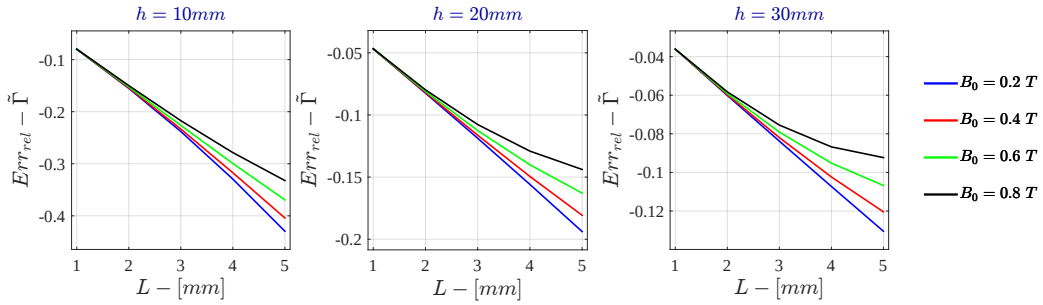

Figure G.24: *Monodimensional LPM - Voltage Drive*
Relative Error - $\tilde{\Gamma}$ *for* $\sigma = 10^3$ S/m *-* $r_{out} = 50mm$

G.2 Bidimensional LPM - $\sigma = 10^3 S/m$

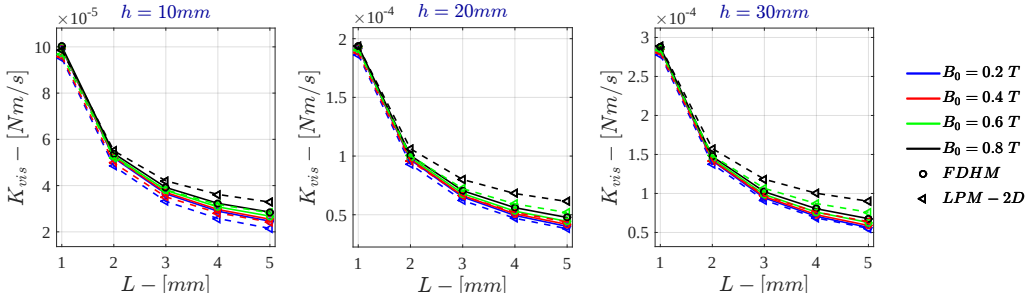

Figure G.25: *Bidimensional LPM*
K_{vis} for $\sigma = 10^3$ S/m - $r_{out} = 50mm$

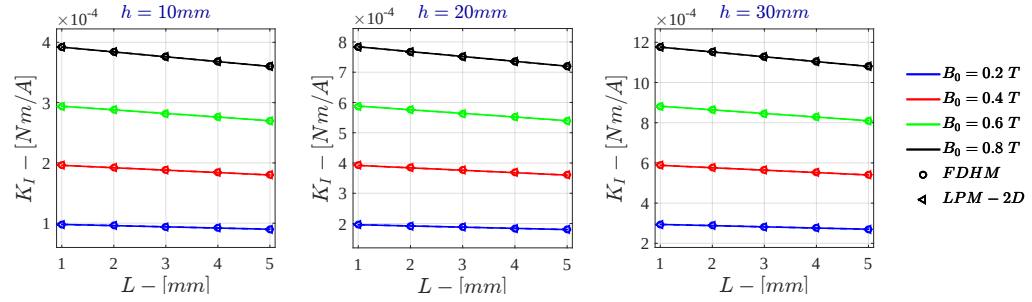

Figure G.26: *Bidimensional LPM*
K_I for $\sigma = 10^3$ S/m - $r_{out} = 50mm$

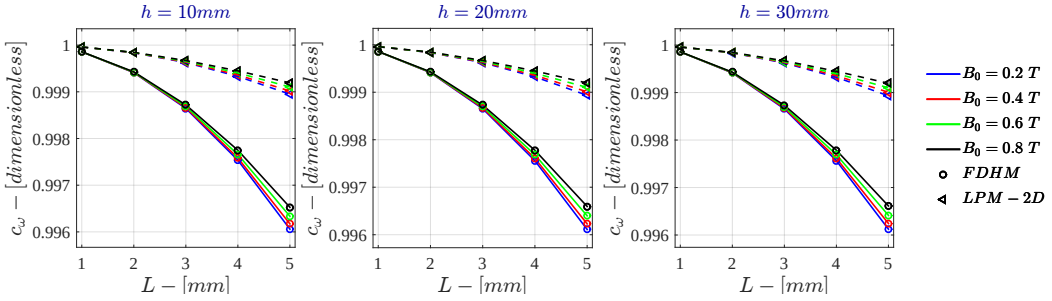

Figure G.27: *Bidimensional LPM*
c_ω for $\sigma = 10^3$ S/m - $r_{out} = 50mm$

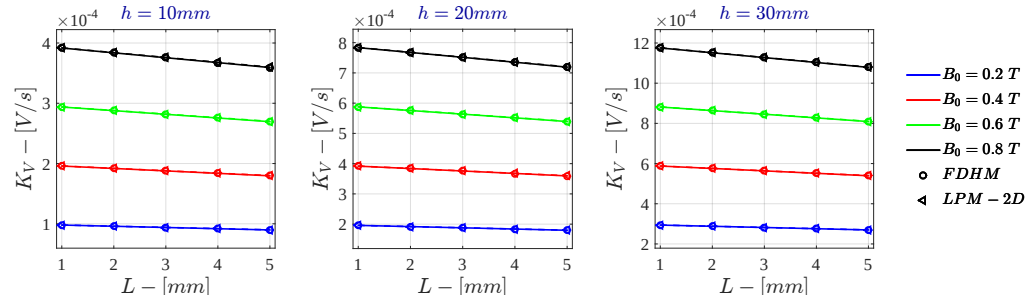

Figure G.28: *Bidimensional LPM*
K_V for $\sigma = 10^3$ S/m - $r_{out} = 50mm$

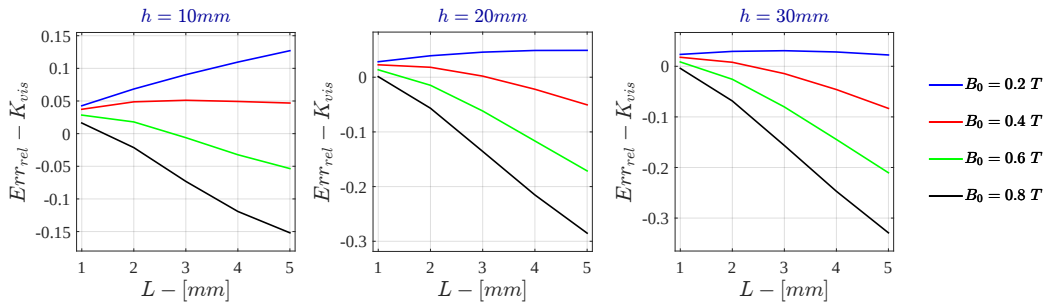

Figure G.29: *Bidimensional LPM*
Relative Error - K_{vis} for $\sigma = 10^3\ S/m$ - $r_{out} = 50mm$

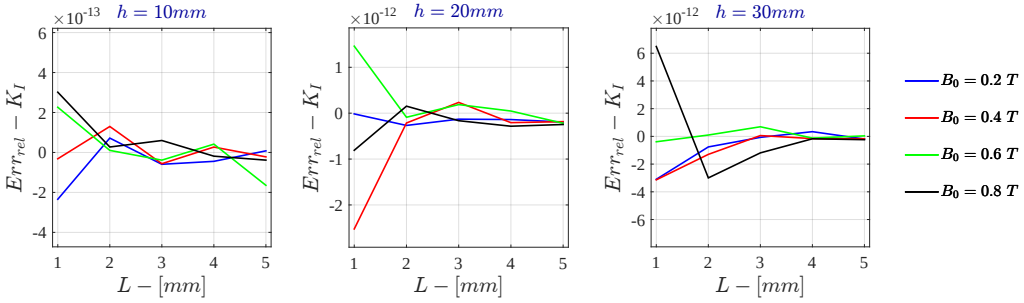

Figure G.30: *Bidimensional LPM*
Relative Error - K_I for $\sigma = 10^3\ S/m$ - $r_{out} = 50mm$

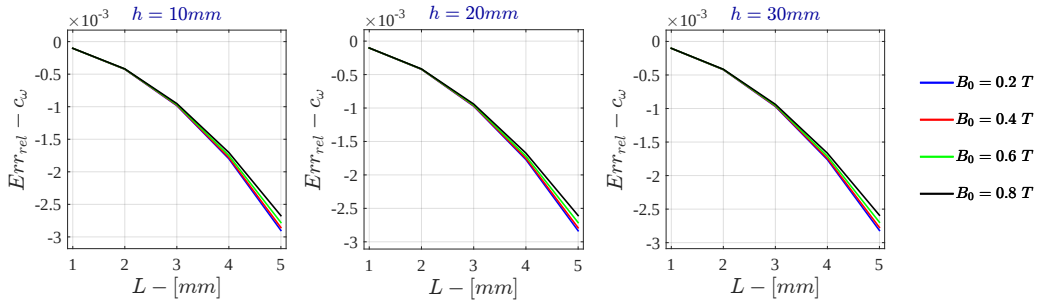

Figure G.31: *Bidimensional LPM*
Relative Error - c_ω for $\sigma = 10^3\ S/m$ - $r_{out} = 50mm$

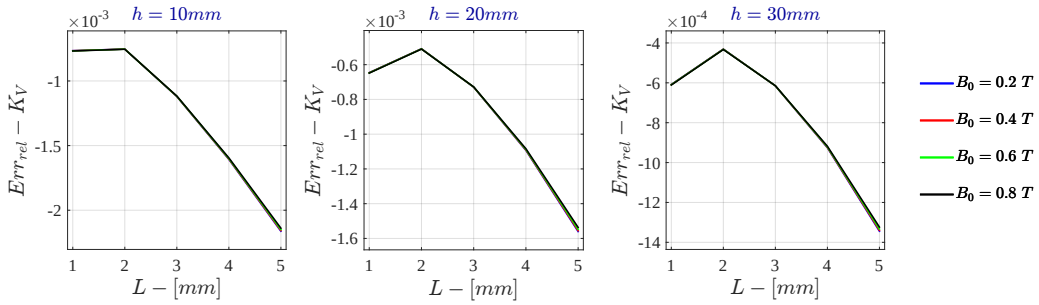

Figure G.32: *Bidimensional LPM*
Relative Error - K_V for $\sigma = 10^3\ S/m$ - $r_{out} = 50mm$

G.2.1 Current Drive

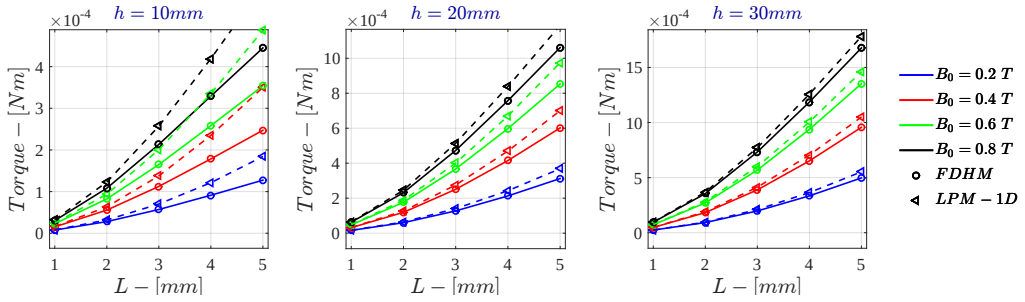

Figure G.33: *Bidimensional LPM - Current Drive* $\dot{\Gamma}$ *for* $\sigma = 10^3\ S/m$ *-* $r_{out} = 50mm$

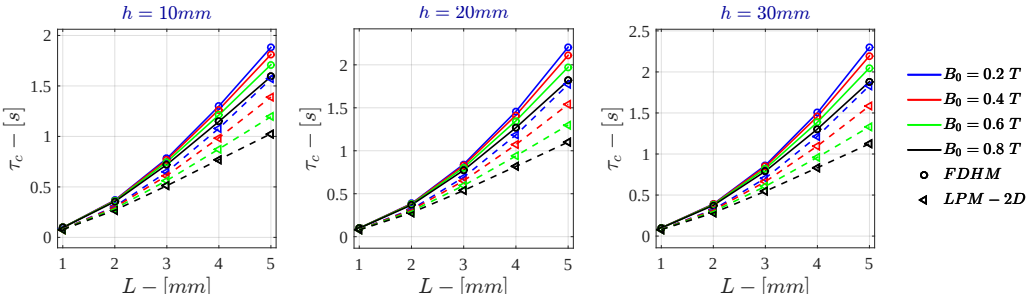

Figure G.34: *Bidimensional LPM - Current Drive* τ_c *for* $\sigma = 10^3\ S/m$ *-* $r_{out} = 50mm$

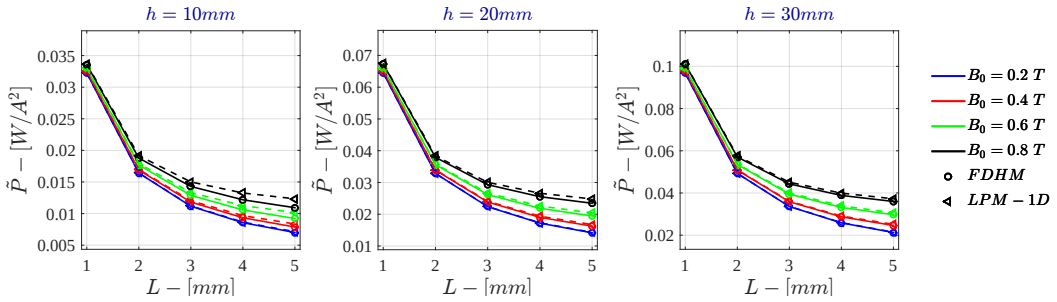

Figure G.35: *Bidimensional LPM - Current Drive* $\tilde{P}$ *for* $\sigma = 10^3\ S/m$ *-* $r_{out} = 50mm$

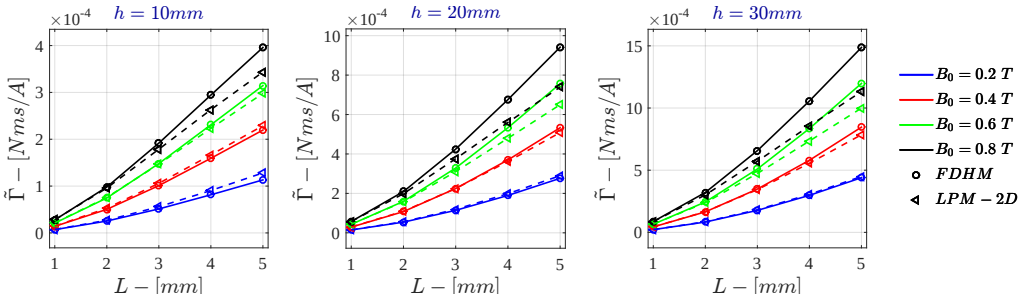

Figure G.36: *Bidimensional LPM - Current Drive* $\tilde{\Gamma}$ *for* $\sigma = 10^3\ S/m$ *-* $r_{out} = 50mm$

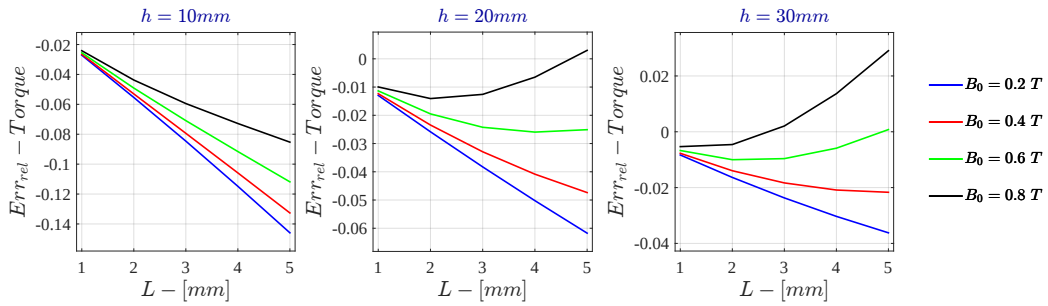

Figure G.37: *Bidimensional LPM - Current Drive Relative Error - $\dot{\Gamma}$ for $\sigma = 10^3\ S/m$ - $r_{out} = 50mm$*

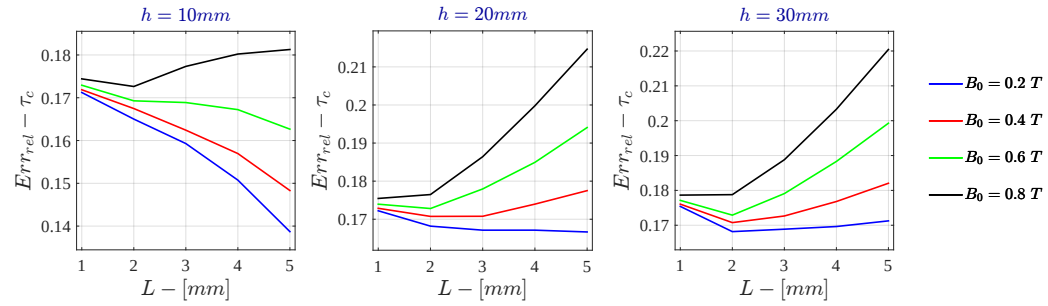

Figure G.38: *Bidimensional LPM - Current Drive Relative Error - τ_c for $\sigma = 10^3\ S/m$ - $r_{out} = 50mm$*

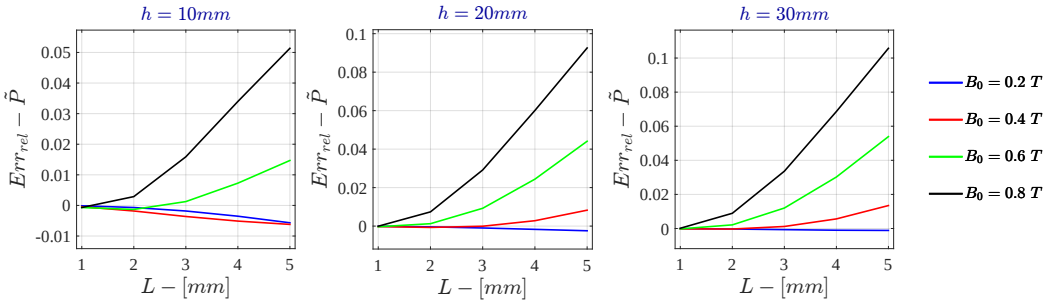

Figure G.39: *Bidimensional LPM - Current Drive Relative Error - $\tilde{P}$ for $\sigma = 10^3\ S/m$ - $r_{out} = 50mm$*

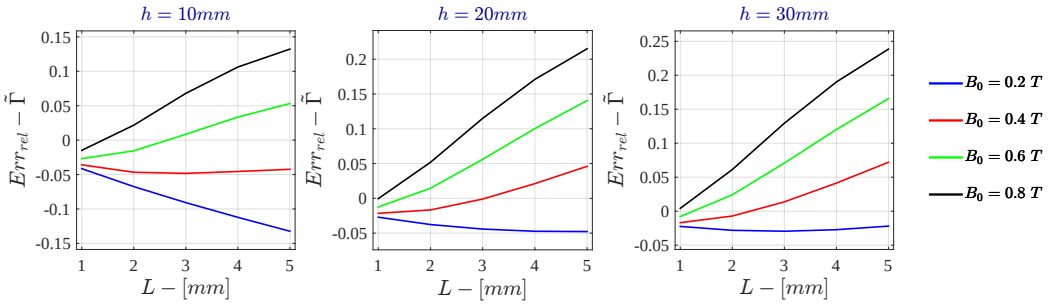

Figure G.40: *Bidimensional LPM - Current Drive Relative Error - $\tilde{\Gamma}$ for $\sigma = 10^3\ S/m$ - $r_{out} = 50mm$*

G.2.2 Voltage Drive

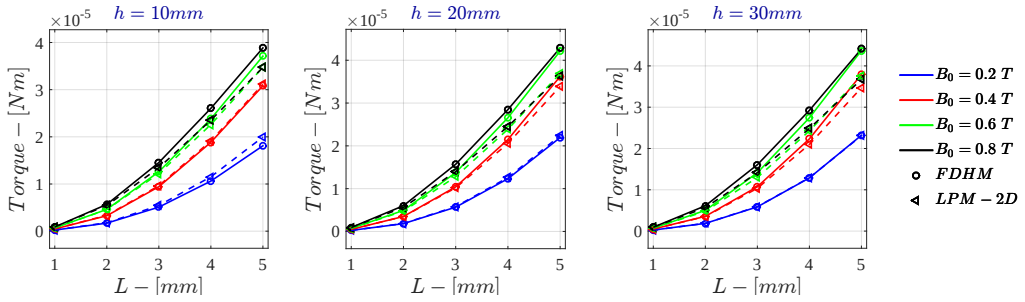

Figure G.41: *Bidimensional LPM - Voltage Drive* $\dot{\Gamma}$ *for* $\sigma = 10^3\ S/m$ *-* $r_{out} = 50mm$

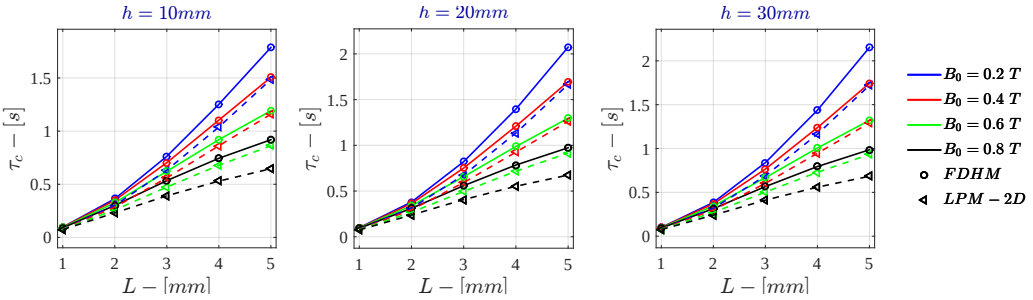

Figure G.42: *Bidimensional LPM - Voltage Drive* τ_c *for* $\sigma = 10^3\ S/m$ *-* $r_{out} = 50mm$

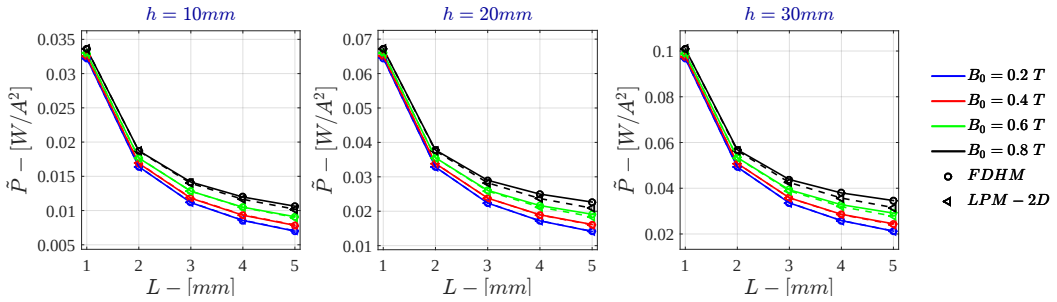

Figure G.43: *Bidimensional LPM - Voltage Drive* $\tilde{P}$ *for* $\sigma = 10^3\ S/m$ *-* $r_{out} = 50mm$

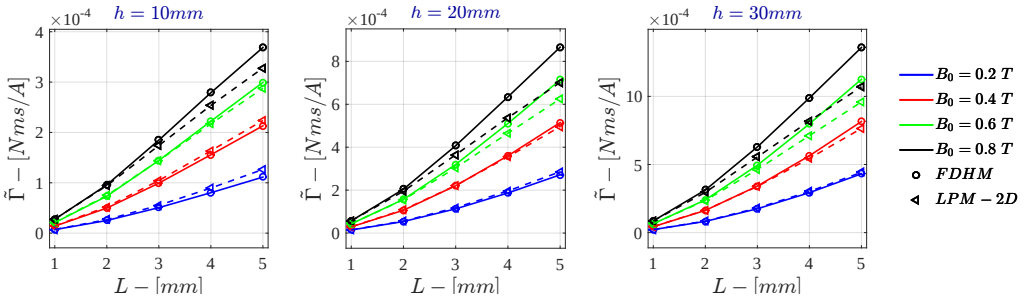

Figure G.44: *Bidimensional LPM - Voltage Drive* $\tilde{\Gamma}$ *for* $\sigma = 10^3\ S/m$ *-* $r_{out} = 50mm$

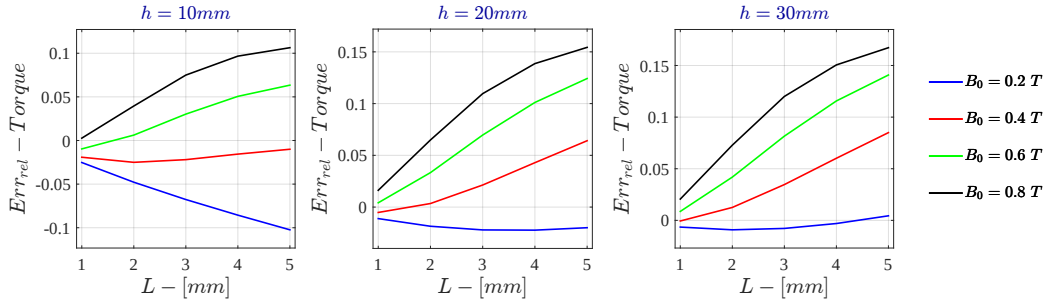

Figure G.45: *Bidimensional LPM - Voltage Drive Relative Error -* $\dot{\Gamma}$ *for* $\sigma = 10^3\ S/m$ *-* $r_{out} = 50mm$

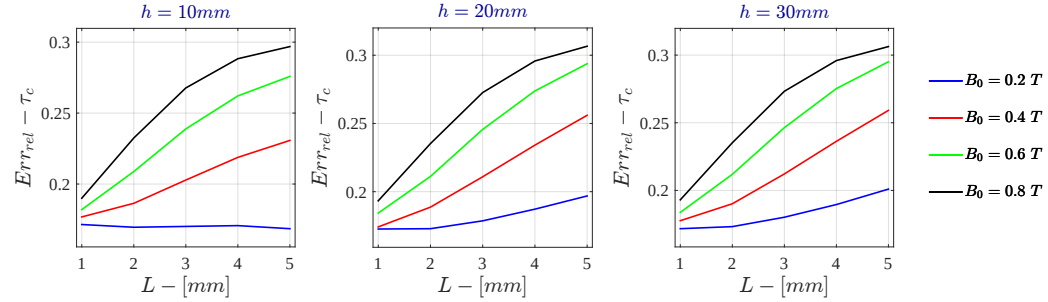

Figure G.46: *Bidimensional LPM - Voltage Drive Relative Error -* τ_c *for* $\sigma = 10^3\ S/m$ *-* $r_{out} = 50mm$

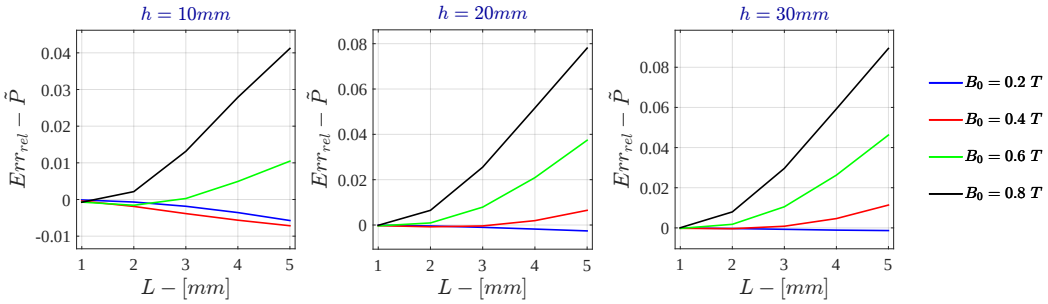

Figure G.47: *Bidimensional LPM - Voltage Drive Relative Error -* $\tilde{P}$ *for* $\sigma = 10^3\ S/m$ *-* $r_{out} = 50mm$

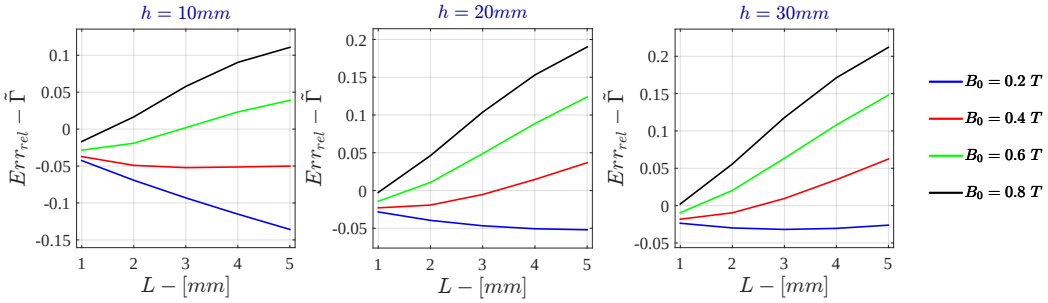

Figure G.48: *Bidimensional LPM - Voltage Drive Relative Error -* $\tilde{\Gamma}$ *for* $\sigma = 10^3\ S/m$ *-* $r_{out} = 50mm$

Appendix

H

Comparison between FDHM and LPM: $\sigma = 10^4\ S/m$

H.1 Monodimensional LPM - $\sigma = 10^4 S/m$

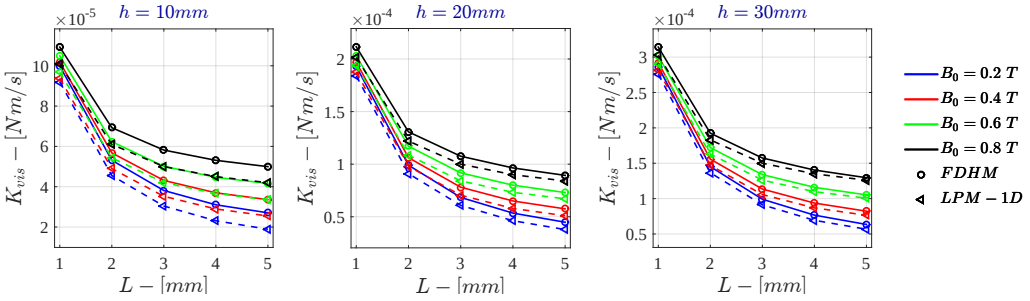

Figure H.1: *K_{vis} for $\sigma = 10^4\ S/m$ - $r_{out} = 50mm$ - Monodimensional LPM*

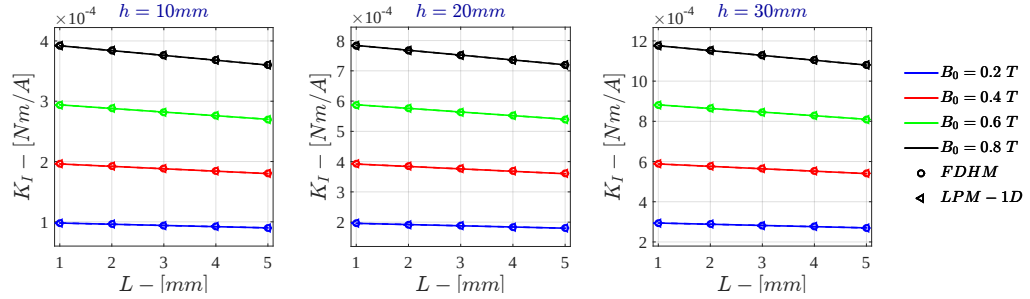

Figure H.2: *Monodimensional LPM*
K_I for $\sigma = 10^4\ S/m$ - $r_{out} = 50mm$

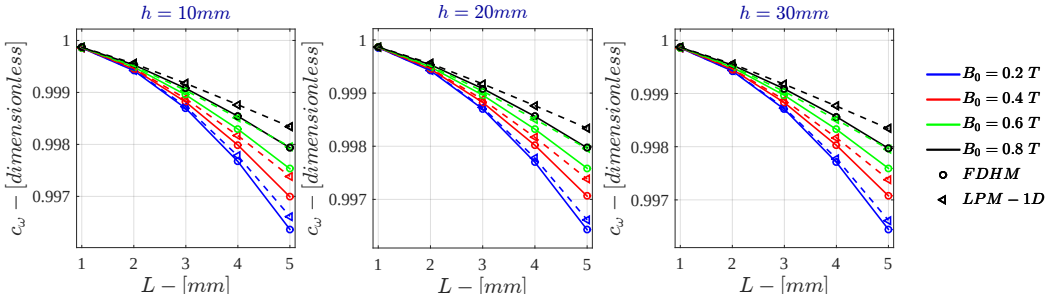

Figure H.3: *Monodimensional LPM*
c_ω for $\sigma = 10^4\ S/m$ - $r_{out} = 50mm$

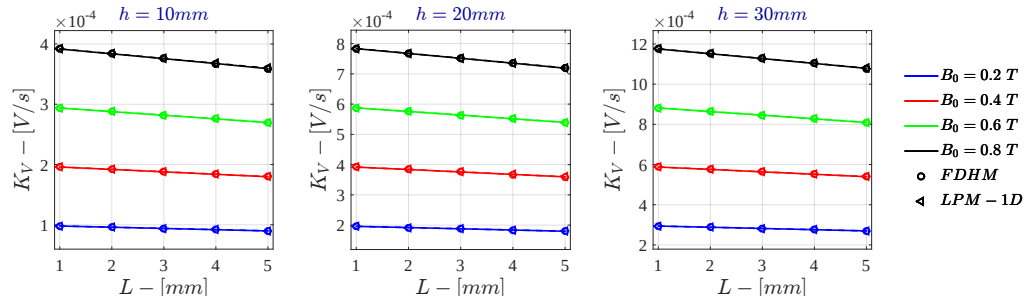

Figure H.4: *Monodimensional LPM*
K_V for $\sigma = 10^4\ S/m$ - $r_{out} = 50mm$

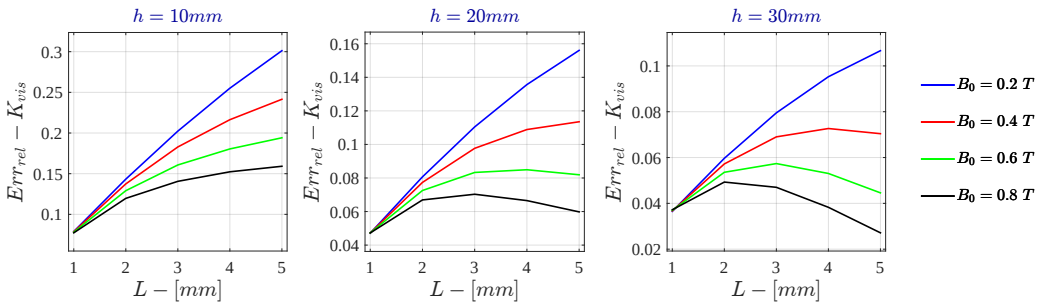

Figure H.5: *Monodimensional LPM*
Relative Error - K_{vis} for $\sigma = 10^4\ S/m$ - $r_{out} = 50mm$

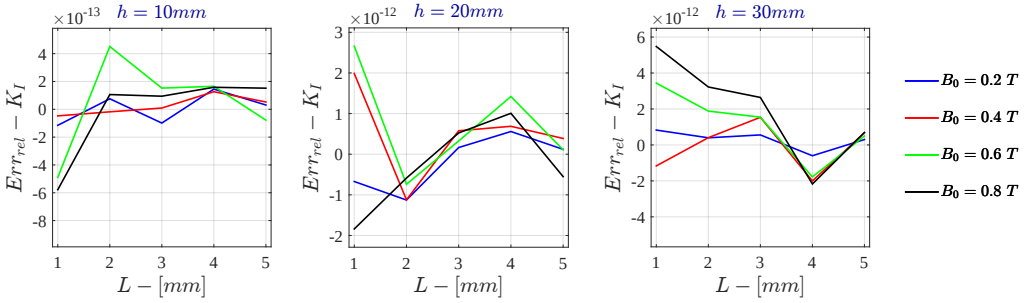

Figure H.6: *Monodimensional LPM*
Relative Error - K_I for $\sigma = 10^4\ S/m$ - $r_{out} = 50mm$

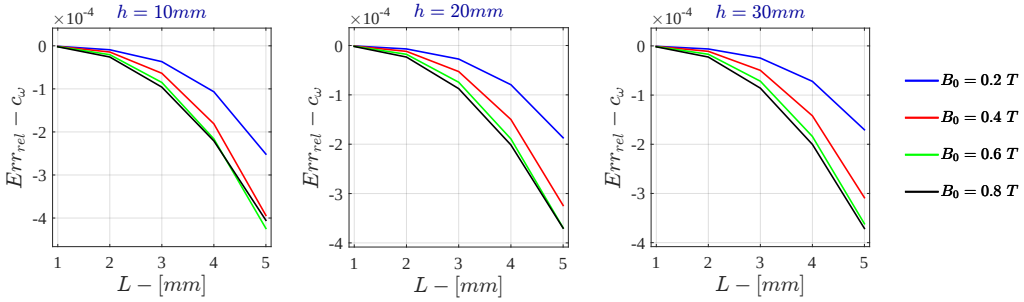

Figure H.7: *Monodimensional LPM*
Relative Error - c_ω for $\sigma = 10^4\ S/m$ - $r_{out} = 50mm$

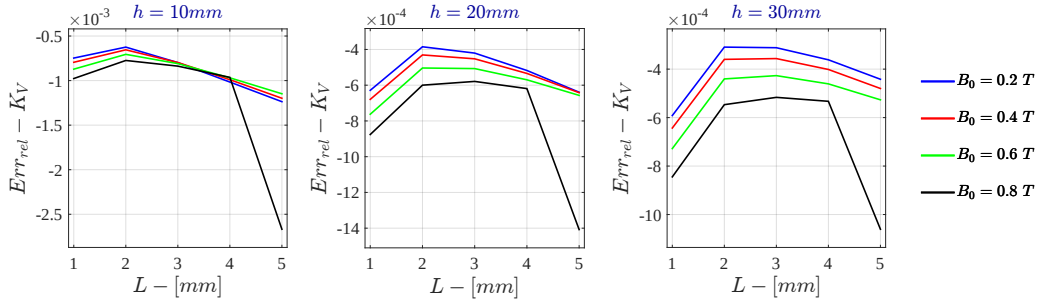

Figure H.8: *Monodimensional LPM*
Relative Error - K_V for $\sigma = 10^4\ S/m$ - $r_{out} = 50mm$

H.1.1 Current Drive

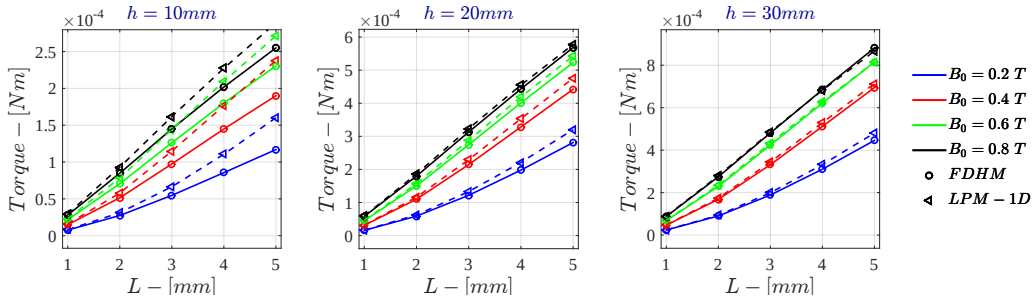

Figure H.9: *Monodimensional LPM - Current Drive* $\dot{\Gamma}$ *for* $\sigma = 10^4$ S/m - $r_{out} = 50mm$

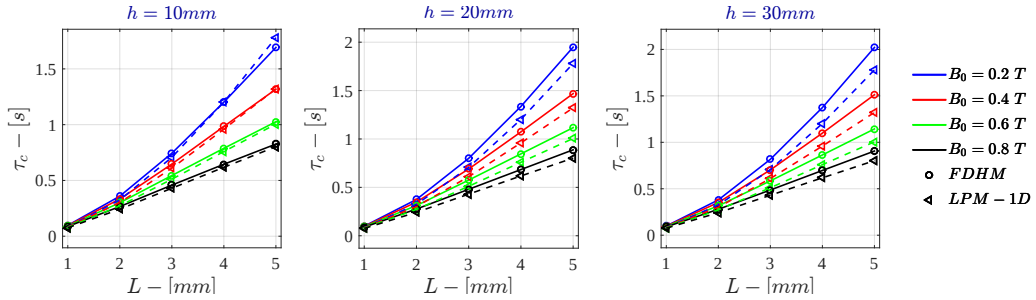

Figure H.10: *Monodimensional LPM - Current Drive* τ_c *for* $\sigma = 10^4$ S/m - $r_{out} = 50mm$

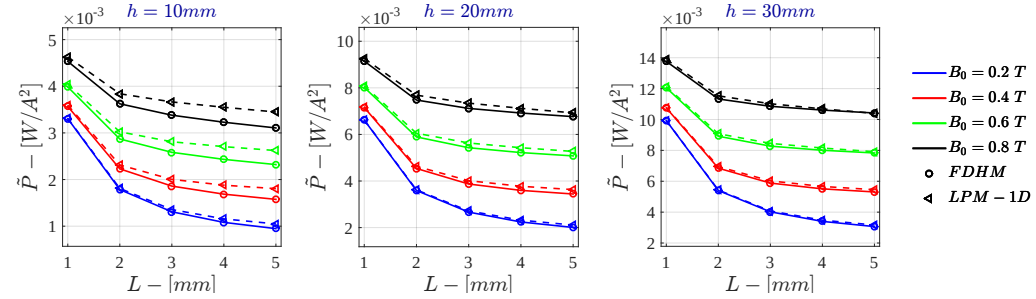

Figure H.11: *Monodimensional LPM - Current Drive* $\tilde{P}$ *for* $\sigma = 10^4$ S/m - $r_{out} = 50mm$

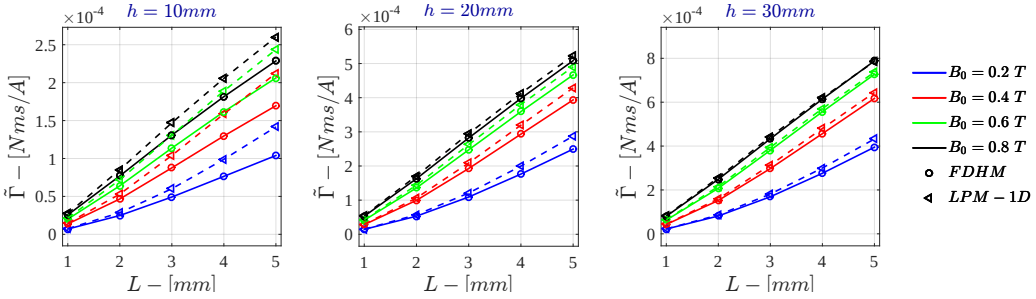

Figure H.12: *Monodimensional LPM - Current Drive* $\tilde{\Gamma}$ *for* $\sigma = 10^4$ S/m - $r_{out} = 50mm$

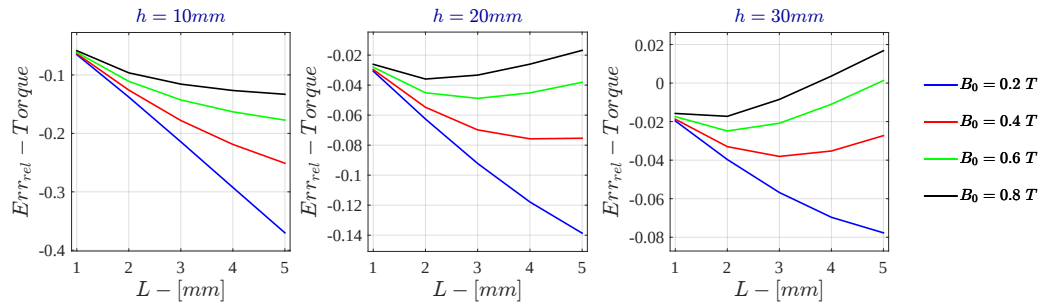

Figure H.13: *Monodimensional LPM - Current Drive*
Relative Error - $\dot{\Gamma}$ *for* $\sigma = 10^4\ S/m$ *-* $r_{out} = 50mm$

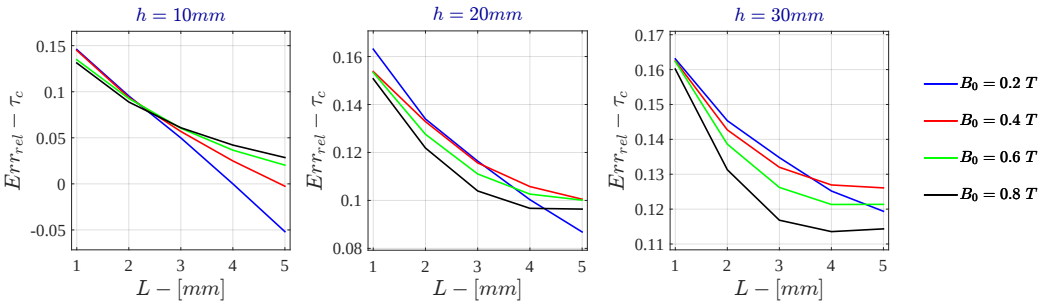

Figure H.14: *Monodimensional LPM - Current Drive*
Relative Error - τ_c *for* $\sigma = 10^4\ S/m$ *-* $r_{out} = 50mm$

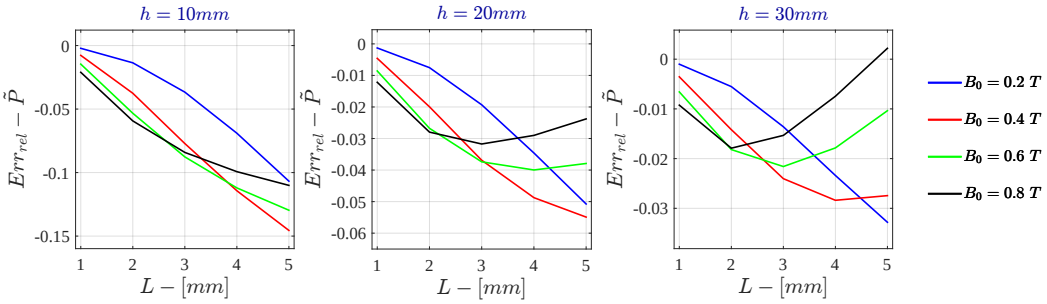

Figure H.15: *Monodimensional LPM - Current Drive*
Relative Error - $\tilde{P}$ *for* $\sigma = 10^4\ S/m$ *-* $r_{out} = 50mm$

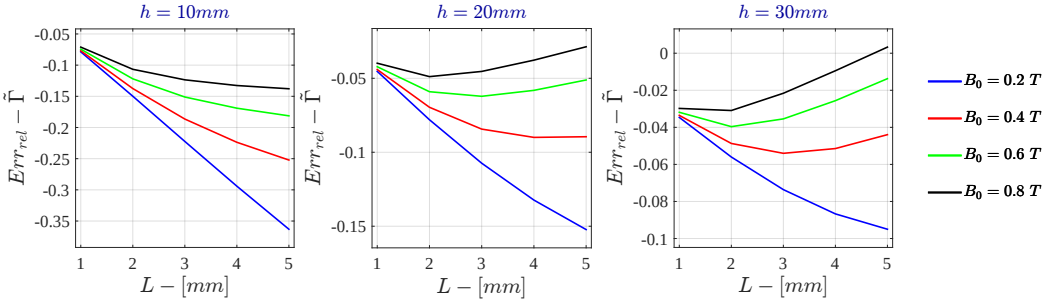

Figure H.16: *Monodimensional LPM - Current Drive*
Relative Error - $\tilde{\Gamma}$ *for* $\sigma = 10^4\ S/m$ *-* $r_{out} = 50mm$

H.1.2 Voltage Drive

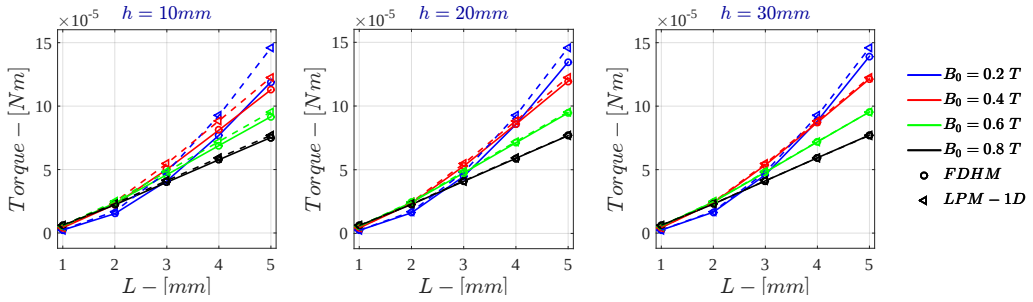

Figure H.17: *Monodimensional LPM - Voltage Drive* $\dot{\Gamma}$ *for* $\sigma = 10^4\ S/m$ *-* $r_{out} = 50mm$

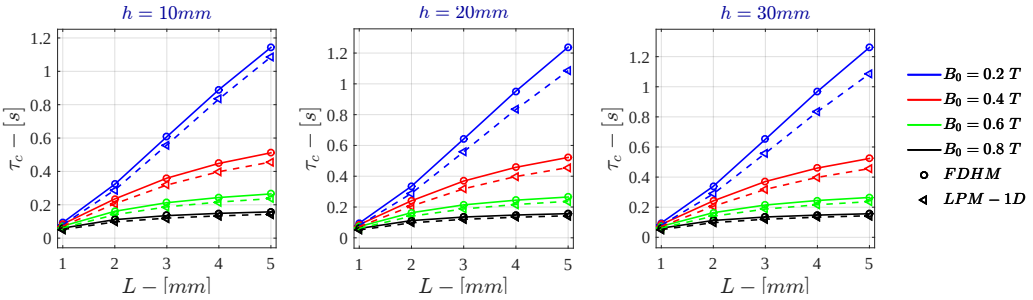

Figure H.18: *Monodimensional LPM - Voltage Drive* τ_c *for* $\sigma = 10^4\ S/m$ *-* $r_{out} = 50mm$

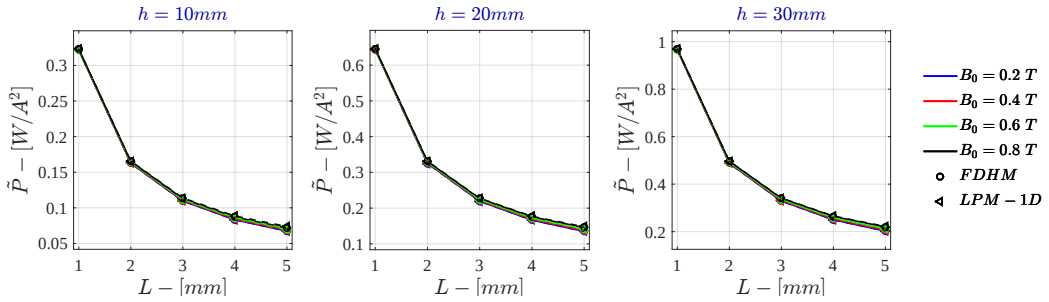

Figure H.19: *Monodimensional LPM - Voltage Drive* $\tilde{P}$ *for* $\sigma = 10^4\ S/m$ *-* $r_{out} = 50mm$

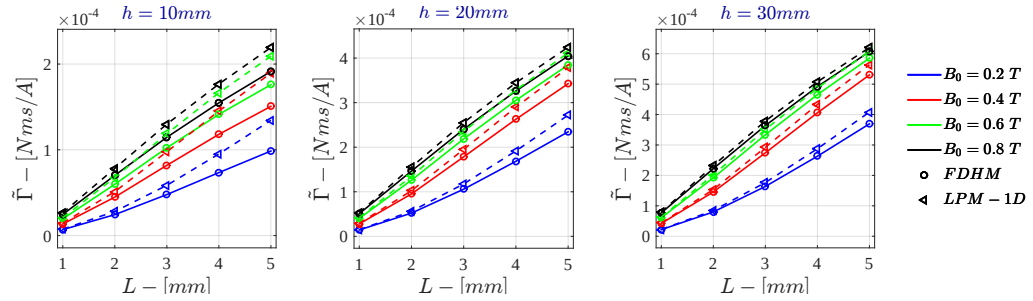

Figure H.20: *Monodimensional LPM - Voltage Drive* $\tilde{\Gamma}$ *for* $\sigma = 10^4\ S/m$ *-* $r_{out} = 50mm$

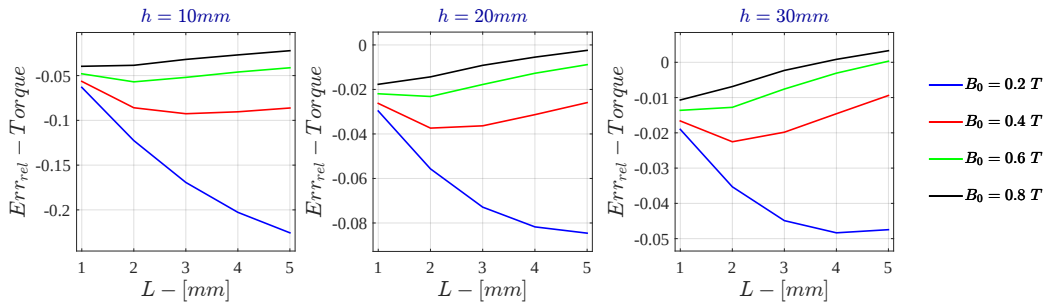

Figure H.21: *Monodimensional LPM - Voltage Drive*
Relative Error - $\dot{\Gamma}$ *for* $\sigma = 10^4\ S/m$ *-* $r_{out} = 50mm$

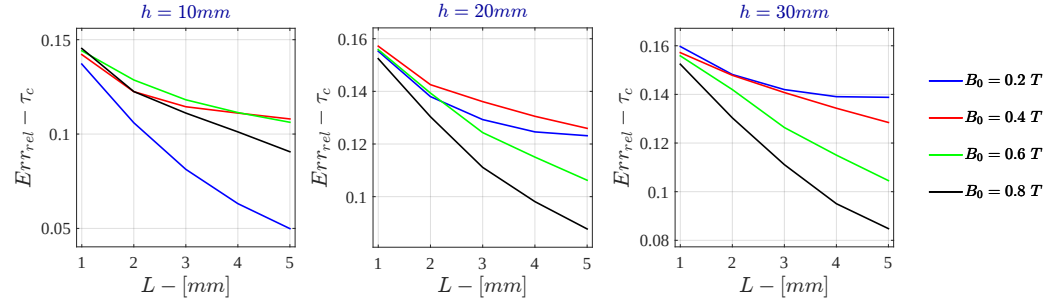

Figure H.22: *Monodimensional LPM - Voltage Drive*
Relative Error - τ_c *for* $\sigma = 10^4\ S/m$ *-* $r_{out} = 50mm$

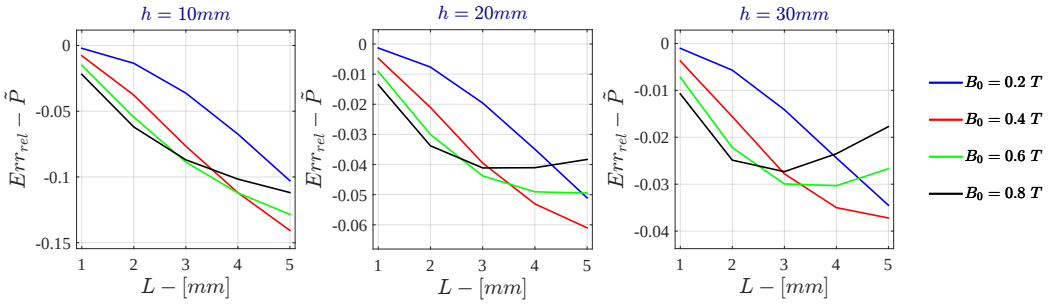

Figure H.23: *Monodimensional LPM - Voltage Drive*
Relative Error - $\tilde{P}$ *for* $\sigma = 10^4\ S/m$ *-* $r_{out} = 50mm$

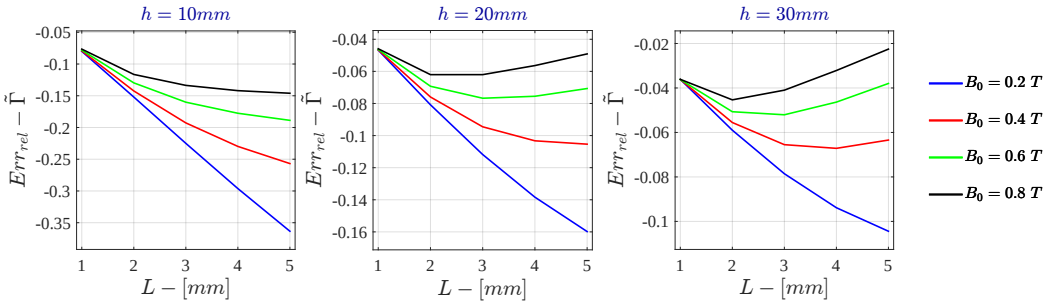

Figure H.24: *Monodimensional LPM - Voltage Drive*
Relative Error - $\tilde{\Gamma}$ *for* $\sigma = 10^4\ S/m$ *-* $r_{out} = 50mm$

H.2 Bidimensional LPM - $\sigma = 10^4 S/m$

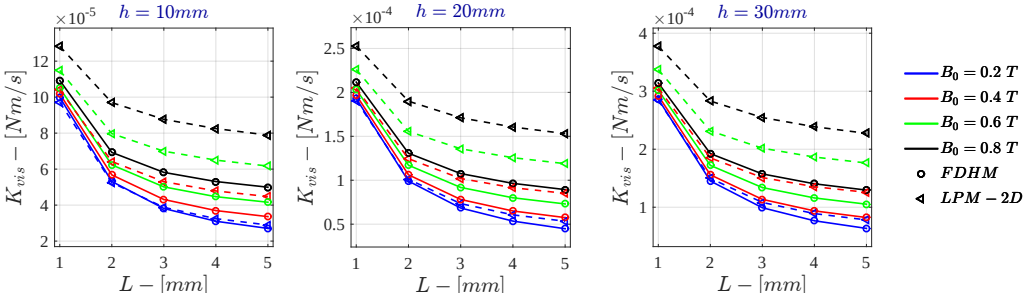

Figure H.25: *Bidimensional LPM* K_{vis} *for* $\sigma = 10^4\ S/m$ - $r_{out} = 50mm$

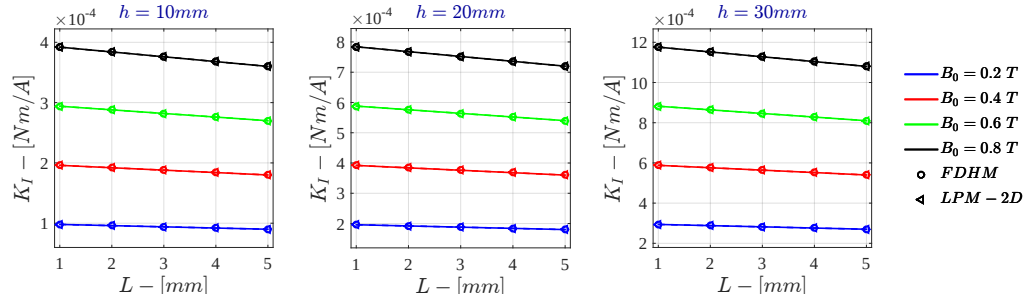

Figure H.26: *Bidimensional LPM* K_I *for* $\sigma = 10^4\ S/m$ - $r_{out} = 50mm$

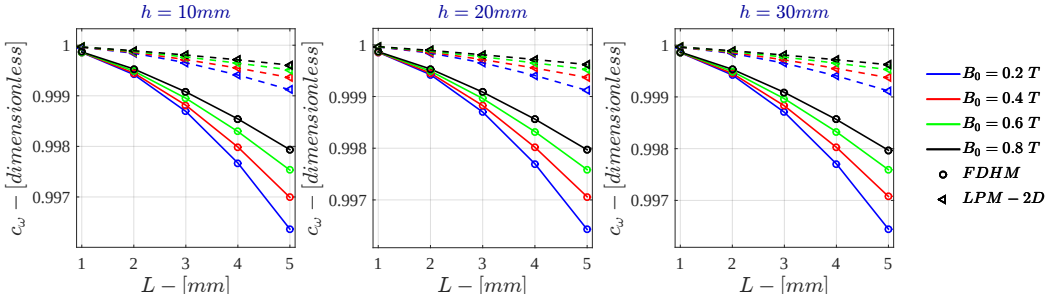

Figure H.27: *Bidimensional LPM* c_ω *for* $\sigma = 10^4\ S/m$ - $r_{out} = 50mm$

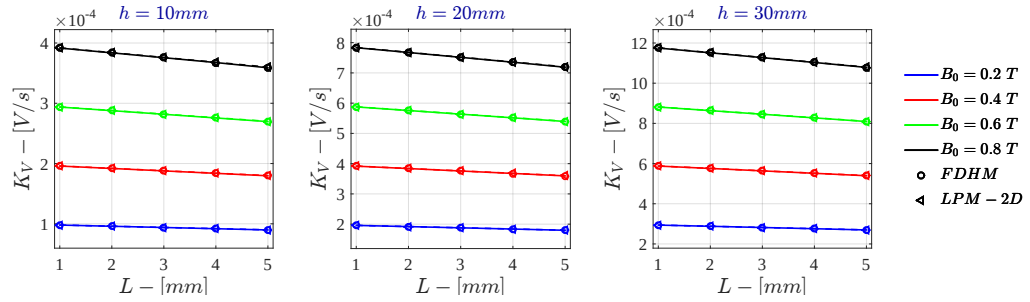

Figure H.28: *Bidimensional LPM* K_V *for* $\sigma = 10^4\ S/m$ - $r_{out} = 50mm$

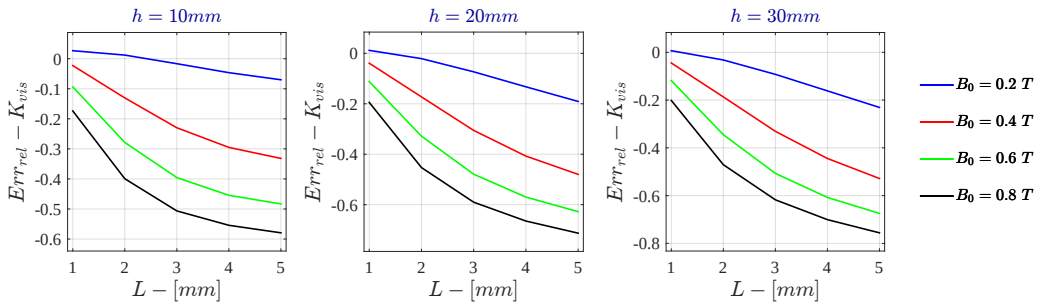

Figure H.29: *Bidimensional LPM*
Relative Error - K_{vis} for $\sigma = 10^4\ S/m$ - $r_{out} = 50mm$

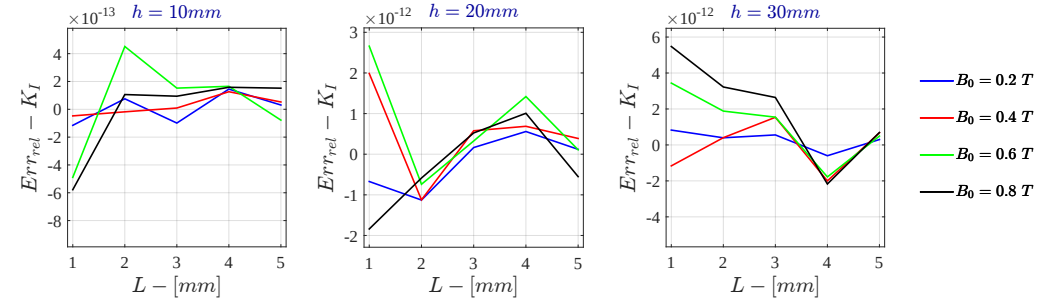

Figure H.30: *Bidimensional LPM*
Relative Error - K_I for $\sigma = 10^4\ S/m$ - $r_{out} = 50mm$

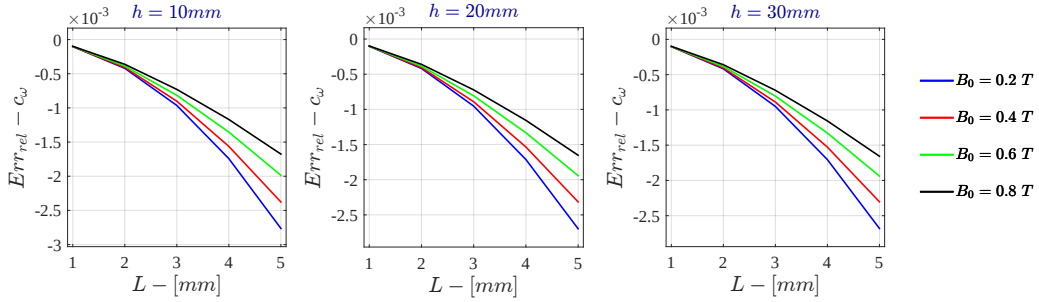

Figure H.31: *Bidimensional LPM*
Relative Error - c_ω for $\sigma = 10^4\ S/m$ - $r_{out} = 50mm$

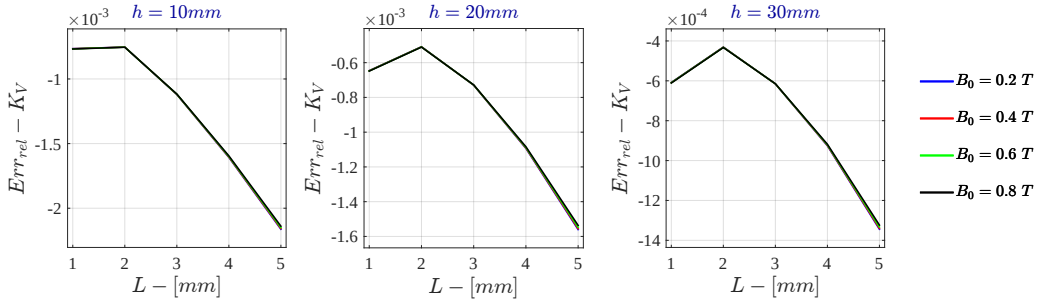

Figure H.32: *Bidimensional LPM*
Relative Error - K_V for $\sigma = 10^4\ S/m$ - $r_{out} = 50mm$

H.2.1 Current Drive

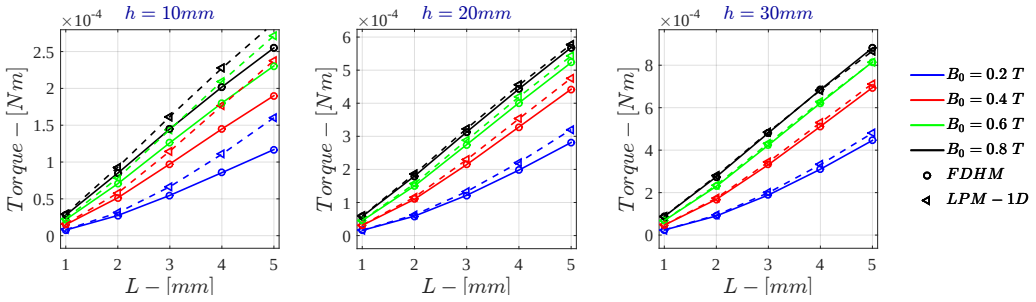

Figure H.33: *Bidimensional LPM - Current Drive* $\dot{\Gamma}$ *for* $\sigma = 10^4$ *S/m -* $r_{out} = 50mm$

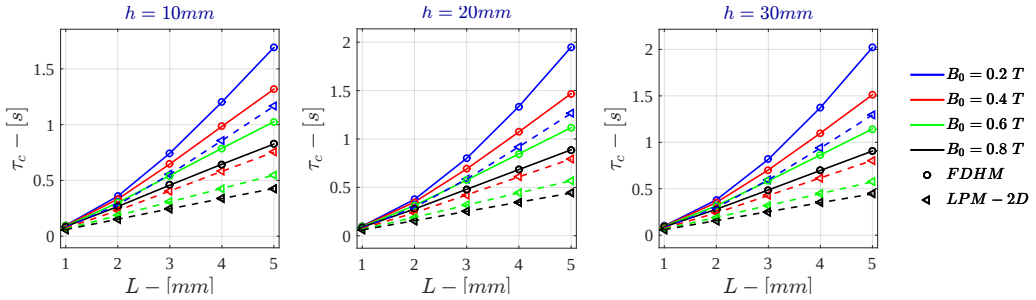

Figure H.34: *Bidimensional LPM - Current Drive* τ_c *for* $\sigma = 10^4$ *S/m -* $r_{out} = 50mm$

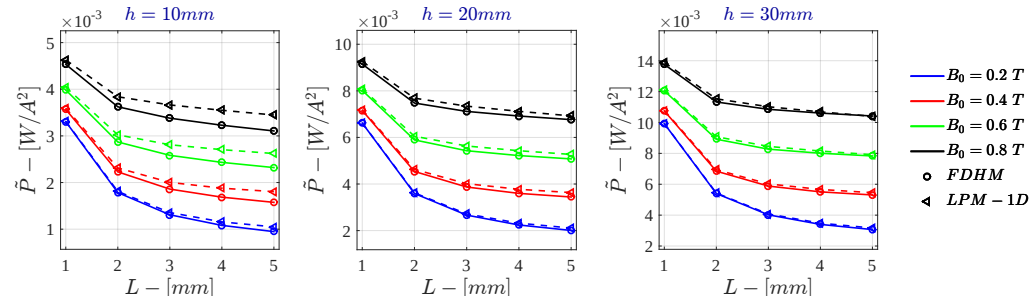

Figure H.35: *Bidimensional LPM - Current Drive* $\tilde{P}$ *for* $\sigma = 10^4$ *S/m -* $r_{out} = 50mm$

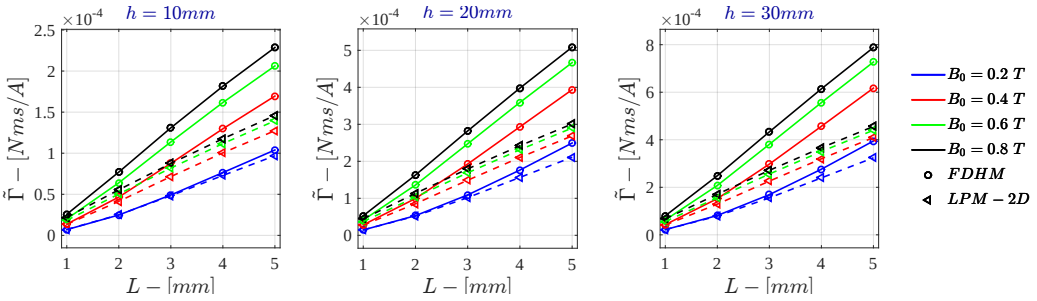

Figure H.36: *Bidimensional LPM - Current Drive* $\tilde{\Gamma}$ *for* $\sigma = 10^4$ *S/m -* $r_{out} = 50mm$

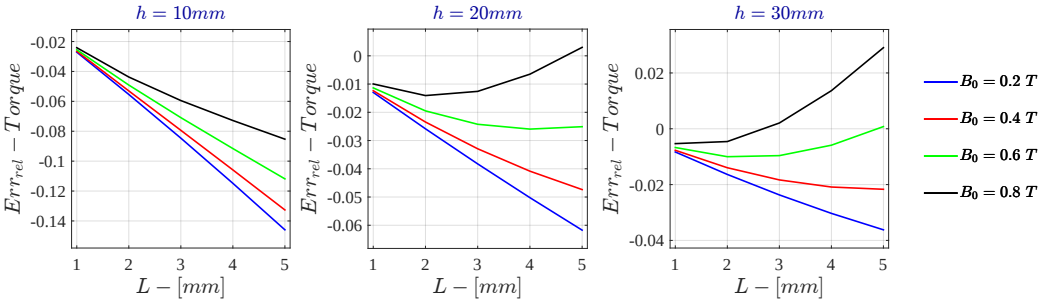

Figure H.37: *Bidimensional LPM - Current Drive*
Relative Error - $\dot{\Gamma}$ *for* $\sigma = 10^4\ S/m$ *-* $r_{out} = 50mm$

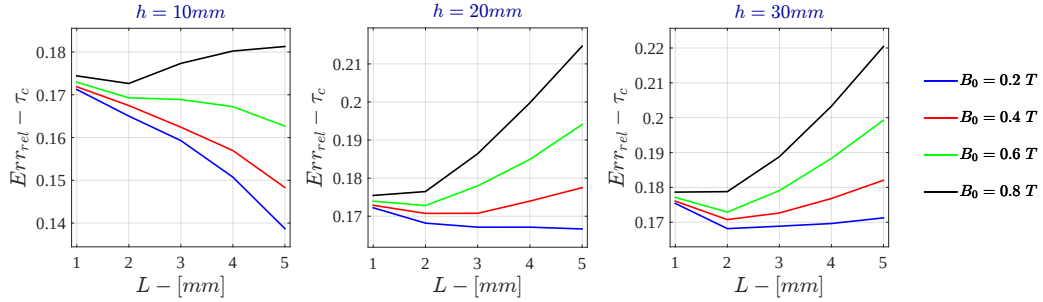

Figure H.38: *Bidimensional LPM - Current Drive*
Relative Error - τ_c *for* $\sigma = 10^4\ S/m$ *-* $r_{out} = 50mm$

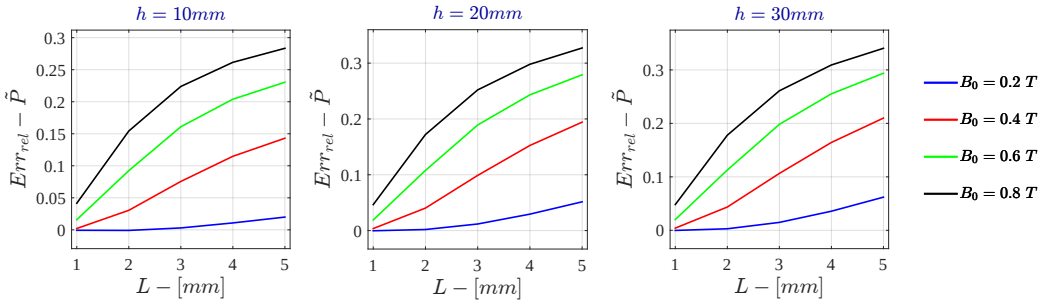

Figure H.39: *Bidimensional LPM - Current Drive*
Relative Error - $\tilde{P}$ *for* $\sigma = 10^4\ S/m$ *-* $r_{out} = 50mm$

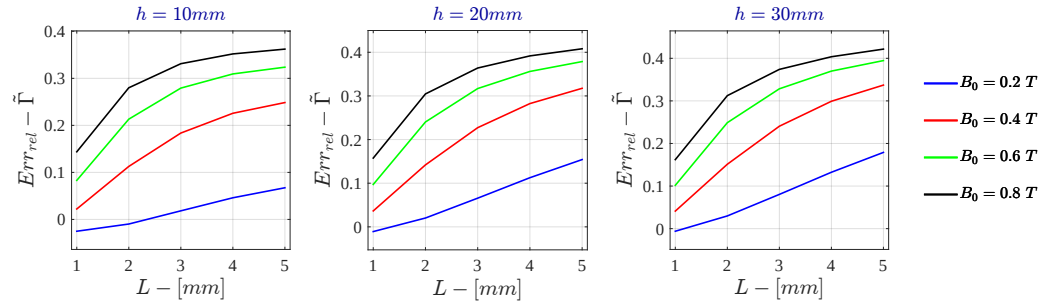

Figure H.40: *Bidimensional LPM - Current Drive*
Relative Error - $\tilde{\Gamma}$ *for* $\sigma = 10^4\ S/m$ *-* $r_{out} = 50mm$

H.2.2 Voltage Drive

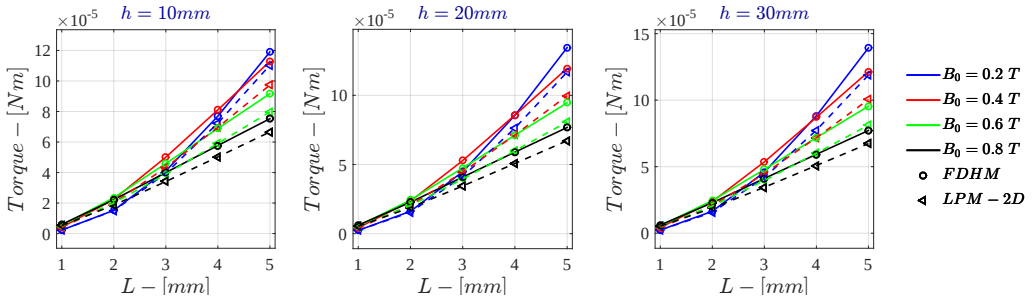

Figure H.41: *Bidimensional LPM - Voltage Drive* $\dot{\Gamma}$ *for* $\sigma = 10^4$ S/m - $r_{out} = 50mm$

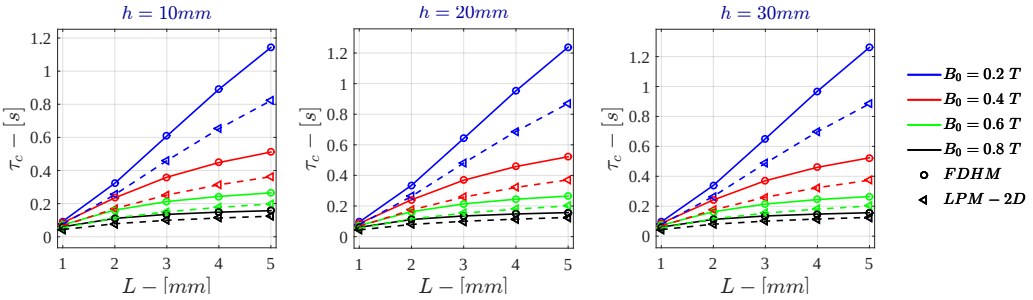

Figure H.42: *Bidimensional LPM - Voltage Drive* τ_c *for* $\sigma = 10^4$ S/m - $r_{out} = 50mm$

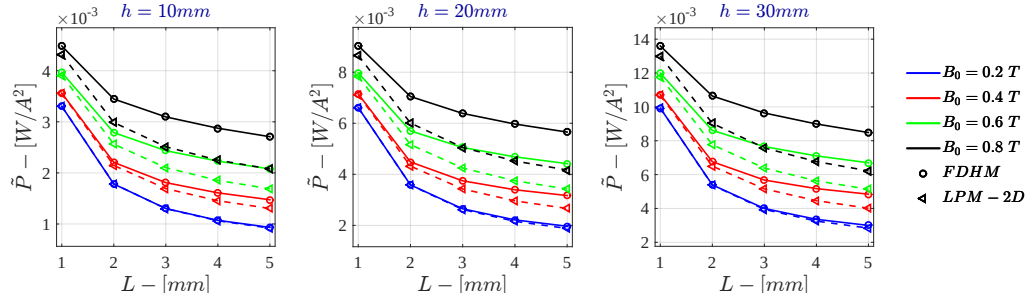

Figure H.43: *Bidimensional LPM - Voltage Drive* $\tilde{P}$ *for* $\sigma = 10^4$ S/m - $r_{out} = 50mm$

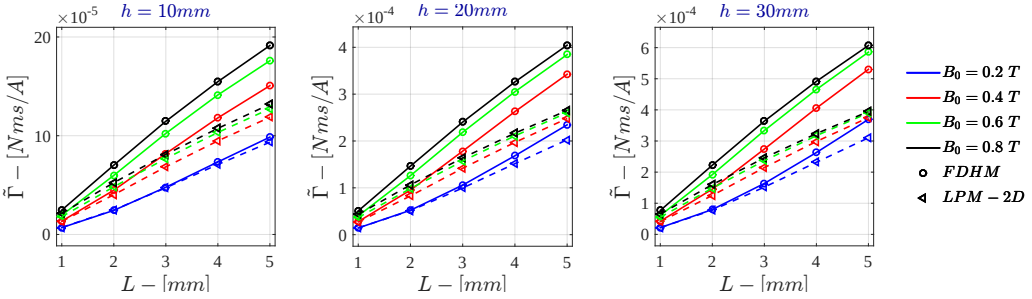

Figure H.44: *Bidimensional LPM - Voltage Drive* $\tilde{\Gamma}$ *for* $\sigma = 10^4$ S/m - $r_{out} = 50mm$

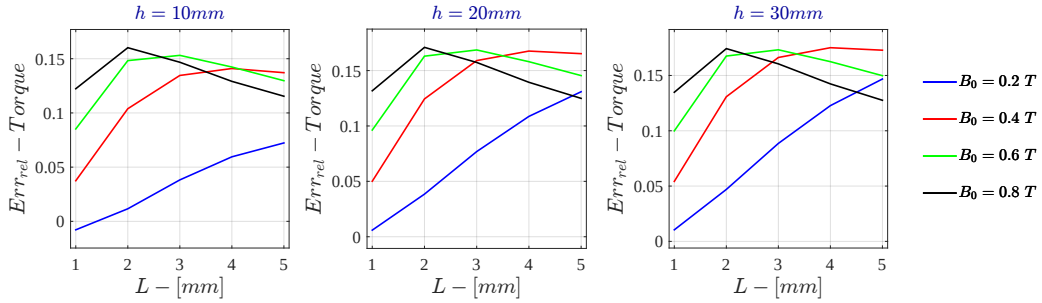

Figure H.45: *Bidimensional LPM - Voltage Drive Relative Error -* $\dot{\Gamma}$ *for* $\sigma = 10^4\ S/m$ *-* $r_{out} = 50mm$

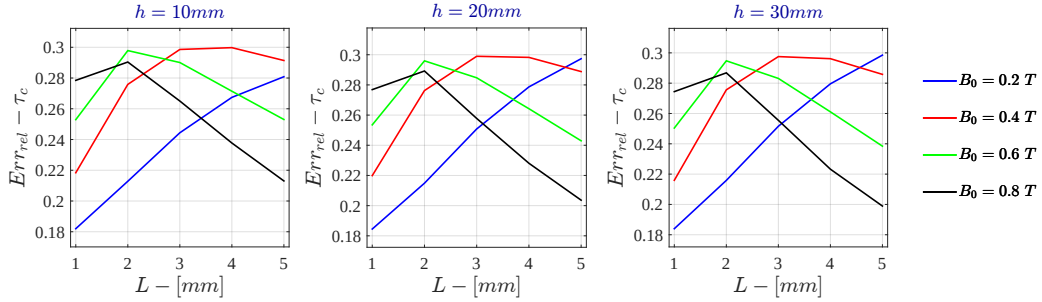

Figure H.46: *Bidimensional LPM - Voltage Drive Relative Error -* τ_c *for* $\sigma = 10^4\ S/m$ *-* $r_{out} = 50mm$

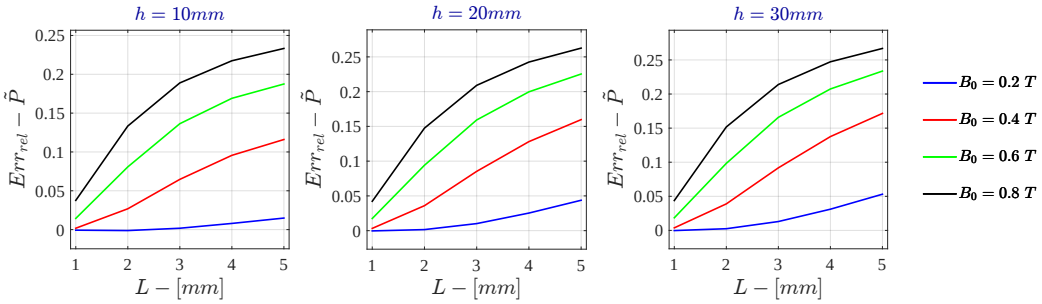

Figure H.47: *Bidimensional LPM - Voltage Drive Relative Error -* $\tilde{P}$ *for* $\sigma = 10^4\ S/m$ *-* $r_{out} = 50mm$

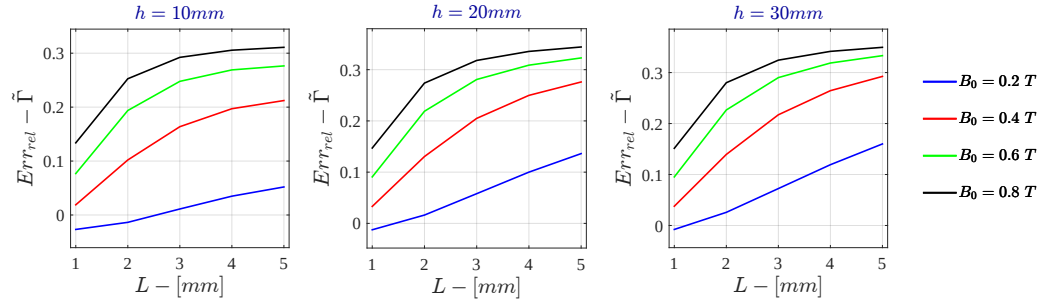

Figure H.48: *Bidimensional LPM - Voltage Drive Relative Error -* $\tilde{\Gamma}$ *for* $\sigma = 10^4\ S/m$ *-* $r_{out} = 50mm$

Appendix

I Comparison between FDHM and LPM: $\sigma = 10^5\ S/m$

I.1 Monodimensional LPM - $\sigma = 10^5 S/m$

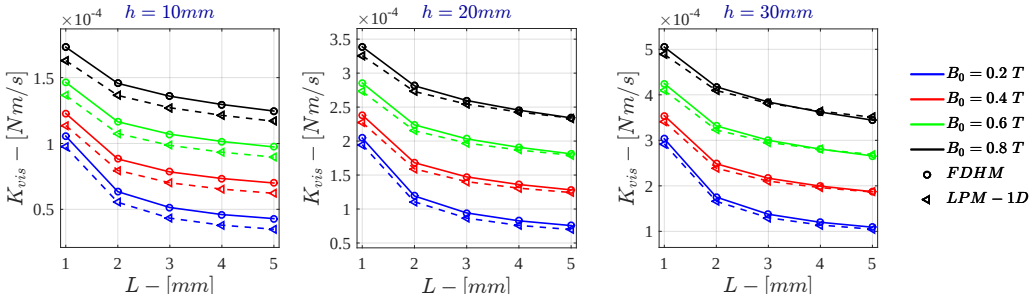

Figure I.1: K_{vis} *for* $\sigma = 10^5\ S/m$ - $r_{out} = 50mm$ - *Monodimensional LPM*

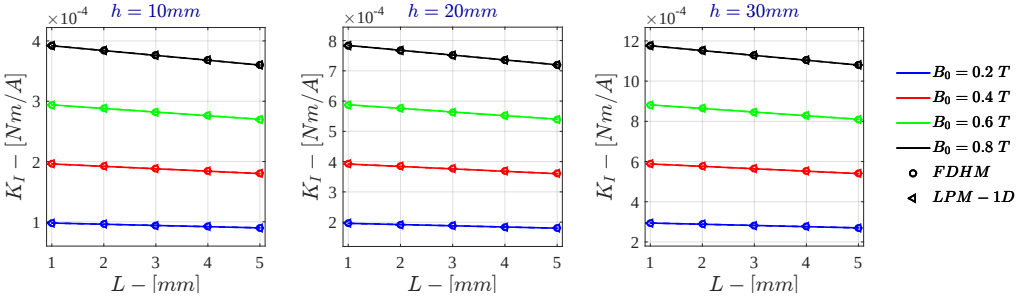

Figure I.2: *Monodimensional LPM*
K_I *for* $\sigma = 10^5\ S/m$ - $r_{out} = 50mm$

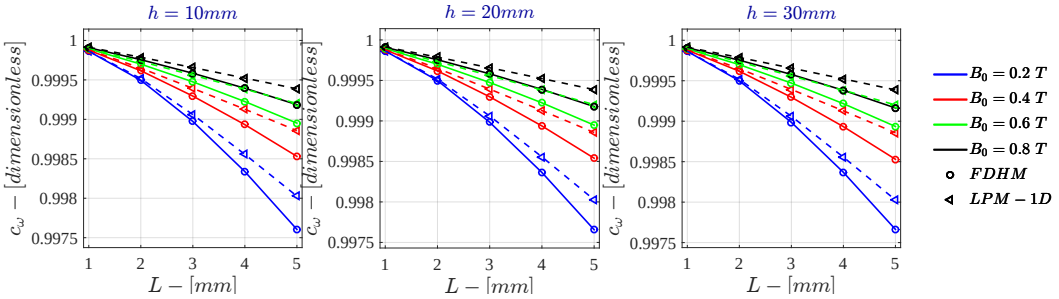

Figure I.3: *Monodimensional LPM*
c_ω *for* $\sigma = 10^5\ S/m$ - $r_{out} = 50mm$

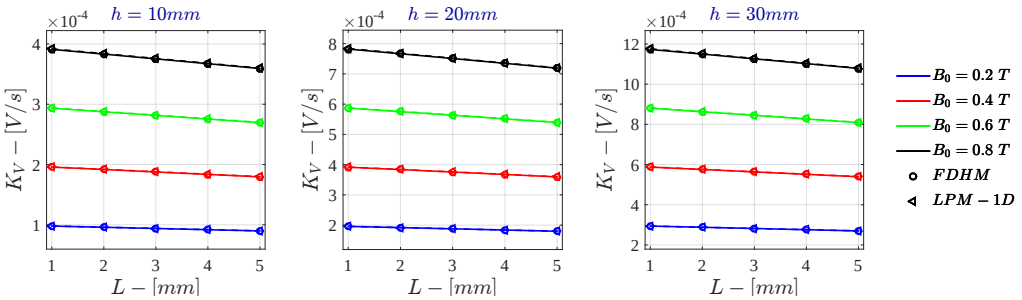

Figure I.4: *Monodimensional LPM*
K_V *for* $\sigma = 10^5\ S/m$ - $r_{out} = 50mm$

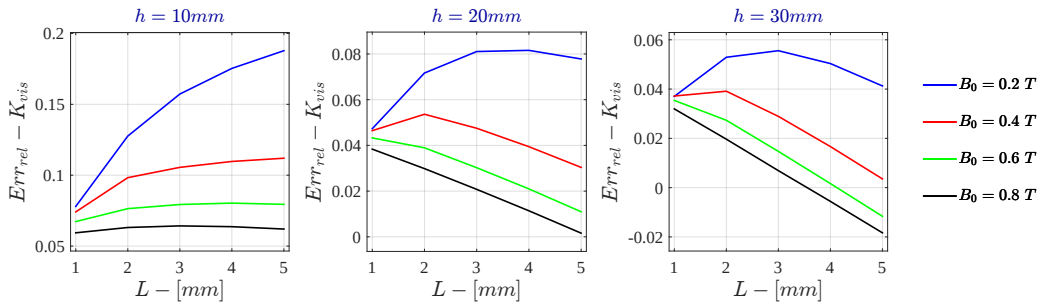

Figure I.5: *Monodimensional LPM*
Relative Error - K_{vis} for $\sigma = 10^5\ S/m$ - $r_{out} = 50mm$

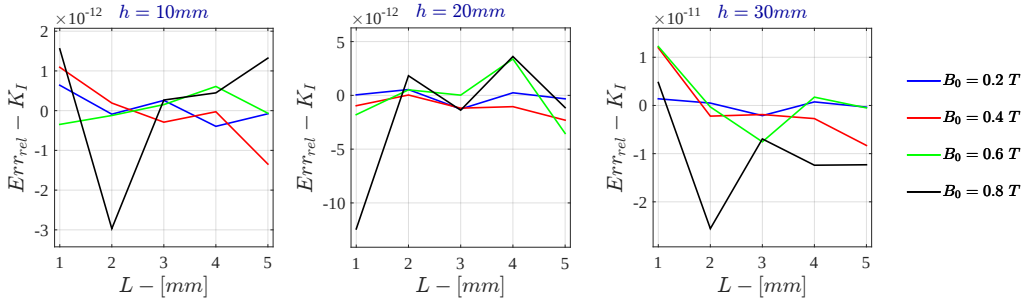

Figure I.6: *Monodimensional LPM*
Relative Error - K_I for $\sigma = 10^5\ S/m$ - $r_{out} = 50mm$

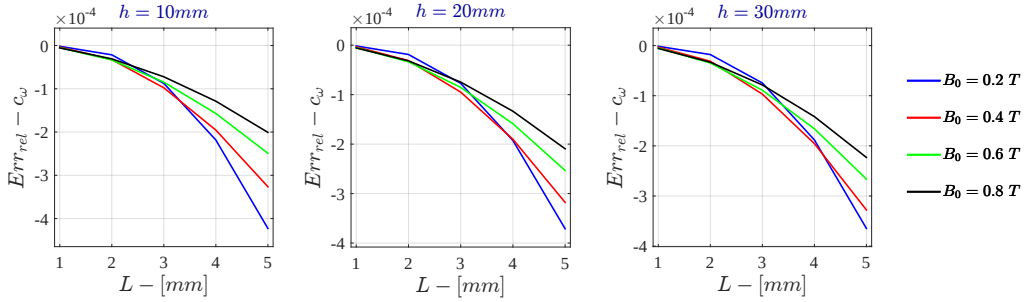

Figure I.7: *Monodimensional LPM*
Relative Error - c_ω for $\sigma = 10^5\ S/m$ - $r_{out} = 50mm$

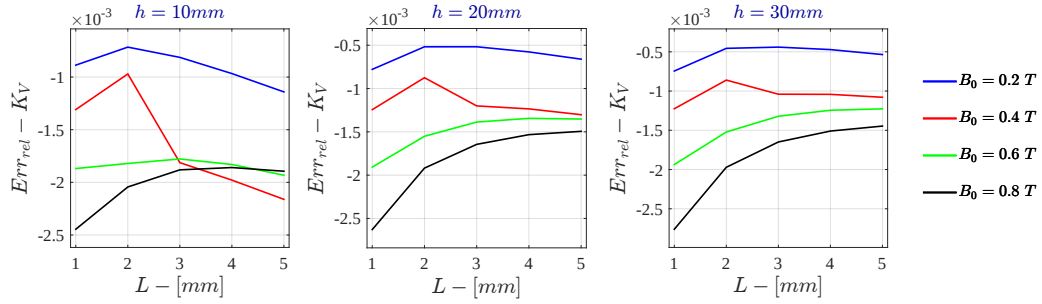

Figure I.8: *Monodimensional LPM*
Relative Error - K_V for $\sigma = 10^5\ S/m$ - $r_{out} = 50mm$

I.1.1 Current Drive

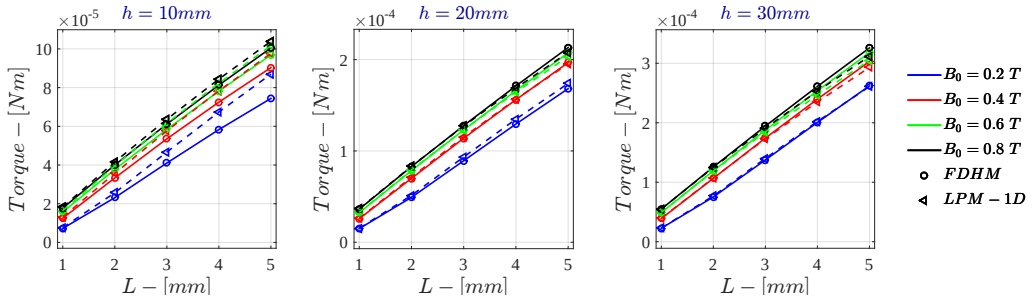

Figure I.9: *Monodimensional LPM - Current Drive* $\dot{\Gamma}$ *for* $\sigma = 10^5$ *S/m -* $r_{out} = 50mm$

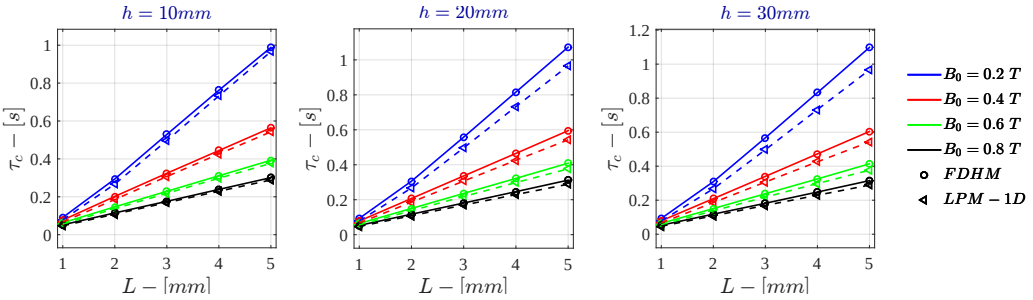

Figure I.10: *Monodimensional LPM - Current Drive* τ_c *for* $\sigma = 10^5$ *S/m -* $r_{out} = 50mm$

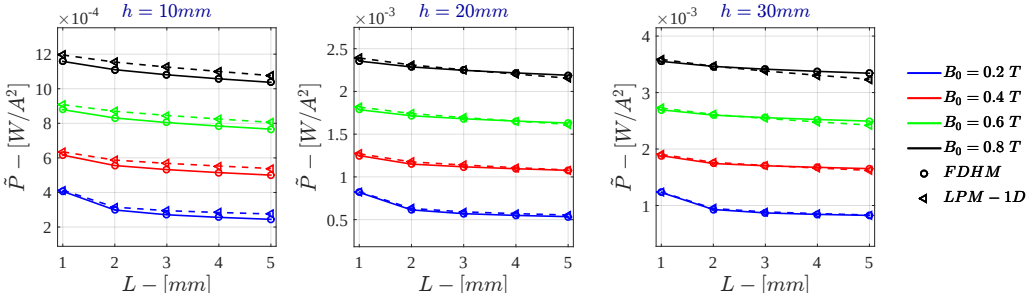

Figure I.11: *Monodimensional LPM - Current Drive* $\tilde{P}$ *for* $\sigma = 10^5$ *S/m -* $r_{out} = 50mm$

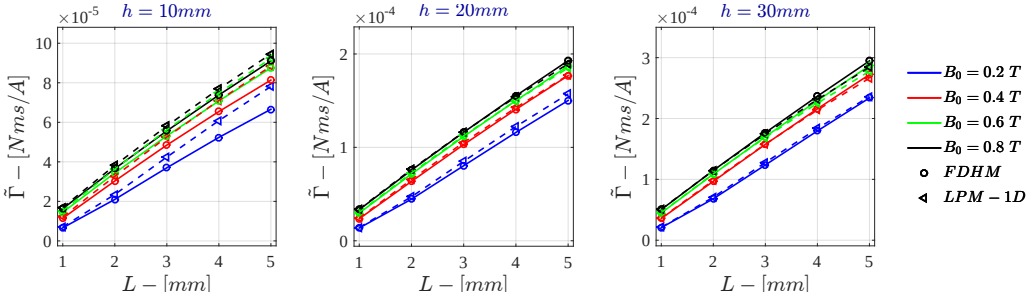

Figure I.12: *Monodimensional LPM - Current Drive* $\tilde{\Gamma}$ *for* $\sigma = 10^5$ *S/m -* $r_{out} = 50mm$

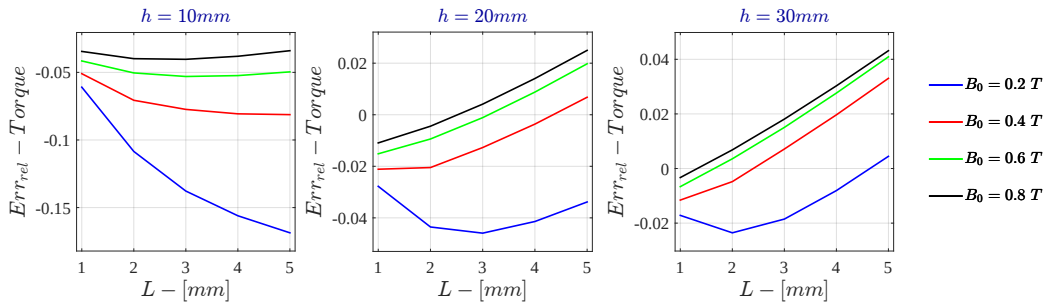

Figure I.13: *Monodimensional LPM - Current Drive Relative Error -* $\dot{\Gamma}$ *for* $\sigma = 10^5\ S/m$ *-* $r_{out} = 50mm$

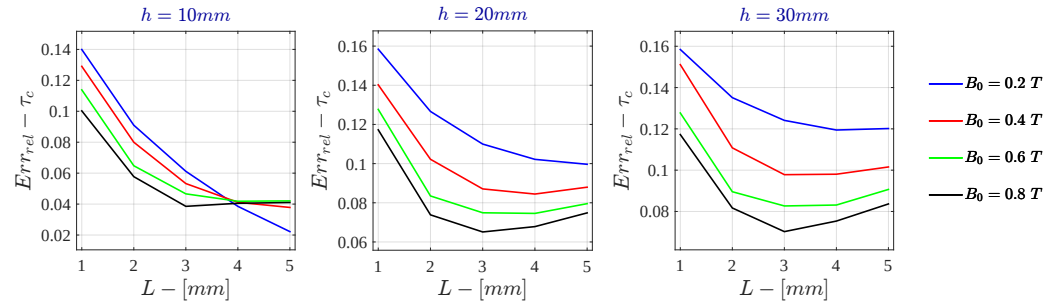

Figure I.14: *Monodimensional LPM - Current Drive Relative Error -* τ_c *for* $\sigma = 10^5\ S/m$ *-* $r_{out} = 50mm$

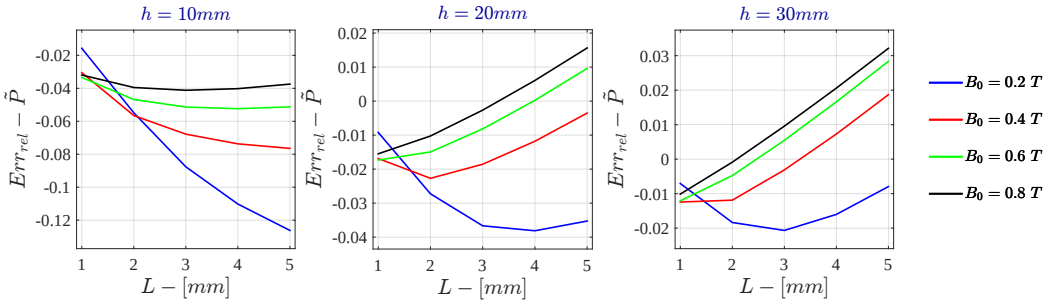

Figure I.15: *Monodimensional LPM - Current Drive Relative Error -* $\tilde{P}$ *for* $\sigma = 10^5\ S/m$ *-* $r_{out} = 50mm$

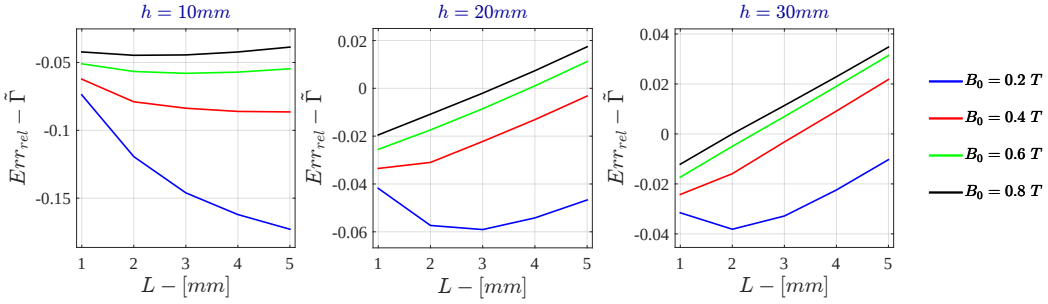

Figure I.16: *Monodimensional LPM - Current Drive Relative Error -* $\tilde{\Gamma}$ *for* $\sigma = 10^5\ S/m$ *-* $r_{out} = 50mm$

I.1.2 Voltage Drive

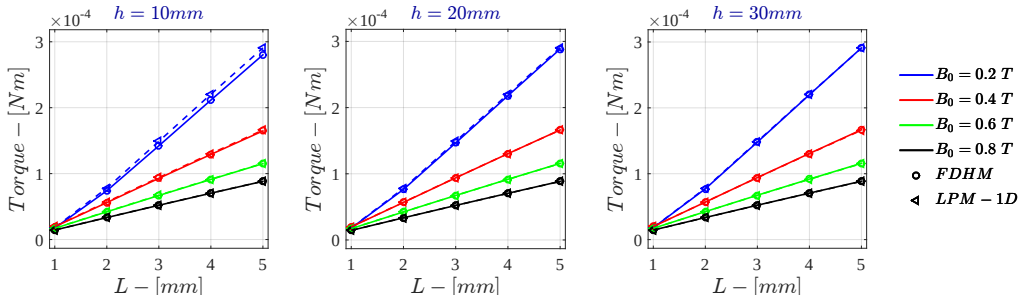

Figure I.17: *Monodimensional LPM - Voltage Drive* $\dot{\Gamma}$ *for* $\sigma = 10^5\ S/m$ - $r_{out} = 50mm$

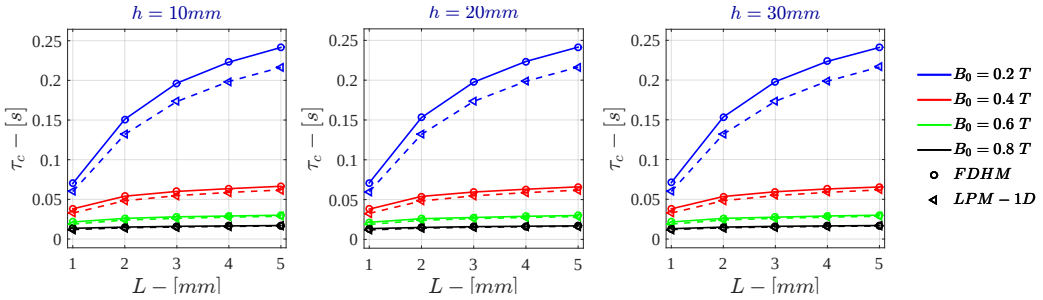

Figure I.18: *Monodimensional LPM - Voltage Drive* τ_c *for* $\sigma = 10^5\ S/m$ - $r_{out} = 50mm$

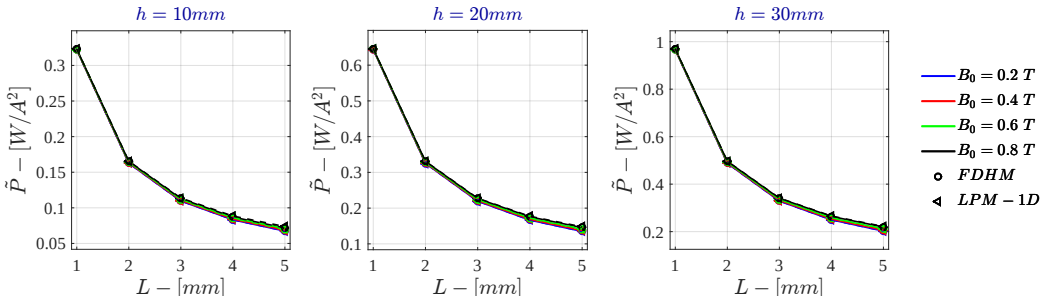

Figure I.19: *Monodimensional LPM - Voltage Drive* $\tilde{P}$ *for* $\sigma = 10^5\ S/m$ - $r_{out} = 50mm$

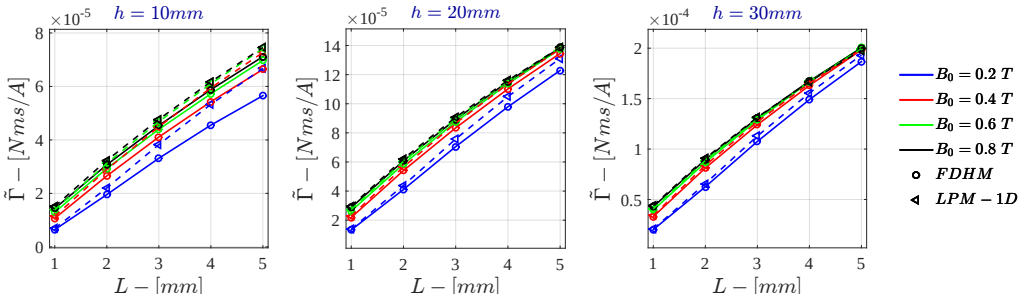

Figure I.20: *Monodimensional LPM - Voltage Drive* $\tilde{\Gamma}$ *for* $\sigma = 10^5\ S/m$ - $r_{out} = 50mm$

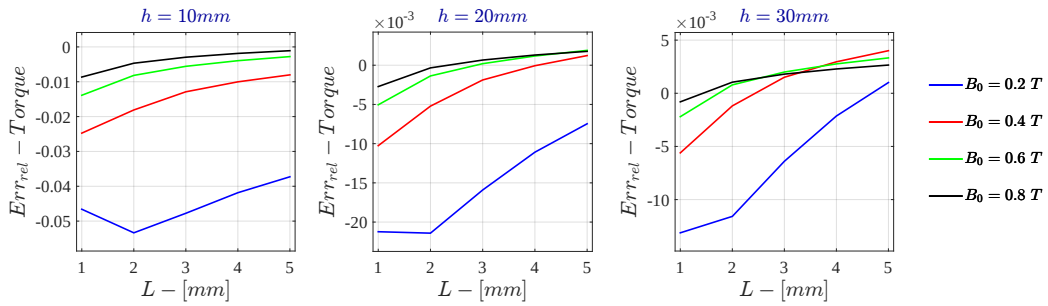

Figure I.21: *Monodimensional LPM - Voltage Drive*
Relative Error - $\dot{\Gamma}$ *for* $\sigma = 10^5\ S/m$ *-* $r_{out} = 50mm$

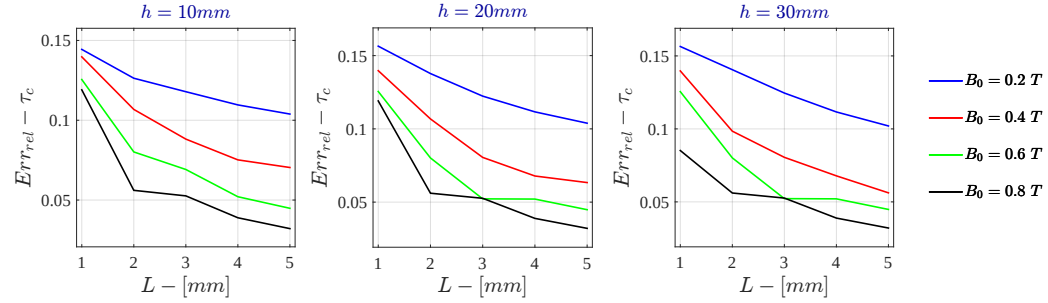

Figure I.22: *Monodimensional LPM - Voltage Drive*
Relative Error - τ_c *for* $\sigma = 10^5\ S/m$ *-* $r_{out} = 50mm$

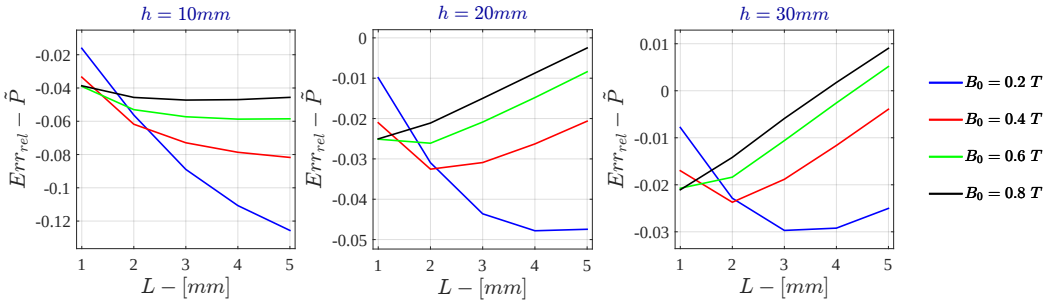

Figure I.23: *Monodimensional LPM - Voltage Drive*
Relative Error - $\tilde{P}$ *for* $\sigma = 10^5\ S/m$ *-* $r_{out} = 50mm$

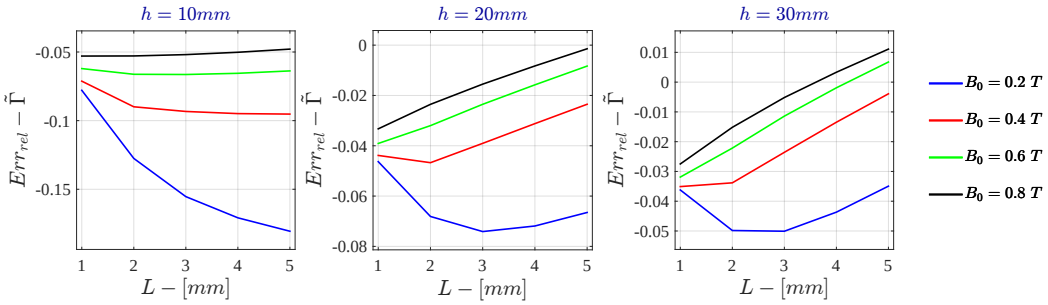

Figure I.24: *Monodimensional LPM - Voltage Drive*
Relative Error - $\tilde{\Gamma}$ *for* $\sigma = 10^5\ S/m$ *-* $r_{out} = 50mm$

I.2 Bidimensional LPM - $\sigma = 10^5 S/m$

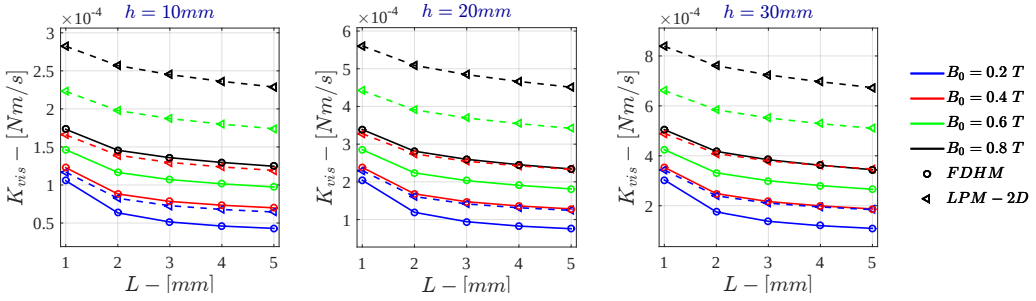

Figure I.25: *Bidimensional LPM* K_{vis} *for* $\sigma = 10^5\ S/m$ - $r_{out} = 50mm$

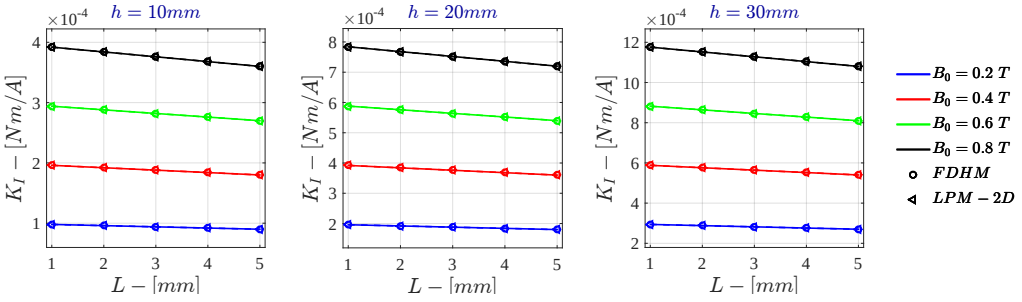

Figure I.26: *Bidimensional LPM* K_I *for* $\sigma = 10^5\ S/m$ - $r_{out} = 50mm$

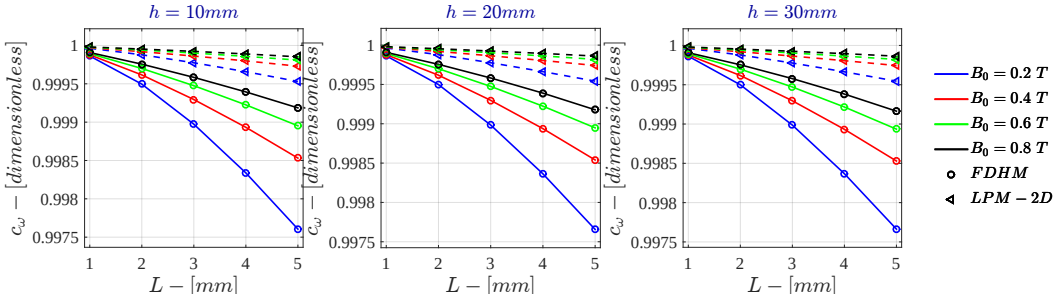

Figure I.27: *Bidimensional LPM* c_ω *for* $\sigma = 10^5\ S/m$ - $r_{out} = 50mm$

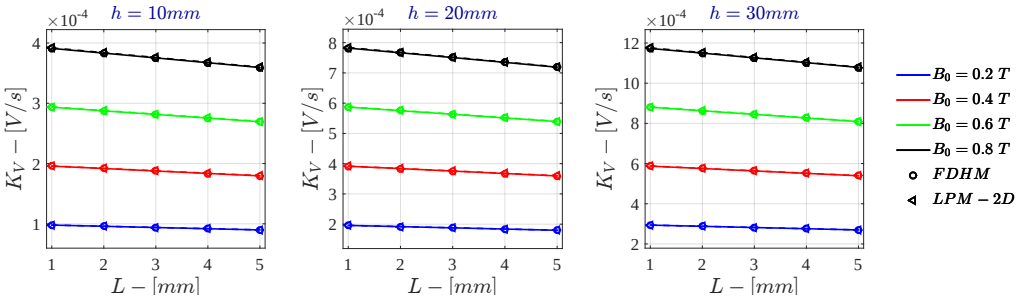

Figure I.28: *Bidimensional LPM* K_V *for* $\sigma = 10^5\ S/m$ - $r_{out} = 50mm$

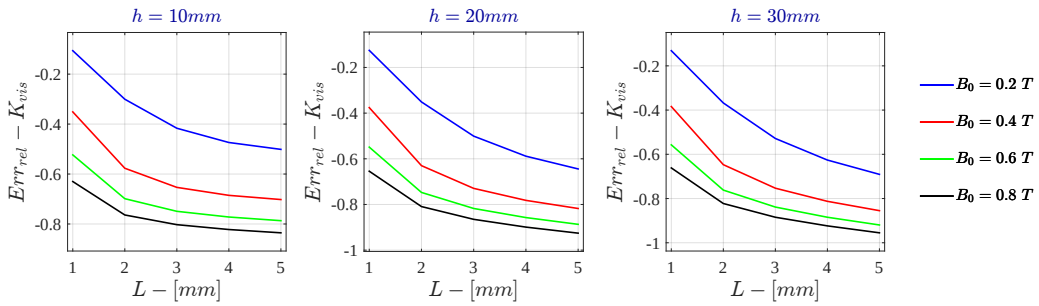

Figure I.29: *Bidimensional LPM*
Relative Error - K_{vis} for $\sigma = 10^5\ S/m$ - $r_{out} = 50mm$

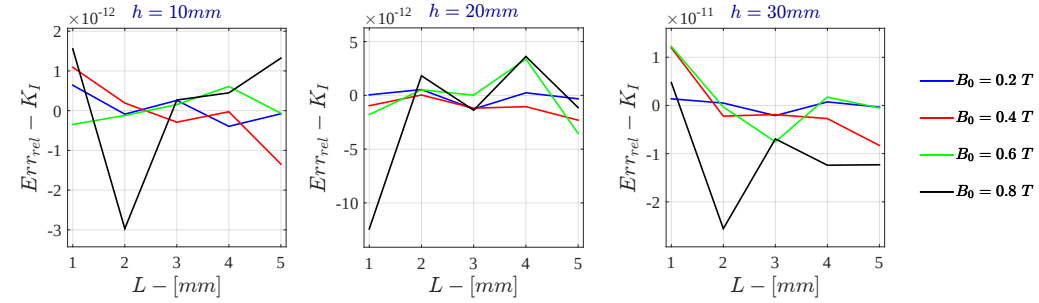

Figure I.30: *Bidimensional LPM*
Relative Error - K_I for $\sigma = 10^5\ S/m$ - $r_{out} = 50mm$

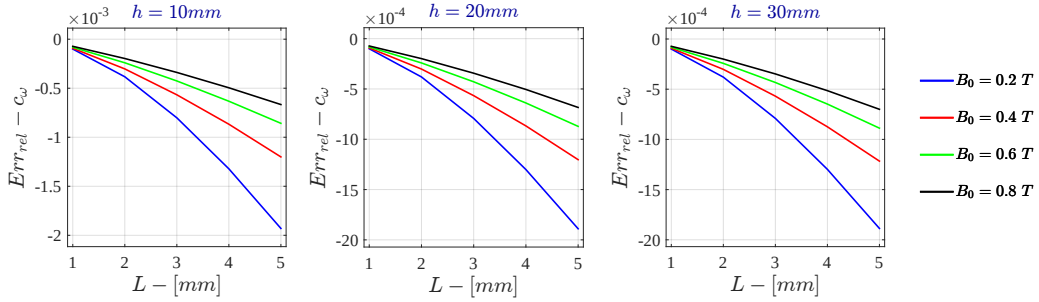

Figure I.31: *Bidimensional LPM*
Relative Error - c_ω for $\sigma = 10^5\ S/m$ - $r_{out} = 50mm$

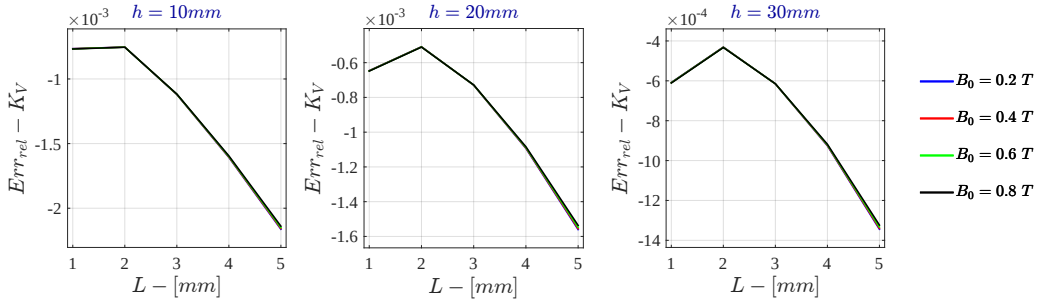

Figure I.32: *Bidimensional LPM*
Relative Error - K_V for $\sigma = 10^5\ S/m$ - $r_{out} = 50mm$

I.2.1 Current Drive

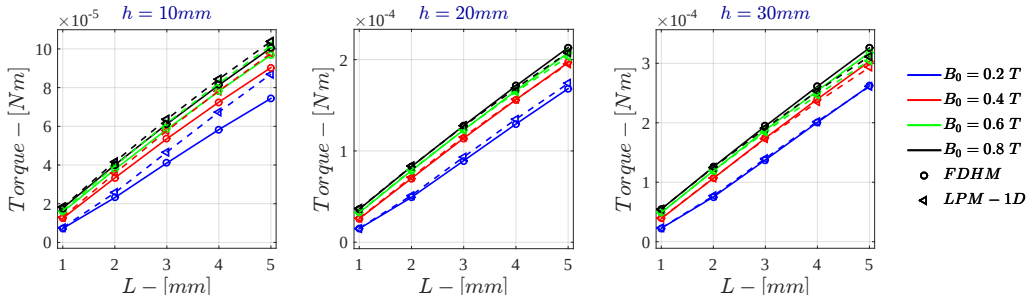

Figure I.33: *Bidimensional LPM - Current Drive* $\dot{\Gamma}$ *for* $\sigma = 10^5$ S/m - $r_{out} = 50mm$

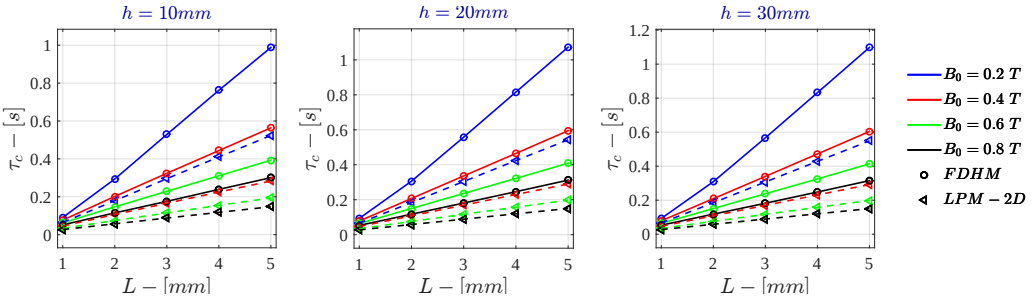

Figure I.34: *Bidimensional LPM - Current Drive* τ_c *for* $\sigma = 10^5$ S/m - $r_{out} = 50mm$

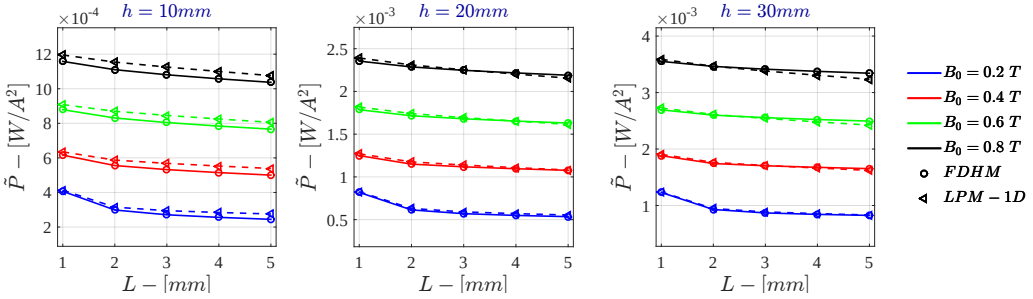

Figure I.35: *Bidimensional LPM - Current Drive* $\tilde{P}$ *for* $\sigma = 10^5$ S/m - $r_{out} = 50mm$

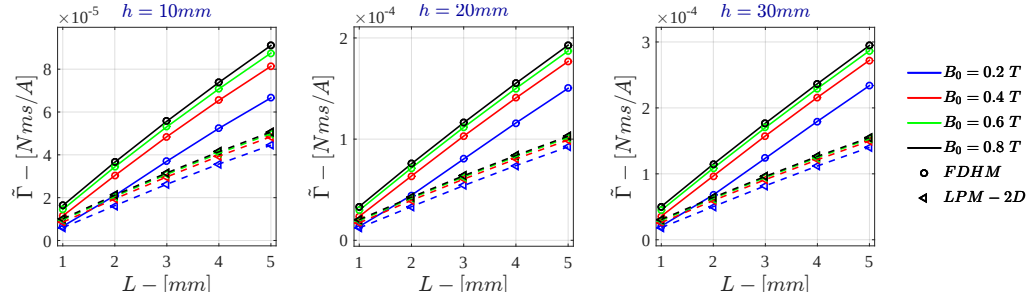

Figure I.36: *Bidimensional LPM - Current Drive* $\tilde{\Gamma}$ *for* $\sigma = 10^5$ S/m - $r_{out} = 50mm$

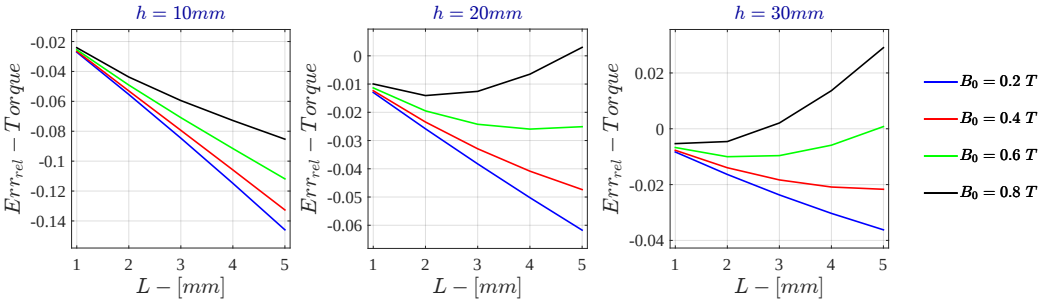

Figure I.37: *Bidimensional LPM - Current Drive*
Relative Error - $\dot{\Gamma}$ *for* $\sigma = 10^5\ S/m$ *-* $r_{out} = 50mm$

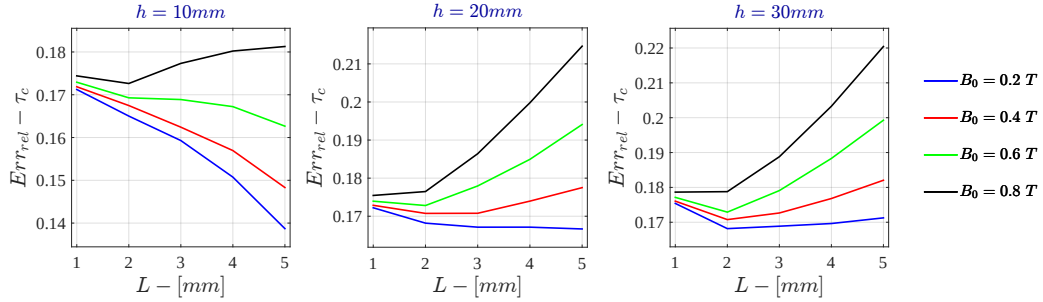

Figure I.38: *Bidimensional LPM - Current Drive*
Relative Error - τ_c *for* $\sigma = 10^5\ S/m$ *-* $r_{out} = 50mm$

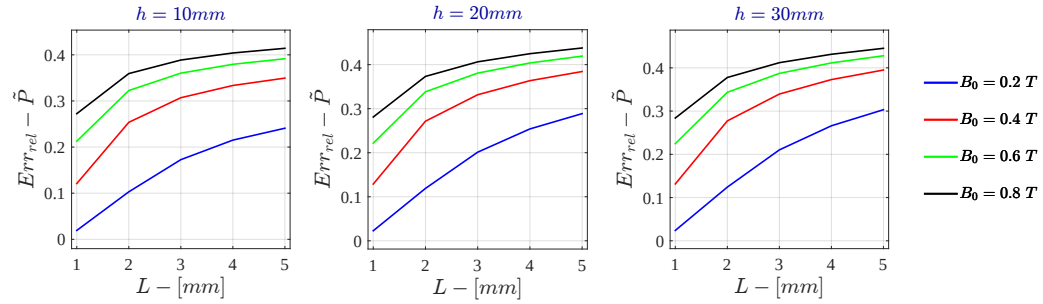

Figure I.39: *Bidimensional LPM - Current Drive*
Relative Error - $\tilde{P}$ *for* $\sigma = 10^5\ S/m$ *-* $r_{out} = 50mm$

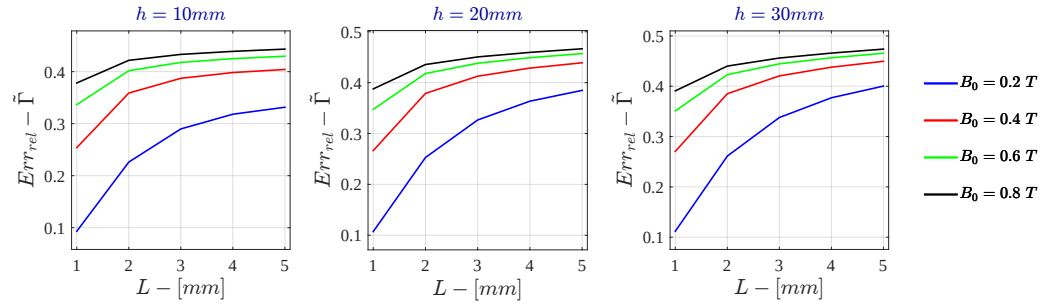

Figure I.40: *Bidimensional LPM - Current Drive*
Relative Error - $\tilde{\Gamma}$ *for* $\sigma = 10^5\ S/m$ *-* $r_{out} = 50mm$

I.2.2 Voltage Drive

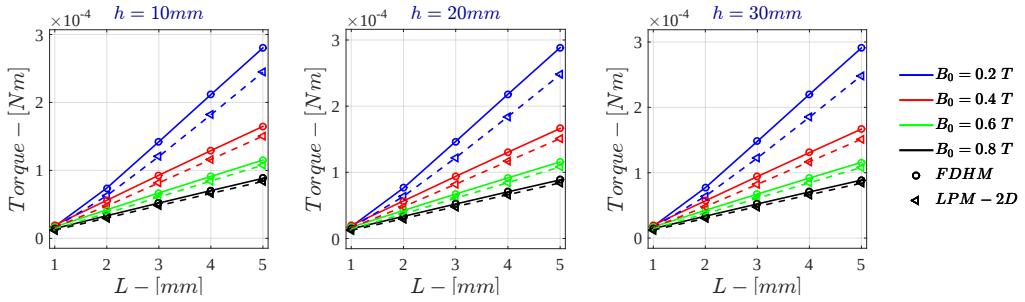

Figure I.41: *Bidimensional LPM - Voltage Drive* $\dot{\Gamma}$ *for* $\sigma = 10^5\ S/m$ *-* $r_{out} = 50mm$

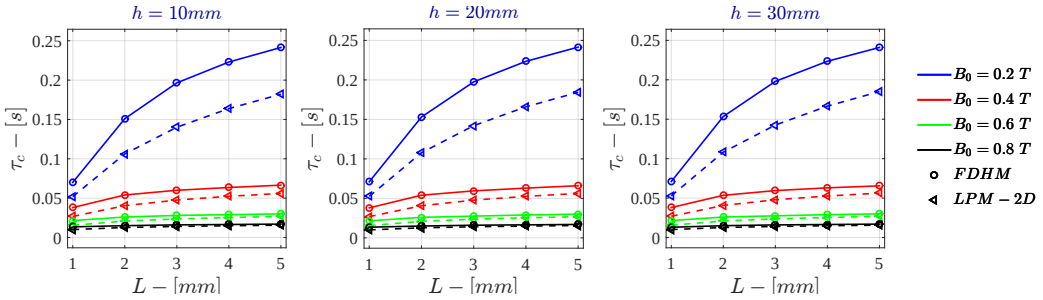

Figure I.42: *Bidimensional LPM - Voltage Drive* τ_c *for* $\sigma = 10^5\ S/m$ *-* $r_{out} = 50mm$

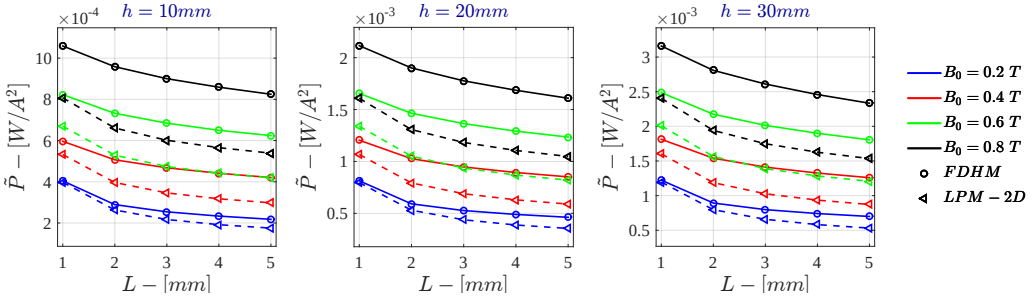

Figure I.43: *Bidimensional LPM - Voltage Drive* $\tilde{P}$ *for* $\sigma = 10^5\ S/m$ *-* $r_{out} = 50mm$

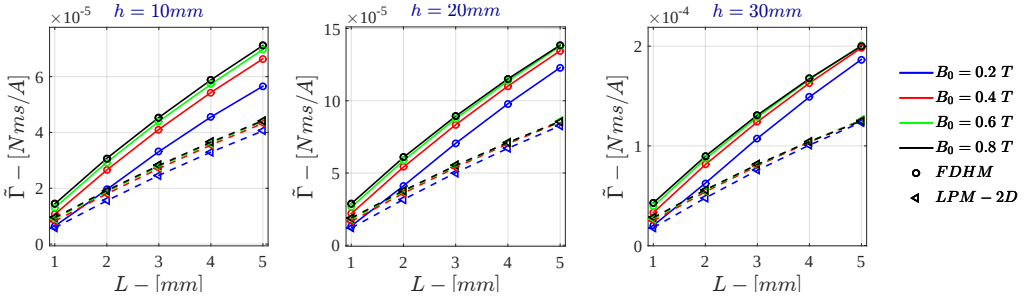

Figure I.44: *Bidimensional LPM - Voltage Drive* $\tilde{\Gamma}$ *for* $\sigma = 10^5\ S/m$ *-* $r_{out} = 50mm$

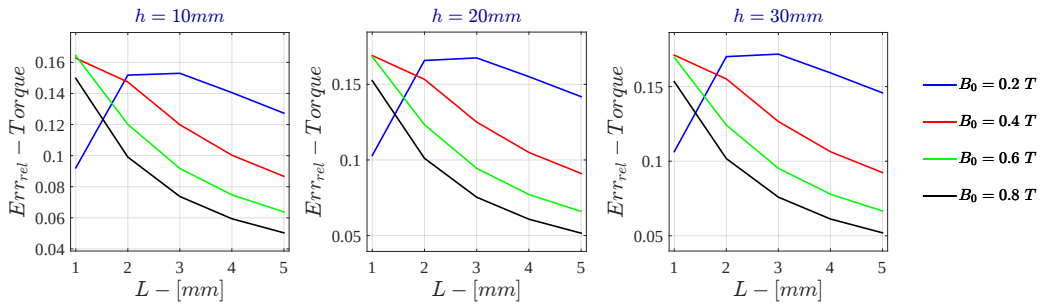

Figure I.45: *Bidimensional LPM - Voltage Drive*
Relative Error - $\dot{\Gamma}$ *for* $\sigma = 10^5\ S/m$ *-* $r_{out} = 50mm$

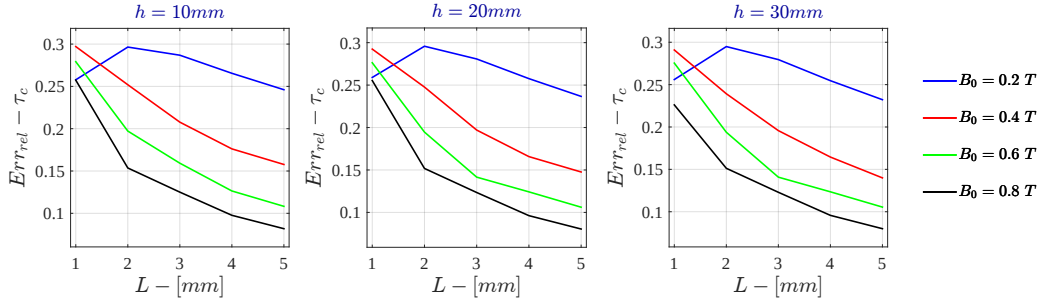

Figure I.46: *Bidimensional LPM - Voltage Drive*
Relative Error - τ_c *for* $\sigma = 10^5\ S/m$ *-* $r_{out} = 50mm$

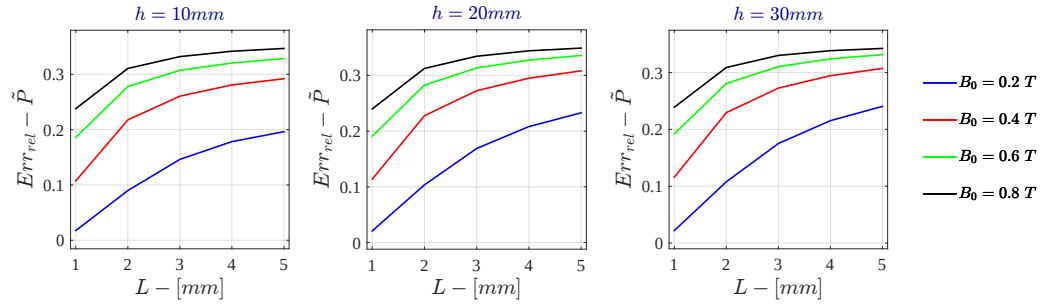

Figure I.47: *Bidimensional LPM - Voltage Drive*
Relative Error - $\tilde{P}$ *for* $\sigma = 10^5\ S/m$ *-* $r_{out} = 50mm$

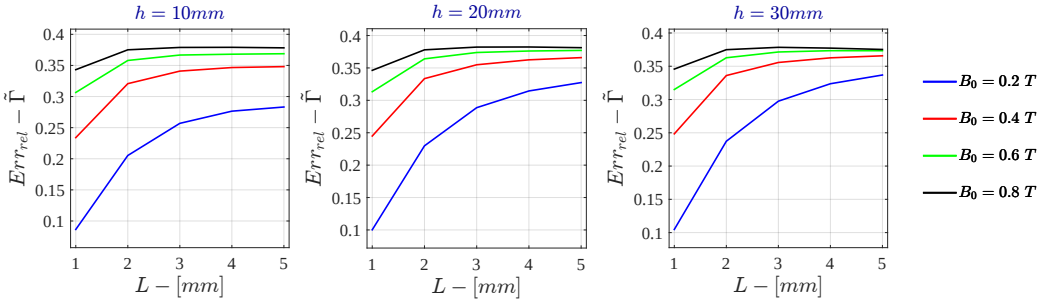

Figure I.48: *Bidimensional LPM - Voltage Drive*
Relative Error - $\tilde{\Gamma}$ *for* $\sigma = 10^5\ S/m$ *-* $r_{out} = 50mm$

Bibliography

[1] N. A. Nobari and A. K. Misra, "Satellite Attitude Stabilization Using Four Fluid Rings," *AIAA Guidance, Navigation, and Control Conference, Toronto, Canada*, 2010.

[2] K. D. Kumar, "Satellite Attitude Stabilization Using Fluid Rings," *Acta Mechanica Online*, Vol. 208, No. 1 2, 2009, p. 335 348.

[3] C. Casteras, Y. Lefevre, and D. Harribey, "Magnetohydrodynamic inertial actuator," 2013. WO Patent App. PCT/EP2013/053,101.

[4] D. R. Laughlin, "Magnetohydrodynamic (MHD) Actuator Sensor," 2007. U.S. Patent n. 7.171.853 B1.

[5] D. R. Laughlin, H. R. Sebesta, and D. E. Ckelkamp-Baker, "A Dual Function Magnetohydrodynamic (MHD) Device for Angular Motion Measurement and Control," *Advances in the Astronautical Sciences*, Vol. 111, 2002, p. 335 348.

[6] D. Noack and K. Brieb, "Laboratory investigation of a fluid-dynamic actuator designed for CubeSats," *ActaAstronautica*, Vol. 96, 2014, p. 78 82.

[7] T. C. I. Boris J. Lurie, J. Alan Schier, "Fluid-Loop Reaction System," 1991. U.S. Patent n. 5.026.008.

[8] N. A. Nobari and A. K. Misra, "Attitude Dynamics and Control of Satellites with Fluid Ring Actuators," *Journal of Guidance, Control, and Dynamics*, Vol. 35, No. 6, November December 2012, p. 1855 1864.

[9] R. P. Haviland, "Orientation Control for a Space Vehicle," 1958. U.S. Patent n. 2.856.142.

[10] J. C. R. Hunt and D. G. Malcolm, "Some electrically driven flows in magnetohydrodynamics Part 2. Theory and experiment," *J. Fluid Mech.*, Vol. 33, No. 4, 1968, p. 775 801.

[11] A. Salvati and F. Curti, "MHD Reaction Wheel for Spececraft Attitude Control: Configuration and Lumped Parameter Model," *IAA-AAS-DyCoSS2*, Rome 2014.

[12] J. A. Baylis and J. C. R. Hunt, "MHD flow in an annular channel: theory and experiment," *J. Fluid Mech.*, Vol. 48, No. 3, 1971, p. 423 428.

[13] U. Muller and L. Buhler, *Magneto-fluid-dynamics in Channels and Containers*. Springer.

[14] M. S. Tillack and N. B. Morley, *Magnetohydrodynamics*. McGraw Hill, 14th ed., 1998.

[15] P. Davidson, *An Introduction to Magnetohydrodynamics*. Cambridge University Press, 1st ed., 2001.

[16] M. C. P.J. Wang, C.Y. Changa, "Simulation of two-dimensional fully developed laminar flow for a magneto-hydrodynamic (MHD) pump," *Biosensors and Bioelectronics*, Vol. 20, 2004, p. 115 121.

[17] M. Kinet, "MHD Turbulence at Low Magnetic ReynoldsNumber: Spectral Properties and Transition Mechanism in a Square Duct," 2009. Universite Libre de Bruxelles - Phd Thesis.

[18] S. Cuevas and B. E. Picologlou, "Liquid-Metal MHD flow in rectangular ducts with thin conducting or insulating walls: Laminar and turbulent solutions," *Int. J. Engng Sci.*, Vol. 35, No. 5, 1997, p. 485 503.

[19] R. M. e. a. M. J. Ni, "A current density conservative scheme for incompressible MHD flows at a low magnetic Reynolds number. Part I: On a rectangular collocated grid system," *Journal of Computational Physics*, Vol. 227, 2007, p. 174 204.

[20] S. Vantieghem and B. Knaepen, "Direct numerical simulation of quasi-static magnetohydrodynamic annular duct flow," *V European Conference on Computational Fluid Dynamics, Lisbon, Portugal*, June 2010.

[21] J. A. Shercliff, "Steady motion of conducting fluids in pipes under transverse magnetic fields," *Mathematical Proceedings of the Cambridge Philosophical Society*, Vol. 49, No. 01, 1953, p. 136 144.

[22] J. C. R. Hunt, "Magnetohydrodynamic flow in rectangular ducts," *J. Fluid Mech.*, Vol. 21, No. 4, 1965, p. 577 590.

[23] J. C. R. Hunt, "Magnetohydrodynamic flow in rectangular ducts. II," *J. Fluid Mech.*, Vol. 23, No. 3, 1965, p. 663 681.

[24] A. Geri and G. Veca, "Performance analisys of a conduction pump with a superconducting magnet by means 0f a lumped-parameter model," Vol. 31, No. 1 2, 1995, p. 135 140.

[25] D. C. Moynihan and S. G. Bankoff, "Magnetohydrodynamic circulation of a liquid of finite conductivity in an annulus," *Appl. sci. Res.*, Vol. 12, No. B, 1964, p. 165 202.